Dissertation
submitted to the
Combined Faculties for the Natural Sciences and for Mathematics
of the Ruperto-Carola University of Heidelberg, Germany
for the degree of
Doctor of Natural Sciences

presented by
Dipl. Phys. Steffen Beirle
born in Bergisch-Gladbach

Oral examination: 22.12.2004

Estimating source strengths and lifetime of Nitrogen Oxides from satellite data

Referees: Prof. Dr. Ulrich Platt

Prof. Dr. Bernd Jähne

Zusammenfassung

In den letzten hundert Jahren hat sich die chemische Zusammensetzung der Atmosphäre, bedingt durch anthropogene Emissionen, nachhaltig geändert. Eine wichtige Rolle spielen dabei die Stickoxide $NO+NO_2$, die direkt Gesundheit und Umwelt beeinträchtigen, und darüberhinaus eine wichtige Rolle in katalytischen Reaktionen spielen, bei denen in der Troposphäre i.A. Ozon gebildet wird.

Die Messung von Spektren des an der Erde reflektierten Lichtes vom Satelliten aus ermöglicht die quantitative Bestimmung verschiedener Spurengase, darunter NO_2. In dieser Arbeit wurden Spektren von den Satelliteninstrumenten GOME und SCIAMACHY dazu verwendet, troposphärische Säulendichten von NO_2 zu ermitteln. Der resultierende Datensatz, der mittlerweile einen Zeitraum von 8 Jahren bei globaler Abdeckung umfasst, ermöglicht Untersuchungen über die Identifikation, Charakterisierung und Quantifizierung verschiedener Quellen von Stickoxiden. So konnten verschiedene anthropogene Quellen sowie Blitze und Biomassenverbrennung getrennt untersucht und z.T. quantifiziert werden.

Die räumliche Auflösung des GOME-Nachfolgers SCIAMACHY ermöglicht ferner die eindeutige Lokalisierung einzelner Quellen wie z.B. Städte oder größere Kraftwerke. Dies kann dazu beitragen, räumlich aufgelöste Emissionsinventare zu verbessern.

Schließlich konnten die Satellitendaten genutzt werden, um die Lebensdauer von Stickoxiden in der Troposphäre für verschiedene Regionen und Jahreszeiten zu bestimmen. Dies ermöglicht zum ersten mal den Vergleich von gemessener und modellierter Lebensdauer auf globaler Skala.

Abstract

Over the last hundred years, the chemical composition of the atmosphere has changed significantly due to anthropogenic emissions. Nitrogen oxides ($NO+NO_2$) play an important part, as they directly affect human health and environment, and are involved in chemical key reactions, leading to ozone production in the troposphere.

Spectral measurements from satellite platforms of the light reflected by the earth allow the retrieval of several trace gases, e.g. NO_2. In this thesis, the spectra of the satellite instruments GOME and SCIAMACHY were used to determine tropospheric column densities of NO_2. The resulting dataset, comprising eight years with global coverage, allows the identification, characterization and quantification of the different sources of nitrogen oxides. In this way different anthropogenic sources as well as lightning and biomass burning could be studied separately and partly be quantified.

The spatial resolution of the GOME successor SCIAMACHY allows furthermore the unequivocal localisation of individual sources like large cities or power plants. This helps to improve spatially resolved emission inventories.

Finally, the satellite data has been used to estimate the mean lifetime of nitrogen oxides in the troposphere for different regions and seasons. For the first time, this allows to compare measured and modelled lifetimes on a global scale.

Contents

Introduction

With the onset of the industrial revolution in the 19th century, anthropogenic emissions of several pollutants perturbed the natural balance of atmospheric composition. This has (and will have) severe impact on nowadays and future environment and climate:

- The release of ChloroFlouroCarbons (CFCs) leads to effective depletion of stratospheric ozone (“Ozone hole”), thus destructing the earth’s natural shield against UV-radiation in polar regions.
- The massive use of fossil fuels for energy production resulted in a large increase of atmospheric CO_2 levels, that (besides other greenhouse gases) probably will lead to an increase of global surface temperature and sea level rise over the next century.
- The exhaust from fossil (and bio-) fuel combustion leads to the phenomenon of urban air pollution (smog). Trace gases like nitrogen oxides or sulfur dioxide are directly affecting health (attacking the respiratory tract) and environment (e.g. through the formation of acid rain).

The links between atmospheric chemistry, radiative budget and biospheric and oceanic response are highly complex, and only partly understood today. However, the obvious diminution of quality of life by air pollution, as well as the potential impact of climate change (e.g. temperature increase, sea level rise and increase of extreme weather events) lead to an awareness of environmental protection issues. International treaties like the Montreal and the Kyoto protocol are hopefully a first step in controlling the release of different emittents on a global scale.

For a better understanding of the processes taking place in the atmosphere, it is essential to know location and strength of sources, and to get global information of the state of the atmosphere. Such information can be provided by satellite instruments.

Over the last decades, the potential of remote sensing measurements on satellite platforms were increasingly used to analyze various parameters of the state of the earth, e.g. daily weather, magnetic field, topography, land cover, ocean waves or temperature. Satellite data has also successfully been used to analyze the chemical composition of the atmosphere by measuring spectra of the light reflected (or emitted) by the earth’s ground and atmosphere. Such measurements were (and are) performed by instruments using different spectral ranges (e.g. UV, IR, microwave) and viewing geometries, with different potentials and limitations.

In 1995, the Global Ozone Monitoring Experiment (GOME), a UV-vis spectrometer, was launched on ERS-2. As suggested by its name, GOME was designed for the monitoring of (mainly stratospheric) ozone. However, it proved to be also useful for the determination of other trace gases, like OClO, BrO, CH_2O, SO_2 and NO_2.

As measurements from GOME (and its successor SCIAMACHY) are performed in the UV-vis spectral range in a nadir viewing geometry, they are in fact also sensitive to absorbers near the ground, and thus proved to be applicable for the determination of tropospheric trace gases, although in that case one must deal with complications like clouds or aerosols affecting the light path through the atmosphere.

Among the tropospheric species that can be determined by GOME and SCIAMACHY, NO_2 plays an important role: Due to its reactivity, it directly affects human health and environment. Furthermore, it is involved in catalytic cycles that generally form ozone in the troposphere, with impact on the radiative balance and the oxidizing power of the atmosphere. Despite its importance, current knowledge of source strengths and chemistry of nitrogen oxides still has rather high uncertainties. Also knowledge on the lifetime of nitrogen oxides is important, but based (besides model outputs) on very few measurements up to now.

This PhD thesis uses spectral data from GOME and its successor SCIAMACHY (providing global datasets for eight years now) to determine tropospheric column densities of NO_2. The resulting dataset holds a lot of information that was investigated with respect to current questions regarding the role of nitrogen oxides in the atmosphere:

- What are the main sources, and where are they located?
- Can we discriminate the different sources from satellite?
- What are their respective source strengths?
- Which influences do atmospheric transport processes have with respect to the distribution of NO_2?
- How long is the lifetime of nitrogen oxides?

In order to address these questions we make use of the specific advantages of satellite measurements: The global coverage and the long time series. Characteristic patterns in the spatial distribution of NO_2 can be compared to other independent data sets like the geographical location of cities and ship tracks or to emission inventories. Temporal variations on various time scales like weekly cycles, seasonal cycles, variations from year to year or trend studies can be performed with relatively high significance due to the long time series of measurements.

After a review on the chemistry of nitrogen oxides in Chapter 1, we describe the data retrieval in Chapter 2, including a brief overview of the respective satellite instruments, the DOAS technique, radiative transfer, and the separation of stratospheric and tropospheric NO_2 columns. Chapter 3 summarizes the current knowledge of source strengths of nitrogen oxides, and discusses the potential of satellite data to identify and quantify different sources. Some sources are discussed in detail in the subsequent chapters:

Anthropogenic activity in western countries is reduced on weekends, leaving a fingerprint in the NO_2 observed from space (Chapter 4). From this finding information on the relative importance of different anthropogenic sources like industry, traffic, heating, and energy consumption can be deduced.

Chapter 5 deals with emissions from aircrafts that seemingly cannot be detected in satellite NO_2 data.

Highest uncertainty of current knowledge of sources of nitrogen oxides is on the contribution of lightning. In Chapter 6 we describe two studies identifying the effect of lightning on NO_2 and even use GOME data to estimate absolute values.

In Chapter 7 the emissions from biomass burning are discussed. Large burning events leave a clear fingerprint of enhanced NO_2. Quantitative estimates however are complicated due to the complex radiative transfer in the presence of aerosols also produced by biomass burning.

After these discussions of the various sources of nitrogen oxides and their strengths, transport events are investigated: Local emissions may also affect remote regions in the case of long range transport. Such transport events can be observed in satellite data. The impact of single transport events as well as mean effects on longer timescales are analyzed in Chapter 8.

Chapter 9 deals with the spatial information retrieved from highly resolved (<=60km) satellite observation modes. For the first time, the spatial distribution of tropospheric NO_2 could be determined with such a high resolution on a global scale, that even single cities and power plants can be identified. The comparison of our results to emission inventories shows generally a good agreement, but also reveals some inconsistencies in the spatial distribution of NO_2.

An important quantity for translating measured NO_2 column densities to actual emissions is the mean lifetime of nitrogen oxides. In Chapter 10 we demonstrate that satellite data itself can be used to estimate the mean lifetime. This data, based on measurements, is a valuable addition to model estimates.

Finally, we present a study on ship emissions (Chapter 11), as it comprises several aspects discussed before: the clear identification of a pattern of enhanced NO_2 corresponding to a ship track that was possible due to the spatial information; the mean lifetime for this case could be estimated from the satellite data itself; finally an estimate on absolute ship emissions could be given and compared to previous investigations.

Chapter 1
Nitrogen oxides

Nitric oxide (NO) and nitrogen dioxide (NO_2) are rapidly converted into each other in the daytime atmosphere. Therefore they are commonly summed up to the more conservative quantity NO_x:=NO+NO_2, that we term "nitrogen oxides" for simplicity afterwards (however, note that also other oxides of nitrogen exist).

NO_x is produced naturally by lightning, natural fires and emissions from soils, but nowadays the main fraction stems from fossil fuel combustion and biomass burning due to anthropogenic activity. Thus tropospheric levels of NO_x have likely doubled over the last hundred years in the northern hemisphere, and exceed natural background levels (~ppt) by several orders of magnitude for polluted urban air (~ppb) [Seinfeld and Pandis, 1997].

Nitrogen oxides are among the most important trace gases in the atmosphere: As both, NO and NO_2, are radicals, they are highly reactive. Therefore they affect human health, as they attack the respiratory track. Furthermore, they are key substances involved in several chemical reactions and catalytic cycles that destroy ozone in the stratosphere, and provide the only way to produce ozone in the troposphere, thus affecting the radiative budget and the oxidizing capacity of the atmosphere.

Here we give an overview of the general reaction mechanisms where nitrogen oxides are involved. First we discuss the general formation mechanisms of NO_x. Afterwards we summarize basic reactions for NO_x in stratosphere and troposphere; thereby the focus is set (as for the whole thesis) to the latter. Finally we discuss sink mechanisms and lifetime of NO_x. For a more detailed description of the chemistry of Nitrogen Oxides we refer to e.g. [Jacob, 1999; Seinfeld and Pandis, 1997; Solomon, 1999 (stratosphere); Atkinson, 2000 (troposphere)].

1.1. NO - NO_2 coupling and Leighton ratio

Nitric oxide reacts with ozone to nitrogen dioxide:

(R1) $NO + O_3 \rightarrow NO_2 + O_2$ (k1)

In the sunlit atmosphere, NO_2 is photolyzed (at wavelengths below 420 nm) to NO and an oxygen radical:

(R2) $NO_2 + h\nu \rightarrow NO + O$

The latter rapidly reacts with molecular oxygen to ozone:

(R3) $O + O_2 + M \rightarrow O_3 + M$

As this photochemical cycle closely couples NO and NO_2 on a relatively fast timescale, it is useful to treat them as the more conserved sum, usually termed NO_x (=NO+NO_2).

The ratio

(1.1) $L := [NO] / [NO_2] = J(NO_2) / (k1\ [O_3])$

("Leighton ratio") depends on ozone concentration, NO_2 photolysis rate and temperature. We also define the percentage of NO_x present as NO_2 (in equilibrium):

(1.2) $f_{NO2} := [NO_2] / [NO_x] = 1 / (1+L)$

Close to the ground, most NO_x is present in form of NO_2 ($f_{NO2} \sim 0.7$, $L \sim 0.4$), except close to sources where huge amounts of NO are emitted and ozone is titrated via (R1). With increasing altitude, the Leighton ratio is shifted towards NO due to the temperature dependence of (k1) and higher NO_2 photolysis rates; at 10 km, f_{NO2} is about 0.4 ($L = 1.5$).
During night, however, all NO_x is shifted to NO_2 because no photolysis (R2) takes place.

1.2. Formation of NO_x

Most NO_x is primarily emitted as nitric oxide (NO) and subsequently transformed to NO_2 by reaction (R1). The dominating mechanism leading to formation of NO is the "Zel'dovich mechanism" [Zel'dovich and Raizer, 1966]: In connection with high temperatures (>2000K), that arise in burning processes (i.e. any kind of fossil fuel combustion or biomass burning) or lightning, air molecules (particularly O_2) dissociate:

(R4) $O_2 + M \leftrightarrows O + O + M$,

where M is an inert molecule needed for conserving momentum.
NO is subsequently formed in the Zel'dovich reactions:

(R5) $O + N_2 \leftrightarrows NO + N$
(R6) $N + O_2 \leftrightarrows NO + O$

The equilibria (R5) and (R6) strongly depend on temperature and are shifted to the right side for high temperatures. If the gas is exposed to a rapid cooling process (i.e. faster than the time the system needs to achieve equilibrium) the NO is "freezing out".
Further sources of nitrogen oxides are microbiological processes in soils [Yienger and Levy, 1995].
The transport of tropospheric NO_x to the stratosphere is only of minor importance, as they usually are too short lived (see Chapter 10). However, nitrous oxide (N_2O), that is also emitted by soils as well as chemical industry (N_2O is a widely used propellant) is rather inert in the troposphere. In the stratosphere it is photolyzed, but may be also oxidized to NO by reaction with electronically excited oxygen radicals:

(R7) $N_2O + O(^1D) \rightarrow 2\ NO$

(R7) is the most important source of NO_x in the stratosphere.

1.3. Reservoirs of NO_x

Reactions of NO_x lead to several intermediate products containing nitrogen, e.g. HNO_3, NO_3, N_2O_5, HONO, HNO_4. These are usually summed up as NO_y. While HNO_3 is actually removed from atmosphere by rainout (see sections 1.5.3 and 1.5.4), the other NO_y components are usually converted back to NO_x by reactions and/or photolysis, and are thus rather a reservoir than a sink of NO_x. Especially peroxyacetylnitrate (PAN), the product of photochemical oxidation of carbonyl compounds in the presence of NO_x, is of importance, as it is very stable at low temperatures and hence has a rather long lifetime (of up to several months at 250 K [Jacob, 1999]), and is thus the most important compound for the long range transport of NO_x, maintaining NO_x levels of above 10-50 ppt throughout the troposphere.

1.4. Chemistry of NO_x in the stratosphere

1.4.1. Ozone destruction

The stratospheric ozone layer (at about 15-30 km) protects life on Earth by absorbing the sun's UV radiation. It is maintained by a balance of ozone production from photolysis of molecular oxygen ("Chapman mechanism") and ozone destruction by catalytic cycles. Besides hydrogen oxides ($HO_x := OH + HO_2$) and halogen oxides, such a catalytic ozone destruction cycle is also provided by NO_x:
In the stratosphere, NO_2 (alternatively to photolysis (R2)) reacts with atomic oxygen from oxygen photolysis:

(R8) $NO_2 + O \rightarrow NO + O_2$

Reactions (R1) and (R8) represent a catalytic cycle destroying ozone:

net: $O_3 + O \rightarrow 2O_2$

Anthropogenic emissions of N_2O (direct and indirect via the change of land use) and NO (from supersonic aircrafts in the lower stratosphere) thus probably lead (besides the effect of CFCs) to the reduction of the ozone layer over the last decades.

1.4.2. Polar ozone loss

Similar to the ozone destruction by NO_x, Chlorine oxide (ClO) catalyzes ozone loss. However, this cycle is terminated by the reaction

(R9) $ClO + NO_2 + M \rightarrow ClNO_3 + M$

Thus, while NO_x itself provides ozone loss, it slows down the ozone depletion by chlorine oxides by converting ClO ("active chlorine") to the nonradical chlorine reservoirs $ClNO_3$ ("inactive chlorine").
In polar winter, solar radiation is missing and NO_x is transformed to reservoir species NO_y that are not photolyzed any more ("denoxification"). Furthermore, the "polar vortex" forms, i.e. a strong circulation centered at the pole that separates polar air from the midlatitudes.

Temperatures below 190 K allow the formation of polar stratospheric clouds (PSCs) that provide surfaces for the heterogeneous reaction

(R10) $ClNO_3 + HCl \rightarrow Cl_2 + HNO_3$

Over the course of winter, sedimentation of HNO_3-containing PSCs takes place and the reservoirs of nitrogen oxides are effectively removed from the polar vortex ("denitrification"). In spring, when sun rises, photolysis of Cl_2 starts the catalytic ozone destruction cycles that work very efficient and destroy typically all ozone at about 15-20 km in the Antarctic, as (R9) cannot take place due to missing NO_x. The destruction is terminated when the polar vortex breaks up and NO_x is restored by inflow from midlatitudes.

1.5. Chemistry of NO_x in the troposphere

In the troposphere, NO_x chemistry is generally different from the stratosphere. In particular, (R8) is negligible due to low concentrations of atomic oxygen. Furthermore, tropospheric air masses also contain CO, CH_4 and volatile organic compounds (VOCs). The oxidation of these carbon containing compounds in the presence of NO_x results in most cases in ozone production, as explained exemplarily for carbon monoxide in 1.5.1. For very high levels of NO_x, however, increasing NO_x does not lead to higher ozone production any more; this phenomenon of the VOC-limited regime will be described in 1.5.2. Loss reactions and lifetime of NO_x are discussed in 1.5.3.-1.5.4. Finally, we discuss the ozone production efficiency of NO_x in 1.5.5.

1.5.1. Oxidation of CO, CH_4 and VOCs

The oxidation of several atmospheric pollutants is driven by reactions with the hydroxyl radical OH that is produced by the reaction of $O(^1D)$ radicals with water vapour. Due to its high reactivity OH initiates several reaction chains and is sometimes called "cleansing agent" of the atmosphere as it removes several pollutants. The lifetime of several gases (e.g. methane) is directly linked to the global mean OH concentration.
We exemplarily discuss the oxidation of CO: It is initiated by reaction with OH

(R11) $CO + OH \rightarrow CO_2 + H$

The hydrogen radical combines with molecular oxygen:

(R12) $H + O_2 \rightarrow HO_2$

In the presence of nitric oxide, the reaction

(R13) $NO + HO_2 \rightarrow NO_2 + OH$

competes with (R1). The resulting net reaction of (R2, R3, R13) is

net: $CO + 2O_2 \rightarrow CO_2 + O_3$

The oxidation of CH_4 and VOCs is more complex, as several branchings of reaction paths occur. However, generally peroxy radicals (RO_2) are produced that can oxidize NO to NO_2, in analogue to (R13):

(R14) $NO + RO_2 \rightarrow NO_2 + RO$

and lead to ozone production (R2, R3, R14).

Thus the oxidation of CO and VOCs generally leads to ozone production ("ozone pump", see Fig. 1.1), if NO_x levels are high enough to compensate the ozone losses of the HO_x loss cycle. For NO_x levels above ~ 10-30 ppt (i.e. for most regions of the world except very clean, remote regions), ozone is formed.

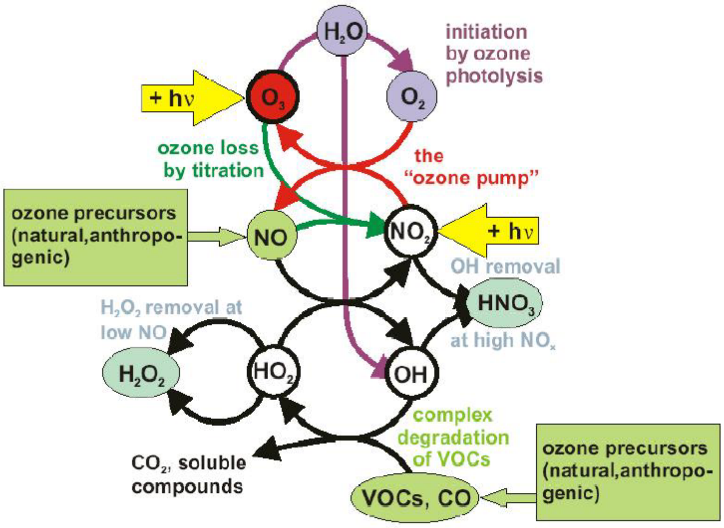

Fig. 1.1. Scheme of tropospheric NO_x chemistry [Schurath, 2003].

1.5.2. VOC limited regime

For very high NO_x concentrations (up to several 100 ppb in urban polluted air), however, the reaction

(R15) $NO_2 + OH \rightarrow HNO_3$

competes with reactions of OH with CO (R11) and VOCs.
Hence, in contrast to the discussion in 1.4.1., the resultant increase in NO_x emissions may reduce ozone concentrations, if not enough VOCs are present for the formation of HO_2 and RO_2. Therefore this is called the "VOC-limited" regime, in contrast to the "NO_x limited" case in 1.4.1., where ozone increases with increasing NO_x emissions. This is illustrated in Fig. 1.2.
For a successful control strategy of ozone air pollution in cities, it is thus crucial to discriminate between VOC limited and NO_2 limited regimes and focus on the reduction of the limiting pollutants [Sillman and He, 2002].

1.5.3. Sinks of NO_x

The catalytic cycles of NO_x in stratosphere and troposphere are terminated by the removal of NO_x. At daytime, NO_2 reacts with OH to HNO_3:

(R15) $NO_2 + OH \rightarrow HNO_3$

At nighttime, reaction with ozone produces NO_3

(R16) $NO_2 + O_3 \rightarrow NO_3 + O_2$

that further reacts with NO_2

(R17) $NO_3 + NO_2 + M \leftrightarrows N_2O_5 + M$

On aerosols, N_2O_5 can react heterogeneously

(R18) $N_2O_5 + H_2O \rightarrow 2HNO_3$

HNO_3 (from R15, R18) is finally removed from atmosphere by precipitation. This is (besides H_2SO_4) the important constituent of acid rain, causing severe damage to natural environments like lakes and forests ("waldsterben").

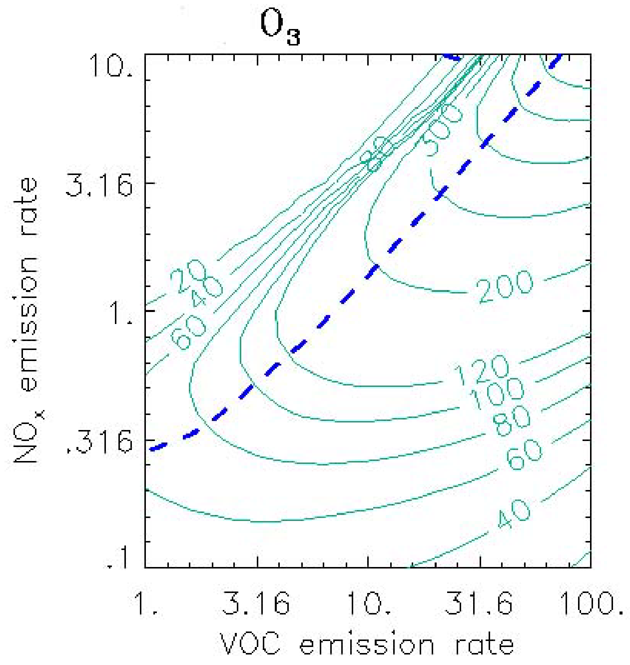

Fig. 1.2: Ozone isopleths (ppb) as a function of the average emission rate for NO_x and VOC (10^{12} molec cm^{-2} s^{-1}) in 0-d calculations. The isopleths (solid green lines) represent conditions during the afternoon following 3-day calculations with a constant emission rate, at the hour corresponding to maximum O_3. The blue dashed line represents the transition from VOC-limited to NO_X-limited conditions (adopted from [Sillman and He, 2002]).

1.5.4. Lifetime of NO_x

NO_x is finally removed from the atmosphere mainly by wet deposition of HNO_3. Hence the lifetime τ of NO_x depends on the concentrations of the species involved in (R 15-18) (i.e. $[O_3]$, [OH] and thus $[H_2O]$), furthermore on aerosol concentration, Leighton ratio, i.e. also temperature and $J(NO_2)$, thus the actinic flux. As a consequence, it is highly variable in time and space. Typical values are of the order of several hours for the polluted lower troposphere up to some days for the upper troposphere (mainly due to the pressure dependency of (R15)). Current knowledge of τ however is gained from some in-situ measurements on the one hand, and from model calculations solving complex VOC-NO_x-chemistry schemes with limited resolution in time and space on the other hand. An estimation of τ using satellite data will be presented in Chapter 10.

1.5.5. Ozone production efficiency

As we saw in 1.4.1. and 1.4.2., the level of tropospheric NO_x controls the production of ozone. In order to forecast the impact of given NO_x emissions on ozone, the concept of ozone production efficiency (OPE) was introduced. OPE ε is defined as ozone molecules produced over the lifetime of one NO_x molecule [Jacob, 1999]:

$$\varepsilon = P(O_3) / L(NO_x) \tag{1.3}$$

ε can be discussed qualitatively by assuming (R13) followed by (R2),(R3) as only source of ozone and (R15) as only sink of NO_x:

$$\varepsilon = k_{13} [HO_2][NO] / k_{15} [NO_2][OH] \tag{1.4}$$

In the case of high NO_x levels, ε is rather low, as the $[HO_2]/[OH]$ ratio is shifted to [OH] by (R13). Values of ε over the United States are typically in the range of 1 - 20 [Jacob 1999]. For low levels of NO_x, on the other hand, ε is several times higher. Thus the effect of a fixed amount of NO_x released to the atmosphere on ozone production depends on the prevailing level of NO_x, and thus emissions in remote, clean regions (e.g. by lightning or ship emissions) have a much higher impact on ozone formation.

Chapter 2
Retrieval

Nitrogen dioxide (NO_2) has narrow absorption structures in the blue and near UV spectral range. Hence it can be detected by absorption spectroscopy techniques. In this thesis, spectral data from satellite instruments (section 2.1) is used to derive column densities of NO_2 (section 2.2). The impact of radiative transfer on the derived column densities is discussed in section 2.3. Section 2.4 deals with stratospheric NO_2, that is of importance especially for polar chemistry. However, within this PhD thesis the focus is set on tropospheric NO_x. For this, stratospheric NO_2 is rather impeding as it masks the tropospheric column. Hence the stratospheric column has to be estimated and subtracted from total column. Finally, in section 2.5 some comparisons of our results with other measurements are shown.

2.1. The satellite instruments GOME and SCIAMACHY

Satellite instruments are established tools for investigating the earth's state. E.g. weather satellites are indispensable for meteorological forecasts nowadays. The remote sensing of atmospheric chemistry started in 1970 with Nimbus 4 with a backscatter ultra violet detector for monitoring atmospheric ozone. This kind of measurements have been continuously improved: data from Total Ozone Mapping Spectrophotometers (TOMS) provide a time series of total ozone columns back to 1978.

2.1.1. European research satellites

In 1995, the European Space Agency (ESA) launched the European Remote Sensing Satellite **ERS-2** (see Fig. 2.1) as successor of ERS 1. It carries several instruments for the investigation of the earth's properties like topography (Radar Altimeter (RA)), wind and wave fields (Active Microwave Instrument (AMI)) or sea surface temperature (Along-Track Scanning Radiometer (ATSR)). The latter allows also to detect temperature hot spots connected with fires.

A new instrument on ERS-2 (that was not part of ERS-1) is the Global Ozone Monitoring Experiment (GOME) that was proposed by J. Burrows and P. Crutzen. GOME allows the detection of several atmospheric trace gases as explained below in 2.2.

In March 2002, the European ENVironmental SATellite **ENVISAT**, the largest research satellite ever, was launched (Fig. 2.2). It has a size of 25m x 7m x10m (with solar panel deployed) and weights 8.2 t at launch. ENVISAT is equipped with 10 instruments, making it an unique, powerful tool for monitoring the state of the earth and impact of human activities on environment and climate. In analogy to ERS-2, it carries a Radar Altimeter (RA-2), combined with a MicroWave Radiometer (MWR) to correct for water vapour, and an Advanced Along-Track Scanning Radiometer (AATSR). Furthermore it carries several new instruments:

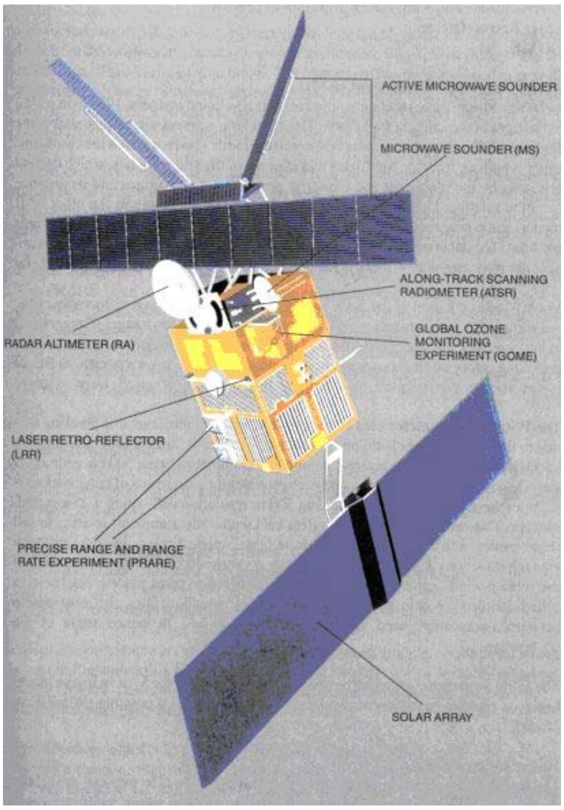

Fig. 2.1: Scheme of ERS-2 (adopted from [Bednarz, 1995])

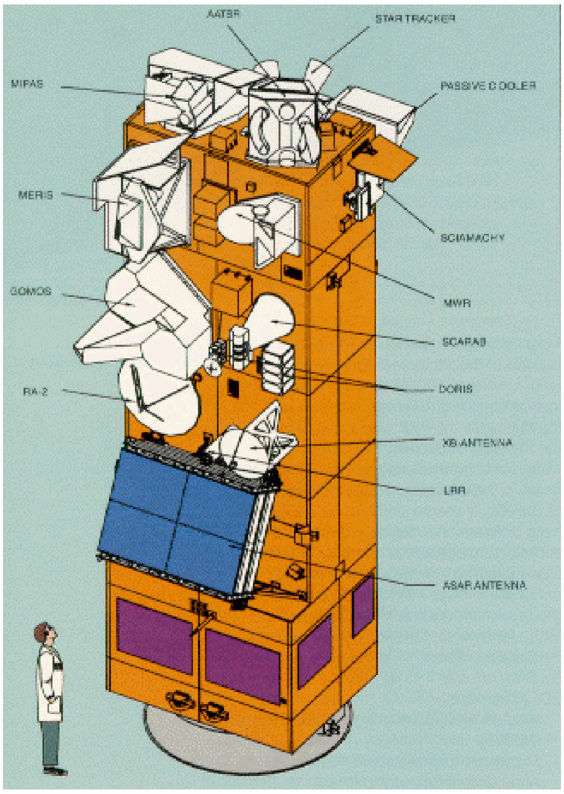

Fig. 2.2: Scheme of ENVISAT (ESA/ ESRIN)

- The Advanced Synthetic Aperture Radar (ASAR) allows to derive topography of the globe, average wave height or ground movements (with a detection limit of 1 mm/year, using interferometry).
- The Medium Resolution Imaging Spectrometer (MERIS) has several channels in the UV-Vis range. Applications are e.g. the determination of chlorophyll concentrations in the ocean, cloud top heights and optical thickness, water vapour content, aerosols, and land cover identification.

Three instruments deal with the exploration of the earth's atmosphere:

- The Global Ozone Monitoring by Occultation of Stars (GOMOS) measures spectra of stellar light passing the earth's atmosphere, allowing the retrieval of vertical profiles of e.g. ozone, NO_2, NO_3, H_2O above 20 km.
- The Michelson Interferometer for Passive Atmospheric Sounding (MIPAS) measures the earth's infrared emission in a limb geometry. This allows the retrieval of stratospheric profiles of several gases like O_3, H_2O, CH_4, N_2O, and HNO_3.
- Finally, ENVISAT also carries the SCanning Imaging Absorption spectroMeter for Atmospheric CartograpHY (SCIAMACHY), the successor of GOME. It will be described in detail in 2.1.3.

The flight characteristics of ERS-2 and ENVISAT are almost identical. Both satellites operate at an altitude of about 800 km on a nearly polar orbit, synchronized to sun. I.e. the local time at equator crossing is 10:30 (ERS-2) and 10:00 (ENVISAT), respectively. The earth is orbited about 14 times per day, corresponding to a satellite speed of about 6.7 km/s. The track of the satellites repeats exactly every 35 days.

2.1.2. GOME

GOME [Bednarz, 1995; Burrows et al., 1999] is a passive UV/vis spectrometer which measures the light reflected from the Earth's surface or scattered from the atmosphere. GOME consists of four separate channels covering the spectral range from 240 to 790 nm with a moderate spectral resolution of 0.17 to 0.33 nm (FWHM) (see Table 2.1).

Table 2.1 Spectral properties of the different channels of GOME

Channel	Spectral range [nm]	Spectral resolution (FWHM) [nm]
1	240 - 316	0.2
2	311 - 405	0.17
3	405 - 611	0.29
4	595 - 793	0.33

Figure 2.3 shows a scheme of GOME. The light enters the GOME instrument via a scanning mirror and two telescope mirrors, then it is separated into the wavelength intervals of the different channels by prisms and beam splitters. For the final dispersion of the light four gratings are used. The spectra are sampled by photodiode arrays of 1024 photodiodes each.
Besides the measurements of the light reflected from the Earth GOME also performs observations of direct sun and moon light. The moon light is measured via the scanning mirror. For the sun measurements the light intensity is reduced by a diffuser plate. Also included in the instrument is a calibration unit consisting of a Pt-Cr-Ne-lamp. The emission lines of these elements are distributed over the whole wavelength range of the GOME instrument.

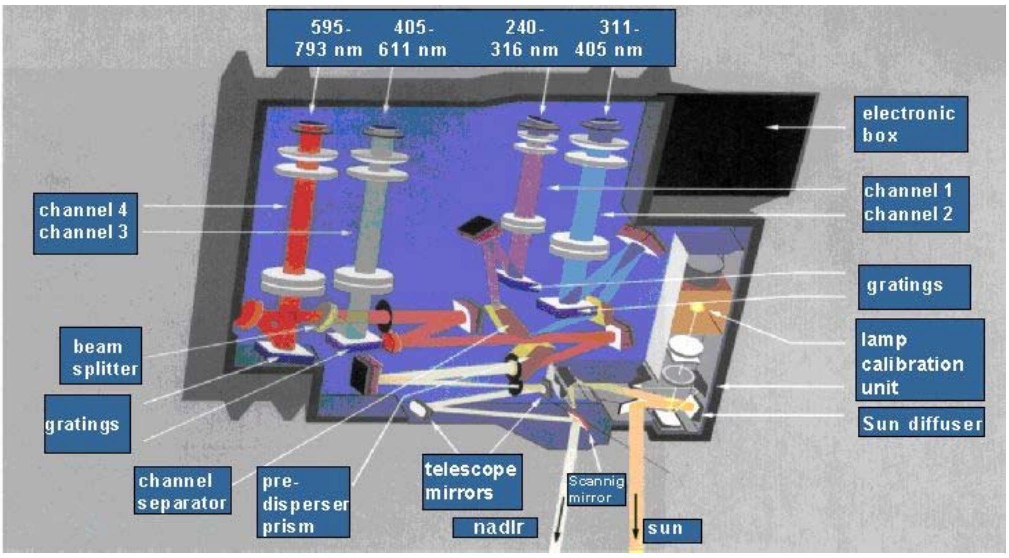

Figure 2.3: Scheme of the GOME spectrometer (adapted from [Bednarz, 1995])

GOME measures earthshine spectra in a nadir viewing geometry, i.e. is looking radial towards the earth. The Earth's surface is scanned with an angular range of ±31.0°, corresponding to a cross track swath width of 960 km. During each scan, three ground pixels are mapped with a spatial resolution of 320 km east-west and 40 km north-south, followed by one backscan pixel with an extent of 960*40 km^2 (see Fig. 2.4).

Besides this standard size mode (SSM), GOME is operated in the so called narrow swath mode (NSM) three days a month (4th/5th, 14th/15th and 24th/25th) since end of June 1997. These measurements are performed with a reduced scan angle of ±8.7°, corresponding to a spatial extent of 80*40 km^2 (forescan) and 240*40 km^2 (backscan) of the ground pixels (see Figs. 2.4 and 2.5).

Although the repeat cycle of the satellite is 35 days, global coverage is already achieved after 3 days (for standard size mode). Towards higher latitudes the overlap of the area observed by GOME for following satellite orbits increases. For example polewards of about 75° the earth's surface is totally covered by GOME within one day.

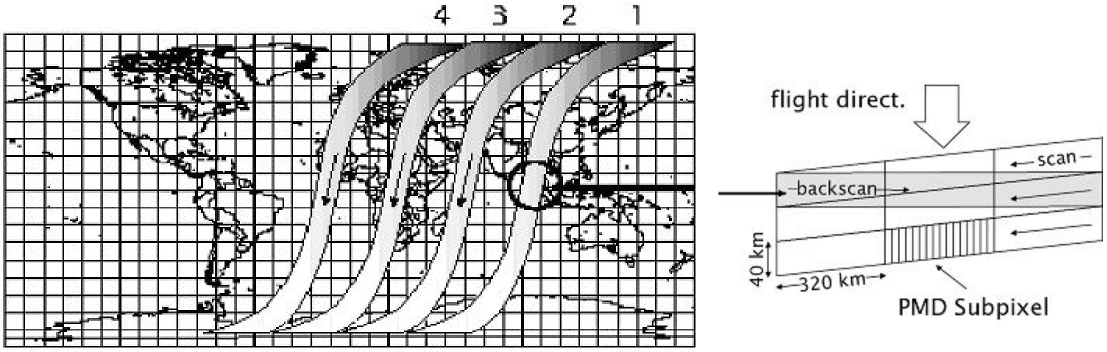

Fig. 2.4: Left: Area covered by GOME measurements for following orbits.
Right: Spatial cover of GOME forescan, backscan and PMD pixels (please note that this scheme is not true to scale).

The spectra measured by GOME are temporarily stored aboard the satellite and transmitted to the receiving stations several times a day. These spectra contain the raw signal of the photodiode arrays (level 0 data). In order to derive radiometrically calibrated spectra (level 1 data) several corrections have to be applied to the level 0 data. These include a spectral calibration, a radiometric calibration, and a correction of the polarisation sensitivity of the instrument [Bednarz, 1995]. The resulting spectra are used as input data for the spectral analysis of the absorptions of the atmospheric trace gases (see section 2.2).

Besides the four channels of the GOME spectrometer the instrument is additionally equipped with three so-called 'Polarisation Measurement Devices' (PMD, silicon photodiodes) which are sensitive to light over broad spectral ranges similar to the spectral ranges covered by the spectrometer channels (see Table 2.2). The PMDs are used to determine the degree of polarisation of the observed light [Aben et al., 1996; Stammes et al., 1997; Tanzi et al., 2000]. Since GOME is sensitive to the polarisation of the measured light the PMD information is necessary for the radiometric calibration of the spectra.

Because of the broad spectral sensitivity of the PMDs they receive more light compared to an individual photodiode of the diode array detector. Thus the integration time of the PMDs is about 16 times shorter resulting in a much higher spatial resolution compared to the size of the ground pixels of the GOME spectrometer (see Figure 2.4). Thus the PMD measurements can be used in particular to detect the cloud coverage across one GOME ground pixel [Kurosu et al., 1997; Wenig, 1998; Grzegorski et al., 2003].

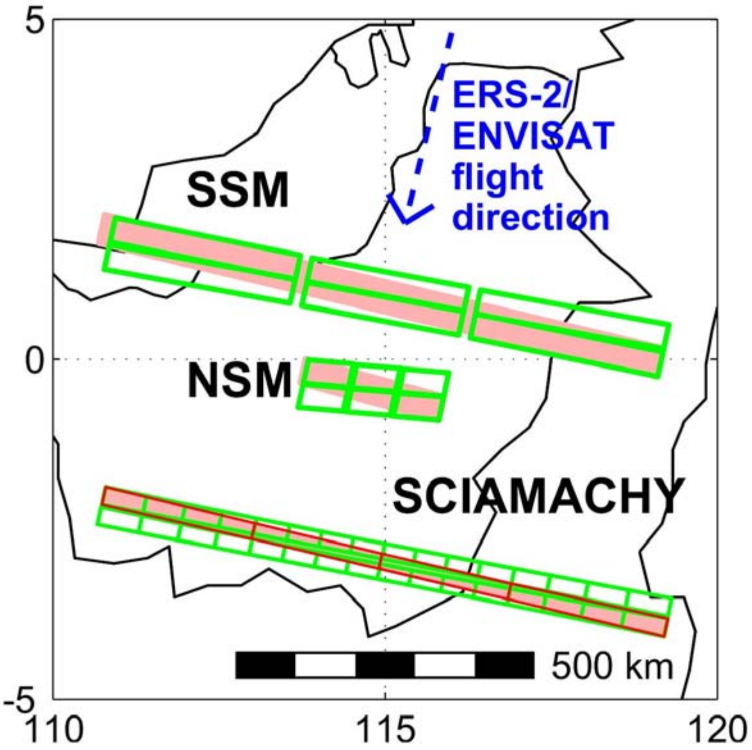

*Fig. 2.5: Spatial extension and geometry of the GOME and SCIAMACHY ground pixels. Snapshots of the GOME standard size mode (SSM, 320*40 km^2), GOME narrow swath mode (NSM, 80*40 km^2) and SCIAMACHY (60*30 km^2) are shown at the equator (Borneo). The forescan pixels are green, the subsequent backscans red. For GOME, the backscan has three times the length of the forescans (960 km in SSM, 240 km in NSM). For SCIAMACHY, the backscan comprises four pixels of 240 km width each.*

Table 2.2: Spectral ranges of the PMDs.

PMD	spectral range [nm]
1 (UV)	295 -397
2 (blue, green)	397 - 580
3 (red)	580 - 745

GOME was designed for about 5 years of operation, but is still in orbit and taking spectral data. However, several parts of the instrument are degrading [Tanzi et al., 2000]. Furthermore, the measurement of the direct solar spectrum failed from August 2001 till October 2002. Finally, on 22 June 2003 the tape recorder on board failed. Since then only data that is directly transmitted to ground stations (especially in Kiruna) is stored, covering an area reaching from the North Pole towards Southern Europe.
In this thesis, we consider data from GOME for the time period 1996-2001.

2.1.3. SCIAMACHY

SCIAMACHY - the **SC**anning **I**maging **A**bsorption Spectro**M**eter for **A**tmospheric **CH**artograph**Y** - was launched in March 2002 onboard the ESA satellite ENVISAT. A description of the instrument can be found in [Bovensmann et al., 1999]. Its general layout (see Fig. 2.6) and measuring principle is similar to GOME, but in comparison to GOME, SCIAMACHY has been improved widely. First, the spectral range is drastically increased (Fig. 2.7): SCIAMACHY consists of 8 spectral channels that now cover also the near IR. This allows for the first time the retrieval of greenhouse gases (CH_4, CO_2, N_2O) and CO on a global scale [Frankenberg et al., 2004a,b] in unexpected quality.

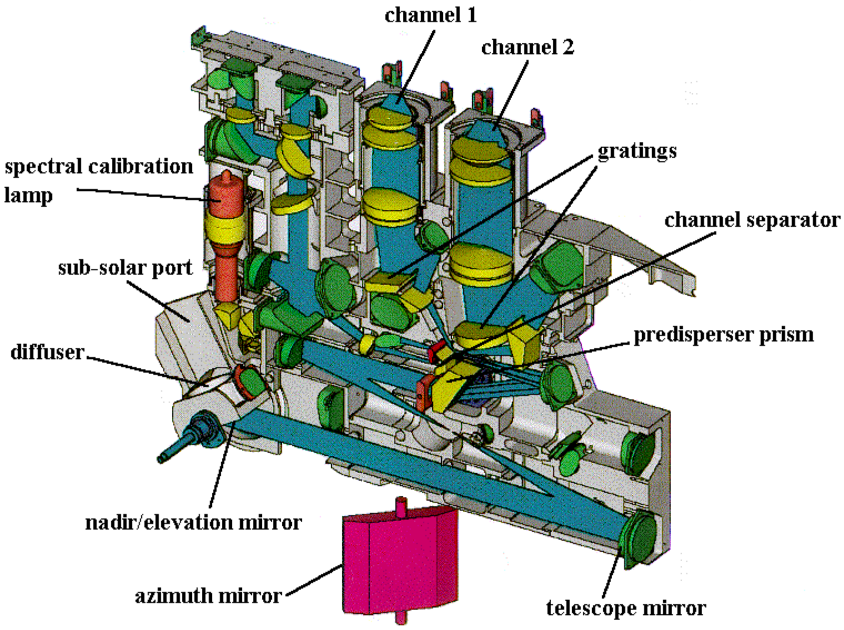

Fig. 2.6: Scheme of SCIAMACHY (picture courtesy by TNO-TPD).

Second, SCIAMACHY provides additional viewing geometries, namely limb and direct occultation of sun, moon and stars (Fig. 2.8). Especially for trace gases that exist in both stratosphere and troposphere (like NO_2), information on the tropospheric burden needs to separate the stratosphere first, as discussed in detail in section 2.4. Due to the limb-nadir-matching [Bovensmann et al., 1999] of SCIAMACHY (Fig. 2.8c), i.e. the alternation of viewing geometries, information about the stratospheric profile can be used to subtract the stratospheric from total column, resulting in tropospheric column densities (see section 2.4).

Third, the ground pixel size of SCIAMACHY is much smaller. Measurements are made with a ground pixel size of 15*30 km^2, but due to the restricted band width for the data transmission, usually 4 observations are integrated on board, leading to a standard ground pixel size of 60*30 km^2 (see Fig. 2.5). The backscan is divided into 4 pixels of 240 km width each. The benefit of the improved spatial resolution of SCIAMACHY will be discussed in detail in Chapter 9.

However, due to the alternating viewing geometries, there are gaps along track, leading to a checker-board pattern. The limb-nadir alternation is timed in such a way that the areas missed during one scan are covered by the next overpass 3 days later. Thus SCIAMACHY achieves global coverage after 6 days at the equator.

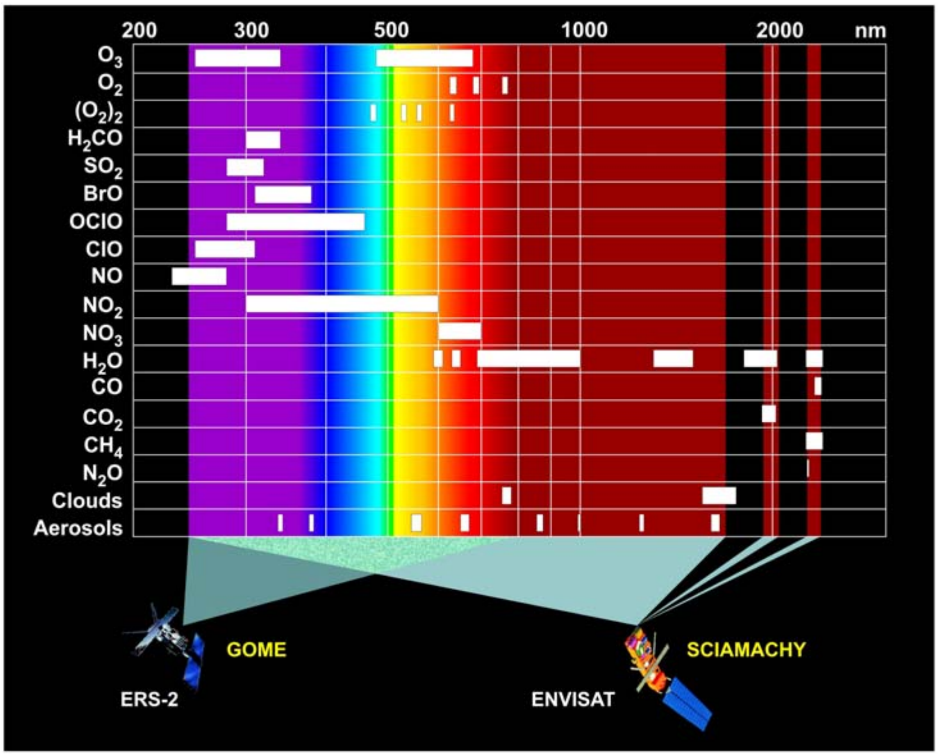

Fig. 2.7: Wavelength range of GOME and SCIAMACHY and detectable atmospheric absorbers [Bovensmann et al., 1999]. Compared to GOME, SCIAMACHY is also equipped with channels in the near IR spectral region.

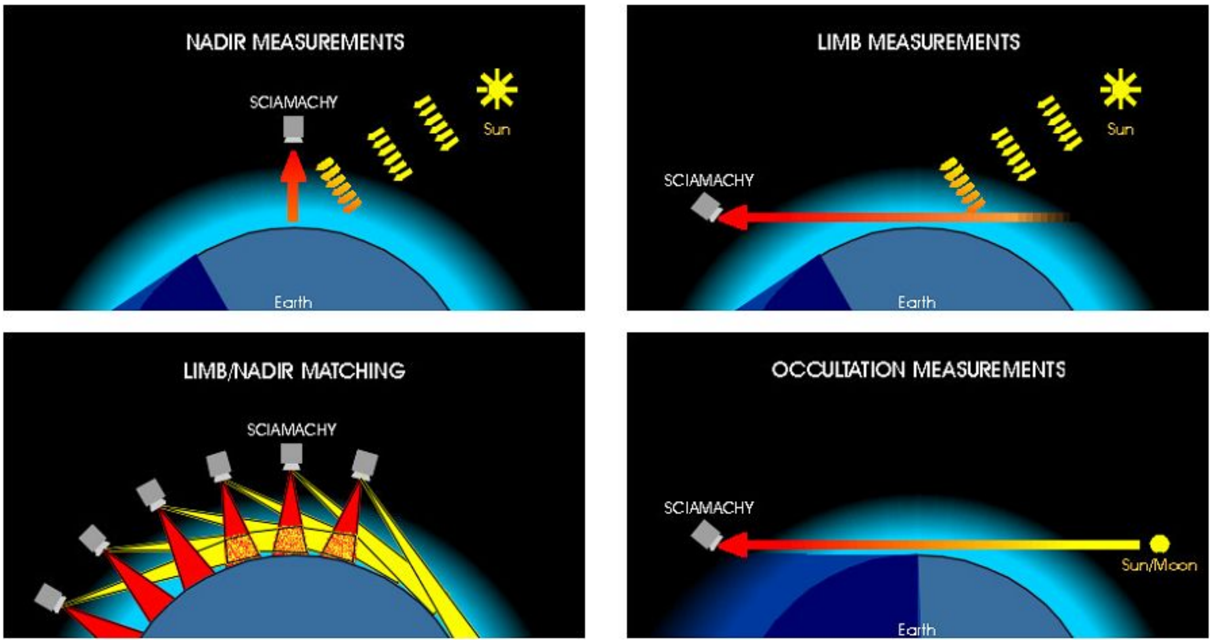

Fig. 2.8: Viewing geometries of SCIAMACHY (Stefan Noël, personal communication). a) Nadir mode (as for GOME). b) Limb mode. c) Limb and nadir measurements are performed alternately ("Limb-nadir-matching"). d) Direct occultation of sun and moon light.

2.2. Absorption spectroscopy of atmospheric trace gases

UV-vis absorption spectroscopy using extraterrestrial light sources is a widely used technique for the measurement of atmospheric trace gases from various platforms, e.g. on ground, aircraft, balloon or satellite. Satellite measurements are used in particular for remote sensing of stratospheric species. However, despite the reduced sensitivity towards the troposphere and the more complex radiative transfer (see Chapter 2.3), also tropospheric species can be clearly determined.

GOME and SCIAMACHY measure the solar radiation scattered from the earths atmosphere or reflected from its ground. Fig. 2.9 compares a solar spectrum (photon flux) directly measured by GOME with an "earthshine" spectrum. The solar spectrum shows high frequent structures (called "Fraunhofer lines" after the physicist Josef Fraunhofer, 1787 – 1826, who discovered dark lines in the solar spectrum) that are due to absorption processes occurring in the solar photosphere.

The "earthshine" spectrum shows additional strong absorption lines and bands of atmospheric gases, e.g. the strong absorption of ozone in the UV ("Huggins-band") or strong oxygen lines.

The absorption and emission of photons by molecules changes the energetic state of the molecule by causing electronical, vibrational and rotational transitions. The absorption cross sections are characteristic for the absorbing molecule. In principle the analysis of absorption spectra allows the retrieval of atmospheric trace gas abundances, as will be explained below. Please note, however, that the solar Fraunhofer lines are the dominating structures in the measured spectra.

The solar radiation varies with time due to several phenomena (e.g. the solar cycle of sun spot activity with a periodicity of 11 years). However, in the UV-vis range these variations are rather small (less than 1% beyond 300 nm [Brasseur and Solomon, 1984]).

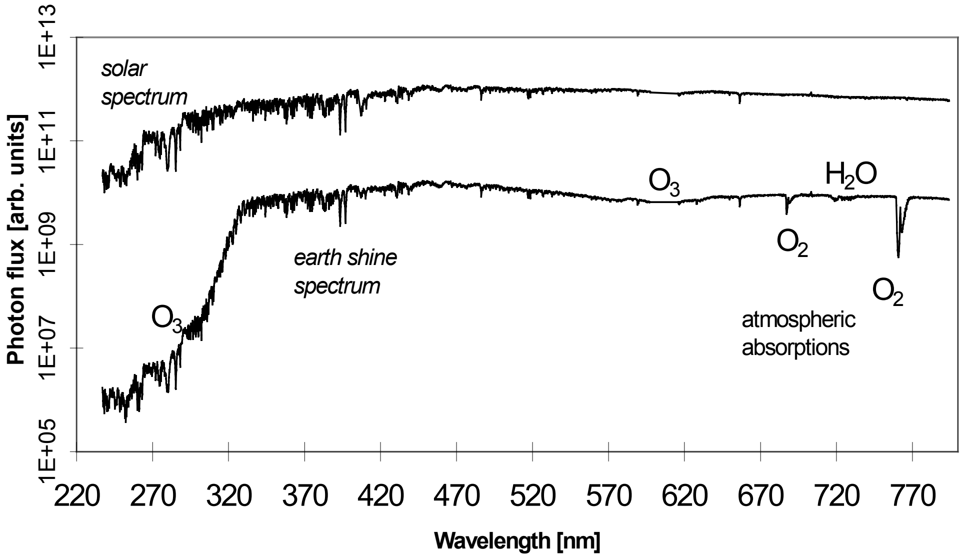

Figure 2.9: GOME spectra (photon fluxes) of the direct sun light and the light reflected from the earth. Both spectra show large structures (Fraunhofer lines) which are caused by absorptions in the solar atmosphere (especially below about 450 nm). In the earth shine spectrum also some prominent atmospheric absorptions of O_2, H_2O and O_3 can bee seen. It should be noted that the absorptions of many atmospheric species (i.e. NO_2) are about two orders of magnitude smaller.

2.2.1. The Beer-Lambert Law

The absorption of radiation by matter is described by the Beer-Lambert law. The absorption of light of the intensity $I(\lambda)$ at the wavelength λ as it passes through an infinitesimally thin layer of an absorbing matter *ds* is:

$$dI(\lambda) = I(\lambda) \cdot c(s) \cdot \sigma(\lambda, T) ds \tag{2.1}$$

Here $\sigma(\lambda,T)$ is the absorption cross section of the absorbing species which depends on the wavelength and temperature and $c(s)$ is its concentration. Integration of equation (2.1) for a finite light path through the absorbing species leads to the relationship between the incident light intensity $I_0(\lambda)$ and the transmitted light intensity $I(\lambda)$, known as the Beer-Lambert law:

$$I(\lambda, \sigma) = I_0(\lambda) \cdot e^{-\sigma(\lambda,T)\int c(s)ds} \tag{2.2}$$

The logarithm of the ratio of the measured I and I_0 is called optical density $\tau(\lambda)$.

$$\tau(\lambda) = -\ln\left(\frac{I(\lambda,\sigma)}{I_0(\lambda)}\right) = \sigma(\lambda,T)\int c(s)ds =: \sigma(\lambda,T) \cdot S \tag{2.3}$$

with

$$S := \int c(s)ds \tag{2.4}$$

S is the concentration of the absorbing gas integrated along the light path and usually called the “Slant Column Density” (SCD). If $\sigma(\lambda,T)$ is known (from laboratory measurements), S can in principal be determined by measurement of the optical density τ, i.e. the intensities I and I_0. If the concentration c is constant along the absorption path it can also be derived.

2.2.2. The Differential Optical Absorption Spectroscopy (DOAS)

The Beer-Lambert law describes the intensity reduction of light of a specific wavelength by the characteristic absorption σ of a specific atom/molecule. However, in the real atmosphere several trace gases are present. Thus absorption takes place simultaneously by several absorbers having different cross sections. Furthermore, light is also scattered by molecules and aerosols (including cloud droplets). Finally, earthshine spectra measured by satellite also depend on the reflection characteristics of the ground.

Atmospheric absorption of several absorbers can thus be described by

$$I(\lambda) = I_0(\lambda) \cdot e^{-\Sigma\sigma_i(\lambda,T)S_i(\lambda)} g(\lambda) \tag{2.5}$$

Here $g(\lambda)$ describes the additional attenuation of intensity by Rayleigh and Mie scattering in the atmosphere and reflection on the ground.

Taking the logarithm yields

$$\ln\left(\frac{I(\lambda)}{I_0(\lambda)}\right) = -\sum \sigma_i(\lambda, T) S_i(\lambda) + \ln(g(\lambda)) \tag{2.6}$$

The measurement of a I and I_0 for a set of wavelengths results in an overdetermined linear equation system for S_i. However, eq. (2.6) cannot be solved as the actual shape of $g(\lambda)$ is not known.

This restriction can be solved by applying the method of Differential Optical Absorption Spectroscopy (DOAS). The DOAS method was introduced by Perner and Platt [1979], a detailed description can be found in Platt [1994].

The key principle of DOAS is to make use of the fact that the effects summed up in $g(\lambda)$ reveal rather broad spectral features, while characteristic absorption lines have usually narrow spectral features. The influence of broad band effects like scattering can thus be removed by applying a high pass filter to eq. (2.6), i.e. splitting the cross sections into a portion $\sigma_c(\lambda)$ which varies only 'slowly' with the wavelength λ and into a portion $\sigma'(\lambda)$ which shows ‘rapid’ variation with λ (see Fig. 2.10).

$$\sigma(\lambda) = \sigma_c(\lambda) + \sigma'(\lambda). \tag{2.7}$$

The definition of the threshold between 'slow' and 'rapid' variation of the absorption cross-section (i.e. the choice of the high-pass filter characteristics) depends on the considered wavelength interval and the width of the absorption bands to be detected. Commonly the spectra are filtered by dividing by a fitted polynomial or by a smoothed spectrum. Conventionally $\sigma'(\lambda)$ is called differential absorption cross-section.

As several absorbing trace gases can be simultaneously determined by their specific absorption characteristics, the DOAS method is widely used for atmospheric measurements.

For optically thick absorbers, like water vapour or methane in the IR, however, modifications to the DOAS approach have to be introduced [Frankenberg et al., 2004a].

2.2.3. The spectral fitting process

The measured spectrum is fitted by the absorption spectra of the trace gases absorbing in the respective spectral range and a polynomial of a specified degree by means of a non linear least squares fitting algorithm [Gomer et al., 1993; Stutz and Platt, 1996].

Since the spectra are recorded with discrete elements the obtained signal by a single unit (e.g. a diode) represents the integrated intensity over the wavelength range which is covered by this diode:

$$I(\lambda_i) = \int_{\lambda_{i,low}}^{\lambda_{i,high}} I'(\lambda')\,d\lambda' \tag{2.8}$$

Here λ_i denotes the centre wavelength of the diode element, $\lambda_{i,low}$ the shortest wavelength and $\lambda_{i,high}$ the longest wavelength covered by the element.

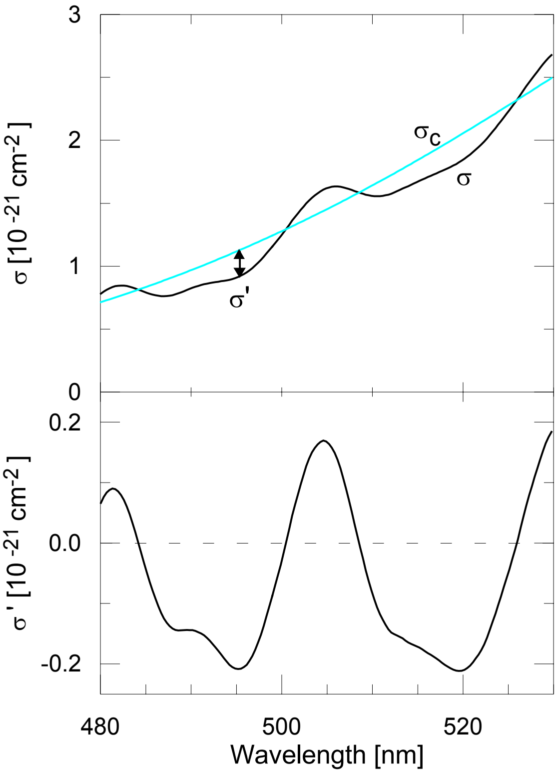

Figure 2.10: Splitting of the absorption cross section into a 'slowly' and a 'rapidly' varying part σ' and σ_c [Wagner, 1999].

The aim of the linear fitting process is to minimize the sum over the measured optical depths $\tau(\lambda_i)$ of the individual diode elements of the selected wavelength range:

$$(2.9) \qquad \sum_i \left(\ln(I) - \ln(I_0) + R - \sum_k S_k \cdot \sigma_k(\lambda_i) - \sum_j b_j \lambda_i^j\right)^2 \rightarrow min$$

Here $\sigma_k(\lambda_i)$ denotes the differential cross section of the kth trace gas taken into account by the fitting routine. The derived fit coefficient S_k is the desired SCD of this species. $\sum_j b_j \lambda_i^j$ is a polynomial used to account for broad band features, i.e. realizes the high pass filtering. The initial intensity I_0 (“Fraunhofer reference” or “solar reference”) is taken from the direct measurement of the solar spectrum from the satellite. This removes the strong Fraunhofer lines that dominate both I and I_0 over most of the UV-vis range. Furthermore a Ring spectrum R is included in the fitting procedure (see 2.2.3.1).

In practice, eq. (2.9) has to be modified because the wavelength mapping between the absorption cross sections $\sigma(\lambda)$ and the measured intensity $I(\lambda)$ is not known exactly and furthermore changes with time (e.g. due to temperature variations of the detector or due to the Doppler-effect). Thus, for the fitting routine the wavelength calibration of reference spectra is varied with respect to the measured spectrum to achieve the best match of the absorption features. For that purpose the reference spectra are interpolated and the grid points λ_i are replaced by the values of the new wavelength $\lambda_{f(i)}$. In the actual fitting routine linear shifts and also squeezes of the reference spectra were allowed according to f(i) = a + b·i, where a and b are determined by the fit.

This least square fitting is realized using the Levenberg-Marquard method [Levenberg, 1944; Marquardt, 1963]. Thereby the linear and the non-linear parts of the equation system are solved separately, following the approach by Ottoy and Vansteenkiste [1981]. This leads to a faster convergence and less computational effort for the fitting routine (for details see [Wenig, 2001]). The implementation of these algorithms for the evaluation of satellite data was realized by Carsten Leue, Mark Wenig and Stefan Kraus ([Leue, 1999; Wenig, 2001; Kraus, 2004]). The identification of appropriate fitting parameters for the different trace gases was carried out by Wagner [1999].

The difference of the measured optical depth and the fit result is called the residual structure (or residual). It is a measure for the quality of the spectral fitting. When the optical depth of the residual is small compared to the trace gas absorption derived in the fitting procedure the respective trace gas can be well detected. The random structures of the residual allow the determination of the statistical error of the derived SCDs [Stutz and Platt, 1996]. Often, however, the residuals contain systematic spectral structures which can be caused by e.g. errors in the spectral calibration of the reference spectra, the temperature dependence of the cross sections, instrumental artifacts, scattering processes, the fine structure of the solar spectrum or unknown atmospheric absorptions. Such systematic structures have to be considered carefully in order to optimize the spectral fitting procedure and to determine the uncertainty of the derived SCDs [Ferlemann, 1998]. The resulting systematic uncertainties are usually higher and harder to determine than the comparably small statistical errors.

2.2.3.1 The Ring effect

In addition to Rayleigh- and Mie-scattering which are elastic scattering processes in the Earth's atmosphere the solar radiation also undergoes Raman-scattering whereby the photon's energy changes. Rotational Raman scattering is thought to be the (most probable) cause for the so called 'Filling in' of the Fraunhofer lines [Bussemer, 1993; Burrows et al., 1995; Vountas et al., 1998; Wagner et al., 2001c].

The number of photons (per dλ) in a narrow wavelength band at $\lambda_0 \pm d\lambda$, revealing a strong Fraunhofer line, is smaller than for slightly higher and lower wavelengths. Thus, by inelastic scattering the number of photons scattered *in* the considered wavelength band is higher than that of photons scattered *out*, and the resulting spectrum shows a less deep Fraunhofer line after passing the atmosphere.

This effect was first discovered by Grainger and Ring [1962] and referred to as Ring-effect. Although the Ring effect is only of the order of a few per cent it masks weak atmospheric absorptions and thus has to be accounted for in the DOAS fit.

Usually the correction of the Ring effect is realized by including a further spectrum ("Ring spectrum") into the fitting process [Solomon et al., 1987]. The Ring spectrum can be calculated by ratio of the cross sections for Raman and Rayleigh scattering. (For details and other methods for retrieving a Ring spectrum see [Wagner, 1999; Wagner et al., 2001c, 2002a]). Here we use a calculated ring spectrum.

2.2.3.2. The "solar I_0 effect"

The spectral resolution of DOAS instruments in the UV/vis region is usually in the range of about a few tenths to several nanometers. Thus the natural line widths of the atmospheric absorptions are not resolved. To account for this the absorption cross sections of the trace gases have to be convoluted by the instrumental slit function f(λ) before they are used as input for the fitting routine.

$$\sigma^*(\lambda) = f * \sigma(\lambda) = \int \sigma(\lambda') \cdot f(\lambda - \lambda') d\lambda \tag{2.10}$$

However, in 'reality' this convolution occurs in the spectrometer where the incoming *intensity* I(λ) is convoluted with the instrument slit function:

$$I^*(\lambda) = f * I(\lambda) = f * (I_0(\lambda) \exp(-\sigma(\lambda) \cdot S)) \neq f * I_0(\lambda) \exp(-f * \sigma(\lambda) \cdot S)) \tag{2.11.}$$

The convolution and the exponential function can not be exchanged. Thus the fitting of convoluted cross sections to low resolved spectral data is not strictly correct.
As the impact of this effect is determined by the structures of I_0 it is usually called the "(solar) I_0 effect" [Platt et al., 1997; Richter, 1997; Aliwell et al., 2002]. It can be accounted for by calculating "I_0 corrected" cross sections as suggested by Johnston [1996].
However, the impact of the solar I_0-effect turned out to be of minor importance for the NO_2 retrieval and is accounted for by smoothing the reference spectra. This procedure at the same time accounts for the undersampling of the GOME spectra (see [Roscoe et al., 1996; Wenig, 2001; Wagner, 1999]).

2.2.3.3. Instrumental shortcomings

The spectral transmission function is affected by the different parts of the instrument, e.g. the reflectivity of the mirror or the quantum efficiency of the photodiode array. Most of these effects are assumed to be constant with time. Even if they cause errors in the absolute radiometric calibration this is only of minor importance because such effects cancel out when the measured spectrum is divided by the Fraunhofer spectrum. However, there exist also other effects like the transmission of the dichroic filter (used as channel separator, see Figure 2.3) or the etalon structure due to water ice on the surface of the photodiode array which vary with time. Although they are corrected for according to the measurements of the GOME calibration unit in some cases (e.g. after power shut down) the changes can be very rapid and spectral structures remain which can interfere with the trace gas absorptions.
Especially the diffuser plate used for the direct measurements of solar spectra revealed to cause artificial spectral structures interfering trace gas retrievals [Richter et al., 2002a; Richter and Wagner, 2001; Wenig et al., 2004] (see 2.2.4.1). Finally the study of Tanzi et al. [2000] revealed that the instrumental characteristics of GOME are degrading with time of mission. These instrumental limitations affect our retrieval, and the caused systematic errors are usually larger than the (quite small) statistical fit errors.

2.2.4. NO_2 analysis

2.2.4.1. GOME

The retrieval of NO_2 SCDs from GOME was developed and implemented by Thomas Wagner [Wagner, 1999], Carsten Leue [Leue, 1999] and Mark Wenig [Wenig, 2001]. The NO_2 absorptions are analyzed using pixels 170-270 of the spectral GOME data from channel 3, corresponding to a spectral range from 430 to 450 nm (see Figure 2.11). The measured spectra and the cross sections are smoothed by convoluting with a Gaussian function with a FWHM of about 2.5 pixels. Included in the fitting procedure are the reference spectra listed in Table 2.3 and a polynomial of degree 2.

The cross sections of O_3 and NO_2 were chosen for T=221 K, as they are both strong stratospheric absorbers. It has been demonstrated by Boersma et al. [2004a] that this leads to a underestimation of tropospheric columns of NO_2 (of higher temperature) of up to 20%.

Table 2.3: Reference spectra used for the GOME NO_2 analysis [Wagner 1999].

Reference spectrum	temperature	Source
O_3	221 K	GOME [Burrows et al., 1999a]
NO_2	221 K	GOME [Burrows et al., 1998]
H_2O	293 K	HITRAN (Rothman et al. [1992])
Calculated Ring spectrum	250 K	MFC, Bussemer [1993]
Fraunhofer spectrum	-	GOME direct sun light Standard retrieval: Fixed (1 June 1997)

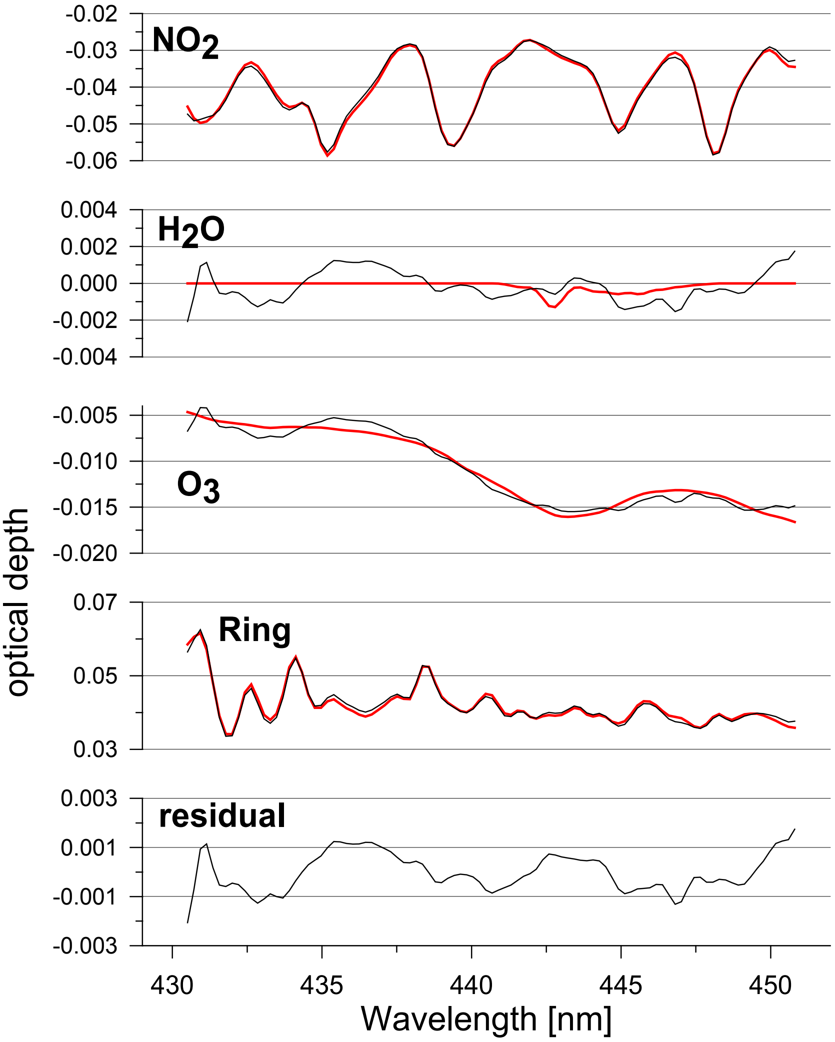

Figure 2.11: Example for the NO_2 evaluation of an atmospheric GOME spectrum (GOME orbit 71127003, 01:27:50, SZA: 88.9°). Black lines show the optical depths that are not explained by the other absorbers, red lines are the respective fit results [Wagner, 1999].

The study of Richter et al. [2002a] and Richter and Wagner [2001] revealed that the reflection of the sunlight at the diffuser plate causes artificial spectral structures that interfere with the NO_2 cross section. Even worse, these structures vary with time. This leads to an artificial yearly cycle of NO_2 SCDs. To get rid of this artifact, the solar spectrum of one selected day (i.e. the 1st June of 1997) instead of the actual daily solar spectrum was taken as Fraunhofer reference for the whole time period (see also [Wenig et al., 2004]). This method proved to remove the artificial temporal fluctuations in the NO_2 SCD. However, it is unknown how far the chosen solar reference spectrum is affected by the diffuser plate. Hence the retrieved NO_2 SCDs are shifted by a constant (unknown) bias.

2.2.4.2. SCIAMACHY

Our retrieval algorithm of slant column densities from SCIAMACHY spectra is quite similar to the established settings for the GOME instrument. The same spectral range 430-450 nm was used for the DOAS fitting procedure. The solar reference was taken from the daily SCIAMACHY measurements. Table 2.4 gives an overview over the reference spectra used for the DOAS fit.

As NO_2 reference spectrum a highly resolved Fourier Transform Spectrum (FTS) from IUP Bremen was chosen and convolved with the SCIAMACHY slit function. This cross section reveals to have less deep absorption structures compared to the NO_2 spectrum used for the GOME fit. The effect on retrieved SCDs is of the order of 20% and was corrected for by scaling down the resulting SCIAMACHY SCDs for comparability.

Table 2.4: Reference spectra used for the SCIAMACHY NO_2 analysis [Wagner et al., 2002b].

Reference spectrum	temperature	Source
O_3	221 K	GOME [Burrows et al., 1999a]
NO_2	223 K	IUP Bremen, FTS high pressure
H_2O	293 K	HITRAN (Rothman et al. [1992])
O_4	296 K	Greenblatt et al. [1991]
Calculated Ring spectrum	250 K	MFC, Bussemer [1993]
Fraunhofer spectrum	-	SCIAMACHY direct sun light

2.2.5. Creating mean maps

For the calculation of temporal and spatial averages, the GOME and SCIAMACHY pixels are projected to maps. The standard resolution was chosen as 0.5°×0.5° for GOME SSM observations and 0.1°×0.1° for GOME NSM and SCIAMACHY observations. For some comparison studies, we modified the grid size to that of the respective data set (mostly 1° resolution).

2.3. Radiative Transfer

2.3.1. The concept of air mass factor

With the DOAS method, SCDs of absorbing molecules, i.e. the integrated concentration along the light path, are determined. To derive a more general quantity (that is especially independent from the viewing geometry), the SCDs are usually converted to vertical column densities (VCDs), i.e. the integrated concentration from ground to the top of atmosphere. The conversion is realized using the so-called air mass factor (AMF), defined as

(2.12) $\mathrm{AMF} := \mathrm{SCD}/\mathrm{VCD}$, thus

(2.13) $\mathrm{VCD} = \mathrm{SCD}/\mathrm{AMF}$

Fig. 2.12 shows a scheme of the geometry of nadir satellite observations. The light path and thus the AMF strongly depends on the solar zenith angle θ (SZA). For simple reflection of the sunlight at the ground the increase of the light path is 1/cos(θ). This results in the "geometric AMF"

(2.14) $\mathrm{AMF}_{\mathrm{geom}} = 1 + 1/\cos(\theta)$ (nadir viewing)

that is a good approximation for the conversion of SCDs to VCDs for stratospheric absorbers and SZAs below about 70°.

For trace gases in the troposphere the determination of AMFs is more complex. The actual light path is determined by the ground albedo, aerosols and clouds. For a cloudfree scene with high ground albedo, the light is predominantly reflected at the ground. For dark surfaces (or high aerosol load) the role of light scattered in the atmosphere increases. For a clouded scene, finally, the air masses below the cloud may be completely shielded and are "invisible" for the satellite.

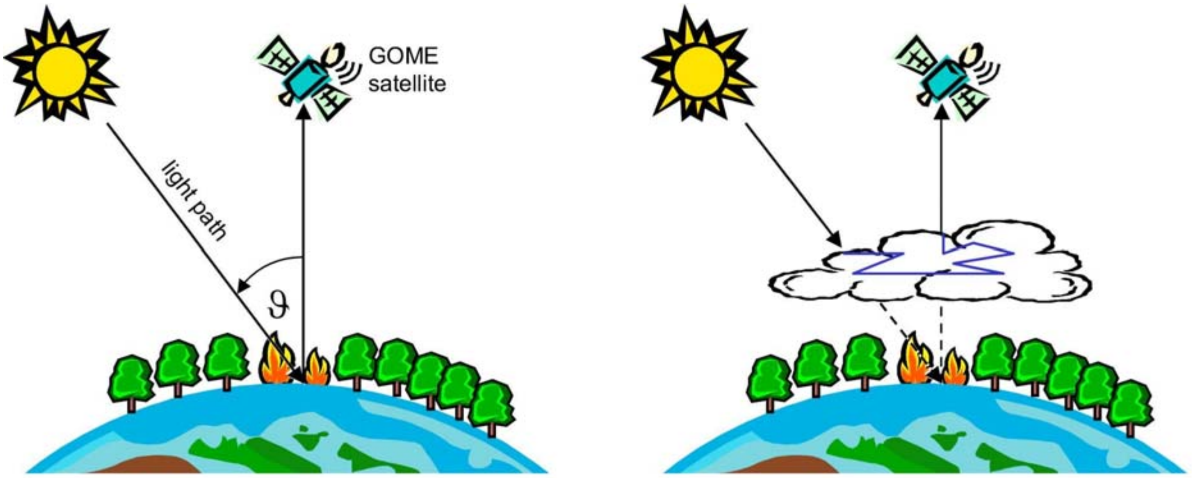

Fig. 2.12: Scheme of the nadir viewing geometry (adopted from Leue [1999]). In a cloudfree scene (left), the light path crosses the troposphere. Situation is more complex for a clouded scene (right), where the troposphere is shielded. The dominating light path entering the detector depends on clouds, aerosols and ground albedo.

The resulting AMF depends on the actual light path and furthermore the trace gas profile: For trace gases close to the ground, AMFs can be rather low (e.g. <1 for a trace gas below 1 km at 430 nm, 20° SZA and 5% ground albedo) and increase with profile height (about 2 for same settings but the trace gas at 10 km height) [Leue, 1999].

2.3.2. Radiative transfer modelling

AMFs can be calculated with radiative transfer models (RTMs). For this purpose we use the Monte-Carlo model TRACY, developed recently at the IUP Heidelberg by Christoph von Friedeburg [von Friedeburg, 2003; Hönninger et al., 2004], based on AMFTRAN [Marquard and Platt, 1997]. The advantage of a Monte-Carlo approach for modelling radiative transfer is that "real" processes can be individually modelled. Furthermore, also multiple scattering can be realistically described.

However, to calculate adequate AMFs, knowledge of ground albedo, trace gas profile, aerosol load and scattering characteristics, and clouds is necessary.

- The ground albedo can be estimated from the GOME total intensities as demonstrated by Koelemeijer et al. [2003]. However, this dataset gives a climatology of ground albedo (monthly means over the time period 1996-2001), and thus does not account for rapid changes of the ground albedo (e.g. snow cover for a short time period).
- NO_x emitted from the ground is commonly mixed in the boundary layer. Thus, NO_2 profiles can be well represented by a box of typically 500-1000 m height. However, over source regions, profile heights are probably lower. On the other hand, also in the free troposphere enhanced NO_x levels occur due to lightning, aircraft emissions and convective transport of polluted boundary layer air masses. Information on tropospheric profiles can in principal be gained from models, with the respective uncertainties. Data from measurements, however, is rather sparse.
- Aerosol data can be retrieved by other satellite instruments (e.g. TOMS, MERIS or the Moderate Resolution Imaging Spectroradiometer MODIS). However, these measurements usually do not coincide with the GOME measurement. Furthermore, the impact of aerosols (and clouds) interferes with the trace gas profile: a high aerosol load (cloud fraction) reduces the AMF for trace gas amounts below, but increases it for trace gas amounts above the aerosol (cloud) layer. Finally, essential information (e.g. on the single scattering albedo) is not provided sufficiently.
- Cloud properties can be directly determined from GOME data. These methods and the impact of clouds is discussed below (2.3.3.).

The calculation of appropriate AMFs for tropospheric trace gases for satellite observations of tropospheric NO_2 has been investigated in several studies, for instance Leue [1999], Wenig [1999], Wagner [1999], Richter and Burrows [2002b], Martin et al. [2002], Boersma et al. [2004a].

In this study however, we follow a rather simple approach where we correct the difference of total and stratospheric VCD by a constant factor of 2 to retrieve a tropospheric VCD. This corresponds to an tropospheric AMF of 1 for zenith sun, as calculated by Richter and Burrows [2002b] for a tropospheric box profile of 1.5 km height, a surface albedo of 5% and typical maritime aerosols. We refrain from correcting each measurement with an individual AMF, as the uncertainties of the required information and the RTM are rather high.

Our simple AMF approach has the advantage that our resulting NO_2 VCDs are independent from external datasets. This is a quite crucial point for the interpretation of our results. For instance, if we would use a-priori information (i.e. input from models) that assume lower profiles of NO_2 over source regions (resulting also in lower AMFs), we would retrieve higher NO_2 VCDs over those regions even if the GOME measurement would be the same. Thus errors in the a-priori assumptions on the profile height (as well as ground albedo or aerosol load) would systematically affect the resulting VCDs, and the retrieved spatial patterns of the tropospheric NO_2 distribution would not be an independent information anymore.

In this thesis, typically the relative spatial and temporal variations of NO_2 VCDs are investigated. The respective results are not affected by the potential systematic underestimation of the absolute values.

However, it has to be kept in mind that if the NO_2 VCDs are to be interpreted quantitatively, the AMF has to be revised. This will be done in Chapter 6 and Chapter 11, where we modified the AMF for the specific considered conditions.

2.3.3. Clouds

The observation of tropospheric trace gases from space is severely affected by clouds. A thick, unbroken cloud layer completely shields the air masses below from being detected. On the other hand, the sensitivity of satellite measurements towards trace gases above the clouds is enhanced by the bright surface. In the case of partly clouded scenes and optically thin clouds, radiative transfer becomes rather complex.

Information on cloud cover can be obtained from GOME data itself, using a variety of cloud sensitive parameters [Wagner et al., 2002c, 2003a]. Routine cloud algorithms are currently based on the O_2 A-band absorption [Kuze and Chance, 1994; Koelemeijer et al., 2001 (FRESCO)] or data from the polarisation monitoring devices (PMDs) [Wenig et al., 2001 (CRUSA); see also von Bargen et al., 2000]. Here we use cloud fractions from the HICRU database [Grzegorski, 2003a/b]. The HICRU algorithm uses PMD intensities to determine cloud fractions by an iterative approach using image sequence analysis. Comparisons with other cloud retrieval algorithms generally show good agreement, but HICRU has proven to solve their specific shortcomings. Especially for the crucial retrieval of low cloud fractions, HICRU proves to be quite successful.

We discuss the impact of clouds on some of the performed studies, where it is of importance, in the respective chapters. In some cases we consider only (nearly) cloud free observations. However, we do not generally skip clouded pixels in our dataset. One important reason for this decision is that we cannot reliably differentiate between clouded pixels and snow cover that could be misinterpreted as cloud: for midlatitudes in wintertime, only few data would be left if the observations would be skipped. Furthermore, though weakened, also the observations of partly clouded scenes still carry a signal of tropospheric pollution (see Chapter 9).

2.4. Stratospheric NO_2

Fig. 2.13 shows the monthly mean map of total NO_2 VCDs as derived from GOME for February 1997 as an example. This mean composite reflects primarily the stratospheric NO_2 column that dominates the total column for most cases. Stratospheric NO_2 shows a strong latitudinal dependency: for February, very high VCDs are found in the Antarctic, since NO_y is almost completely converted to NO_x and loss reactions are suppressed due to the low humidity and permanent sunshine. On the opposite, the Arctic shows very low VCDs of NO_2 due to denoxification and denitrification in arctic winter (see section 1.4.2). Over the tropics, N_2O is lifted up to the stratosphere; the subsequent production of NO_x via (R 7) takes place while the air masses are transported polewards, resulting in a gradient of minimal VCDs over the tropics.

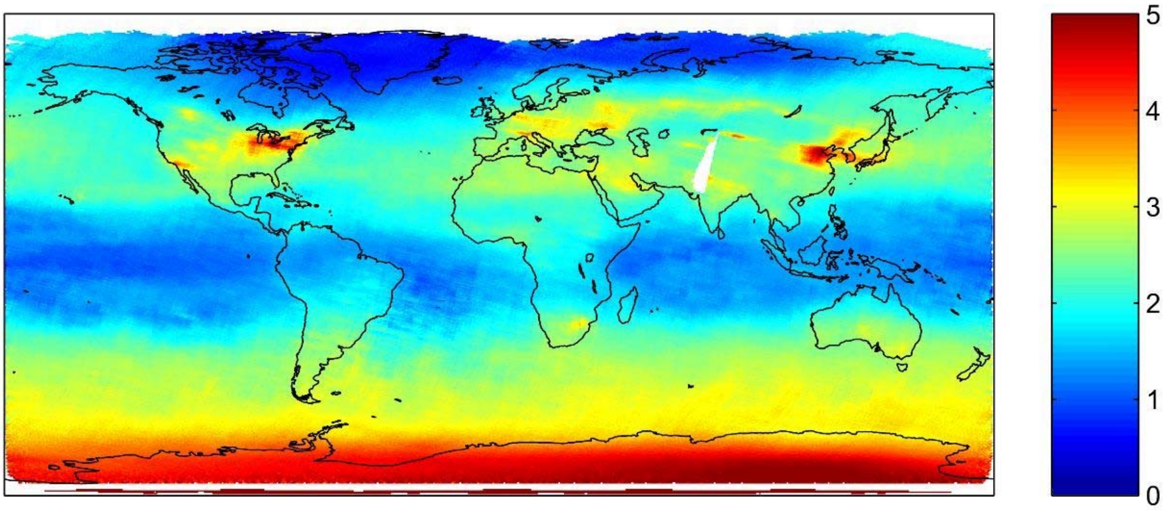

Fig. 2.13: Mean NO_2 VCD for February 1997 in 10^{15} molec/cm^2.

GOME data thus holds valuable information on NO_2 in the stratosphere. Wenig et al. [2004] presented an analysis of stratospheric NO_2 VCDs on a global scale for 1996-2000, that allows to study general features of stratospheric chemistry, principally confirming our current knowledge.

Also for the surprising polar vortex split in austral winter 2002, GOME data of NO_2 (in combination with ozone and OClO) allowed to investigate the actual evolution of this particular event [Richter et al., 2004a].

However, the focus of this thesis is set on tropospheric sources of NO_x. Largest NO_x source in the troposphere is fossil fuel combustions that takes place to large parts in the US, Europe and Eastern Asia. This can be already identified in Fig. 2.13. However, for a direct investigation of tropospheric NO_2 it is necessary to estimate the stratospheric columns and subtract them from the total columns.

2.4.1. Estimating the stratospheric NO_2 VCD

For the retrieval of tropospheric VCDs of NO_2 it is important to subtract the stratospheric from total columns. Here we discuss some approaches for estimating stratospheric VCDs. First, we investigate the use of external (model) data in sections 2.4.1.1 and 2.4.1.2. In sections 2.4.1.3-2.4.1.5 we describe different approaches of stratospheric estimations using the GOME dataset itself, to be independent from external (model) data.

2.4.1.1. Tropopause heights

High and low pressure systems control meteorological conditions of the troposphere, but also lead to variations of the height of the tropopause, thereby shifting the stratospheric profile of NO_2. Assuming that the NO_2 mixing ratios are not affected by the height variations, an increased tropopause height should lead to a reduced VCD of NO_2. We studied the correlation of GOME NO_2 VCDs with tropopause height data derived from ECMWF wind fields. It turned out that, in contrast to our expectation, we found rather low correlations. Hence this approach has not proven to give a reliable stratospheric estimation. The reasons for the bad correlations are not yet understood.

2.4.1.2. Stratospheric Chemistry Model SLIMCAT

The VCDs derived by GOME have been compared to results from the model SLIMCAT [M. Chipperfield, 1999]. SLIMCAT is a three-dimensional (3D) off-line chemical transport model, using wind and temperature fields from meteorological analyses to specify the atmospheric transport and calculating the abundances of chemical species in the stratosphere.

Fig. 2.14 shows the February 1997 monthly mean VCD of NO_2 as derived from SLIMCAT (a) and GOME (b) (same as Fig. 2.13 but regridded to SLIMCAT resolution). SLIMCAT VCDs are calculated from the MPC 320 data by Sven Kühl. The model output time was chosen to match the GOME overpass time. As shown in Fig. 2.14c, the GOME data highly correlates to the SLIMCAT model results. The deviations of higher GOME VCDs for low SLIMCAT VCDs (blue dots in Fig. 2.14c) are due to tropospheric pollution (especially over the US, Europe, and China). If we skip polluted regions (i.e. those regions where the mean tropospheric NO_2 VCD is above 5×10^{14} molec/cm^2), only the red dots remain, and we find a correlation of R=0.976. However, a linear fit (forced through zero) results in a slope of 0.71, thus the absolute numbers deviate by about 30%.

By discussing the deviations, one has to keep in mind that the artificial spectral structures stemming from the optical parts of the instrument, especially the diffuser plate, may introduce a total offset for the retrieved SCDs (see section 2.2.4.1). However, this constant offset of the retrieved NO_2 SCD would result in very different relative deviations of the respective VCD, depending on the SZA and the true atmospheric NO_2 VCD, and would thus rather lead to increased scatter than a consistent slope.

For a decision whether GOME VCDs are too low or SLIMCAT VCDs are too high, further independent information is needed.

Nevertheless, the spatial patterns agree very well. The model data reflects spatial variations of stratospheric NO_2 realistically, e.g. low NO_2 VCDs within the arctic polar vortex. Thus SLIMCAT data can be used to estimate the stratospheric NO_2 column, and subtract it from GOME total VCDs after scaling the SLIMCAT data down appropriately [A. Richter, personal communication]. However, the resulting GOME data product would not be independent any more. Furthermore for cases with high gradients (i.e. at the polar vortex edge), slight deviations of the spatial patterns result in large errors.

2.4.1.3. Reference Sector

A simple (already established) method to estimate the stratospheric NO_2 columns is to use the fact that the distribution of stratospheric NO_2 is rather smooth longitudinally. Thus for a given latitude the stratospheric NO_2 VCD can be estimated in a reference sector of the same latitude, that is chosen for a region with negligible tropospheric pollution (usually over the remote Pacific) [Richter et al., 2002b; Martin et al. 2002]. The reference sector method gives generally good results, but fails for polar regions (also affecting midlatitudes), if a strong asymmetric vortex is established. For instance in Fig. 2.13, the stratospheric VCD at 70°N (North from Alaska) is obviously not independent from longitude! An analysis of the SLIMCAT results however revealed, that also for low latitudes the reference sector assumption is not always fulfilled; for instance in summer, we find higher stratospheric columns over the Indian ocean than for the Pacific. This leads to artificial "stripes" in the resulting tropospheric maps.

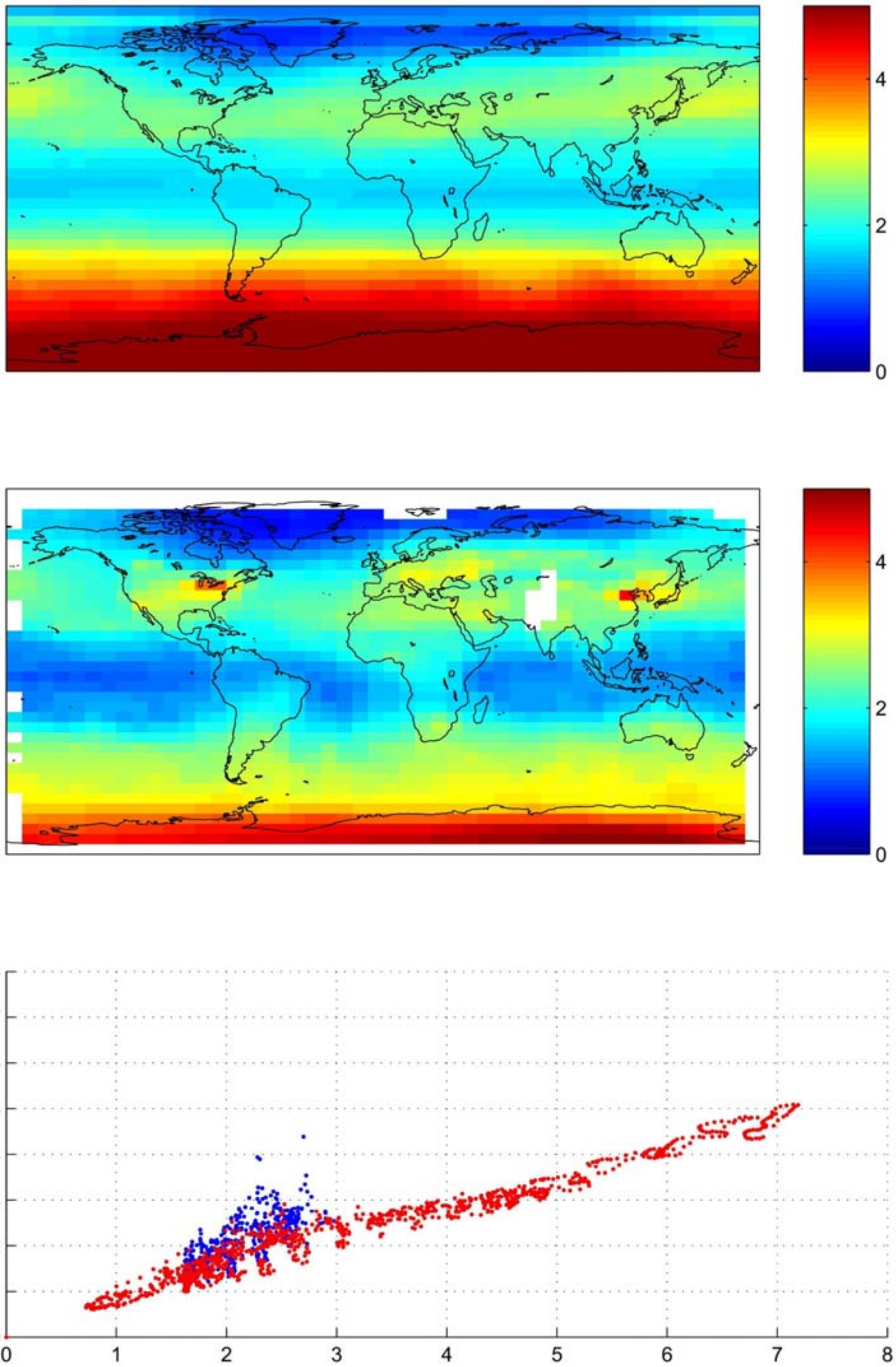

Fig. 2.14: Comparison of monthly mean VCDs of NO_2 *(February 1997) for SLIMCAT (a) and GOME (b) (same as Fig. 2.13, but for SLIMCAT grid size). Plate (c) shows the correlation of both datasets (all units* 10^{15} *molec/cm*^{2}*). The scatter of GOME data (blue dots) is caused by tropospheric pollution.*

2.4.1.4. Two dimensional estimation

The simple reference sector method has been extended by Leue [1999] and Wenig [2001], allowing a more realistic 2-D stratosphere. The stratospheric column is estimated over several oceanic regions. The values for regions in between are interpolated in two dimensions.

This approach has the advantage of a more realistic treatment of the stratosphere as it considers also longitudinal variations.

However, here we refrain from using this method for the following reasons:

- It was one aim of this thesis to detect NO_x produced by lightning. Lightning NO_x is released in the upper troposphere, where lifetimes are enhanced. Thus the distribution of NO_x from lightning is rather smooth und would be misinterpreted to be stratospheric in a 2-D approach. The same holds for aircraft emissions.
- NO_2 columns over some oceanic regions are also strongly influenced by transport, e.g. the Atlantic at the African westcoast. If the reference regions reach too close to coastal regions, this has an impact on the stratospheric estimate.
- Due to the large extension of continents (with tropospheric sources of NO_x) and coastal regions that have to be cut out in the 2-D algorithm, the stratospheric estimation has to be extrapolated over a large region, especially for the northern hemisphere. Thus the benefit of the 2-D estimation (compared to the simple reference sector method) is rather small for e.g. the critical stratospheric estimation over the arctic vortex.

The simple 1-D reference sector method furthermore has the advantage that it can be easily smoothed over time; this has been proven to be essential for the analysis of the weekly cycle (Chapter 4).

2.4.1.5. Cloud slicing (NO_2 above clouds)

Another method to separate tropospheric and stratospheric columns is the so-called “cloud-slicing” that has been successfully applied to ozone data [Ziemke et al., 2001]. The idea is to choose observations of clouded scenes, where the troposphere is shielded, hence the measured VCD is stratospheric. To check the usability of this method for NO_2, Fig. 2.15 compares NO_2 VCDs for cloud free (i.e. cloud fractions below 10%) with clouded (i.e. cloud fractions above 60%). (Please note that these are tropospheric VCDs where the stratosphere is already removed by the reference sector method). It is clearly visible that NO_2 VCDs over strong source regions (like China, Europe and the US Eastcoast) are reduced for clouded scenes. In cloud free cases, the map shows steep gradients of NO_2 VCDs from continents to oceans. For clouded scenes, these gradients are strongly reduced.

However, even for cloud covers above 60%, mean NO_2 VCDs are enhanced over source regions. Furthermore, over large parts of the oceans, the NO_2 VCDs for cloudy conditions are higher than that for cloud free conditions, indicating that the measured stratospheric VCDs are not independent on cloud fraction. In some cases, we also find enhanced VCDs that are probably of tropospheric origin, but lifted up to the upper troposphere, where they are better visible in the clouded composite (south-east of South Africa). Finally, the plume of the Chinese Mega City Urumqi (marked in Fig. 2.15) is even better visible in the “clouded” composite, probably due to the high albedo during snow cover in winter that is misinterpreted as cloud cover.

Hence observations of NO_2 for clouded scenes hold valuable information on stratospheric NO_2, but situation is too complex as this could be directly applied for a stratospheric estimation.

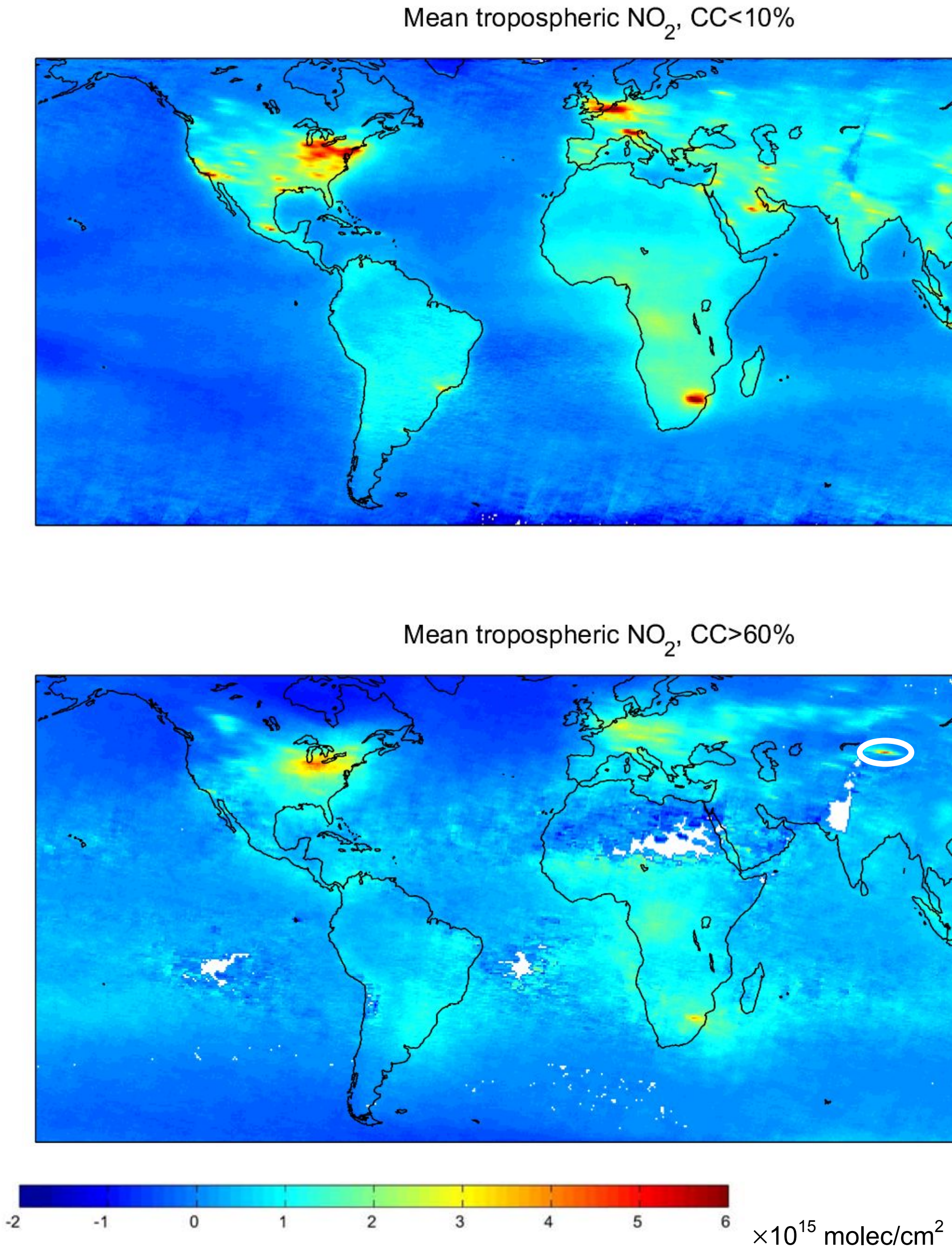

Fig. 2.15: Comparison of mean NO_2 VCDs for cloud free (above) and clouded scenes (below). Data comprises 1996-2001. These VCDs are already tropospheric, the stratosphere has been estimated with the reference sector method. The white ellipse in the lower plot marks Urumqi (see text).

2.4.1.6. Limb-Nadir-matching

The additional limb-modus of SCIAMACHY allows the direct estimation of the stratospheric column of NO_2: due to the alternating viewing modes, a given stratospheric air parcel is scanned twice, first in limb, later in nadir mode (“limb-nadir-matching”) [Bovensmann et al., 1999]. As the atmosphere is scanned with different elevation angles, profiles of stratospheric trace gases can be determined by inversion methods [Rodgers, 2000].

Stratospheric column densities can then directly be integrated from the retrieved profile. This method has been successfully used to determine adequate stratospheric columns [Andreas Richter, pers. comm.] even e.g. for the polar vortex, where the reference sector method fails.

The ongoing collection of SCIAMACHY data will allow to compare the performance of different approaches of stratospheric estimations systematically, and will likely help to improve also the methods used for GOME.

Within this study, we use a simple reference sector method, as it is stable, fast and easy to handle. As a reference sector we chose a stripe in the Pacific Ocean where lightning activity is minimal.

After subtracting the stratospheric column from the total column, we retrieve tropospheric VCDs. In the following, these are abbreviated as TVCDs.

2.5. Validation

Validation of the results from satellite measurements are necessary to quantify systematic and random errors.

In the last years, several validation studies have been performed [Burrows and Platt, 2004]. Especially for SCIAMACHY, large efforts were set on the validation of total and tropospheric VCDs of several trace gases from different platforms.

Here we present the results from 3 studies where we compare total VCDs from GOME to ground based measurements in Antarctica (2.5.1), and SCIAMACHY results to aircraft measurements in Germany (2.5.2).

Please note that the comparison of local measurements with satellite data is affected by the spatial resolution of the latter: the satellite measurements take the average VCD over the ground pixel.

2.5.1. Antartica

2.5.1.1 Neumayer Station

Fig. 2.16 shows a time series of VCDs as retrieved from GOME (blue) compared to the results of ground based DOAS measurements for Neumayer station (70°S, 8°W). These measurements were performed by Udo Frieß [Frieß, 2001]. For the plot measurements for sunset and sunrise at a fix SZA of 90° are shown.

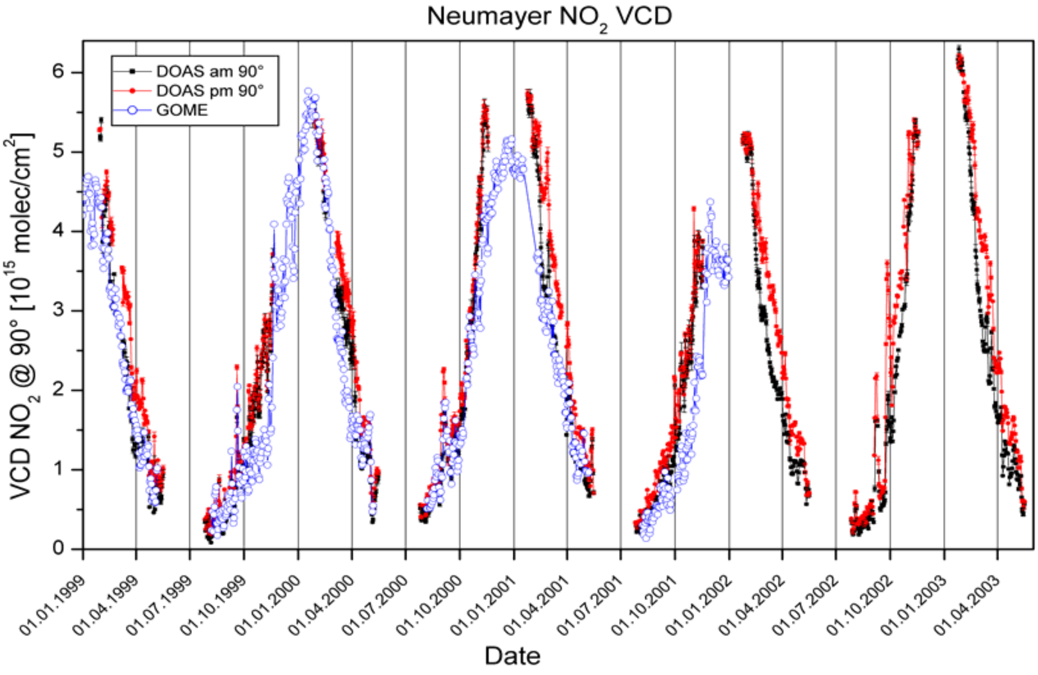

Fig. 2.16: Time series of VCDs from GOME and ground based DOAS measurements at Neumayer Station, Antarctica [Udo Frieß, personal communication].

2.5.1.2 Terra Nova Bay

In a second study, we present a comparison of VCDs measured from GOME with the ground based DOAS measurements performed in Terra Nova Bay (74.5°S, 164°E) with the "Gas Absorption Spectrometer Correlating Optical Differences" (GASCOD). Fig. 2.17 shows the correlation of both datasets for 2001 in a scatterplot.

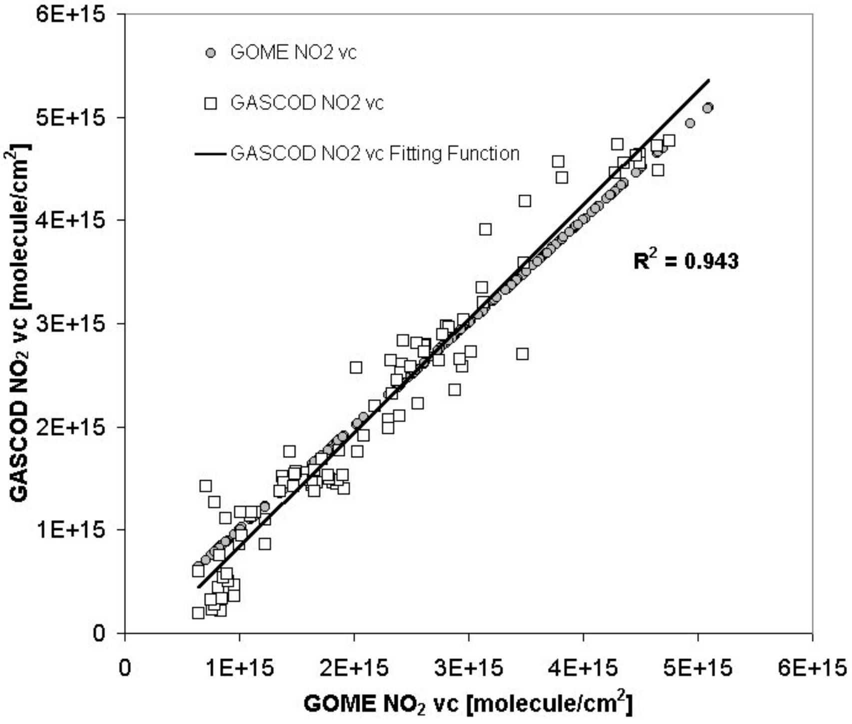

Fig. 2.17: Comparison of GOME NO_2 VCDs and ground based DOAS measurements at Terra Nova Bay in 2001 [D. Bortoli, personal communication]. Both datasets are highly correlated.

These examples show a good agreement of the VCDs derived from GOME and from ground.

2.5.2. Validation of SCIAMACHY VCDs

In the context of SCIAMACHY validation, measurements have been performed with an Airborne Multi AXis DOAS (AMAXDOAS) instrument [Heue et al., 2004a,b] that was set on the research aircraft FALCON. The instrument covers the spectral range 300-550nm and measures light from different telescope elevation angles (nadir, zenith, +-2° elevation) [Bruns et al., 2004]. Flying at 11 km altitude in midlatitudes, we can assume the zenith viewing telescope to observe the stratosphere and the nadir viewing to observe the troposphere (plus stratosphere). The horizontal resolution is about 6.6 km.

For the DOAS fit, the reference spectrum was taken from a measurement for cloudfree conditions over unpolluted regions (here in Northern Sweden).

Fig. 2.18 shows the total vertical NO_2 columns resulting from SCIAMACHY and AMAXDOAS measurements on 10 March 2003. Both measurements have been taken within 45 min: SCIAMACHY passed Germany at 9:50 whereas the aeroplane started in Oberpfaffenhofen at 9:45 and overflew the Ruhr region between 10:30 and 10:37. The general agreement is very good: a strong enhancement of NO_2 VCDs is observed in both datasets over the Ruhr region; VCDs are slightly enhanced over northern Germany and southern Scandinavia. However, the SCIAMACHY measurements results in lower VCDs compared to AMAXDOAS in the Ruhr area. This might be due to the different horizontal resolutions, or to temporal changes in the concentration and cloud coverage. Furthermore the total SCIAMACHY VCDs are derived with a stratospheric AMF, hence the tropospheric column is underestimated.

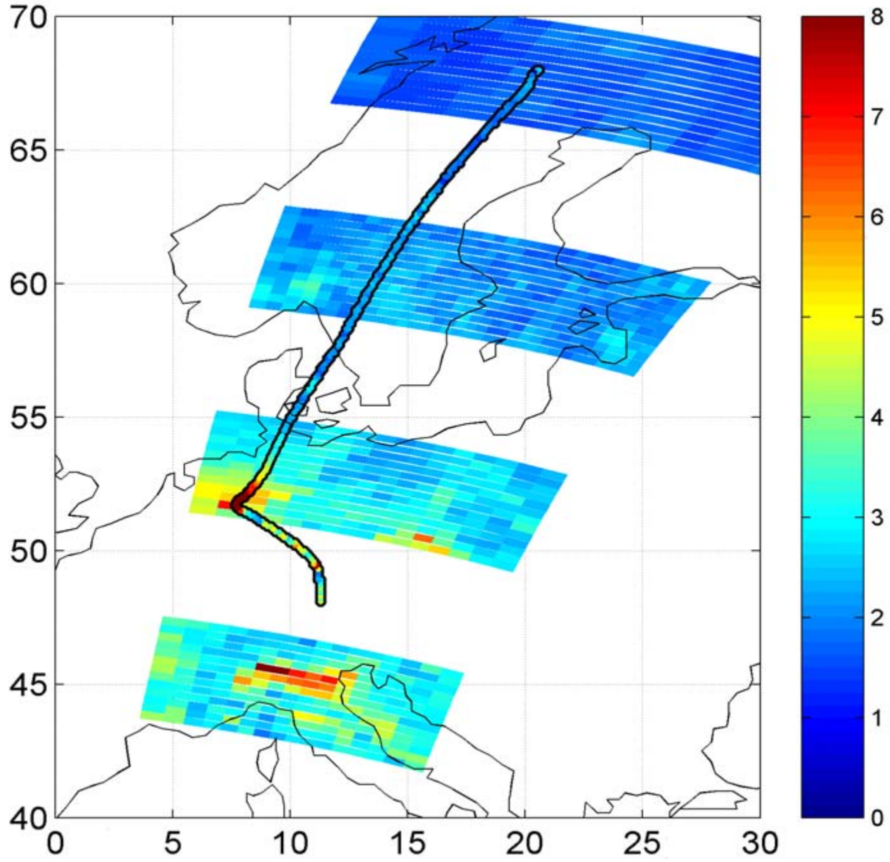

Fig. 2.18. Vertical NO_2 column densities [10^{15} molec/cm^2] observed by SCIAMACHY and AMAXDOAS on 10 March 2003. [Heue et al., 2004a].

Chapter 3

The potential of satellite data for identifying and quantifying NO_x emissions and lifetime

According to the importance of nitrogen oxides for atmospheric chemistry, there is a huge number of studies dealing with estimates of NO_x emissions for the different sources. The review studies by Lee et al. [1997] and Bradshaw et al. [2000] lists best estimates and uncertainties for the respective source strengths. In Table 3.1, these values are adopted, and further recent results are added in column 4.

Table 3.1: Global emission estimates of nitrogen oxides according to Lee et al. [1997], Bradshaw et al. [2000], and some recent estimates. All units are (Tg [N]/year).

Source	Lee et al. [1997]	Bradshaw et al. [2000]	Recent estimate
Fossil fuel combustion	22 (13-31)	23 (16-30)	
Biomass burning	7.9 (3-15)	8.5 (4-16)	7.8[a] [Galanter et al., 2000]
Soil microbial production	7.0 (4-12)	5.5 (3-8)	**13** [Davidson and Kingerlee, 1997] **7.3** (tropics) [Jaegle et al., 2004]
Lightning	5.0 (2-20)	6.5 (3-26)	4 (0.3-22) [Huntrieser et al., 1998]
Aircraft	0.85	0.51 (0.5-0.6)	
Total	44 (23-81)	45.2 (27-86)[b]	

[a] The authors state the uncertainty to be "much less than factor of 2"

[b] Also including oceans (0.5), NH_3 oxidation (0.6) and stratospheric intrusion (0.12).

Largest source of all, making up more than 50% of total emissions, is fossil fuel combustion. This can be further divided into emissions from power generation / heavy industry, traffic and heating. For Germany, these sources contribute about 35%, 60%, and 5%, respectively [Wickert, 2001]. Aircraft emissions also originate from fossil fuel combustion, but are usually considered separately, as they take place in the upper troposphere.

Natural sources of NO_x are lightning, biomass burning and soil emissions. However, biomass burning as well as soil properties are also strongly controlled by mankind by e.g. clearing of forest for agricultural use, energy production for cooking and heating, and by fertilization. Hence, nowadays NO_x emissions by biomass burning and soils are largely anthropogenic, so that the overall NO_x production is by far dominated by human induced activities.

NO_x source strengths of the different source types are usually estimated by bottom-up approaches: the NO_x produced by a basis unit (i.e. a single car, ship or aircraft engine, a single power plant, a single flash or thunderstorm, a kg of burnt biomass etc.) are measured in laboratory or in regional campaigns. The resulting uncertainties stem mainly from the extrapolation of these units to global scale. Especially for lightning, current uncertainties are rather large.

Satellite measurements in principle allow a new, independent method for source strength estimation as a top-down approach: The whole globe is consistently observed with a single instrument. To use this information to quantify emission source strengths, the task is (besides the retrieval of SCDs with DOAS (2.2), stratospheric estimation (2.4) and an appropriate RTM correction (2.3) resulting in quantitatively correct TVCDs) to discriminate the contribution of the different NO_x sources, as the satellite measures the overall sum. Thus the correct classification of a NO_2 signal to be due to a specific source is essential. Furthermore, the conversion of NO_2 TVCDs into emission values requires information on the lifetime of NO_x, as NO_2 accumulates more for longer lifetimes.

Here we discuss the general capability of GOME (and SCIAMACHY) NO_2 data to identify and quantify the different sources of NO_x as well as its lifetime, and refer to the following chapters, where the particular studies are performed in detail.
As SCIAMACHY data became available rather lately, for most of the studies presented GOME data is used, thus our discussion here focusses on GOME. However, SCIAMACHY is also mentioned where its characteristics are relevant.

3.1. Potential of GOME (and SCIAMACHY) data

Due to the specific advantages of satellite observations they have a high potential to help analysing atmospheric chemistry, estimating emission strengths and even quantifying the lifetime of NO_x. The main aspects are:

(a) UV/vis:
GOME is capable of detecting NO_2 even in the lower troposphere.

(b) Long time series:
The GOME instrument is in space since 1995, and is still taking data!
Thus satellite data is a valuable tool for analyzing e.g. seasonal cycles or trends.

(c) Global coverage:
The ERS-2 satellite covers the poles as well as the tropics. Thus totally different phenomena (like stratospheric dynamics in polar regions or NO_x from tropical biomass burning) can be analyzed. The GOME data comprises both, the monitoring of remote regions as well as the highly polluted regions of the world at the same time, with rather stable instrumental characteristics and similar sensitivity.

(d) Temporal resolution:
Global coverage is reached after 3 days at the equator and every day for latitudes above 70°. This allows to analyze temporal variations on different time scales (i.e. weekly or seasonal cycles) and to trace transport.

(e) Spatial resolution:
By mapping the NO_2 TVCDs, characteristic patterns of the NO_2 distribution allow the identification of specific sources.

(f) Synergistic use of satellite data:
With the DOAS algorithm, also column densities of other trace cases can be evaluated, that for instance help to understand polar ozone loss (O_3, OClO) or allow the identification of biomass burning events (CH_2O, CO).
Furthermore, other independent satellite data can be consulted (e.g. fire counts, flash counts, light pollution by night, aerosols, land cover) and compared to the GOME/SCIAMACHY results.

However, GOME observations are still subject to important shortcomings that have to be kept in mind:

(a) The sensitivity for the troposphere is low and depends on many parameters like surface albedo, cloud cover, aerosol load and trace gas profile, as discussed in section 2.3, and current uncertainties are still rather large.

(b) 8 years of data are not really "long" if it comes to trend studies. GOME also suffers from degradation [Tanzi et al., 2000] (see section 2.2). One has thus to maintain caution while predicting trends.
However, the ongoing measurements from SCIAMACHY, OMI (launched onboard AURA 2004) and GOME 2 (to be launched 2005) continue the current time series.

(c/d) global cover is reached after 3 days for GOME (and 6 days for SCIAMACHY), leaving temporal gaps that affect the monitoring of e.g. transport events or irregular emissions like lightning or biomass burning. Furthermore, since GOME measures always at the same local time, diurnal dynamics are not resolved. For this purpose a geostationary satellite is essential, that hopefully will be realized in future.

(e) the GOME resolution east-west is rather coarse (320 km). This results in a "smearing out" of actually separated NO_2 plumes (see Chapter 9), and complicates the identification of specific sources (e.g. a single city). However, the narrow swath mode of GOME and the meanwhile available SCIAMACHY data provide a higher spatial resolution, the benefit of which will be discussed in Chapter 9.

(f) the spectral range of GOME is restricted to the UV/Vis. This wavelength range is well suited for the retrieval of TVCDs of several trace gases, especially NO_2. But greenhouse gases and CO cannot be retrieved by GOME. SCIAMACHY, however, also provides IR channels that allow the retrieval of VCDs of further trace gases, especially CO_2, CH_4 and CO [Frankenberg, 2004]. The latter provides new, additional information on biomass burning and industrial sources.

3.2. Identification of NO_x sources

Within this PhD study, the potential of satellite observations of tropospheric NO_2 is used for the identification of different sources of NO_x. In specific cases also quantitative estimates of source strengths are given.

Fig. 3.1 shows the mean global distribution of tropospheric VCDs (TVCDs) of NO_2 for 6 years as seen by GOME. This figure already illustrates that GOME data holds plenty of information on the different sources of nitrogen oxides.

The impact of ***fossil fuel combustion*** is visible on first view: large parts of the US, Europe and Eastern Asia reveal clearly enhanced levels of NO_2 TVCDs. Further polluted regions are the South African "Highveld", where several of coal power plants are located. Even the emissions from Megacities like Los Angeles, Mexico City or Hong Kong are detectable.

However, to identify other (weaker and less localized) NO_x sources, more detailed studies are needed. Typically, enhanced NO_2 TVCDs are attributed to a specific source, if spatial and/or temporal patterns match. As indicator for the occuring of e.g. biomass burning, lightning or ship emissions, external datasets like fire, flash or ship counts, respectively, are consulted. The large amount of GOME data allows statistical evaluations of long time series as well as case studies on single, extraordinary events.

The following chapters deal with detailed studies on the identification of the different sources of NO_x from GOME data:

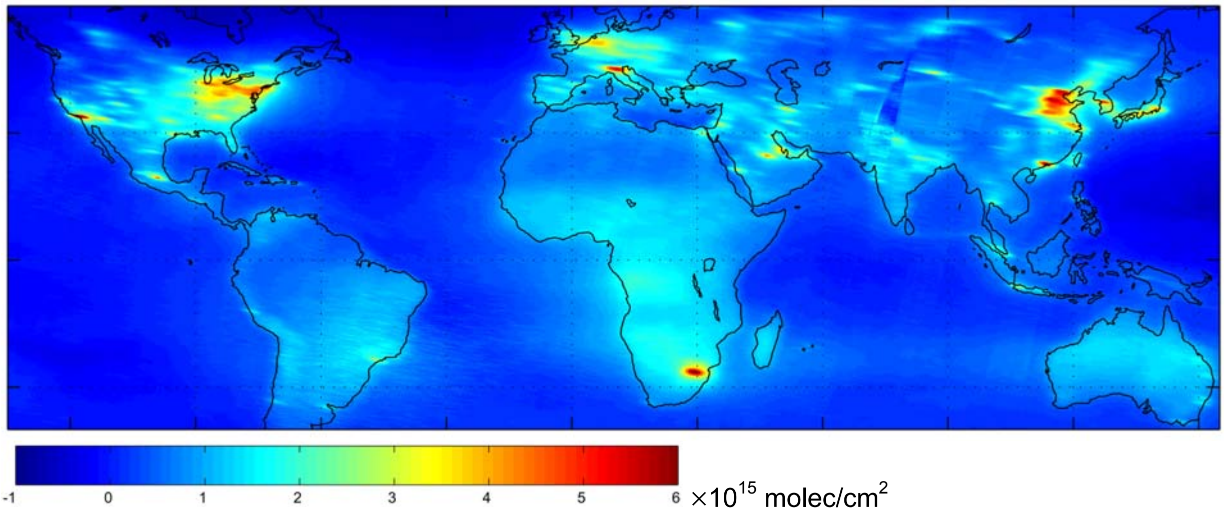

Fig. 3.1: Mean global distribution of NO_2 TVCDs as derived from GOME (1996-2001).

To study specific characteristics of anthropogenic sources due to fossil fuel combustion, we analyze the ***weekly cycle*** of NO_2 TVCDs in Chapter 4. This holds in principle information on the contribution of traffic, power plants/industry and heating.

Emissions from ***aircrafts*** are rather low (Table 3.1) and are seemingly not detectable from GOME; this is discussed in Chapter 5.

The NO_x production by ***lightning*** has the highest uncertainty of all sources (Table 3.1) and at the same time strong impact on ozone production. In Chapter 6, we present a correlation of NO_2 TVCDs and lightning counts that allows a quantitative estimate of lightning NO_x. Furthermore, we show an extraordinary lightning event coinciding with high NO_2 VCDs above cloud cover.

The impact of ***biomass burning*** is investigated in Chapter 7 by analyzing temporal correlations of NO_2 TVCDs and fire counts. However, due to the strong release of aerosols, radiative transfer is complex and quantitative estimates are difficult.

The ***spatially highly resolved*** results from SCIAMACHY give totally new insights on the actual location and strength of pollution sources (like single cities or power plants), and some inconsistencies show up by comparisons with emission inventories (Chapter 9).

Furthermore, the satellite data is used to analyze the role of ***transport*** of NO_2. As the range of NO_2 transport depends on wind as well as the NO_x ***lifetime***, the satellite data holds information on the latter.

In Chapter 8, the impact of ***long-range transport*** of NO_2 is investigated. However, Fig. 3.1 reveals that we generally find local enhancements of NO_2 TVCDs over source regions, indicating a rather ***short lifetime*** of boundary layer NO_x. In Chapter 10, we analyze the effects of downwind transport, and also the weekly cycle, to estimate the lifetime of NO_x quantitatively, again making use of the characteristic strengths of satellite measurements.

Finally, we estimate the NO_x emissions from ***ships*** in Chapter 11. Therefore we use the estimated lifetime for the specific conditions.

Chapter 4
Weekly cycle of tropospheric NO_2

4.1. The "weekend effect"

Industrial activity and traffic in "western" countries are reduced during weekends leading to lower levels of emitted pollutants. Compared to working day levels the weekend emissions of NO_x, e.g. in Germany, are reduced by approximately 35% [Wickert, 2001]. However, measurements revealed that Sunday levels of tropospheric ozone are on the same level or even higher than during working days (e.g. [Cleveland et al., 1974; Marr and Harley, 2002]). This phenomenon has been called "weekend effect" or "Sunday effect". On the other side, reduced levels of tropospheric ozone on Sundays have also been reported, mainly for conditions supporting summer smog, i.e. high solar radiaton, high temperatures, and low wind speeds [Elkus and Wilson, 1977; Brönnimann and Neu, 1997].

The early studies on the weekend effect were motivated by the potential effect on ozone. The higher NO_x emissions on working days have two reverse effects (see Chapter 1):

- since the NO_x emissions by fossil fuel combustions are mainly in form of NO, O_3 is reduced by (R 1) on working days
- the enhanced levels of NO_2 increase the catalytic production of tropospheric O_3 (R 14, R2, R3), if the system is NO_x limited (see section 1.5.1-1.5.2). For VOC-limited regimes, on the other hand, the higher working day NO_x emissions result in lower tropospheric O_3. Studies on the weekend effect can thus be used to categorize VOC-sensitive regimes, and forecast the effects of emission reduction programs.

The degree of reduction of industrial activity and traffic may differ from country to country and even from region to region, but a Sunday minimum of NO_x emissions is generally expected for all countries having a Christian tradition (or being influenced by western industry, like Japan), celebrating Sunday as the day of rest.

4.2. Weekly cycle of NO_2 TVCDs from GOME

A first evidence for a weekly cycle in NO_2 TVCDs was presented by Wenig [2001] for the large industrialized regions in the US and Europe. In this chapter, the long time series of GOME data is used to analyze weekly cycles of NO_2 statistically for single cities in different regions of the world (4.2.2). However, as this study is restricted by some specific GOME characteristics; we first repeat those here and discuss their influence (4.2.1). The results from this chapter have been published in Beirle et al. [2003].

4.2.1. Characteristics of GOME observations with respect to weekly cycle analysis

For the interpretation of weekly cycles from GOME one has to keep in mind that:

- For every considered city, we only choose GOME observations that actually include the city center. Please note, however, that the coverage of one GOME pixel is about 40 km north-south by 320 km east-west. The total area of pixels containing a specific location is thus 80×640 km^2 (since the city center may be situated in the upper right corner of the GOME pixel as well as in the lower left corner), implying possible interferences with other sources, mostly neighboured cities.

- The flight track of the ERS-2 satellite has a periodicity of 35 days. This influences the analysis of weekly cycles, since 35 is a multiple of 7. Hence each day of the week is scanned with a different spatial sampling. This implies that, by monitoring a certain location, the influence of neighbouring regions differs for every day of the week. This effect is in general of minor importance, but may cause artefacts in the weekly cycle of NO_2 TVCD in a few cases (as discussed below).
- The retrieval of tropospheric information from satellite data can be strongly affected by clouds: an enhanced cloud cover might 'shield' the troposphere and lead to the observation of a reduced TVCD. In principle, there could even be a systematic weekly cycle of cloud cover. In fact, Cerveny and Balling Jr [1998] report a weekly cycle of precipitation.

  By analysing the weekly cycle of cloud fractions from HICRU [Grzegorski et al., 2004] we found no evidence of a weekly pattern of enhanced cloud cover on Sundays. In the case of Germany, for instance, the mean cloud cover (1996-2001) is 0.450 on weekdays and 0.457 on Sundays. The weekday cloud covers (i.e. the fraction of the area covered by clouds) vary between 0.431 (Tuesday) and 0.479 (Friday); the standard deviation of the five mean weekday values is 0.018. Especially the fact that for Germany the day with the highest cloud cover shows no irregular features in the NO_2 TVCD gives us confidence that the influence of cloud cover on our study is negligible. We did not observe enhanced cloud cover on Sundays for the US either.

4.2.2. Weekly cycle of NO_2 in different industrialized regions

In this study, we focus on four regions of the world with enhanced NO_2 TVCD values: 1. the eastern USA, 2. western Central Europe, 3. East Asia and 4. the Middle East, as well as 5. some individual cities, as marked in Fig. 4.1. Rural areas with other predominant sources of NO_x (soil emissions, biomass burning, lightning) show no indication for a weekly NO_x cycle.

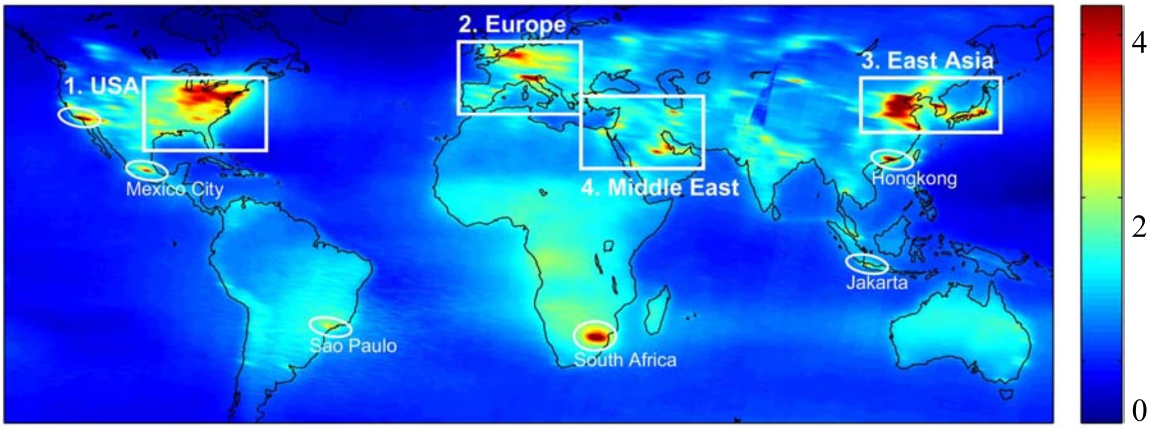

Fig. 4.1. Six years mean (1996-2001) of global NO_2 TVCD in 10^{15} molecules/cm^2. The weekly cycle of the framed areas 1. US East Coast, 2. Europe, 3. East Asia and 4. Middle East, as well as 5. the marked individual Metropolises are considered in detail in this study.

The weekly cycle of NO_2 TVCD is visualized in two ways. Fig. 4.2 shows maps of the NO_2 TVCD for the regions under consideration for the different days of the week (mean over 1996-2001). This provides information about the absolute source strength in the different

regions. The effect of the 35 day periodicity of GOME is reflected by the stripe-like structures parallel to the ERS-2 flight direction.
In addition, Fig. 4.3 shows plots of weekly cycles for some selected cities to illustrate the relative reduction of the NO_2 TVCD during the day of rest. For each day of the week we calculated the mean (and its statistical error) of all GOME observations (1996-2001) containing the respective location. These values are normalized to the median weekly value for better comparison. (The median was chosen as reference in order to avoid a bias by the Sunday minimum: The mean of all days would shift from the normal weekday level towards the lower Sunday level, and consequently, the weekdays normalized to the mean would be higher than unity.) The normalisation allows to calculate relative errors. The error bar of each subplot is the maximum of all individual relative errors. We chose a logarithmic scale since we focus on relative changes in the weekly cycle. Furthermore, the length of the relative error bar is independent from the actual mean.

Both figures show the same general features: the level of NO_2 TVCD is similar for the different working days, but there is a significant reduction of NO_2 TVCD during the weekend, especially on Sunday, for the US (1), Europe (2), and Japan (3a). In all cities considered in these regions, there is a minimum on Sunday. The NO_2 TVCD is reduced by about 25-50% and even 60% (Milan (2)). A Sunday minimum can also be seen in Johannesburg and Mexico City (5).

In China (3b), no indications for a weekly cycle can be found in Fig. 4.2 or Fig. 4.3. China has a different economic, cultural, and religious background. Nevertheless, there is also a seven day week and a work free weekend. The absence of a weekend effect in our data probably indicates that the Chinese NO_x emissions are dominated by power plants and heavy industry, operating throughout the week. On the other hand, in the US and in Europe individual transport appears to contribute significantly to the NO_x sources.

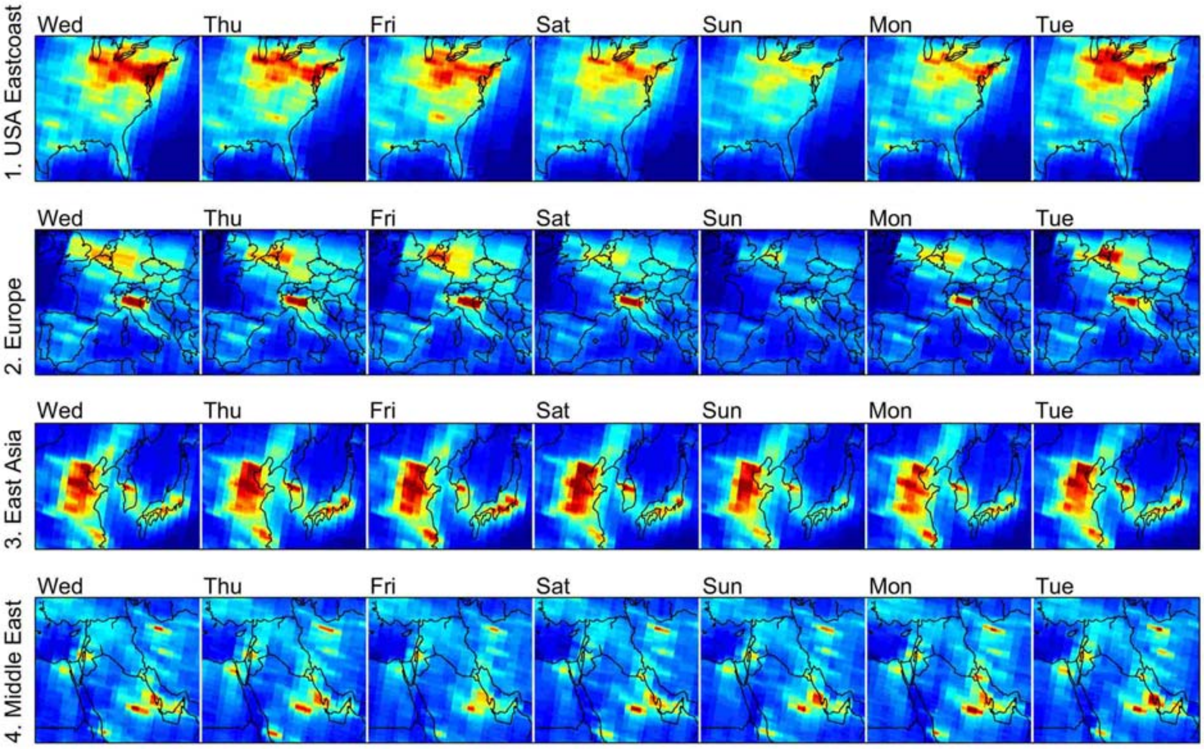

Fig. 4.2: Mean NO_2 TVCD (1996-2001) for the regions of interest, as marked in Fig. 4.1, for the different days of the week separately. Colour scale and unit are the same as in Fig. 4.1.

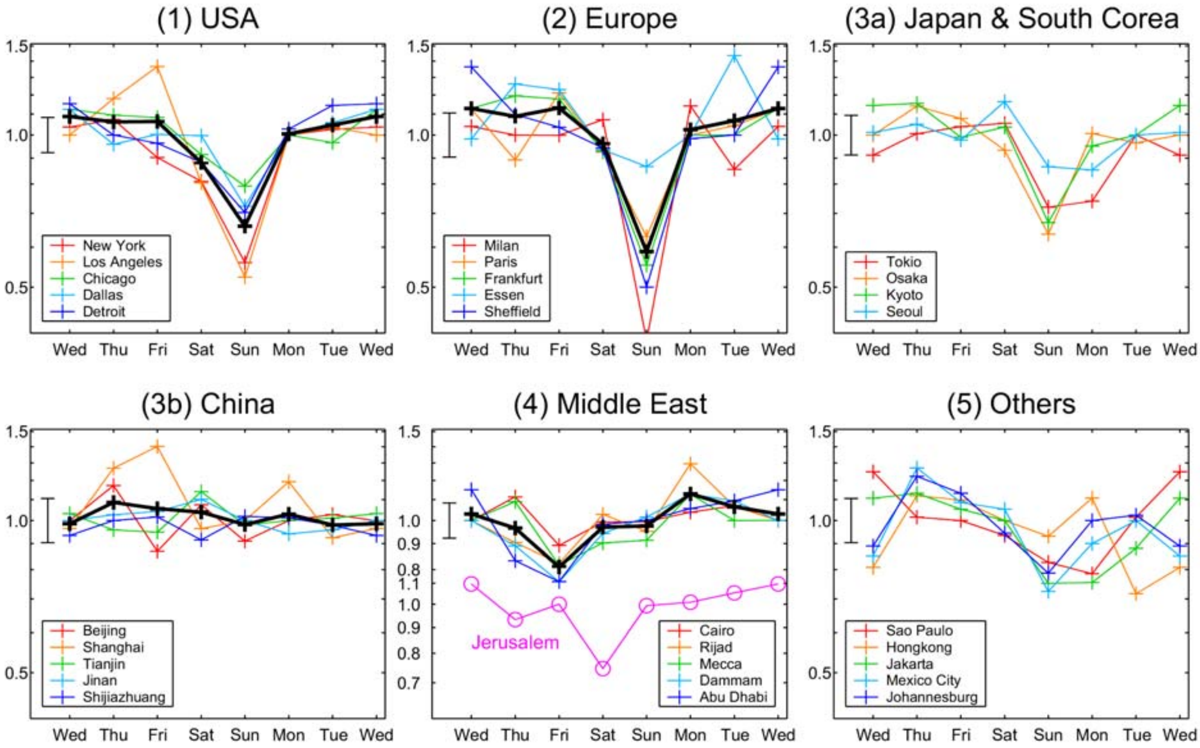

Fig. 4.3: Weekly cycle of mean (1996-2001) NO_2 TVCDs for the considered locations (as marked in Fig. 4.1). The values are normalized with respect to the median weekly value (relative units). Black lines are averaged curves. The error bar to the left of every plot indicates the maximum relative error (standard error of the mean) of all data points. The scale is logarithmic to emphasize relative features.

The cities in the Middle East (4) show a shifted weekly cycle due to different religious traditions, i.e. other days of rest. In Israel, Saturday (Sabbath) is the day of lowest NO_2 TVCD. In Islamic cities, there is a slight weekly effect with lowest emissions on Friday.

Besides the noticeable minimum on Sunday, there are two more days of interest in the weekly cycles of the western cities: a) Saturday, since it is also a working free day for most professions in western countries (reduced industrial activity), but a preferred day for shopping or short trips (possible increase of individual transport), and b) Monday, since it starts with relatively clean air, whereas for the other working days the measured air masses might be influenced by the pollution of the day before, as the lifetime of NO_x in the troposphere is about one day (see also Chapter 10).

a) Saturday NO_2 values are slightly reduced in most western cities. But in some places they are quite high, reaching normal working day levels (e.g. Milan, Dallas, Tokyo).

b) Monday values in the US and Europe are almost on working day level, whereas there are uncommonly low levels in Tokyo and Seoul (3a) as well as in Sao Paulo and Jakarta (5).

To understand these features in the weekly cycle in detail, further information about local emissions, wind speed and direction, and lifetime of NO_2 is necessary. Another aspect is the daily cycle of emissions, especially the starting time of work in the morning which differs from region to region, whereas the local observation time of GOME is the same (about 10:30). A rather late start of human activity in the morning could possibly explain the Monday minimum in the weekly cycle for e.g. Sao Paulo. The fixed observation time also affects the level of the Sunday minimum, since on Sundays generally emissions start later (Sunday trips or shopping (in the USA) take place mainly after the GOME overpass).

The 35 day periodicity of the ERS-2 satellite flight track should be, in general, of minor influence. However, it is thought to be the most probable reason for some unusually high values, e.g. the Tuesday values in Essen or the high Wednesday values in Sheffield (Fig. 4.3 (2)). For instance, in the Tuesday scans, the polluted regions of West Germany (Ruhr area) and the Netherlands are largely covered by a single track of GOME pixels, whereas there are two neighbouring tracks on Wednesdays (see Fig. 4.2(2)). This leads to a higher observed NO_2 TVCD on Tuesdays compared to Wednesdays. Also the relative high Sunday values in Essen seem to derive from this effect.

4.2.3. Seasonal differences

We compared the weekday and Sunday levels of tropospheric NO_2 in Europe and the USA for summer and winter separately (Fig. 4.4), and could observe a significant Sunday reduction for both regions and both seasons. In principle, a quantitative comparison of the weekly cycles for summer and winter should hold information on the contribution of different anthropogenic sources (see table 4.1): On Sundays, industrial activity and traffic (before 10:30 ERS-2 overpass!) is minimal. This baseline can be estimated in summer for e.g. Germany (where no heating takes place). In contrast, during weekdays the additional NO_x from traffic and working day industry is added. In winter, the contribution of heating is supplemented. For the southern parts of the US, heating probably plays only a minor role, while the higher energy consumption in summer due to air conditioning is likely increasing the NO_x baseline.

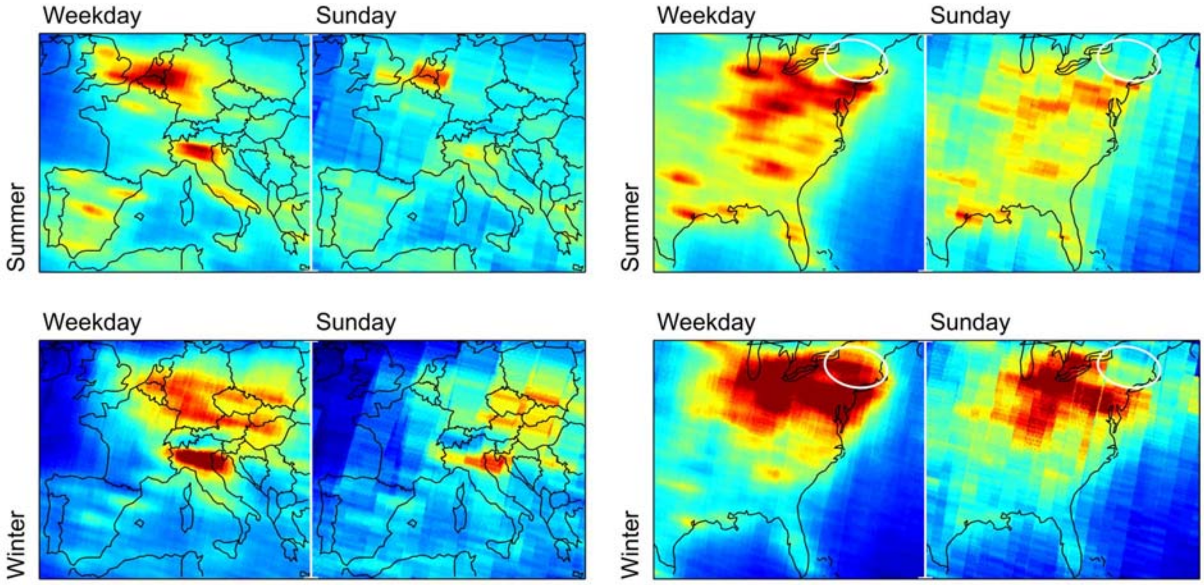

Fig. 4.4: Mean NO_2 TVCD (1996-2001) for Europe (left) and US east coast (right), separated for summer (upper row) and winter (lower row). The mean workday level is compared to the respective Sunday plot. Colour scale and unit are the same as in Fig. 4.1. The marked area in the northeastern US is discussed in the text.

Table 4.1: Weekend/weekday differences of the source types of NO_x separated for summer and winter. Please note that the actual contribution of the different source types differs for different regions (i.e. is especially different for China).

	Weekdays	**Sundays**
Summer	Full Industry + air conditioning + traffic	Industry baseline + air conditioning
Winter	Full Industry + heating + traffic	Industry baseline + heating

However, such a quantitative analysis seems to be not feasible yet:

- The reduction of data (3 months per year instead of 12) increases the statistical error by a factor of 2.
- Obviously, the stratospheric bias (see section 2.4) depends on season. Mainly in winter we retrieved negative tropospheric columns over the Atlantic e.g. around Ireland or east of Florida (Fig. 4.4, lower row).
- The lifetime of NO_x is higher in winter (see Chapter 10). This also influences the weekly cycle, i.e. the Sunday minimum (in winter, when lifetime is longer, there is more NO_x from Saturday remaining).

Nevertheless, Fig. 4.4 reveals some new insights. For instance, while the Netherlands/ Belgium/ Germany plume vanishes almost completely on Sundays in winter (Fig. 4.4, lower left panel), indicating transport as main source of NO_x, the TVCD over Austria/ Hungary/ Czechia/ Slovakia/ Poland almost stays the same. This indicates that here the predominant source of NO_x has no weekly cycle, i.e. is very probably heating. (Buildings in Eastern Europe are worse isolated, which leads to higher energy consumption for heating [Bayer et al. 2002]).

Another quite astonishing result is the north-eastern region of the US between Lake Ontario and Boston (Fig. 4.4, marked ellipse, right panels): While this region is quite clean in summer (on weekdays as well as on Sundays), it is highly polluted on winter workdays, but much less on Sundays. This indicates a weekly cycle in NO_x - either due to source, visibility to GOME, or sink - not existing in summer. At present we do not understand this feature.

4.3. Outlook

The existence of a weekly cycle is an obvious signature of anthropogenic sources. However, the analysis of the weekly cycle holds more than just confirming emission patterns or detecting cultural habits. The low level of the Sunday minimum in the western cities provides information about the fraction of periodic anthropogenic sources of NO_x. In principle, the analysis of the weekly cycle (for different seasons) could help to discriminate manmade from natural sources (lightning, biomass burning, soil emissions) and assess the contribution of local traffic to the NO_x sources.

Furthermore, the characteristics of the weekly cycle, i.e. the ratio of the Monday values and Sunday minima, allow a rough estimate of the mean lifetime of boundary-layer NO_x. This will be discussed in detail in section 10.4.

The quantitative interpretation of features of the weekly cycle requires background information about the considered regions. Weekly as well as daily patterns of emissions, the predominant source of NO_x (traffic, heavy industry, or heating) and the lifetime of tropospheric NO_x differ for different levels of industrialisation, religious and cultural customs and meteorological conditions.

The statistical errors of the data points in Fig. 4.3 are quite small due to the large amount of data. Systematical errors due to the estimation of the stratospheric column and the large spatial extent of the GOME pixels, as described in section 2.1, have to be borne in mind. The better spatial resolution (nominal 30×60 km^2) provided by SCIAMACHY will allow the improved analysis of weekly cycles of tropospheric NO_2 and will afford quantitative estimates of different types of anthropogenic emissions for different seasons and different regions of the world.

The SCIAMACHY potential of limb viewing enables better stratospheric estimates, so that weekly cycles can be also studied more quantitatively. Furthermore, the analysis of weekly cycles of satellite data of formaldehyde (CH_2O) - as indicator of VOCs - and of tropospheric ozone could give direct insight on whether a city is in a NO_x or a VOC sensitive regime (see also [Martin et al., 2004]).

Chapter 5
Aircraft emissions

Aircraft emissions are, compared to other sources, only a minor contribution to the total budget of nitrogen oxides (< 1Tg [N]/yr, compare table 3.1). Though, they are quite important, as they take place in the upper troposphere, since flight altitudes of intercontinental flights are about 8-12 km. Here background levels of NO_x are rather low, and thus the natural composition is severely disturbed. Consequently, aircraft NO_x emissions have a high ozone production efficiency. Hence, while the uncertainty of the total NO_x released by aircraft is, in absolute numbers, quite small, it is several times higher for the resulting ozone production. Furthermore, the impact of aircraft emissions is supposed to grow in future, as air traffic is expected to increase in the next years.

Fig. 5.1 shows the global distribution of aircraft NO_x emissions as estimated by the DLR-project FATE (“Four-dimensional calculation of Aircraft Trajectories and Emissions”) in a bottom-up-estimate [Holger Pabst, personal communication; see also Brunner and Fehr, 2000]. Numbers from other studies (e.g. Fig. 1 in [Velthoven et al., 1997]) are similar. Most aircraft traffic takes place on routes connecting central Europe with destinations in North America. Shortest connections follow great circles, thus emissions are highest for a rather narrow flight corridor passing the southern tip of Greenland.

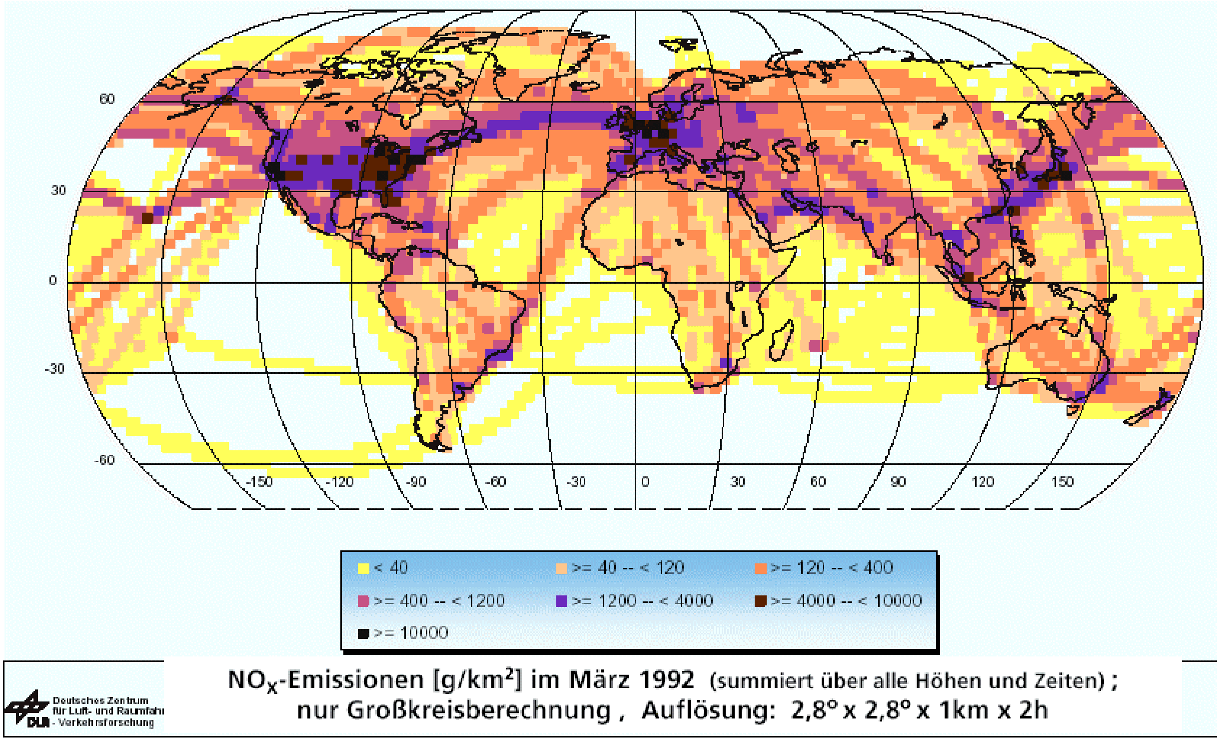

Fig. 5.1: Global aircraft NO_x emissions for March 1992, assuming all flight tracks on great circles. Integrated emissions (over time and altitude) are given in g/km^2. [Data from DLR, Holger Pabst, personal communication].

Using the given numbers, we estimate the resulting enhancement of NO_2 TVCD we could expect due to aircraft emissions. An emission of 2000 g [NO_x] per km^2 and month (see Fig. 5.1) corresponds to emissions of about 10^{14} molec [NO_x] per cm^2 and day. For the upper troposphere, most NO_x is present as NO (about 60-80% [Klemm et al., 1998; Ziereis et al., 2000]), thus leading to lower observed NO_2 TVCDs. On the other hand, the NO_x lifetime is of the order of some days for the upper troposphere, and NO_2 accumulates. Hence, we expect enhanced TVCDs of NO_2 of roughly 10^{14} molec/cm^2 within the flight track. Of course, the emissions are also diluted due to transport. Nevertheless one could expect to find a footprint of aircraft NO_x in mean composites of GOME and SCIAMACHY, since emissions occur in a rather narrow flight corridor, and wind direction is mainly eastwards, i.e. parallel to the track.
However, in the mean TVCD composite of GOME data (e.g. Fig. 3.1) no indication for aircraft emissions can be found. As the determination of NO_2 TVCDs for the Northern Atlantic is interfered by the polar vortex in wintertime, we also checked if we could find an aircraft signature of NO_2 for summer months alone. Additionally, we only considered clouded pixels, as for clouded scenes the sensitivity towards NO_2 above the clouds is enhanced [Hild et al., 2000]. The resulting composite is shown in Fig. 5.2. Again, we see not the slightest indication for aircraft NO_x, even for the colourscale adopted to low levels. TVCDs are negative south from Greenland (due to the stratospheric estimation) and do increase further southwards, but do not decrease again as aircraft emissions do. Hence this increase is due to other factors, probably outflow of polluted air from North America towards the Atlantic.

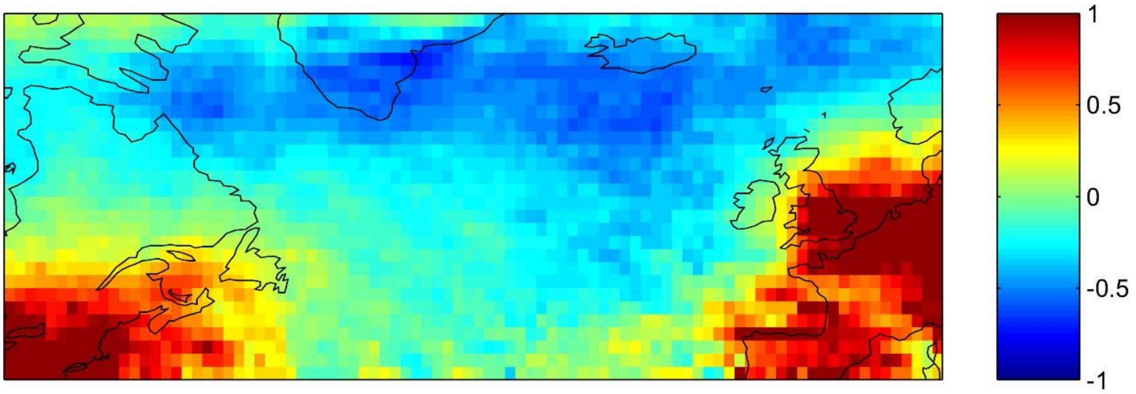

Fig. 5.2: Mean GOME TVCD [10^{15} molec/cm^2] of all clouded summertime observations for the northern Atlantic.

The detection of aircraft NO_x is interfered by the longer lifetime of NO_x in the upper troposphere as well as very high wind speeds within the jet stream hinder the formation of sharp patterns. Furthermore, the assumption of great circles is a simplification, and considerable deviations from shortest flight routes occur if weather conditions suggest. This is accounted for by “second generation” aircraft emission inventories, resulting in a broader spreading of emissions in the Atlantic flight corridor [Holger Pabst, personal communication]. Still emissions are concentrated in a band of about 50°-60°N at 30°W. However, expected levels of TVCD enhancement are probably too low to be detected by GOME.

The SCIAMACHY limb mode will probably result in a better stratospheric estimation (see section 2.4) and thus in unbiased TVCDs over the Northern Atlantic. The better spatial resolution, though, will probably not be a breakthrough for studying flight routes, as aircraft NO_x is spreaded out over a wider range. However, it might be possible with highly resolved data (from SCIAMACHY or OMI) to study aircraft emissions at airports if the latter are not too close to a city.

Chapter 6
Lightning

Lightning is an important natural source of nitrogen oxides. In the upper troposphere, it is the only direct NO_x source besides aircraft emissions. Portions of nitrogen oxides may also be uplifted from surface sources due to deep convection, or transported down from the stratosphere, but in regions with high lightning activity the lightning produced NO_x generally is thought to give the largest contribution (i.e. 80% over land masses in the tropics [Jourdain and Hauglustaine, 2001]). In addition, the impact of lightning NO_x on atmospheric chemistry, i.e. ozone production and OH concentration [Labrador et al., 2004], is amplified by the relatively long lifetime of NO_x in the upper troposphere of up to several days [Jaeglé et al., 1998].

In this chapter, we present two studies on observation of lightning produced NO_x by GOME in sections 6.4 and 6.5. However, first we discuss the particular mechanism of NO_x formation by lightning (6.1.), current estimates and their uncertainties (6.2.), and the specific potential of satellite data for lightning NO_x studies (6.3.).

6.1. Formation of lightning NO_x

The mechanism of NO_x formation by lightning has first been described by Zel'dovich and Raizer (1966); a more recent description is given in Goldenbaum and Dickerson (1993). Generally, due to the high temperatures in the lightning channel, the air molecules (mainly O_2) are partly dissociated, leading to the formation of NO (see (R4)-(R6), Chapter 1). However, though the general mechanism is clear, there is still a debate about the detailed processes, e.g. whether the heating takes place in the hot lightning channel alone or also in the shock front generated by the rapid energy release, or whether the "freezing out" of NO takes place by a rapid drop in temperature or in pressure (see the discussion in Stark et al. [1996]).

Lightning produced NO_x is often abbreviated as "LNO_x", and we use this abbreviation hereafter.

6.2. Estimates of global lightning NO_x production

In the overview paper given by Lee et al. [1997], LNO_x is estimated to contribute approx. 12% to the total release of NO_x, i.e. 5 (2-20) Tg[N]/year (see table 3.1). However, the estimates of recently published studies still vary between 0.9 and 12.2 Tg[N]/year [Nesbitt et al., 2000; Price et al., 1997], illustrating that lightning is the most uncertain source of nitrogen oxides.

Over the last decades, several studies, using different approaches, have been performed to estimate LNO_x production. A common way (as discussed by Lawrence et al. [1995] and Price et al. [1997]) is to quantify

(a) the production of NO_x per energy unit,
(b) the released energy per flash and
(c) the global frequency of flashes,

and estimate the global LNO_x production as the product of these quantities. Estimates for (a) and (b) are given by several studies based on theoretical calculations and laboratory experiments. Price et al. [1997] give an overview on these studies, and show that the literature values range over some orders of magnitude ((a) 2-2500 x 10^{16} molecules per Joule; (b) 10^8 – 10^{10} Joule per flash), as a result of the many assumptions involved and necessary extrapolations of laboratory measurements. The global total flash frequency (c) was first estimated by Brooks [1925] to be of the order of 100 flashes per second. The recent estimate of Mackerras et al. [1998] gives a slightly smaller number of 65 flashes per second.

The situation of estimating LNO_x by this approach is complicated by the fact that it revealed to be necessary to distinguish intra-cloud (IC) and cloud to ground (CG) flashes. IC flashes are more frequent by a factor of about 2 [Prentice and Mackerras, 1977] and up to 100 for a single thunderstorm [Dye et al., 2000]. On the other hand, CG flashes are generally thought to have a higher LNO_x production rate, and statements range between the both extremes that IC LNO_x production rates are below 10% [Price et al., 1997] up to 50% and more [De Caria et al., 2000] of CG lightning rates. Ground based lightning detection networks are usually only sensitive to CG flashes, thus the number of IC flashes is rather unknown. Here obviously still more effort is needed to quantify the lightning frequencies for IC and CG flashes separately as well as the produced LNO_x for both types.

During the last decades, also several direct measurements of LNO_x have been performed, using ground based remote sensing techniques (e.g. [Noxon, 1976]) or in-situ instruments on aircraft (e.g. [Höller and Schumann, 2000]). These measurements typically estimate the LNO_x production per flash (thus comprising steps (a) and (b)) or per thunderstorm. The study by Huntrieser et al. [1998] gives a comprehensive overview on the results of several campaigns, where global LNO_x estimates range from 0.9-220 Tg [N] per year. In their own study, Huntrieser et al. [1998] found global LNO_x production to be 4 (0.3-22) Tg [N] per year, and they state that “airborne measurements are rather rare, difficult to perform, and not always easy to interpret”. Skamarock et al. [2003] also discuss the problems arising when results from local measurements (limited in space and time) are extrapolated to global LNO_x estimates.

In recent years, a new method involving general circulation models (GCMs) was used to restrict the range of LNO_x production estimates. The typical procedure is to choose different values of global LNO_x production as model input, and compare the resulting (spatially resolved) NO_x concentrations with measurements, to find a most probable value as well as lower and upper boundary for total LNO_x production. Levy et al. [1996] give a range of 2-6 Tg [N] per year, Tie et al. [2002] 3.5-7 Tg [N] per year, and Jourdain and Hauglustaine [2001] find 5 Tg [N] per year as best estimate for global LNO_x production.

The fact that several independent approaches result in a global LNO_x production of about 5 Tg [N] per year gives trust that at least the order of magnitude is correct. However, the uncertainties of the different methods are still quite high, indicating the need of further (independent) information.

6.3. New potential of satellite measurements

Satellite measurements offer such a new and independent approach to the estimation of LNO_x production. Again, the characteristic strengths of satellites, i.e. long time series of global measurements, allow analyzing the influence of lightning statistically as well as in single case studies.

Furthermore, also satellite information on lightning distribution can be used for comparison (6.3.1.). However, the specifics of LNO_x has to be carefully considered (6.3.2.).

6.3.1. Satellite detection of lightning: The Lightning Imaging Sensor (LIS)

The Lightning Imaging Sensor (LIS) is a NASA Earth Observing System instrument on the Tropical Rainfall Measuring Mission (TRMM) platform [Christian et al., 1999]. The TRMM orbits the earth with an inclination of 35 degrees, thus allowing LIS to observe lightning activity in the tropical regions of the globe. Optical impulses are detected to identify flashes

(cloud to ground as well as cloud to cloud or intracloud) inside a 600×600 km^2 window. The TRMM orbit is not synchronized with respect to the sun, thus local measurement time varies from day to day: In the period of one month, measurements at every time of the day are available for a given location. So monthly means are, in contrast to daily measurements, a good quantity to represent average conditions. To retrieve actual monthly mean flash rates, the number of flashes counted by LIS has to be scaled with regard to the viewing time: e.g. a location of 25° latitude is observed 100 sec., i.e. 0.117%, per day. Accordingly, the number of measured flashes is multiplied with a factor of 854.7.
Fig. 6.1 shows a climatology of global lightning activity as observed by LIS and its predecessor OTD (Optical Transient Detector). Please note that OTD operated on a near polar orbit, thus was not restricted to the tropics as LIS. However, the OTD mission ended in March 2000. Therefore we have chosen the LIS lightning frequency product for this study to gain a longer overlap with the GOME time series.

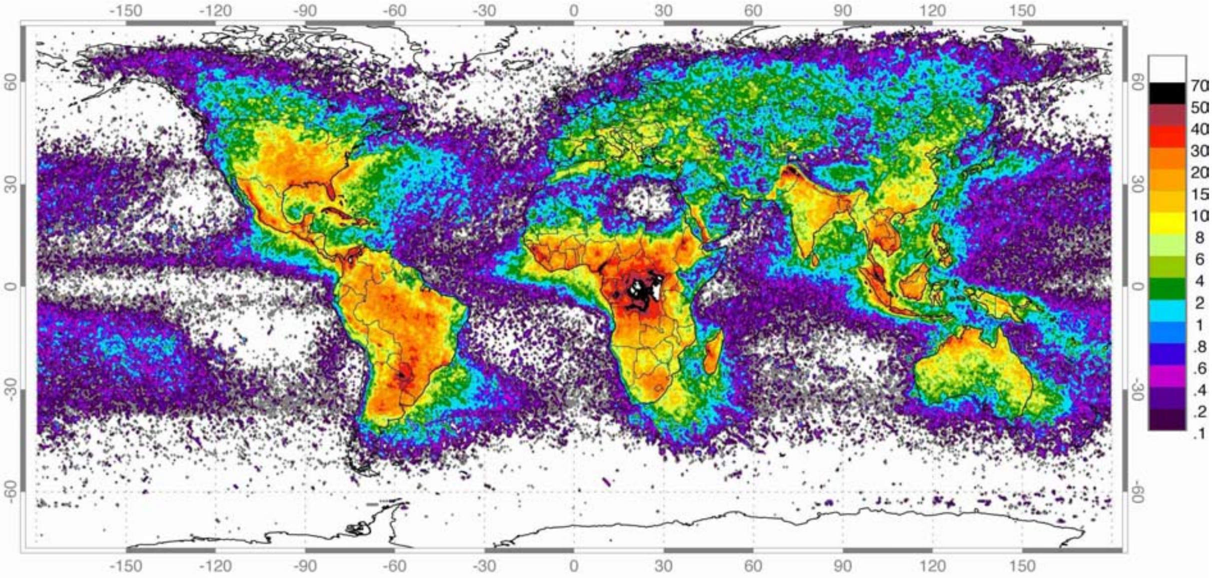

Fig. 6.1: Global distribution of lightning (April 1995-February 2003) from the combined observations of the NASA OTD and LIS instruments. Flash rate densities are given in flashes per km^2 and year.

6.3.2. Detection of LNO$_x$ from GOME

Using GOME data for studying LNO$_x$ one has to keep in mind that:

- The investigation of LNO$_x$ from space is complicated by the fact that thunderstorms coincide with cloudiness, due to which the NO$_2$ formed may be not completely visible for GOME. But a large fraction of the produced NO$_x$ in a thunderstorm is uplifted to the top [Fehr et al., 2004], resulting in a pronounced C-shaped profile, and NO$_x$ lifted above the clouds has an increased visibility [Hild et al. 2000].
- The GOME measurement takes place before local noon, whereas most thunderstorms occur in the evening. Thus GOME measures rather the LNO$_x$ produced the days before that could accumulate due to the long lifetime of NO$_2$ in the upper troposphere of several days [Penner et al., 1998; Jaeglé et al., 1998].

In literature, satellite data has been used to examine LNO_x:
A statistical approach has been used by Zhang et al. [2000] who used data from the Upper Atmosphere Research Satellite (UARS) to substantiate a link between lightning activity and high levels of NO_2 in the upper troposphere . However, due to limitations of the instrument, the statements have been kept rather qualitative.
Hild et al. [2000] analyzed a single lightning event coinciding with GOME measurement in the Indian ocean in detail.
Here we present two studies on LNO_x identification and estimation from GOME data:
In section 6.4 we give the first quantitative estimation of lightning produced NO_x using GOME data. For this we relate monthly means of lightning frequency and the tropospheric vertical column densities of NO_2 over Central Australia, where other NO_x sources have only minor contribution.
In section 6.5 we present a further case study of very high GOME TVCDs that coincide with a large lightning event in the Caribbean sea.

6.4. Lightning in central Australia

For the identification of LNO_x with satellite data it is essential to find a region where interference with other NO_x sources is minimal. It turned out that Australia is well suited for a lightning case study. This study has been published in Beirle et al. [2004a].

6.4.1 Global lightning distribution

Fig. 6.1 illustrates that lightning takes place around the world, but is distributed quite inhomogeneously. The regions of highest activity are located over tropical land masses. In those regions, a direct estimation of LNO_x is complicated by the fact that also other, probably more predominant NO_x sources like industry (USA, South Africa) or regular biomass burning (South America, Central Africa, Indonesia) are present (see also Chapter 7). Unfortunately, the Himalaya region, where lightning rates are quite high, is not covered by GOME measurements, as calibrations are performed each time the satellite overpasses this region.
So the challenge was to find a region with sufficient lightning activity, where other NO_x sources are of minor importance. Moreover, to analyze the influence of lightning with statistical methods, it is helpful to have a strong temporal variability of lightning activity, i.e. a yearly cycle. Therefore, we have chosen Central Australia, i.e. the terrain 120°-140° East and 20°-30° South, as marked in Fig. 6.2 (box in July in the upper row).

6.4.2 Sources of NO_x in Central Australia

The chosen desert region is nearly uninhabited and remote from large cities. Sydney, for instance, is about 1200 km away from the eastern border of the considered area. Anthropogenic emissions can be neglected, because in the boundary layer wind velocities are moderate (about 5 m/s=432 km/day) and the lifetime of NO_2 is quite low (about 12h, see Chapter 10). Furthermore, transport of non-anthropogenic NO_x (e.g. LNO_x) inside and/or outside the considered area may occur. But the incoming NO_x is expected to balance out the outflowing amounts in our long term statistical analysis. Biomass burning is monitored by the ATSR sensor; fire counts are low in Central Australia. Soil emissions of NO_x are also relatively low for the Australian desert, but probably not negligible. Source strengths of soil emissions in literature are about 30-60 mg [N] m^{-2} yr^{-1} [Potter et al., 1996; Davidson and Kingerlee, 1997; Yienger and Levy, 1995]. This corresponds to a daily column density of 0.5-1×10^{14} molec $[NO_2]/cm^2$, assuming a NO_2/NO_x ratio of 0.75 and a lifetime of 18 hours for NO_x in the lower troposphere, as upper bound.

In principle, the amount of soil emissions may correlate with lightning activity, since soil emissions are partly driven by precipitation [Yienger and Levy, 1995]. Nevertheless, we believe that this is only of minor importance for our study, because the monthly data set of soil emissions from Potter et al. [1996] shows no clear yearly cycle. In particular, July shows maximum soil emissions in spite of absence of occurrences of lightning.

Finally, convection coming along with thunderstorms may lift NO_x from the boundary layer to the upper troposphere. But Huntrieser et al. [1998] found, that even for regions with high levels of NO_x in the boundary layer (Germany and Switzerland), 50%-75% of the NO_x-enhancement in thunderstorms is still due to LNO_x. So for the Australian desert, where NO_x concentrations in the boundary layer are low, convection is expected to have only minor influence.

Thus, we expect that the correlation of NO_2 and lightning activity we present below is actually due to the production of LNO_x.

6.4.3 Correlation of NO_x and lightning activity

As LIS observations are only short snapshots for a given location, we consider monthly means of LIS frequencies and GOME TVCDs for a quantitative comparison (see also 6.3.1). For the GOME TVCDs we apply a modified tropospheric AMF of 1.33 (1-2), since the Australian desert is almost cloud free and the observed NO_2 is in the upper troposphere where GOME has a high sensitivity. (Please note that the numbers in Figs. 6.2 and 6.3 differ from the published study [Beirle et al., 2004a], since we here apply the AMF correction prior to plotting in contrast to the publication.)

Figure 6.2 shows monthly means of the lightning activity in Australia (measured with the satellite instrument LIS) in comparison with mean NO_2 TVCDs for different months of 1999. The yearly cycle can clearly be seen (high activity in January and nearly no lightning in July); this cycle is obviously reflected in the corresponding NO_2 TVCDs. In Figure 6.3, NO_2 is plotted against the lightning activity for the years 1999-2001. Every data point is a monthly mean value integrated over the considered area. (September 2000 is excluded due to high fire activity).

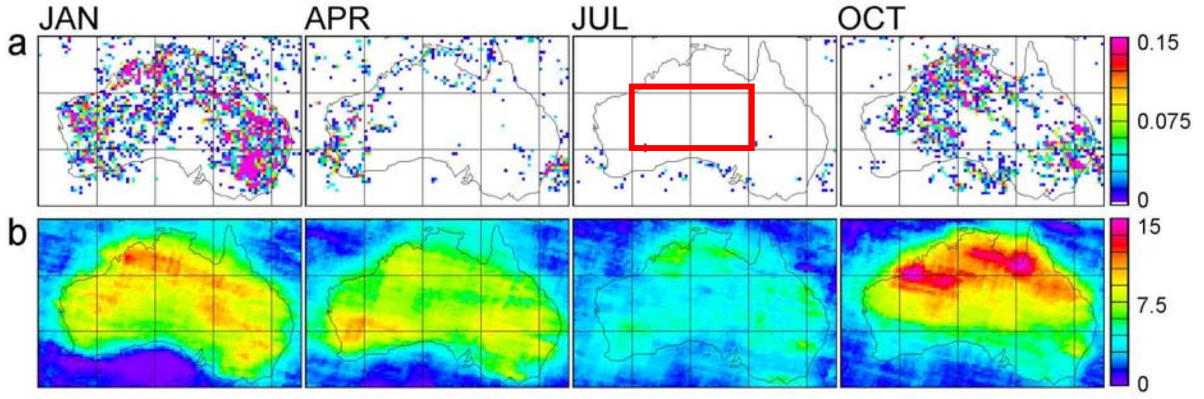

Fig. 6.2: Monthly means of LIS flash counts (upper row, flashes per day and km^2) and GOME NO_2 TVCD (lower row, 10^{14} molec/cm^2) in Australia for several months in 1999. The rectangle (120°-140° E, 20°-30° S) in July in the upper row indicates the area defined here as "Central Australia" considered for the correlation study. Scale in b) differs from [Beirle et al., 2004a], as AMF correction is applied prior to plotting.

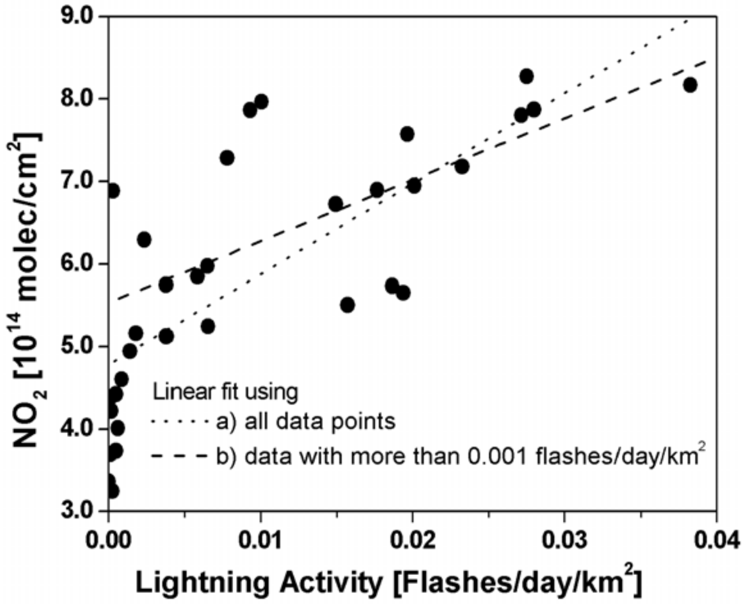

Fig. 6.3 Correlation of monthly means of NO_2 TVCDs and Lightning activity (LIS counts) for Central Australia. Scale on y-axis differs from [Beirle et al., 2004a], as AMF correction is applied prior to plotting

A clear correlation (R=0.76) can be seen: High lightning activity obviously involves high NO_2 values. The background NO_2 TVCD is in reasonable agreement with the assumption that it is due to of soil emissions. However, the high values of the background NO_2 TVCD observed by GOME may indicate, that the lifetime of NO_2 is larger than one day in the boundary layer of the Australian desert, probably due to low humidity and therefore lower OH concentrations.

We use the correlation to give a rough estimation of LNO_x:

In Figure 6.3, two linear fits are performed, using (a) all data points and (b) only those with a lightning activity of more than 0.001 flashes per day per km^2. The resulting slopes are (a) 110 and (b) 75, the errors are about 17 (all units 10^{14} molec cm^{-2} / (flashes day^{-1} km^{-2}) = 10^{24} molec / (flashes day^{-1})). For our estimation, we assume a slope of 90±20. This is closer to the second fit, since we emphasize those measurements where lightning actually took place. This means, lightning increases the observed NO_2 TVCD by 90×10^{24} molec / (flashes day^{-1}).

To estimate the daily LNO_x production, we have to scale this number by the inverse NO_2 /NO_x ratio (to translate NO_2 into NO_x) and the inverse mean lifetime τ (see Chapter 10). The NO_2/NO_x ratio is 0.4 (0.2-0.6) for the upper troposphere [Ziereis et al., 2000]. The lifetime τ of NO_2 in the upper troposphere is taken as 4 (2-6) days. [Jaeglé et al., 1998; Penner et al., 1998].

This results in a daily NO_x production of $1/(0.4\times4)\times NO_2 \approx 0.63\times NO_2$. Lower and upper boundaries for this factor are estimated to be 0.2 and 3.3, respectively, using the extreme values for the assumed factors and a tropospheric AMF uncertainty range of 1-2. The resulting LNO_x production is 57 (18-300)$\times10^{24}$ molec [NO_x]/flash. This is equivalent to 95 (30-500) mol/flash, i.e. 1.33 (0.4-7) kg [N] per flash.

Under the assumption that this value is valid for all flashes and assuming a total number of 2×10^9 flashes per year [Mackerras et al., 1998], this leads to a worldwide NO_x production by lightning of 2.7 (0.8-14) Tg [N]/yr.

This result is in good agreement with literature values. However, at the moment we can not reduce the range of uncertainty.

6.5. A strong lightning event in the Caribbean Sea

As stated above, lightning frequency is highest in late afternoon, whereas GOME measurements take place before noon. However, due to the large amount of GOME data, the direct observation of lightning during an ERS-2 overpass can succeed for some “lucky strikes”. Information of the lightning activity from LIS - that was of great use for the statistical approach in 6.4 - is rather useless for studying a particular event, as the coincidence of a large lightning event with ERS-2 and TRMM overpass at the same time is very unlikely. For the case study presented here we therefore use data from the USA National Lightning Detection Network (NLDN) [Cummins et al., 1998]. This network detects electromagnetic signals from lightning discharges. The efficiency of CG flash detection is 80-90%, but decreases with distance from the coast over the sea.

An unique event of GOME capturing LNO_x just produced is found on 30 August 2000 over the Gulf of Mexico. A sequence of ~10 GOME pixels detects enhanced NO_2 TVCDs (Fig. 6.4a). Fig. 6.4b depicts the flashes taken place before the GOME overpass as detected from the NLDN. As turned out from cloud data, the enhanced columns are observed for a totally cloudy scene (Fig. 6.4c) of a height of about 10 km (Fig. 6.4d). Therefore we have to adjust our AMF as the NO_2 is obviously (at least partly) above the clouds, resulting in increased visibility. The numbers in Fig. 6.4a of 2.5 up to 5 x 10^{15} molec/cm^2 are resulting for an AMF of 2.

Cloud data in Fig. 6.4c/d is taken from the Fast Retrieval Scheme for Cloud Observables (FRESCO, available at www.temis.nl). Please note that HICRU cloud fraction is very similar to 6.4c; we chose the FRESCO dataset, though, as we need information on the cloud top height.

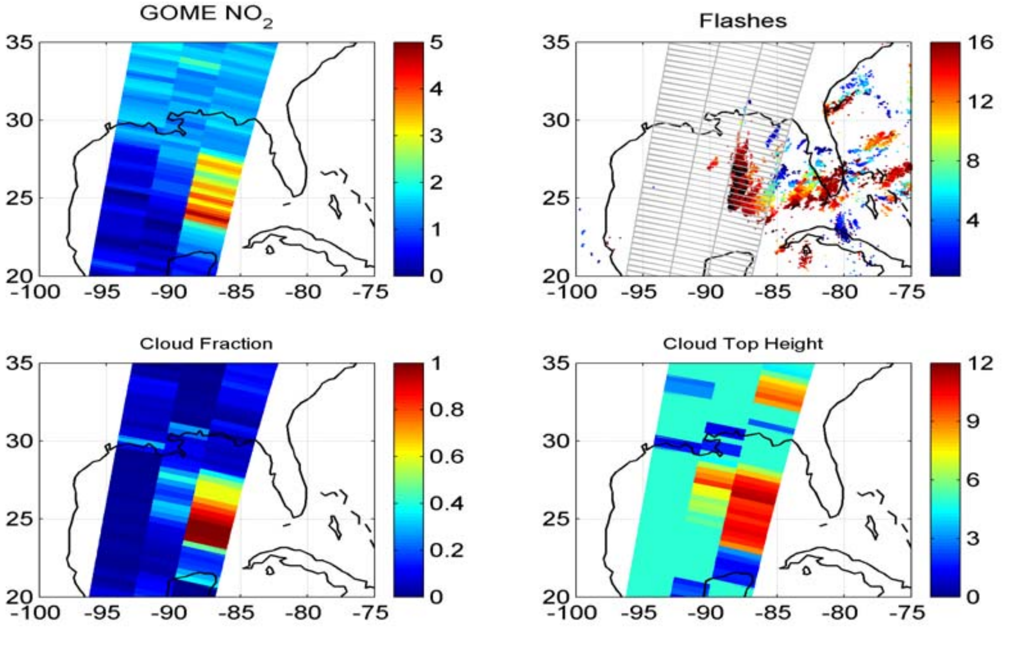

Fig. 6.4: Lightning event on 30 Aug 2000 in the Gulf of Mexico.
(a) GOME NO_2 TVCD (10^{15} molec/cm^2).

(b) Flashes detected by the NLDN. Every detected flash is plotted as dot. Colour codes the time of measurement (UTC). The high NO_2 VCD observed by GOME was taken at 16:48. The dark red dots are for lightning from 16:00-16:40, black dots mark lightning from 16:40-16:48. In grey, the GOME pixel location is indicated as a reference grid for comparison.
(c) Cloud fraction derived from GOME (FRESCO).
(d) Cloud top height (km) derived from GOME (FRESCO).

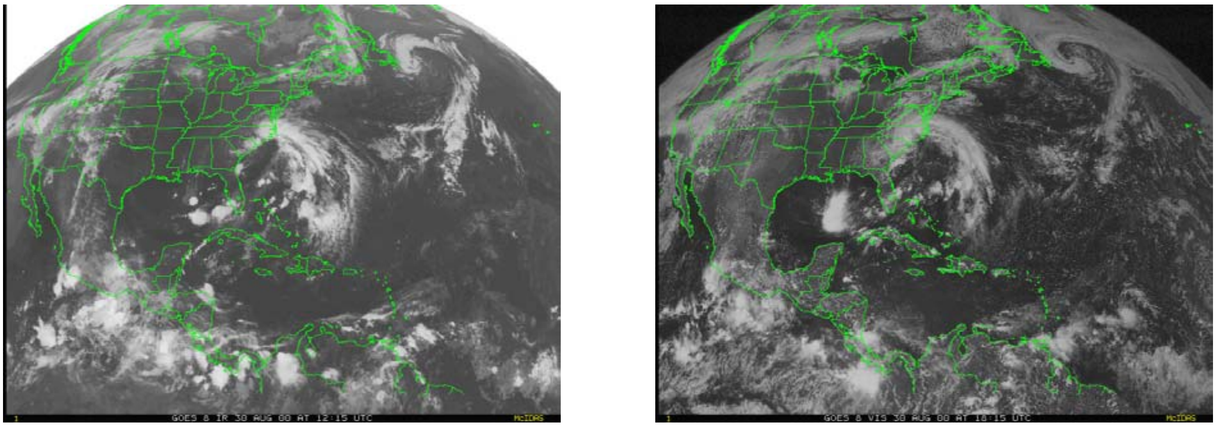

Fig. 6.5: Satellite image (GOES) for 30 August 2000 12:00 UTC (left) and 18:00 (right).

Additionally, Fig. 6.5 displays satellite images for 30 August , illustrating the deep convection taking place in the Gulf of Mexico.
The spatial patterns of enhanced NO_2 TVCDs and detected flashes match very well. However, the highest TVCDs are found at ~24°N, i.e. the southern end of the detected flashes. The main reasons for the virtual southward shift in the GOME signals are:

- LNO_x produced during the last hours is likely transported within the movement of the Low pressure system southwards.
- The NLDN detection efficiency decreases with distance from land. Whereas it is 80% for New Orleans, it is only about 20% for the southern tip of the thunderstorm (according to Fig. 9 in [Cummins et al., 1998]), and additional lightning further south might have been overseen.

This situation of highly increased NO_2 TVCDs for a cloudy scene is quite unique; comparably high TVCDs are extremely rare over oceans. This particular event is unprecedented as the lightning activity coincides perfectly with the GOME measurement both in space (the area affected by lightning fits in the eastern GOME subpixels) and in time (most flashes have taken place during the last 45 minutes).
As discussed above, LNO_x is principally hard to distinguish from NO_x from fossil fuel combustion, biomass burning or soil emissions lifted up by frontal systems and convection. However, in this case the lightning event was over sea and remote from polluted regions. Backtrajectories revealed, that the observed air masses resided in the upper troposphere the days before. The observed enhanced NO_2 TVCDs are thus unambiguously due to LNO_x.
As far as we know, such a clear and direct detection of LNO_x from satellite has never been reported before.

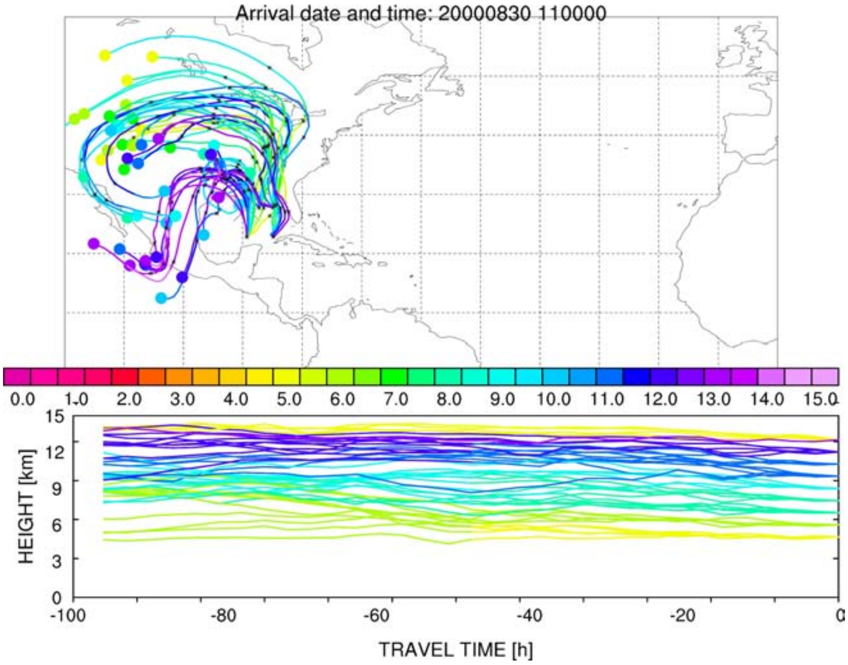

Fig. 6.6: Backward trajectories for 30 August 2000. (calculated with FLEXTRA, Nicole Spichtinger, personal communication).

6.6. Conclusion

The detection of LNO_x from GOME is a challenging task: GOME has a rather coarse spatial resolution. The retrieval of tropospheric NO_2 values demands assumptions of the stratospheric fraction, the NO_2 profile, tropospheric air mass factor, and surface albedo. Clouds accompanying lightning affect the GOME measurement. And in most regions different sources are superimposed to lightning. Furthermore the NO_2/NO_x ratio is reduced in the upper troposphere. So it has been even doubted in literature that GOME could detect LNO_x at all [Martin et al. (2003)].

However, in spite of these numerous difficulties LNO_x can clearly be seen by GOME, both in a statistical approach for a region where all other NO_x sources have minor contributions, as well as in single lightning events that match the GOME measurement in space and time.

Though a correct quantitative analysis is constrained by the uncertainties discussed above, a rough estimation results in a global LNO_x production of 2.8 (0.8-14) Tg [N]/year, in good agreement with literature values. However, at the moment we can not reduce the range of uncertainty.

Nevertheless, this study demonstrates the potential of satellite data. A totally new approach to the quantification of LNO_x production is presented. More precise estimations of source strengths are to follow. These include, in particular, a more sophisticated cloud and air mass factor correction. Also other areas besides Australia will be analyzed. However, a recent study by Boersma et al. [2004b], who analyzed correlation of lightning and GOME TVCDs, confirmed that Australia is best suited for such a study, as other sources are negligible.

Future will probably allow better estimates of LNO_x production from satellite through the better spatial resolution of SCIAMACHY and the ongoing collection of data.

Chapter 7
Biomass burning

7.1. NO_x emissions from biomass burning

Biomass fires are triggered naturally by lightning. However, nowadays most fires are the result of deliberate human fire management practices, particularly in tropical and subtropical regions, whereas in remote boreal regions still most fires are started by lightning.
Public awareness of the environmental impacts of biomass burning and justified concern about its consequences are growing, since biomass burning serves a variety of purposes, e.g. the clearing of forests for agricultural use, energy production for cooking and heating, control of pests, insects and weeds, or nutrient mobilization [Crutzen and Merlet, 1990].
Biomass burning causes significant regional pollution, often with severe impacts on the health and safety of the local population. On a global scale, it affects atmospheric chemistry and climate, as it produces a cocktail of ozone precursors, i.e. CO, VOCs and NO_x. Especially the tropical Atlantic shows often enhanced ozone levels that are by large part influenced by biomass burning in Africa (e.g. [Thompson et al., 1996; Valks et al., 2003]).

Current estimates of NO_x emissions by biomass burning are about 8 Tg [N]/year. Galanter et al. [2000] state that „uncertainties in [our] biomass burning sources of CO and NO_x are much less than the a priori factor of 2 implied by previous estimates" as conclusion of model runs with both halved and doubled emissions leading to "unreasonable results through most of the tropical lower troposphere". Nevertheless, biomass burning estimates are based on bottom-up-approaches with the characteristic limitations: NO_x production has to be quantified for different vegetation types and extrapolated correctly to global scales. Furthermore, using a fixed biomass burning NO_x emission inventory does not account for extraordinary strong burning events that from time to time occur in different regions. Here satellite measurements provide valuable information of the emissions from biomass burning that is resolved in space and time.

7.2. Satellite observations of NO_2 from biomass burning events

Several studies report the detection of enhanced NO_2 VCDs from GOME data coinciding with biomass burning events (e.g. Ladstätter-Weißenmayer et al. [1998]; Thomas et al., 1998; Burrows et al. [1999]; Leue [1999]; Richter and Burrows [2002], Beirle et al. [2002]; Damoah et al. [2004]; Spichtinger et al. [2004]). In this chapter, we use two approaches to analyze the impact of biomass burning on NO_2 TVCDs from GOME in more detail. In particular, we discuss regional variations of the impact of biomass burning on NO_2.
Firstly, we compare spatial patterns of NO_2 TVCDs and other satellite data related to biomass burning (especially fire counts, but also formaldehyde (CH_2O) and carbon monoxide (CO)) for selected months. Secondly, we analyze the impact of biomass burning on NO_x production for different regions by comparing time series of fire counts and NO_2 TVCDs. Again we make use of the characteristic strength of satellite data, i.e. global coverage, long time series, and the potential of pattern recognition.

Furthermore, for the clear identification of NO_x produced by biomass burning events, it is helpful to use the potential of the synergistic use of different (satellite) data. As biomass burning events go along with release of huge amounts of aerosols, for instance the aerosol index (e.g. derived from TOMS data) is an indicator for biomass burning. More directly, the **ATSR** instrument onboard ERS-2 (as well as its successor AATSR onboard ENVISAT) allows the detection of temperature hotspots, indicating fires, during the nightside tracks (see also section 2.1).
Furthermore, the burning of organic matter also releases a variety of carbon containing compounds. One of these trace gases is **formaldehyde** (CH_2O) that can also be detected with DOAS in GOME data [Chance et al., 2000; Marbach et al., 2004].
SCIAMACHY is, in addition to the UV-vis channels, also equipped with IR spectrometers. These also allow the retrieval of **carbon monoxide** (CO) VCDs [Frankenberg et al., 2004]).
In the next sections, we compare the response of those datasets to biomass burning for the tropics (7.3.) and higher latitudes (7.4.), and analyze temporal correlations of NO_2 TVCDs and fire counts for different regions in 7.5.

7.3. Tropical biomass burning

The input of biomass burning emissions into the atmosphere is often discussed as a phenomenon of the tropical rain forest and savannas [e.g. Crutzen and Merlet, 1990; Andreae and Merlet, 2001]. Tropical landmasses are exposed to yearly biomass burning, typically with a distinct seasonal cycle.
Fig. 7.1 displays the fire counts from ATSR for August 1997 for the tropics. It indicates large areas burning in South America, southern Central Africa and Indonesia. Whereas the situation for South America and Africa is quite similar from year to year, the Indonesian fires are due to a disastrous fire event where large amounts of peat were burnt, enabled by drainage of swamp areas and the drought during the incidence of El Nino [Langmann et al., 2003].

This is reflected in the monthly mean composite of NO_2 TVCDs for August 1997 (Fig. 7.2) that reveals enhanced TVCDs over biomass burning regions (please note that the high values in South Africa are due to large coal-burning power plants).
Fig. 7.3 shows SCDs of CH_2O for the same month. Over Central Africa, H_2CO SCDs are enhanced with spatial patterns very similar to NO_2 TVCDs. Over Indonesia high formaldehyde levels are found likewise. However, the highest values of CH_2O are found over South America. The obvious differences in the spatial patterns of fire counts, NO_2 and CH_2O is probably due to isoprene tree emissions. A further aspect that might result in different patterns for CH_2O and NO_2, as proposed in Marbach et al. [2004], are differences in the vegetation type (i.e. grass land or rain forest) having different emission characteristics when burnt.

The monthly maximum CO VCDs from SCIAMACHY are shown for August 2003 in Fig. 7.4 [Christian Frankenberg, personal communication]. Please note that for Fig. 7.4 data from the year 2003 is used, as SCIAMACHY data is available only after 2002. The biomass burning over the tropics however shows generally a rather regular yearly cycle. The CO is strongly enhanced over Central Africa, and only moderately for South Africa. Future SCIAMACHY studies will allow a real simultaneous retrieval of several relevant trace gases that hopefully lead to a better understanding on biomass burning emissions .

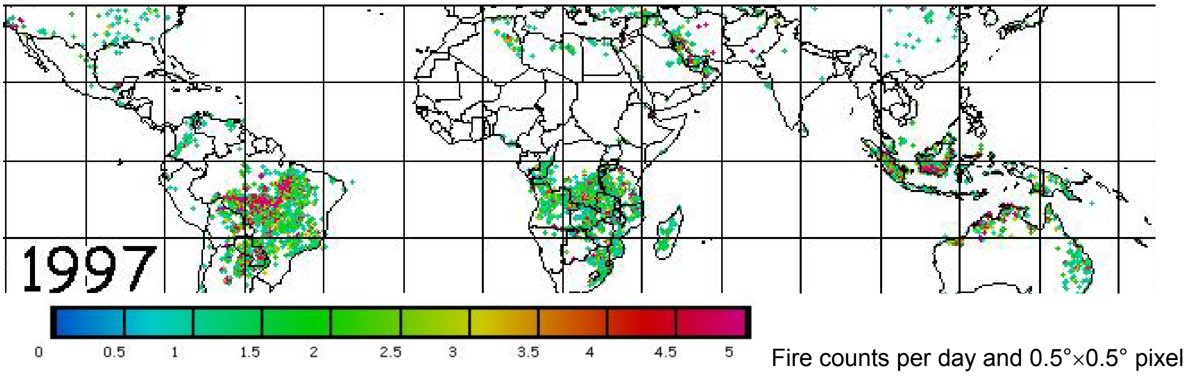

Fig. 7.1: ATSR monthly mean fire counts for August 1997.

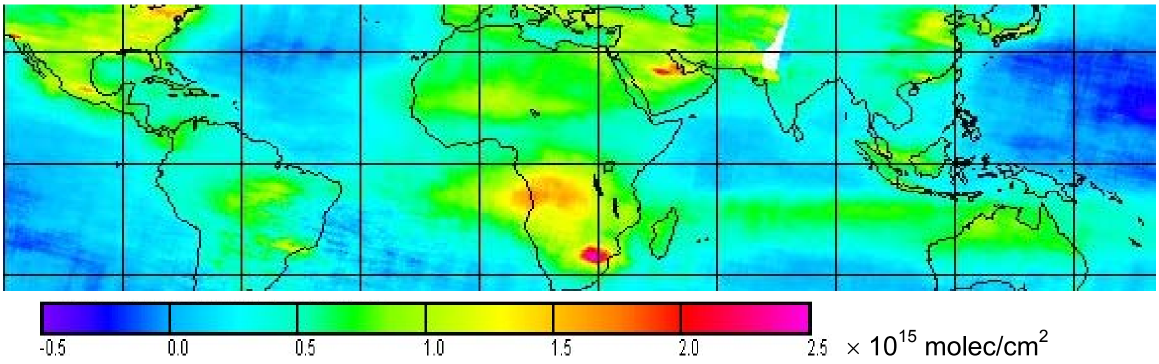

Fig. 7.2: Monthly mean NO_2 TVCD for the tropics (August 1997).

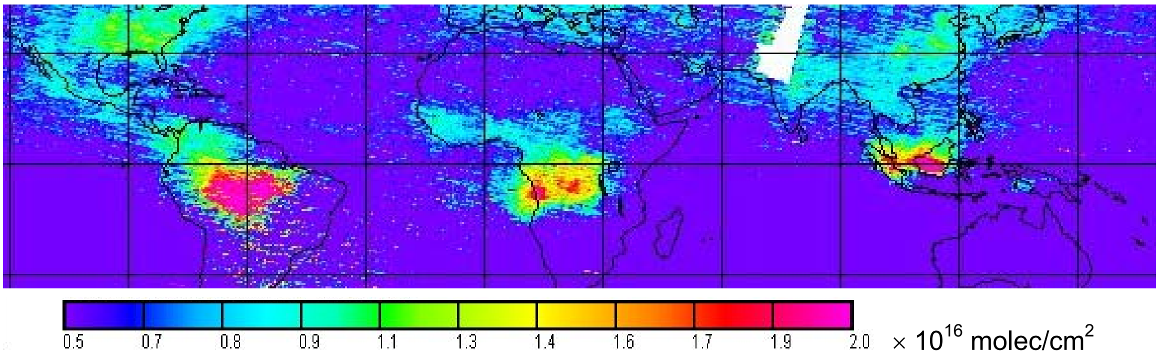

Fig. 7.3: Monthly mean H_2CO SCD for August 1997 [Thierry Marbach, personal communication].

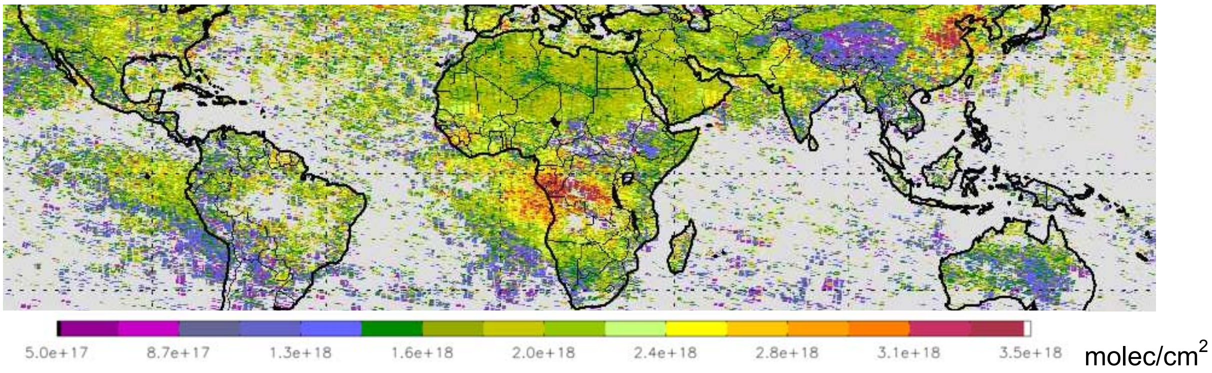

Fig. 7.4: Monthly maximum CO VCD for August 2003 [Christian Frankenberg, 2004b].

7.4. Boreal fires

The boreal forest plays an important role, as it contains one third of the terrestrial carbon storage. Boreal burning emits up to 20 percent of the global biomass burning CO [Conard and Ivanova, 1997]. The lifetimes of many trace gases and aerosols in the atmosphere are much longer in the boreal region than in the tropics. Because low annual average temperatures and dryness lead to accumulation of ground fuel through slow decomposition processes, boreal fires consume large amounts of fuel, burn with high intensity and spread particularly fast. A possible temperature increases as a consequence of climate change [Stocks et al., 1998] probably leads to enhanced fire activity [Flannigan, 1998]. Boreal fires are subjected to a strong inter-annual variability [Amiro et al., 2001]. They occur mainly from May to October [Lavoue et al., 2000] and are most frequent in Canada and Siberia.

Spichtinger et al. [2004] analyzed the difference of the boreal forest fires in 1997, when boreal fires were rather rare, to 1998, revealing high fire activity, for Siberia and Canada; the author of this PhD thesis was involved as a co-author to this study.

Fig. 7.5 shows a comparison of NO_2 VCDs (a) and H_2CO SCDs (b) between 1997 and 1998 for northern latitudes. Both datasets reveal clearly enhanced columns over eastern Russia in 1998, where numerous fires were counted by ATSR in summer 1998 (see Fig. 7.6). The matching patterns of ATSR, NO_2 and H_2CO give a clear evidence that the enhanced trace gas columns are due to boreal biomass burning.

It is quite astonishing, however, that neither NO_2 nor H_2CO columns show any enhancement of monthly mean column densities over Canada for 1998, as there also fire activity was higher for 1998, and Spichtinger et al. [2001] report a transport event of NO_2 from biomass burning in Canada in early August 1998. Furthermore, the recent study of Wooster and Zhang [2004] indicates that Russian fires burn ***less*** intensely (and emit fewer products) than Canadian fires. However, our correlation study presented below suggests that NO_x emissions by boreal fires are generally comparably low.

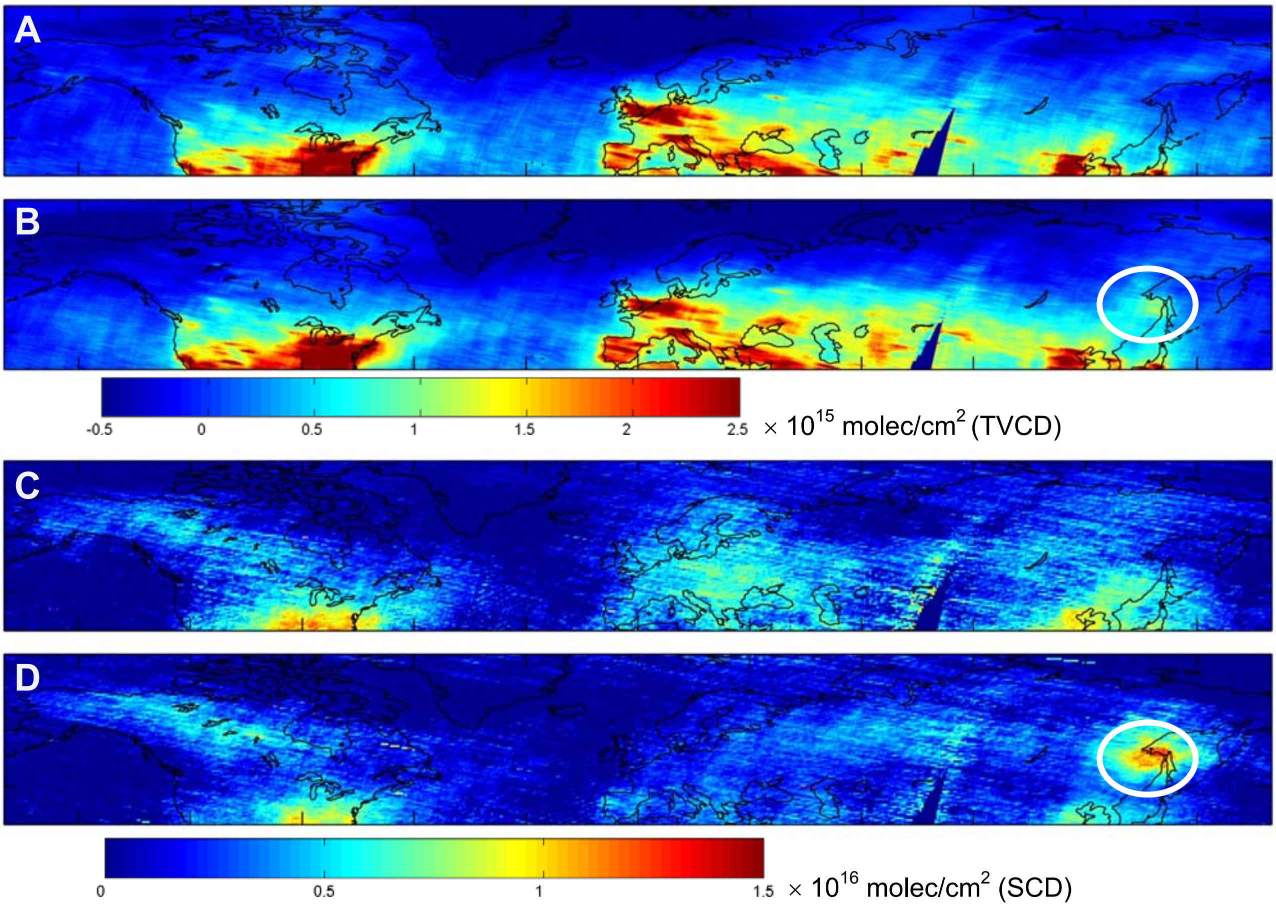

Fig. 7.5: Comparison of mean column densities of NO_2 (upper panels) and H_2CO (lower panels). Subplots show July/August composites for 1997 (a,c) and 1998 (b,d). Levels of both trace gases are enhanced in 1998 over eastern Russia (see circles) due to strong boreal fire activity. Figures from [Spichtinger et al., 2004].

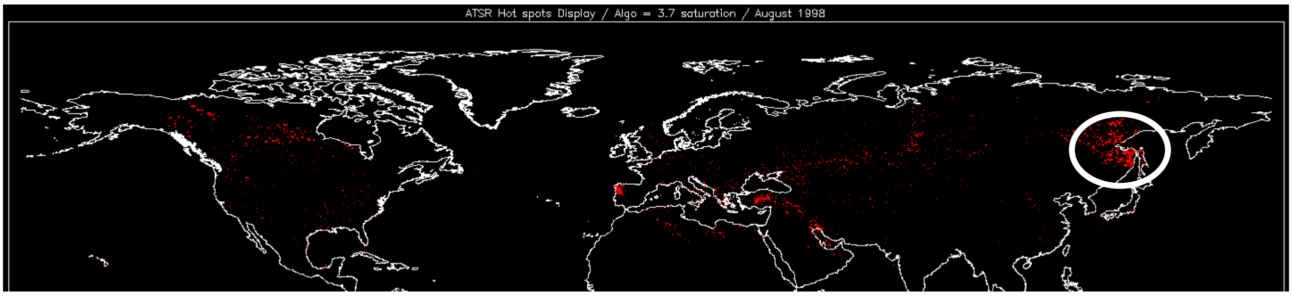

Fig. 7.6: ATSR fire counts for August 1998.

7.5 Time series of NO_2 TVCDs and biomass burning for different regions

Fig. 7.7 shows the mean ATSR fire counts for four years of measurement (1997-2000), clearly indicating the “active” biomass burning regions of the world. To analyze the dependency of NO_x on biomass burning more quantitatively, we computed time series of monthly means of fire activity (from ATSR) and NO_2 TVCDs for some of these regions that are marked with boxes in Fig. 7.7, i.e. (a) South America, (b) Northequatorial Africa, (c) Central Africa (west), (d) Central Africa (east), (e) Indonesia, (f) Northern Australia, and (g) Eastern Russia.

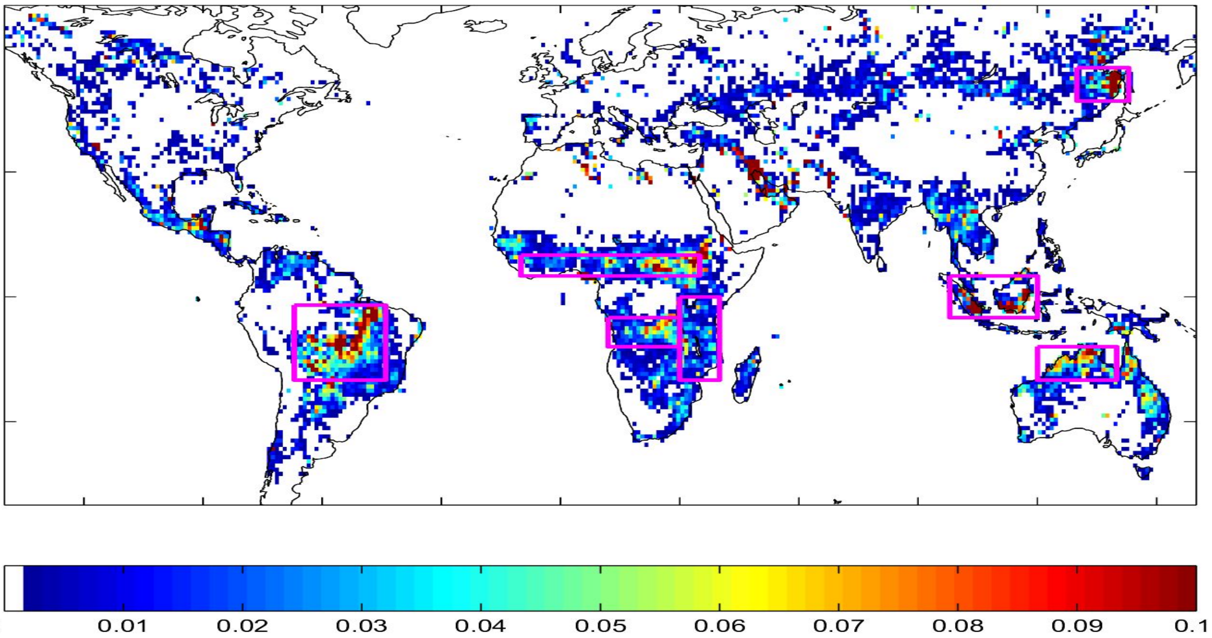

Fig. 7.7 Global fire frequency as seen by ATSR 1997-2000. Unit is fire counts per pixel (0.5°×0.5°) and day. The boxes mark regions of high biomass burning activity that are considered in detail below.

Please note that in principle it is also desirable to analyze correlations for shorter time steps than monthly means. However, since GOME (SCIAMACHY) needs 3 (6) days to reach global coverage, weekly “means” would usually contain only two (one) measurement and are thus rather meaningless. A meaningful analysis of correlations on a finer time grid would actually have to be based on daily measurements.

Fig. 7.8 shows the yearly cycles (monthly means) of fire counts (left column) and NO_2 TVCDs (right column) for these regions. The different years are color coded (reddish), to allow a direct comparison of single years. As additional information, in the left column also monthly means lightning counts from LIS (see Chapter 6) are added.

Please note that the absolute scale of the fire plots is the same for all plots except Indonesia (e) and Eastern Russia (g): Here we see two cases with extremely high fire activity. These are the same months already discussed above, i.e. the strong Indonesian peat fires in summer (and autumn) 1997 (7.3) and the boreal fires in summer 1998 in eastern Russia (7.4).

The scale for the NO_2 time series is the same for all subplots, but the origin of the y-axis is shifted for regions with a baseline of high NO_2 TVCDs (i.e. Central Africa, (c) and (d)), probably due to lightning and/or soil emissions.

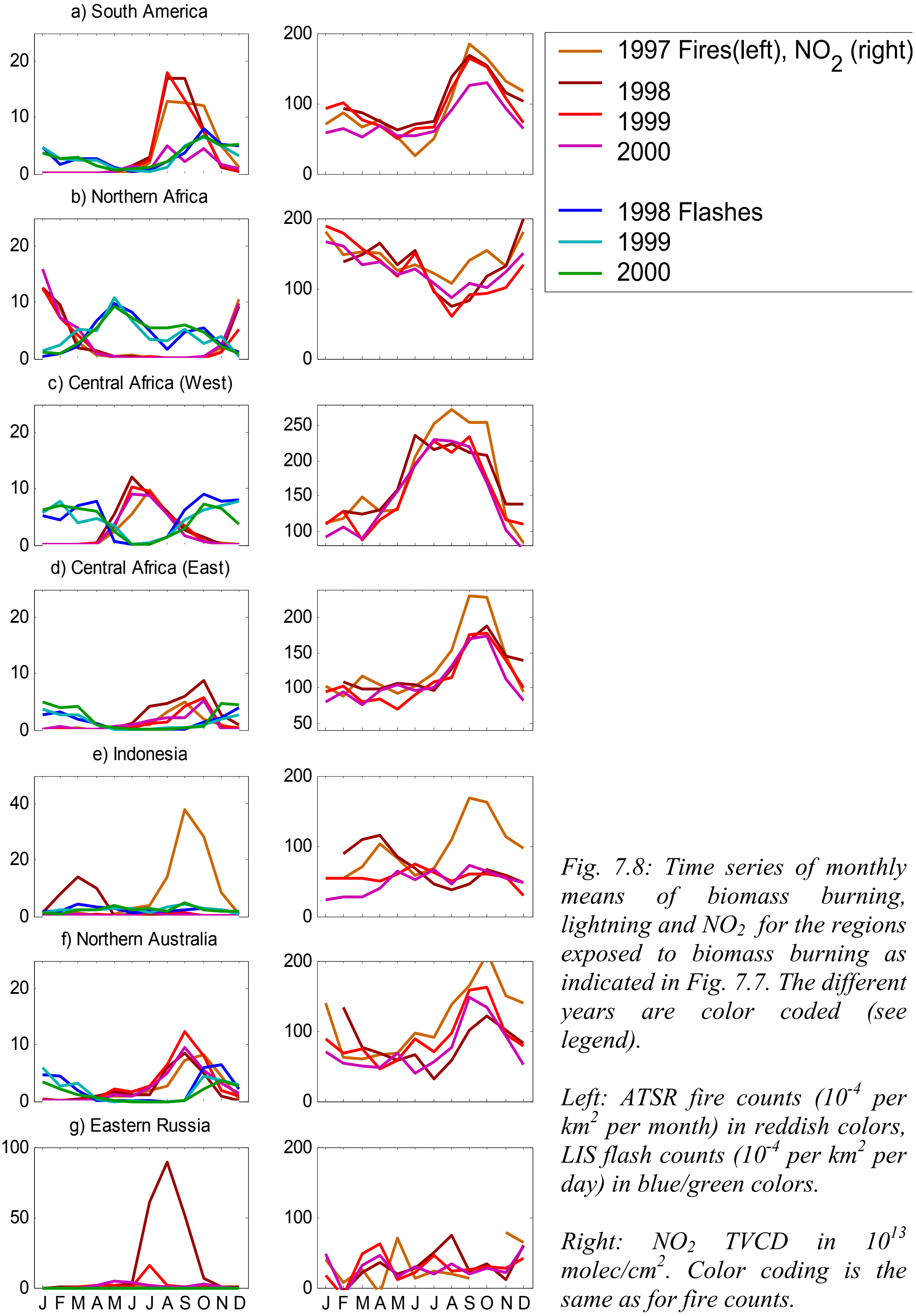

Fig. 7.8: Time series of monthly means of biomass burning, lightning and NO_2 for the regions exposed to biomass burning as indicated in Fig. 7.7. The different years are color coded (see legend).

Left: ATSR fire counts (10^{-4} per km^2 per month) in reddish colors, LIS flash counts (10^{-4} per km^2 per day) in blue/green colors.

Right: NO_2 TVCD in 10^{13} molec/cm^2. Color coding is the same as for fire counts.

We use the time series also to determine correlations of fire counts and NO_2 TVCDs that are shown in Fig. 7.9. ATSR data reveals a clear yearly cycle of biomass burning with maximum in August/September in South America (a). This is clearly reflected in GOME TVCDs, and both datasets are highly correlated (R=0.75). Situation is quite similar for eastern Central Africa ((d), R=0.73) and Northern Australia ((f), R=0.64). Northern Africa (b) shows a shifted cycle of biomass burning in January; the correlation with NO_2 TVCDs is R=0.68. For western Central Africa (c), biomass burning peaks in July and decreases afterwards, while NO_2 TVCDs stay enhanced until October. This discrepancy might be partly explained by lightning that starts in late summer while biomass burning activity is reduced. However, spring has similar lightning activity but much smaller TVCDs. Thus probably the TVCDs are affected by transport from eastern Central Africa where TVCDs peak in autumn. Therefore this region was skipped for the correlation analysis. The time series for Indonesia ((e), R=0.84) and Eastern Russia ((g), R=0.30) are dominated by the strong events discussed above and show no distinct cycle besides these events. Despite fire activity in eastern Russia is highest of all considered regional monthly means, the impact on NO_2 is quite small, and correlation is worst for this region.

In Fig. 7.10, we combine all scatter-plots with uniform scaling, and linear fits are added. The impact of biomass burning on NO_2 TVCDs seems to be strongest in eastern Central Africa and Northern Australia, and slopes for tropical regions are within s=3.5-13.6 $[(10^{13}\ \text{molec/cm}^2)\ /\ (10^{-4}\ \text{fires/km}^2\text{/month})]=[10^{27}\ \text{molec/(fires/month)}]$. The boreal fires seem to have a definitely smaller impact on NO_x production (s=0.38). This probably also explains why we were not able to detect large scale enhancements of NO_2 TVCDs over Canada in 1998 [Spichtinger et al., 2004].

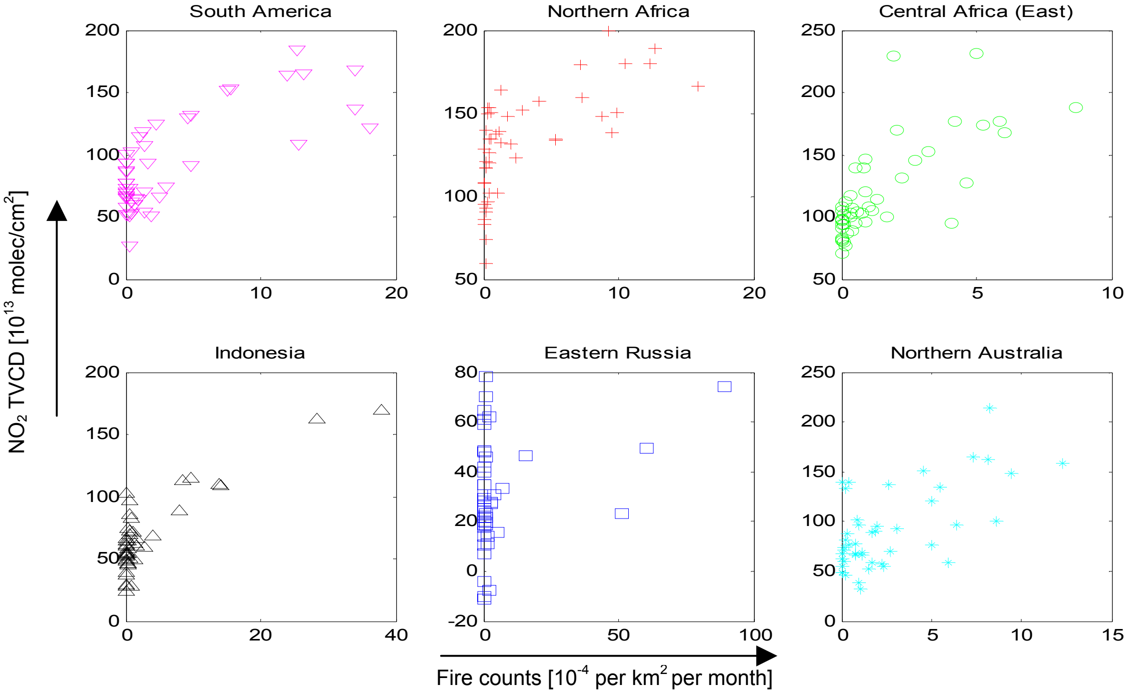

Fig. 7.9: Correlation of ATSR fire counts NO_2 TVCDs for the regions under consideration. All subplots are scaled individually.

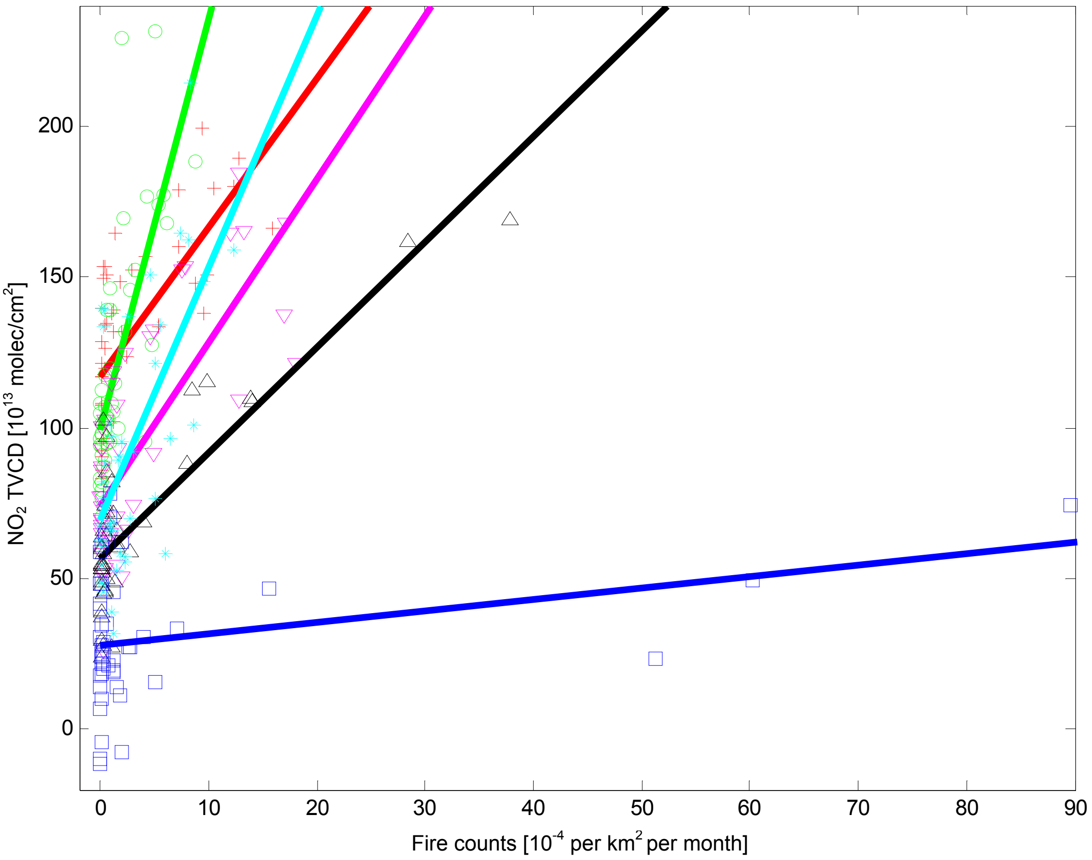

Fig. 7.10: Correlation of ATSR fire counts NO_2 TVCDs for the regions under consideration, uniformly scaled. Color-coding as in Fig. 8. Additionally, a linear fit is performed for each region separately.

We use the slope from Indonesia to give a very rough estimate of global production of NO_x by biomass burning, analogue to the estimate of LNO_x production in section 6.4.3: assuming a slope of 4×10^{27} molec/(fires/month), a mean lifetime of NO_x of 12 hours, and a Leighton ratio of 0.7, and extrapolate to the total number of fires detected by ATSR globally, we find a global production of NO_x by biomass burning of about 1 Tg [N] per year. This is about one order of magnitude lower than current estimates (see Table 3.1). One important reason for this discrepancy is of course our simple AMF approach: biomass burning is usually accompanied by a strong release of aerosols, generally shielding the boundary layer. Another point is the assumed lifetime of 12 hours that may be too long, as the biomass burning plume provides both, elevated OH production due to the release of NO_x as well as aerosol surfaces for heterogeneous removal of NO_x (see also Chapter 10).

7.6. Conclusion

In summary, the NO_2 VCDs derived from GOME are quite sensitive for NO_x emissions due to biomass burning. Temporal and spatial information for the latter can be identified by ATSR fire counts. Further information can also be gained from spectrometers like MERIS or MODIS that allow to identify land cover types and aerosols. From the comparison of images before and after a biomass burning event, the area burned can be determined. This quantity may be better suitable for correlation studies with NO_2 TVCDs: fire counts from satellite are snapshots (ATSR needs about 3 days for global cover as GOME!), whereas the area burnt can also be determined several days after the fire event.

However, the direct identification of biomass burning produced NO_x is sometimes impeded by lightning, especially in the tropics. Additionally, the radiative transfer for biomass burning events (and thus the accurate determination of TVCDs) is generally complicated by the simultaneous emissions of huge amounts of aerosols (also affecting the NO_x lifetime) and the impact of biomass burning on clouds [Andreae et al., 2004]. Furthermore the amount of NO_x emitted differs for different vegetation types. We think that further efforts in these subjects are necessary before a reliable quantitative estimate for the overall production of NO_x by biomass burning can be given from satellite observations.

Chapter 8
Long range transport of NO_x

Compared to other important anthropogenic emissions (as e.g. CO), the lifetime of NO_x is rather short. Thus, the amount and range of NO_x which is transported is rather low. Nevertheless, when NO_x is lifted to the upper troposphere during specific meteorological conditions, it has a longer lifetime. For such events, occasionally intercontinental transport of NO_2 can be observed, as demonstrated in section 8.1. In section 8.2, the influence of the North Atlantic Oscillation (i.e. changing modes of pressure systems) on the pollution pathways to the Arctic will be analyzed. Again, we make use of the potential of satellite data to analyze single events (8.1), but also use the long time series for a statistical approach (8.2).

These transport events of NO_2 have been analyzed in cooperation with Andreas Stohl, Sabine Eckhardt and Nicole Spichtinger from TU Munich, who performed the transport modelling using the Lagrangian tracer model FLEXPART [Stohl et al., 1998].

In this chapter we concentrate on the rather special occurences of long range transport; the transport of NO_x on shorter scales, i.e. the down-wind decay of NO_2 plumes, will be used in Chapter 10 to estimate the lifetime of NO_x.

8.1. Intercontinental transport of NO_x

Long range or even intercontinental transport (ICT) of moderately long-lived species like CO or aerosols has been analyzed in several studies [e.g. Jaffe et al., 1999; Stohl and Trickl, 1999; Forster et al., 2001]. As a consequence of transport, local emissions affect wider areas, and the inflow of pollutants from countries with high emissions often exceeds local productions of rural sites. Especially for the oceans, where naturally background levels are rather low and sources are absent (apart from ship emissions, see Chapter 11), inflow of polluted air masses drastically changes the chemical composition, with possibly large impact on ozone production (as the OPE is high for low background levels of NO_x, see section 1.5.5).

Due to the low lifetime of tropospheric NO_2 below one day, the range of NO_2 transport is generally below about 200 km, and NO_2 pollution is on first view a "local" topic. As will be shown in Chapter 9, the range (i.e. FWHM) of city plumes is typically below 100 km. However, conversion of NO_x to NO_y, mainly PAN with a longer lifetime of up to several months in the upper troposphere (for 250 K), allows transport over large distances and causes general background concentrations of NO_x of about 10-50 ppt [Jacob, 1999] (see also Chapter 1). However, even NO_x itself can be transported quite far, if lifted up in the UT, where its lifetime increases to about 2-10 days [Jaegle et al., 1998]. Some of such episodes have been observed in GOME NO_2 data: Spichtinger et al. [2001] report IT from Canada to western Europe; due to large boreal fires NO_x was released directly into the UT. Wenig et al. [2003] describe a transport event of anthropogenic NO_x emissions (from coal power plants in the South African Highveld) towards Australia. The clearest example, however, was reported by Stohl et al. [2003], where the author of this thesis was involved as a co-author. Please note that, as the study was performed in co-operation with our colleagues from IUP Bremen (Andreas Richter), their NO_2 data was used for figures. However, the fit results of NO_2 SCDs from Bremen and Heidelberg generally agree well, and the evolution of this specific transport event can be seen clearly in both datasets. For this particular study, the tropospheric AMF was roughly doubled to account for the uplift of NO_2 in the free troposphere, leading to increased sensitivity of GOME.

Stohl et al. [2003] report an ICT event, where anthropogenic NO_x emissions from the US eastcoast were transported towards Europe within less than 3 days in a meteorological "bomb". A meteorological "bomb" is defined as an explosively deepening cyclone with a decrease of minimum sea-level pressure of more than 1hPa/hour × $\sin(\varphi) / \sin(60)$ (where φ is the geographic latitude) over at least 24 hours [Sanders and Gyakum, 1980]. Such bombs can attain extremely low core sea level pressures, and thus horizontal pressure gradients and surface winds are extremely high. Bombs occur most often in winter and almost exclusively over oceans. On the Northern Hemisphere, about 50 bombs per year occur with a statistically significant upward trend that is possibly related to global warming [Lim and Simmonds, 2002].

On 7 November 2001, such a meteorological bomb was generated over the western Atlantic. During the 30-hour period from 6 November 18 UTC to 8 November 0 UTC, the bomb's core pressure decreased from 995 hPa to 961 hPa, i.e. dropped by 34 hPa. The specific evolution and travelling of this bomb allows ICT of anthropogenic NO_x from the US eastcoast to Europe, as can be seen in the GOME NO_2 data:

Fig. 8.1 shows the evolution of NO_2 TVCDs from GOME from November 7 to November 11 (left panel; observations with more than 50% CF are skipped). The GOME measurements are compared to FLEXPART model calculations (right panel) with a NO_x tracer, where emissions were taken from the EDGAR 2 inventory and a constant NO_x lifetime of 2 days was assumed. Please note that this is a good approach to estimate the dominating transport pathways, but as the actual lifetime varies and may deviate by a factor of about 2, quantitative comparisons of GOME and FLEXPART are difficult to interpret. The daily plots of the model results are shown for times that, in the region of main interest, coincide best with the GOME overpasses at about 10:30 local time.

(a) On 7 November, the situation can be considered as typical, similar to the NO_2 distributions seen in annually averaged GOME results (see for instance Fig. 3.1). (In contrast to GOME NO_2, the model NO_x tracer shows no enhanced values over Europe, because only North American emissions are considered in the simulation runs.)

(b) On 8 November, FLEXPART indicates starting outflow of NO_x eastwards. However, the respective GOME observation only reveals enhanced levels of NO_2 for the western subpixels. It turned out that the center and eastern subpixel are partly clouded and thus the transported NO_x is probably shielded.

(c) On 9 November, FLEXPART prognoses a filament of enhanced NO_x leaving North America, with the leading edge of the filament south of Greenland at 15 UTC. GOME sees a maximum (about 3×10^{15} molecules/cm^2) northeast of Newfoundland, i.e. relatively far from any significant source of NO_x, but exactly where FLEXPART suggested.

(d) On 10 November, both GOME and FLEXPART show a filament of enhanced NO_2 and NO_x tracer, respectively, stretching from Newfoundland across the Atlantic almost to Scandinavia. According to FLEXPART, the leading tip of the NO_x tracer filament had travelled from south of Greenland to Scandinavia, more than 50° of longitude (or almost 3000 km at 60° N) in only 20 hours, equivalent to average wind speeds above 40 m/s.

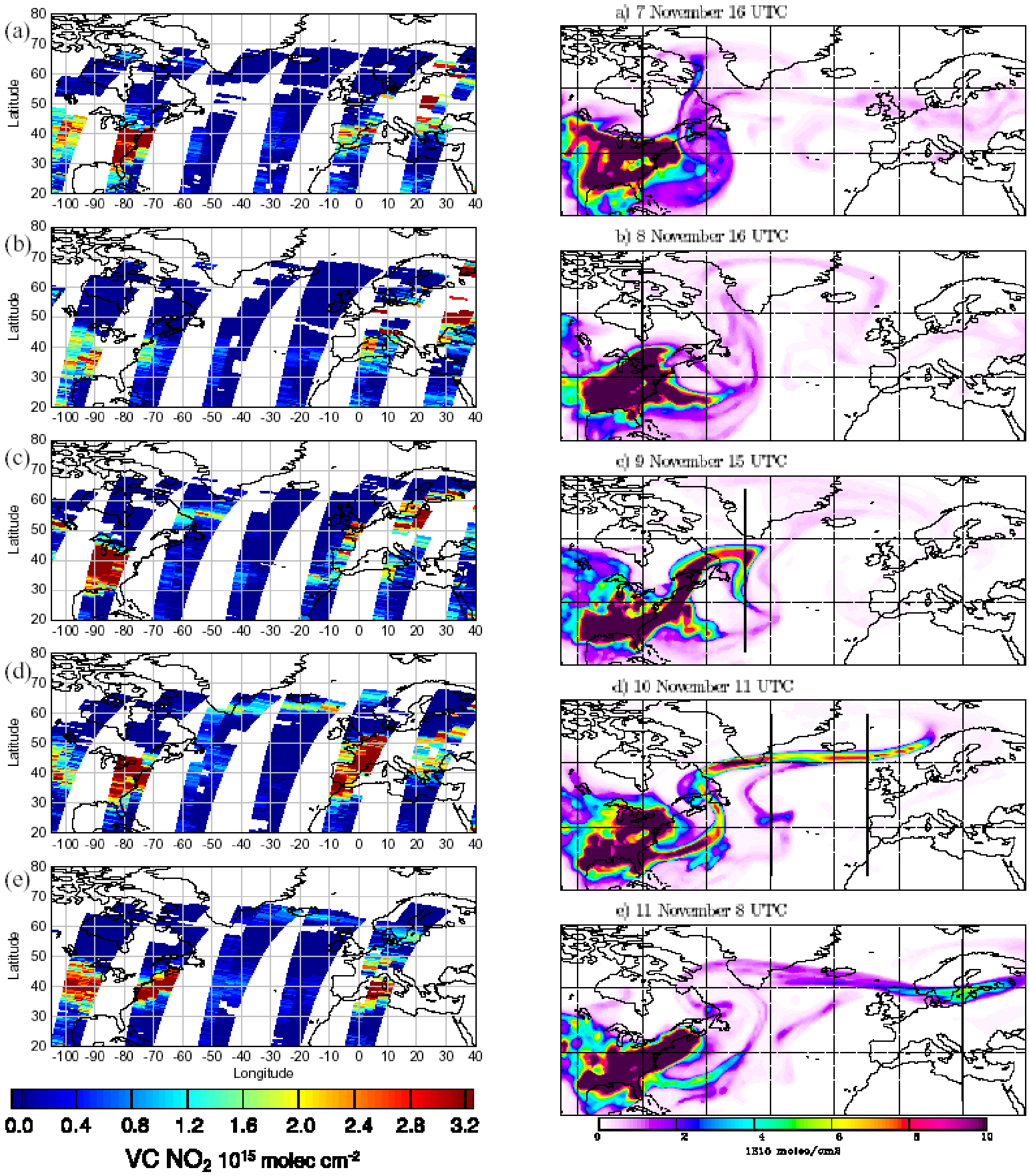

Fig. 8.1. Left: TVCDs of NO_2 (in 10^{15} molecules per cm^2), retrieved from GOME spectral data on (a) 7, (b) 8, (c) 9, (d) 10, and (e) 11 November 2001. White regions indicate that data are missing either because no GOME overpass was available, or because of more than 50% cloud cover.

Right: Total vertical columns of the FLEXPART NO_x tracer (in 10^{15} molecules per cm^2) for the respective days. The columns are average over 1-hour periods ending at 16, 16, 15, 11, and 8 UTC, respectively [Stohl et al., 2003].

The highest NO_2 values observed by GOME in the filament between Iceland and Scotland were 2.5×10^{15} molecules/cm^2. Assuming that the filament's vertical extension was from 3 to 5 km altitude (resulting from the FLEXPART simulation), simple arithmetic yields an average concentration of 1.0 µg/m^3 NO_2, corresponding to almost 1 ppbv at about 4 km altitude, within the plume. Assuming that NO contributes 50% to the NO_x, average NO_x concentrations in the plume can be estimated at nearly 2 ppbv, in good agreement with the NO_x tracer mixing ratios obtained from the model simulation. These are very high NO_x mixing ratios in the free troposphere, which, given sufficient supply with hydrocarbons (which are likely strongly enhanced in the plume, too) and sunlight, can lead to considerable O_3 production.
(e) On 11 November, the main part of the FLEXPART filament extended from southern Greenland to Russia. The maximum vertical columns were lower than before, both because of the further decay of the NO_x tracer, and because the filament broadened, due to mixing with ambient air. Nevertheless, GOME was still able to see the NO_2 signal, showing a band of enhanced NO_2 values between Greenland and the Baltic Sea. The maximum within the band was detected over the Baltic Sea, at the same location where FLEXPART suggested the NO_x tracer maximum.

Few lightning events have been detected within the considered time period by the NLDN (see section 6.5), but their location and strength does not fit the observed NO_2 VCDs. Therefore, lightning can be ruled out to the best of our knowledge as the main source of the NO_2 detected by GOME.

In this study, very good agreement between GOME VCDs and a NO_x tracer modelled with FLEXPART was found. It was demonstrated unambiguously, that anthropogenic surface emissions of NO_x can be transported over intercontinental distances in short time for extreme meteorological conditions like bombs. In this special event, polluted air masses crossed the Northern Atlantic within one day. The pollution levels in the remote ocean reached levels up to 2 ppb, illustrating the possible impact of such transport events on ozone production. A rough calculation (using a 15-years climatology) given by Stohl et al. [2003] suggests that ICT of North American NO_x emissions increases the mean NO_x mixing ratio over Europe by about 2-3 ppt in winter.

8.2. Impact of the North Atlantic Oscillation on air pollution transport to the Arctic

During winter and spring, the Arctic suffers from high levels of anthropogenic pollution [Mitchell, 1957]. This affects visibility ("Arctic haze", [Barrie, 1986]), radiative forcing [Garrett et al., 2002], soil pollution [Meijer et al., 2003], and promotes accumulation of persistent organic chemicals [Wania, 2003]. The accumulation of ozone precursors in the Arctic in winter and their release to lower latitudes in spring furthermore causes a peak in photochemical ozone formation, contributing to the spring-time maximum in photooxidants that is observed throughout wide areas of the northern hemispheric (NH) troposphere [Penkett and Brice, 1986]. Factors that cause the winter/spring maximum of Arctic pollution, i.e. seasonal changes in pollutant removal rates, photochemical processes, local meteorology and pollution transport pathways, are reasonably well understood now [Barrie, 1986; Polissar et al., 2001]. There is also evidence for downward trends of, e.g., sulfate, cadmium, or aerosols that have been related to emission reductions [Bodhaine, 1989; Li et al., 2003]. However, little attention has yet been paid to the influence of climate variability on interannual changes of Arctic air pollution levels.

Here we investigate the influence of the North Atlantic Oscillation on the pollution pathways from northern hemispheric (NH) continents into the Arctic. The results have been published by Eckhardt et al. [2003], where the author of this thesis was involved as co-author.

The climate of the Northern Atlantic is determined typically by a strong pressure gradient between Iceland (low) and the subtropics (high). It turned out that pressure patterns switch between two typical modes, especially in winter and spring. This is called the “North Atlantic Oscillation” (NAO). The NAO is commonly parameterized by the “NAO index” that is derived from the pressure gradient between the subtropical high pressure and the Icelandic low (here we take the sea level pressure (SLP) difference between Ponta Delgada, Azores, and Reykjavik, Iceland). A positive NAO index phase is defined by a stronger than usual subtropical high pressure center and a deeper than normal Icelandic low. The increased pressure difference results in more and stronger winter storms crossing the Atlantic Ocean on a more northerly track. This leads to warm and wet winters in Europe and cold and dry winters in northern Canada and Greenland. In contrast, in the negative NAO index phase the reduced pressure gradient results in fewer and weaker winter storms crossing on a more west-east pathway. They bring moist air into the Mediterranean and cold air to northern Europe. Greenland, however, will have milder winter temperatures.

In positive NAO phases, transport of anthropogenic pollutants from North America and Europe is expected to be pushed towards the Arctic due to the higher pressure gradient. This was studied in Eckhardt et al. [2003] where FLEXPART calculations were used to track anthropogenic emissions (corresponding to the EDGAR-2 emission inventory) from North America and Europe.

For this study a 15-year (1979-1993) climatology has been used. The transport was modeled for months with positive and negative NAO-index separately. The results substantiate that in a positive NAO phase pollutants are transported further towards north: For tracer lifetimes of 5 (30) days, surface concentrations in the Arctic winter are enhanced by about 70% (30%) during high phases of the NAO. This is mainly due to great differences in the pathways of European pollution during positive versus negative NAO phases, but reinforced by North American pollution, which is also enhanced in the Arctic during positive NAO phases.

The model results are confirmed by correlations of CO and black carbon with the NAO for three arctic stations and the Irish west coast [see Eckhardt et al., 2003]. We furthermore used the NO_2 results from GOME data and compared them with the modelled effect of the NAO. Therefore the 15-years climatology could not be applied, as it ends in 1993 before the ERS-2 launch. So we select the 5 months with the highest and lowest NAO indices from the winter months in 1996-2001 (see Table 8.1). Fig. 8.2 shows the difference of the mean NO_2 VCDs for both data sets (a) and the result of the respective FLEXPART calculations (b), using a tracer of 1 day lifetime. Both, GOME measurement and FLEXPART simulation, show enhanced northeastward NO_2 transport and at the same time reduced NO_2 outflow into the North Atlantic from Central Europe during positive NAO phases, resulting in a dipolar pattern. Please note the good agreement of GOME results and FLEXPART calculations, given the rather small amount of data (5 months for positive and negative NAO index each). The rather short lifetime of NO_2 prevents further transport northwards that occurs in the model runs with tracers having longer lifetime (like CO, SO_2 or aerosols would have).

Table 8.1 Considered months for negative and positive NAO phase.

negative NAO phase		positive NAO phase	
month/year	NAO index	month/year	NAO index
12/2001	-4.1	1/1999	1.3
12/1996	-3.7	12/1998	1.6
1/1997	-2.4	12/1999	1.7
12/2000	-2.2	2/1999	2.2
1/1996	-1.8	2/2000	3.1

By interpreting the GOME results, one has to keep in mind that the NAO might also have an influence on clouds (thus affecting radiative transfer) and on stratospheric NO_2 (due to a correlation of NAO and tropopause heights). To investigate a possible influence of clouds, Fig. 8.3 shows the difference in cloud fraction (from HICRU) for positive and negative NAO indices. The NAO influences mean cloud fractions (especially over the Atlantic), but the change can not explain the dipole-pattern of Fig. 8.2. Also changes of tropopause heights cannot explain the resulting NO_2 pattern, as has been analyzed by Eckhardt et al. [2003] using ECMWF data.

The results of the NAO's impact on pollution pathways has possibly important consequences on atmospheric chemistry (due to transport of O_3 precursors) as well as on climate (due to transport of aerosols), as during the past decades a positive trend in the NAO has been reported [Hurrell, 1995]. This might be one reason that climate change takes place faster in the Arctic than elsewhere [Moritz et al., 2002].

Another implication of our results is a (speculative) feedback on the NAO itself, caused by transport of short-lived greenhouse gases (e.g., ozone) and aerosols to the Arctic varying with the NAO phase.

According to our results, the NAO may lead to large interannual and (due to the tendency of the NAO to stay in one phase) decadal variability of nitrogen deposition to the Arctic Ocean, with potentially important ecological implications [Pearl et al., 1999] and feedbacks on climate through the uptake of carbon dioxide. Furthermore, a negative correlation between the NAO and nitrate concentrations in U.K. freshwaters has been reported, but is not yet explained [Monteith et al., 2000]. We suggest that variability in atmospheric transport of nitrogen from the European mainland and the U.K. itself is responsible.

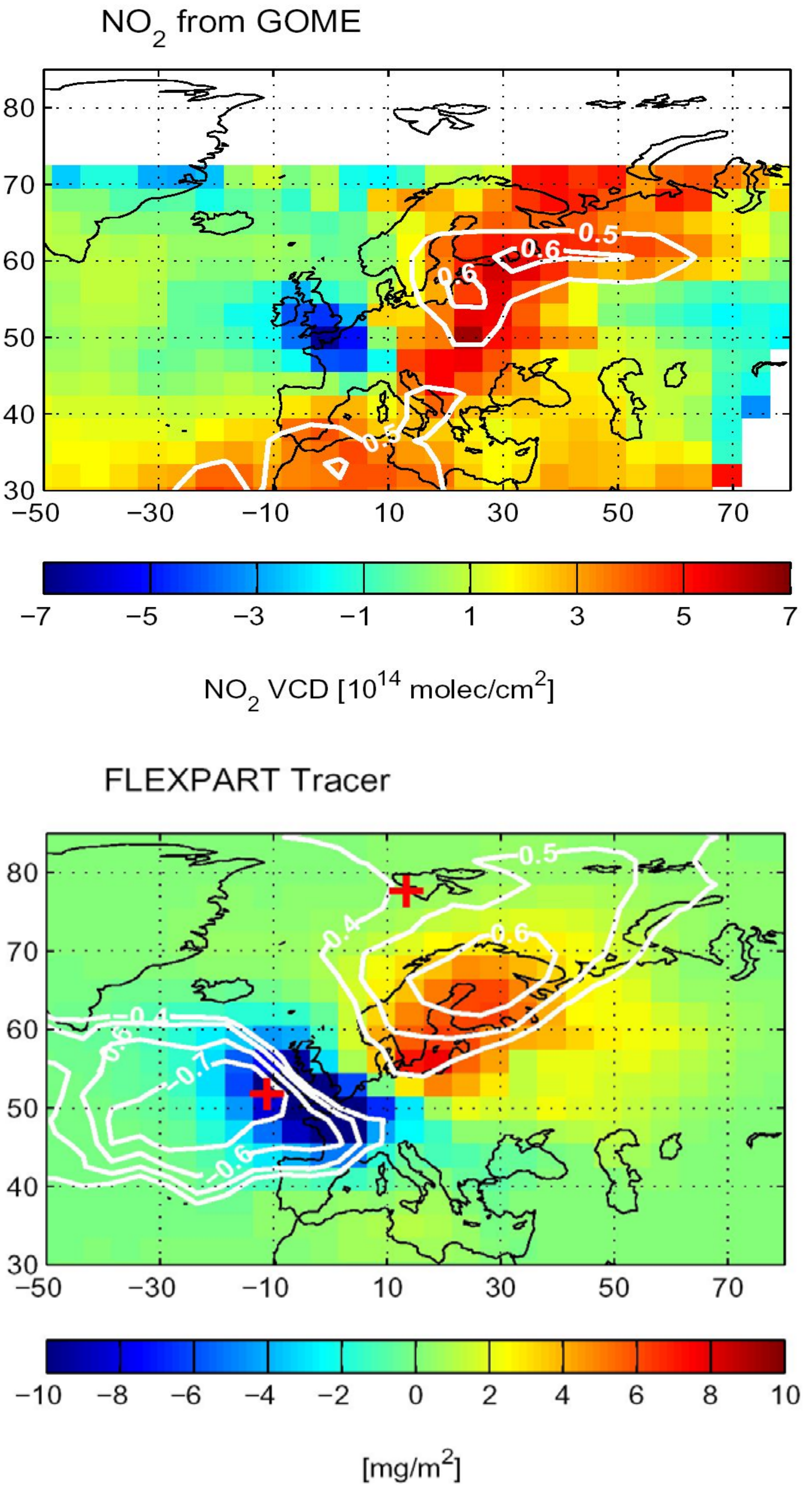

Fig. 8.2: Comparison of observed and simulated NAO signal in pollution transport from Europe. Map of the residual NO_2 vertical columns [10^{14} molecules/cm^2] (above) retrieved from GOME satellite observations for positive NAO minus negative NAO composites during the months listed in Table 8.1 and the respective residuals of vertical columns of the European 1-day-lifetime tracer in [mg/m^2] (below). Superimposed as white lines are the correlation coefficients with NAO indices. Crosses mark the locations of measurement sites at Mace Head and Spitsbergen [Eckhardt et al., 2003].

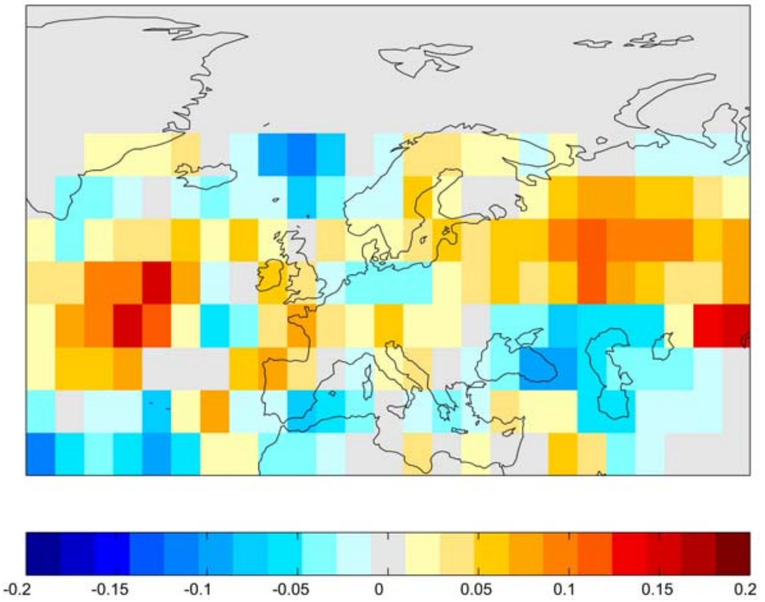

Fig. 8.3: Residual of cloud fraction (HICRU) for positive NAO minus negative NAO months (table 8.1).

Chapter 9
High resolution maps of NO_2 TVCDs from GOME narrow swath mode and SCIAMACHY observations

Data from the Global Ozone Monitoring Experiment (GOME) has successfully been used to analyze the general features of the global distribution of tropospheric NO_2 (e.g. [Leue et al., 2001; Velders et al., 2001; Wenig, 2001; Richter and Burrows, 2002; Martin et al., 2002; Martin et al., 2003]). In the previous chapters, we could in particular demonstrate the potential of GOME data to identify and quantify different sources of NO_x like anthropogenic emissions (Chapter 4, see also Chapter 11), biomass burning (Chapter 7) and lightning (Chapter 6).

However, a general restriction of GOME data is the standard spatial resolution of the ground pixel (320×40 km^2) that is insufficient to draw a detailed picture of the NO_2 distribution on the regional scale. To improve our knowledge of the NO_2 distribution, a better spatial resolution is essential to determine emission locations, to separate sources close together, to study transport, and to allow quantitative estimates of emissions.

This resolution is provided by the GOME narrow swath mode (80×40 km^2) and by SCIAMACHY (60×30 km^2). Results from both these data sources are presented and compared in this chapter. Compared to the standard GOME resolution, these data sets have a four-fold improvement in spatial resolution (and even better for SCIAMACHY). Though this is still rather coarse if one is interested in effects on short length scales (e.g. the NO_2 distribution within a town or a single street), it is the best resolution ever gained for such satellite measurements. Therefore, we use the term “high resolution” for GOME narrow swath mode and SCIAMACHY data.

In this chapter we derive highly resolved composites of the spatial distribution of NO_2 TVCDs from GOME narrow swath mode and SCIAMACHY. In section 9.1, the different ground pixel sizes and relevant satellite characteristics are discussed. Section 9.2 presents the resulting composites and describes the necessary efforts to derive a high quality composite from GOME narrow swath mode data. In section 9.3, the results for the different spatial resolutions are compared and the impact of ground pixel size, in combination with cloud fraction, is analyzed quantitatively. Finally, section 9.4 illustrates the benefit from the high resolution observations, providing new insights on the spatial distribution of NO_x sources. We furthermore compare our results to emission inventories and light pollution by night as proxy for anthropogenic activity (9.5). Parts of this chapter have been published in [Beirle et al., 2004b, 2004d].

9.1. Ground pixel sizes of GOME and SCIAMACHY

As described in section 2.1, GOME scans the Earth’s surface with an angular range of ±31.0°, corresponding to a cross track swath width of 960 km. During each scan, three ground pixels are mapped with a spatial resolution of 320 km east-west and 40 km north-south, followed by one backscan pixel with an extent of 960×40 km^2. Fig. 9.1 shows a snapshot for a sequence of two GOME scans with the intermediate backscan. For this illustration an equatorial region (Borneo) was chosen to minimize projection errors.

Besides this standard size mode (referred to as SSM below), GOME is operated in the so called narrow swath mode (referred to as NSM below) three days a month (4th/5th, 14th/15th and 24th/25th) since end of June 1997. These measurements are performed with a reduced scan angle of ±8.7°, corresponding to a spatial extent of 80×40 km^2 (forescan) and 240×40 km^2 (backscan) of the ground pixels (see Fig. 9.1). Additional information on the GOME viewing geometries can be found in the GOME user's manual [Bednarz, 1995].

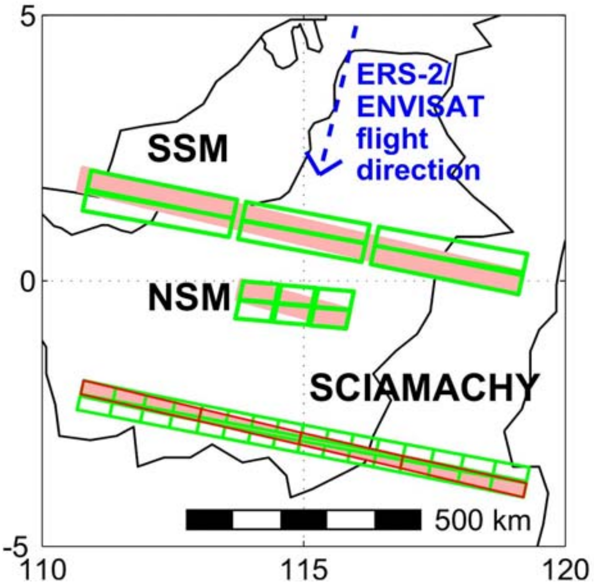

Figure 9.1: Spatial extension and geometry of the GOME and SCIAMACHY ground pixels (compare Fig. 2.5). Snapshots of the GOME standard size mode (SSM, 320×40 km^2), GOME narrow swath mode (NSM, 80×40 km^2) and SCIAMACHY (60×30 km^2) are shown at the equator (Borneo). The forescan pixels are green, the subsequent backscans red. For GOME, the backscan has three times the length of the forescans (960 km in SSM, 240 km in NSM). For SCIAMACHY, the backscan comprises four pixels of 240 km width each.

It is important to note that the NSM largely improves the spatial resolution at the cost of reduced global coverage; both effects are caused by the reduced scan angle. In SSM, GOME achieves global coverage every 3 days, while for the NSM 12 days of measurements are required. Because the NSM is only applied every 10th day, statistically, 120 days are needed to provide global coverage with the NSM orbits. Fig. 9.2 shows the global spatial distribution of the total number of measurements in the NSM during the 5 year period from 1997 to 2001.
One of the important improvements of SCIAMACHY compared to GOME is the higher spatial resolution of 60×30 km^2 for the full track width of 960 km (Fig. 9.1; see also section 2.1). The global coverage of SCIAMACHY is reduced due to the nadir gaps during limb mode; however, SCIAMACHY reaches global coverage in high resolution every 6 days, as compared to the ~120 days required by the seldom-used GOME NSM!

9.2. High resolution maps of tropospheric NO_2

9.2.1. Retrieval of a high quality map from GOME NSM data

Figure 9.3 (a) shows the global map of the mean NO_2 TVCD, using the GOME SSM forescan pixels (320 km across track by 40 km along track) for 1996-2001. Significantly enhanced TVCDs are observed in regions with dense population and/or high industrialisation. However, the emissions of spatially small sources like single cities are "smeared out" due to the large east-west extension of the GOME ground pixels.

Figure 9.3 (b) depicts the mean NO_2 TVCD of all NSM pixels during 1997-2001. The improved spatial resolution reveals many more details of the global distribution of tropospheric NO_2. But whereas Fig. 9.3 (a) shows quite a smooth distribution, Fig. 9.3 (b) exhibits stripe like patterns parallel to the ERS-2 flight direction.

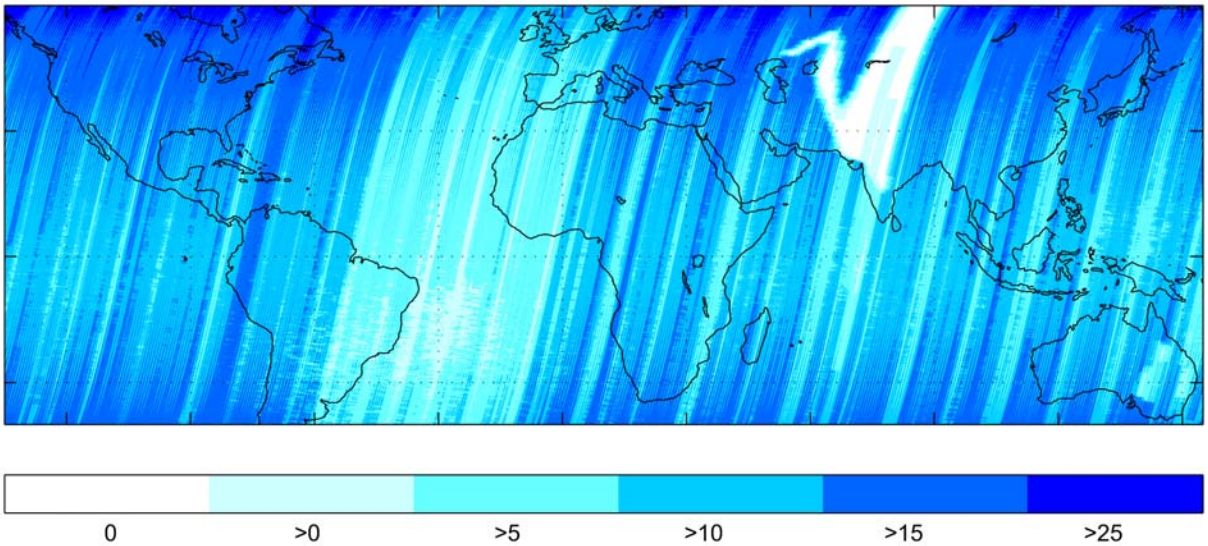

Figure 9.2: Total number of GOME scans in the narrow swath mode (NSM) 1997-2001.

The reason for these stripes is the sparse global coverage together with seasonal changes of NO_2 TVCDs and/or possible instrumental artifacts. In the NSM, each point on the Earth is scanned only about 10-15 times during a five year time period (see Fig. 9.2). Moreover, these measurements are not distributed homogeneously over the year. For instance, Table 9.1 lists the dates of NSM overpasses for the spots A and B in a typical biomass burning region in central Africa as shown in Fig. 9.4. For site A, all measurements are taken between July and October, whereas there is only one summertime scan of site B. This temporal inhomogeneous sampling obviously biases the mean TVCD, as far as the NO_2 burden is subjected to seasonal variations. This is indeed the case for the Congo region, where NO_2 TVCDs are highest in the biomass burning season from June to September (see Chapter 7). As a consequence, the mean TVCD at spot A is higher than at spot B by a factor of about 2, while the mean of the SSM (Fig. 9.3 (a)) shows no difference for both spots. The stripes also occur in other regions, where seasonal variations of the NO_2 TVCD are also present, for example in the equatorial Atlantic Ocean (probably due to outflow from the Congo region), Central Australia (Lightning, see Chapter 6) and even the Sahara (possibly due to albedo variations). Thus we find that the main reason for the stripe structure is that the local measurements are not distributed uniformly throughout the year. Therefore we call it the 'seasonal effect', because the measured NO_2 TVCD depends on the season in which the majority of the measurements were made.

Our goal in this section is to produce a multi-year average free of artifacts arising from seasonal variations. The stripe structure could be reduced by spatially smoothing the data, at the cost of spatial resolution. However, it is the main idea of this investigation to obtain a map of the NO_2 distribution with high spatial resolution from the NSM data. Therefore, to account for the patchy temporal coverage, we apply a more sophisticated method to deseasonalize our data. For this procedure we use our knowledge of the mean distribution of NO_2 VCD from the SSM as displayed in Fig. 9.3a.

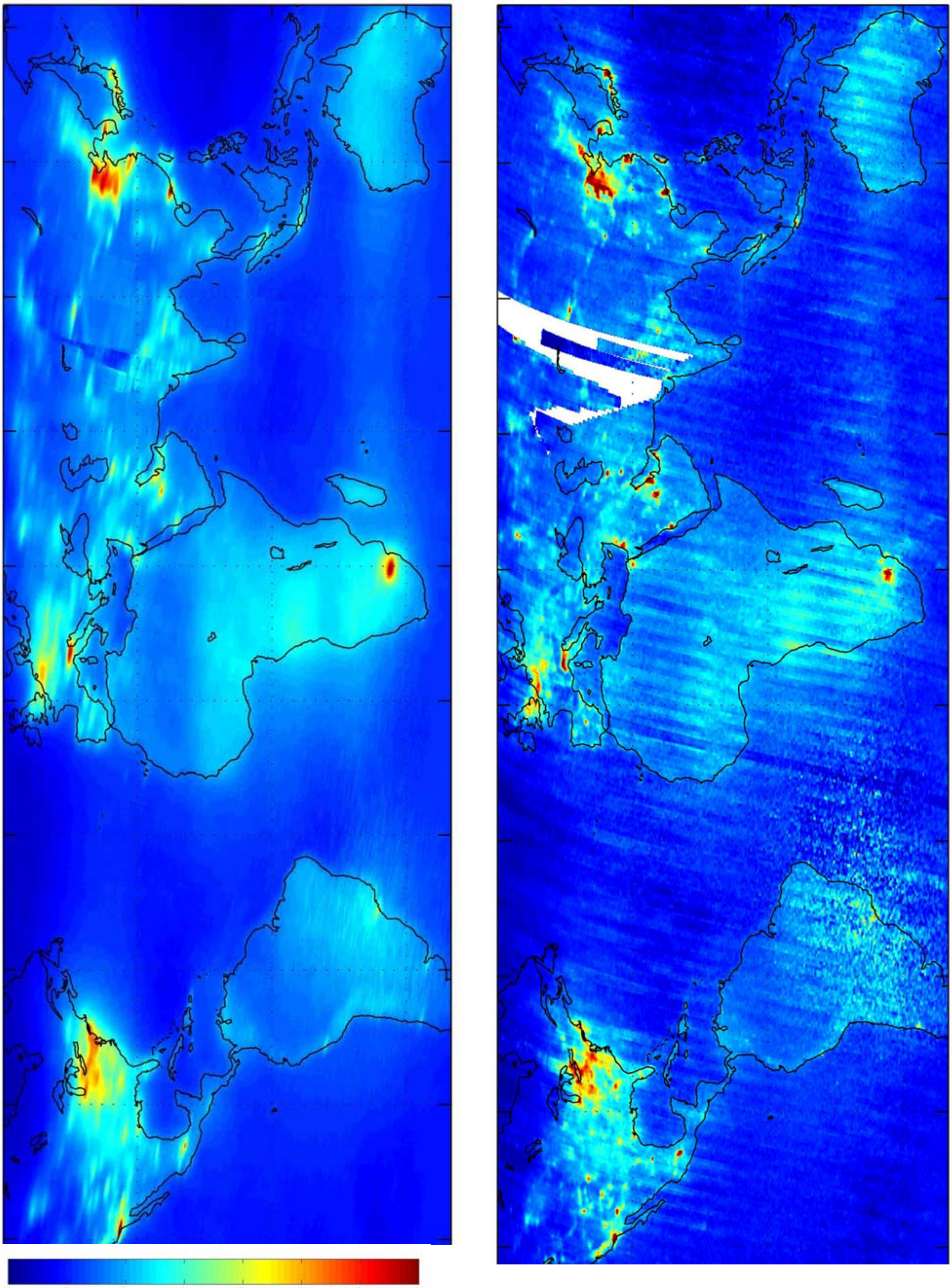

Figure 9.3:
(a) Mean NO_2 *TVCD* (10^{15} *molecules/*cm^2*) using all GOME forescan pixels (1996-2001).*

(b) Global mean NO_2 *TVCD of NSM forescan observation only (1997-2001).*

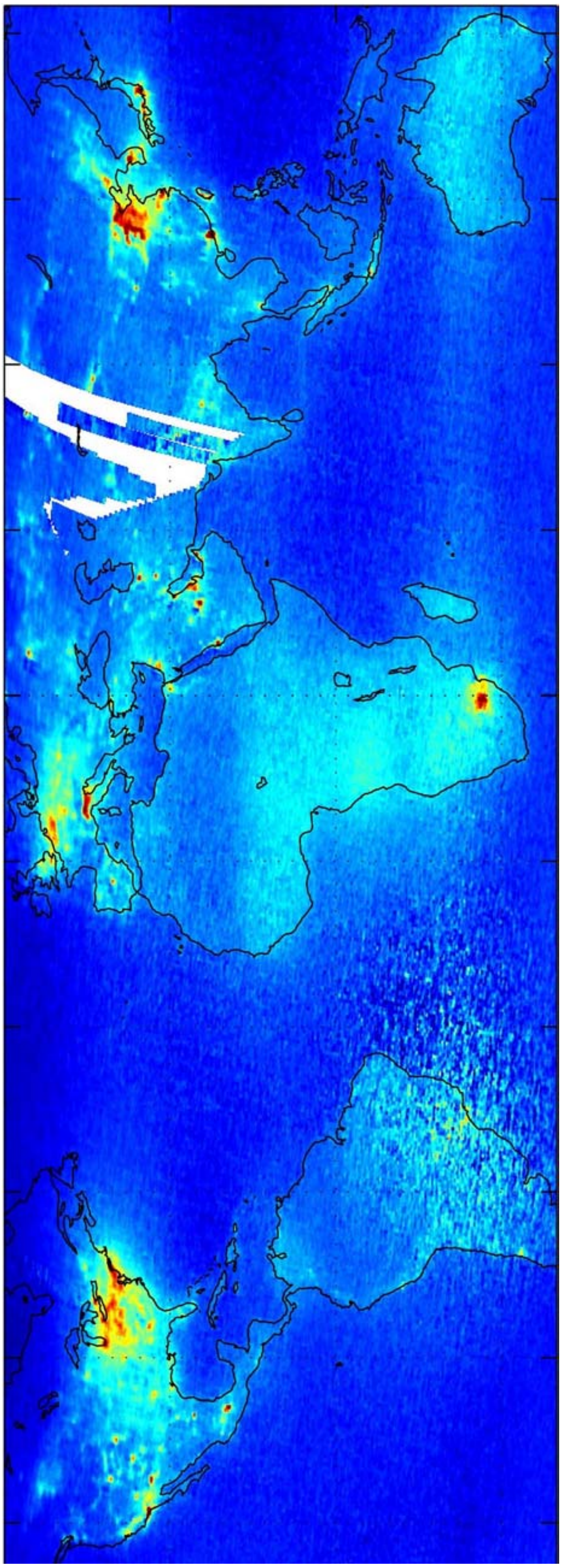

(c) Global mean NO_2 TVCD of NSM forescan observation only (1997-2001), corrected for seasonal effects as described in 9.2.

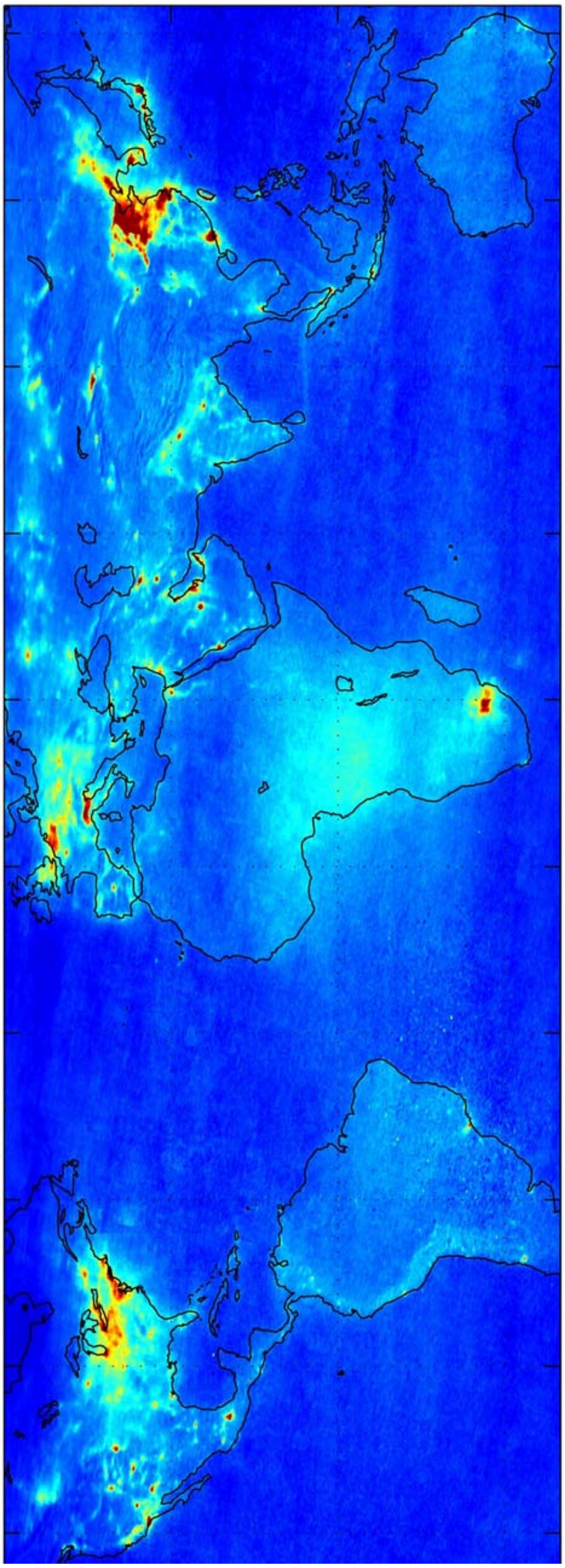

(d) Global mean NO_2 TVCD of SCIAMACHY observations (January 2003 - June 2004).

Each GOME measurement consists of three forescan pixels and a subsequent backscan pixel (see Fig. 1). The NSM forescan observations n_1, n_2, n_3 carry the desired spatial information, but are biased by the seasonal offset b_{season}. In the NSM backscan n_{back}, this high spatial information is averaged over. The spatial resolution of the backscan pixel n_{back} (240×40 km^2), however, is quite comparable to the extent of the SSM forescan pixels s_i (320×40 km^2). Using the full amount of GOME SSM data from 1996-2001, we know the mean, unbiased VCD s_{mean} as displayed in Fig. 9.3 (a), . We can therefore use the difference of the NSM backscan and the mean SSM forescans as an estimate for the seasonal offset of each individual NSM measurement:

(9.1) $b_{season}=n_{back} - s_{mean}$

The deseasonalized NSM VCDs are thus

(9.2) $n'_i= n_i - b_{season}= n_i - n_{back} + s_{mean}$

The resulting seasonally corrected mean NO_2 TVCD distribution of the NSM pixels n_i' is shown in Fig. 9.3 (c). These data are free of the stripelike structures seen in Fig. 9.3 (b), affirming the success of our deseasonalization method. The remaining noisy values around South America are due to the South Atlantic anomaly [Heirtzler, 2002], which is a deformation of the magnetic field of the earth that allows high-energy cosmic radiation to hit the satellite and affects the spectral data.

Fig. 9.3 (c) reveals many details on the tropospheric NO_2 distribution. Especially in the polluted regions in North America, Europe, the Middle East and Far East, structures can be seen with unprecedented spatial resolution. Many "hot spots" show up, and sources of NO_2 can be clearly localized and identified (mostly large cities). This will be discussed in detail in section 9.4. On the other hand, tropical regions of enhanced NO_2 TVCD like Congo show no new spatial information, because the sources (biomass burning, lightning) are not sharply localized in the mean taken over several years.

9.2.2. Retrieval of a high quality map from SCIAMACHY data

For studying the global distribution of NO_2 as seen from SCIAMACHY, we use the complete data set of nadir scans currently available at our institute. This data set comprises approx. 4000 orbits from January 2003 - June 2004. As the number of measurements is not the same for the different months (due to missing data), we first average every single month and calculate the overall mean afterwards, to avoid biases from months with much data.
The whole globe is scanned about 50 times within the considered time period, resulting in an overall mean with little noise (Fig. 9.3 (d)).
Generally, Figs. 9.3 (c) and (d) show a similar distribution of TVCDs, but also show some deviations. In the next section, we compare the results from GOME SSM/NSM and SCIAMACHY quantitatively and investigate different causes for the observed deviations.

Table 9.1: Dates of measurements for the sites marked in Fig. 9.4. Bold typing indicates the ***burning season*** *in Central Africa (June-September).*

Site A	Site B
05.09.1997	15.03.1998
25.09.1998	05.05.1998
05.07.1999	05.01.1999
25.08.1999	25.02.1999
25.10.1999	25.05.1999
25.08.2000	**15.07.1999**
25.07.2001	05.12.1999
	25.01.2000
	25.05.2000
	15.10.2000
	05.12.2000
	05.04.2001
	25.12.2001

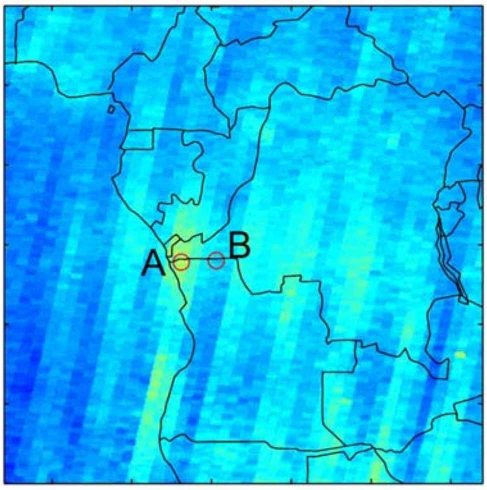

Figure 9.4: Zoom of Fig. 9.3 (b) on Central Africa to explain the stripe like features. Two neighbouring sites with high (A) and low (B) NO_2 TVCD are compared. Table 9.1 reveals that for site (A) almost all (whereas for site (B) only 1) measurements took place during the burning season.

9.3. Comparisons of the datasets

9.3.1 Direct influence of pixel size: smoothing

In the GOME SSM, pollution peaks are obviously “smeared out” due to the 320 km width of the GOME pixel in west-east direction (see Fig. 3a; compare, for instance, the shape of the Hong Kong peak in 9.3 (a) and 9.3 (c). For the same reason the maximum TVCDs measured in the SSM are lower than in the NSM. A quantitative estimation of this effect is illustrated in Fig. 9.5, where we model the dependency of the measured TVCD on spatial resolution for different source extents. (Here we focus on the different cross-track resolutions. The along-track resolutions of GOME (40 km) and SCIAMACHY (30 km) are both comparably good.) Gaussian distributions (black) of NO_2 pollution with a FWHM of 30, 60, 100 or 200 km (i.e. the extent of large cities or congested areas) are scanned with pixels of SSM, NSM and SCIAMACHY size respectively. The actual TVCD is drastically underestimated by SSM observations (blue) at its peak, and overestimated at its edges. The smoothing effect is quite similar for the NSM backscan (green), but much weaker for the NSM forescans (red) and SCIAMACHY pixels (magenta), because their resolution approaches the actual extent of the NO_2 distribution.

Fig. 9.5 also displays the ratio of the modelled maxima in the NSM and the SSM. The ratio is close to 3.6 for a point source and approaches unity for extended sources. For the calculation of these ratios, we have used the “corrected” NSM forescans, where we applied the same offset correction n_{back}-s_{mean} (eq. 9.1/9.2) as for the measurement data, to be able to compare the modelled ratios quantitatively to our observations.

Furthermore, we added the ratio of SCIAMACHY and NSM observations. Measured TVCDs are expected to be higher over hotspots for SCIAMACHY, but the effect (compared to NSM) is rather small and only plays a role for small plume extents (<60 km).

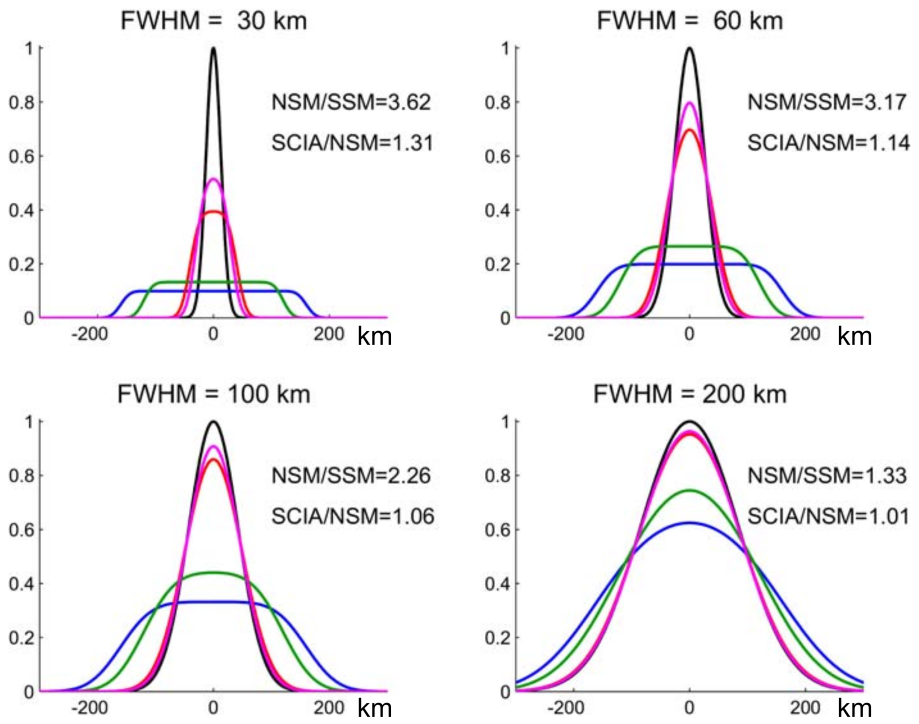

Figure 9.5: Illustration of the smoothing effect of the GOME SSM pixels. The observation of a given pollution distribution (black), assumed to be Gaussian with different FWHM, is modelled for different spatial resolutions. The GOME SSM (blue) drastically underestimates the plume over its maximum, but overestimates over its edges. This effect is similar for the NSM backscan (green), but much weaker for the NSM forescan (red) and the SCIAMACHY observations (magenta).
The given numbers are a) the ratio of the measured maximum in the NSM (corrected for the bias $n_{back}-s_{mean}$ like the actual GOME measurement as explained in 9.2 (eq. 9.2)) and the SSM and b) the ratio of the maxima of SCIAMACHY and NSM observations. These ratios are compared to the measured ratios as listed in Table 9.2.

Table 9.2. Peak NO_2 TVCD (10^{15} molec/cm^2) of several cities for the different satellite instrument ground pixel sizes (columns 2-4). Additionally, columns 5 and 6 give the ratios of NSM/SSM and SCIAMACHY/NSM observations, respectively. Please that the numbers in columns 4 and 6 differ slightly from [Beirle et al., 2004c] since we here apply a modified stratospheric estimation that is analogue to the GOME retrieval.

City	**VCD SSM**	**VCD NSM**	**VCD SCIA**	NSM/ SSM	SCIA/ NSM
Los Angeles	8.70	22.42	17.18	2.58	0.77
New York	4.98	8.30	9.69	1.67	1.17
Mexico City	4.88	15.66	14.99	**3.21**	0.96
Ruhr Region	3.94	5.74	6.09	1.46	1.06
Milan	5.68	8.30	8.90	1.46	1.07
South Africa	6.56	9.22	8.58	1.41	0.93
Jeddah	3.18	8.44	7.99	2.65	0.95
Riyadh	4.32	9.68	11.92	2.24	1.23
Hong Kong	6.16	12.86	14.07	2.09	1.09
Shanghai	4.32	7.84	9.28	1.81	1.18
Beijing	5.70	8.32	11.88	1.46	**1.43**
Seoul	5.46	10.24	12.33	1.88	1.20
Tokyo	4.30	8.74	10.86	2.03	1.24
Istanbul	2.44	5.56	5.25	2.28	0.94
Shijiazhuang	5.86	9.60	13.17	1.64	**1.37**
Zhengzhou	4.66	6.56	13.70	1.41	**2.09**

Table 9.2 lists the observed peak NO_2 TVCDs over some selected cities with high NO_2 burden for the SSM, NSM and SCIAMACHY observations. As expected, the NSM TVCDs are higher compared to SSM. Comparison of the measured NSM/SSM ratios in Table 9.2 with those calculated in Fig. 9.5 allow one to deduce the spatial extent of the observed plume. Mexico city, for instance, where the NSM/SSM-ratio is 3.2, can be regarded as an isolated source spot with a plume extent of about 60 km. The comparison of NSM and SSM thus has the potential to gauge plume extents even below the NSM resolution. The Ruhr region, on the other hand, where the NSM/SSM ratio is only 1.46, has a large extension and is probably also affected by sources in the Netherlands and Belgium.

To further analyse the “smoothing effect” present in SSM measurements, we plotted the difference of the NSM forescans (i.e. high resolution observations), and the NSM backscans (representing nearly the SSM resolution), in Fig. 9.6 for the USA/Mexico and for Europe, where also the location of cities is marked. Fig. 9.6 impressively illustrates the findings of Fig. 9.5, i.e. the underestimation of the SSM observations above the spot and underestimation left and right. This typical pattern can be found for several locations, especially for isolated cities (Mexico City, Madrid, Salt Lake City, Phoenix) and cities with very high NO_2 TVCDs (Los Angeles).

Fig. 9.6 clearly displays locations where the SSM GOME observations overestimate the actual burden due to the ”smearing out” of local peaks. These locations of overestimations are important to consider for the interpretation of GOME studies. For instance, the mean of the SSM GOME pixels (Fig. 9.3 (a)) shows enhanced TVCD of NO_2 over the North Sea between England and the Netherlands. Fig. 9.6 shows that these TVCDs were overestimated in the SSM derived map. The enhancement of NO_2 TVCDs observed in the SSM is not only due to transport by wind, as may be assumed, but to large part also to the fact that each nominal SSM pixel in this area either covers polluted sites in England (Manchester, Sheffield etc.) or the Netherlands (Rotterdam). The TVCD over the western Alpine mountains is also drastically overestimated by the SSM observations due to the short distance from Milan and Turin.

9.3.2 Indirect influence of pixel size: clouds

As a consequence of the lower pixel size in NSM and SCIA, one expects a shift in cloud properties in which the smaller pixels are more often cloud free. As clouds strongly influence the retrieval of tropospheric absorbers, this effect should also have impact on the retrieved means for the different pixel sizes. In this section, we analyze the influence of pixel size on in-pixel cloud cover, and of both on the mean TVCD. Thereby we concentrate on GOME results, as we can use the HICRU cloud product that is not yet available for SCIAMACHY. In the following, we define a GOME observation as “cloud free” if the effective cloud fraction is below 10%. We concentrate on summertime observations (to avoid interferences of snow cover that could be misinterpreted as clouds by cloud algorithms) in the polluted regions (i.e. a mean NO_2 TVCD above 2×10^{15}molec/cm^2) of the northern hemisphere.

The NSM pixels are sampled with a 4 times higher spatial resolution than the SSM pixels. As a consequence, we find that the percentage of cloud free pixels increases for smaller pixel size, i.e. from 28% (SSM backscan) and 39% (SSM forescan) to 42% (NSM backscan) and as much as 49% (NSM forescan). The difference of the cloud fraction distributions in the different observation modes is highly significant.

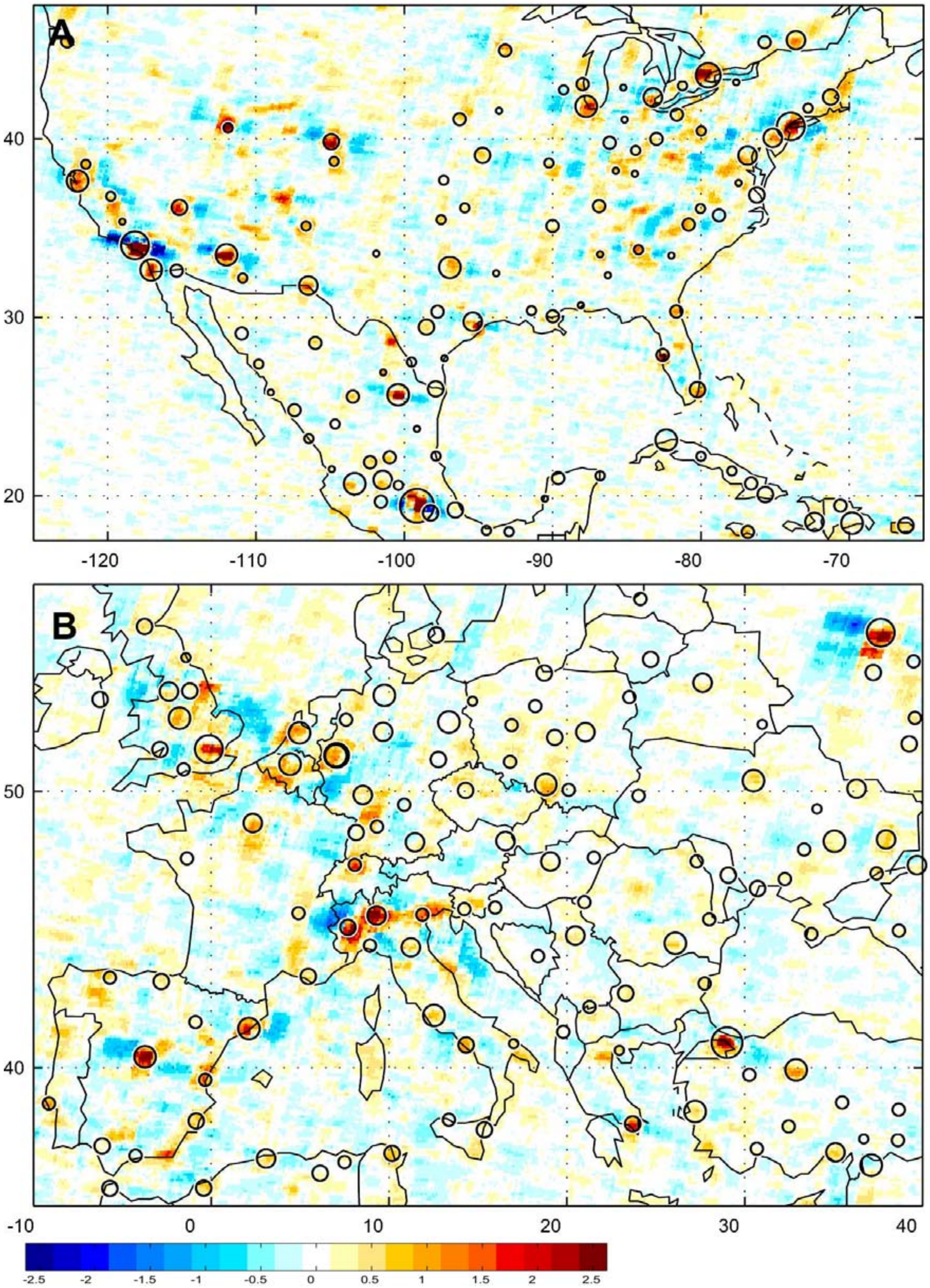

Figure 9.6: Difference of the NSM fore- and backscan pixels (10^{15} molec/cm^2) for North America (A) and Europe (B). Circles indicate the location of cities. Red spots show locations, where the NO_2 TVCD is underestimated by the nominal viewing pixels from GOME (several cities), whereas it is overestimated for the blue spots (e.g. the Alpine mountains).

For a cloudy scene, boundary layer NO_2 would be shielded and thus be „invisible“ for GOME. Furthermore, because the cloud albedo is much higher than the ground albedo, the reflected light observed by GOME comes predominantly from the clouds, leading to a further underestimation of boundary layer NO_2 in the backscan mode. Fig. 9.7 exemplarily illustrates the effect of what happens if a partly clouded scene is scanned in the forescan or the backscan mode respectively. In the given scene with 50% cloud fraction, the tropospheric NO_2 would be totally shielded in the left (clouded) forescan, whereas for the right (cloud free) forescan, half of the actual boundary layer NO_2 VCD_{true} would be detected, corresponding to a tropospheric AMF of 1. The light of the cloud free pixel stems from reflection from the (relatively dark) ground as well as from Rayleigh scattering in the atmosphere, since the respective wavelength range is in the blue (440 nm). For the half-clouded backscan pixel (as well as the middle forescan pixel), about 5/6 of the observed light comes from the clouded part, i.e. the intensity of the cloud free part (i.e. 1/6) is lower by a factor of 5 (compare Fig. 9.9). The resulting total VCD would be $1/6 \times 1/2 \times VCD_{true}$, i.e. 8% of the actual NO_2 burden. The forescans would detect 0% (left), 8% (middle), and 50% (right) of VCD_{true}, thus on average 19%, i.e. more than twice as much as the backscan observation.

Consequently, we expect that the retrieved mean VCDs are systematically larger for smaller pixel sizes. We have tried to verify this effect by comparing the backscan measurements with the mean of the respective forescans (weighted by the area that is actually covered by the backscan, compare Fig. 9.1). Please note that we use the original, non-deseasonalised NSM observations for this comparison study (see section 9.2.1). The result is displayed in Fig. 9.8 for the NSM (a), the SSM (b) and SCIAMACHY (c). In all cases, we find a nearly 1:1 linear relation. This observation means that, in contrast to our expectations, the pixel size has almost **no** influence on the **mean** NO_2 VCD.

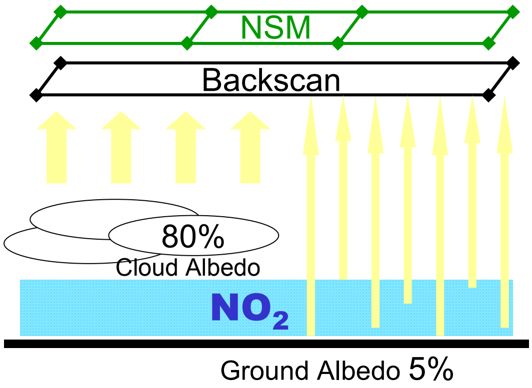

Figure 9.7: Shielding effect of clouds. The boundary layer is partly shielded by clouds. Consequently, the actual NO_2 TVCD is underestimated. Furthermore, the backscan observation lead to systematically lower TVCDs (compared to the averaged forescans), as the backscan intensity is dominated by the bright clouded part (see discussion in paragraph 9.3.2).

This finding can be explained by the fact that the example shown in Fig. 9.7, where a totally clouded pixel is next to a totally cloud free pixel, is extremely rare. This is illustrated in Fig. 9.9, where we have plotted the measured ratio of maximum and minimum intensity within the three forescans, against the corresponding difference in cloud fraction. This figure demonstrates that a) large differences in cloud fraction are very rare (the difference in cloud fractions exceeds 50% only in 10% of all observations) and b) the maximum intensity exceeds the minimum by a factor of 6 in extreme cases, but only by 1.8 on average.

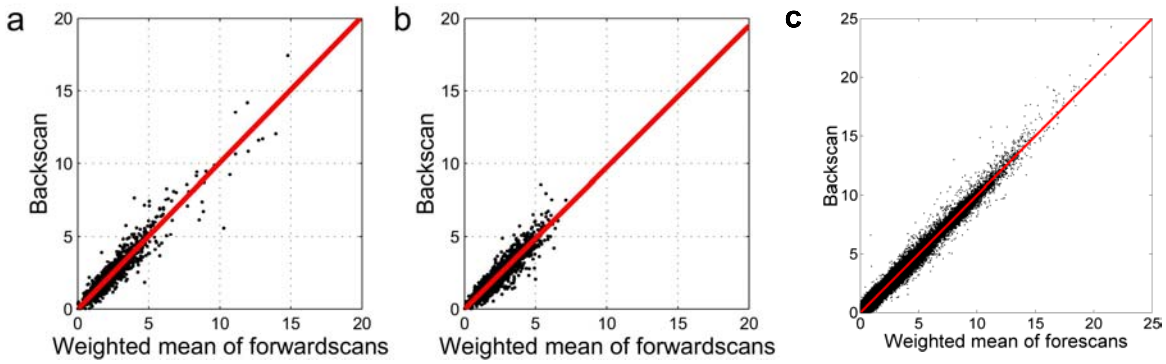

Figure 9.8: Correlation of the mean NO_2 TVCD (10^{15} molec/cm^2) of the original forescans and the respective backscans (all summertime observations for polluted regions of the northern hemisphere) for the NSM (a), the SSM (b) and SCIAMACHY (c). The slopes of the linear fits are 1.006, 0.974, and 1.001, respectively.

We have modelled the expected underestimation of the backscan observations as illustrated in Fig. 9.7, where we assumed an overall constant TVCD that is observed in several scans of three forescan pixels with different cloud fractions, and assume the clouded part of the pixel to be totally shielded. The cloud fraction distribution and the intensity of the reflected light is taken from the actual GOME measurements. Then we compare the mean of the modelled observations (representing the forescan mean) with the intensity weighted mean (that represents the backscan). We found that the general underestimation of the backscan observations is only 2% for the NSM and 4% for the SSM, thus quite negligible, and too small to be significantly detected in Fig. 9.8. However, for SCIAMACHY observations the slope of the linear fit gives 1.0008±0.0002. For SCIAMACHY, the amount of available data is much higher compared to GOME NSM; in Fig. 9.8c, 200,000 data points are plotted. Thus we should be able to detect a deviation of the slope from 1 if it exists. The fact that we do not find the slightest indication for lower backscan VCDs remains thus quite astonishing. However, it possibly could be explained by amounts of NO_2 inside the upper cloud layers or above the clouds, where its visibility is enhanced.

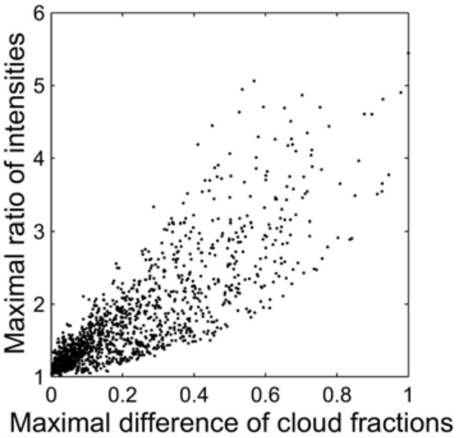

Fig. 9.9: Ratio of the intensities of the brightest and the darkest subpixels (for the 6 subpixels covered by the backscan, compare Fig. 9.1) in dependency of the difference in the respective cloud fractions for the NSM observations. The results for the SSM are quite similar. The example shown in Fig. 9.7 of an extremely heterogeneous cloud cover is thus very rare.

9.3.3. Comparison of GOME NSM and SCIAMACHY

Overall, Figs. 9.3 (c) and (d) show a similar distribution of NO_2 TVCDs, confirming the applicability of our deseasonalization approach. Nevertheless, there are some differences. On first view one can see that the striking scatter of the GOME NSM TVCDs in the southern Atlantic due to the South Atlantic Anomaly is vanished in the SCIAMACHY data, where only a handful of pixels are affected. Obviously, SCIAMACHY is shielded more effectively against cosmic radiation. To illustrate further deviations, Fig. 9.10 shows the difference of SCIAMACHY and GOME NSM NO_2 TVCDs.

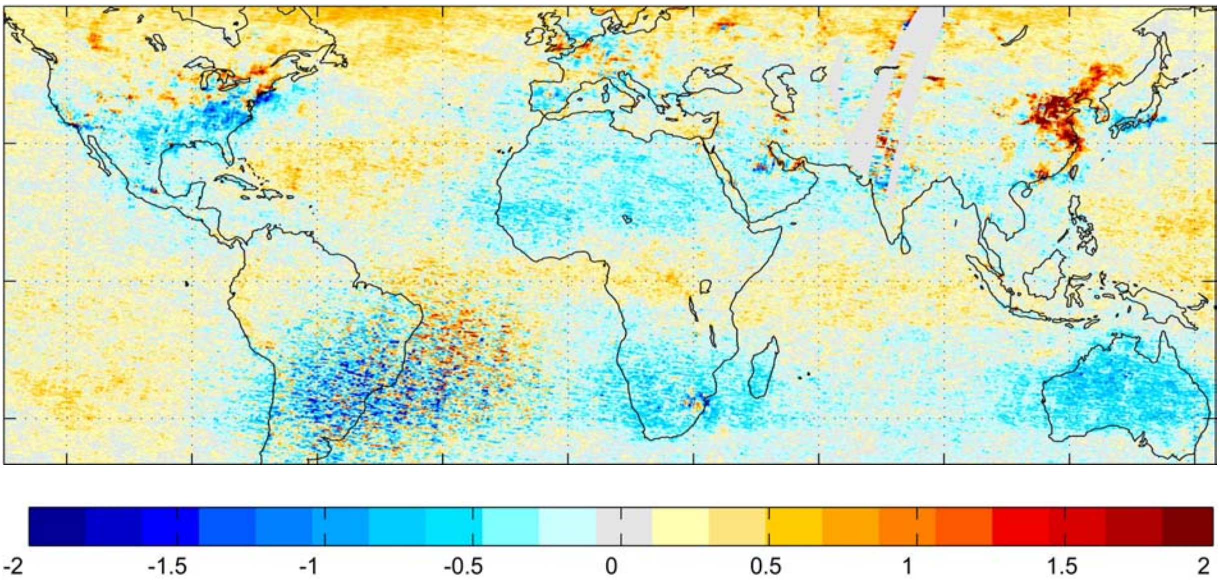

Fig. 9.10. Difference of mean TVCDs (in 10^{15} molec/cm^2) from SCIAMACHY (Fig. 9.3 (d)) and GOME NSM (Fig. 9.3 (c)).

For the discussion of differences of GOME NSM and SCIAMACHY results one has to keep in mind some aspects:

(a) Inter-annual variations:

The SCIAMACHY data enclose only 1.5 years, and is more affected by normal year to year fluctuations than the 6-year GOME data set. For instance the higher SCIAMACHY TVCDs in Central Africa seem to arise from above average NO_x emissions in the biomass burning season in summer 2003.

(b) Seasonal effects:

In the SCIAMACHY composite, the months January-June are represented twice, but July-December only once. This seasonal bias might explain the lower SCIAMACHY TVCDs over Australia, where TVCDs show a strong yearly cycle due to lightning (see Chapter 6).

Choosing only 1 year of SCIAMACHY data instead of 18 months would reduce the data amount and thus increase statistical fluctuations. Therefore, we do not prefer to limit our data period. As a test, we re-created the difference plot in Fig. 9.10 with 1-year of SCIAMACHY data and find only small changes. Therefore (b) cannot explain large discrepancies.

(c) Spatial resolution:

As already discussed in 9.3.1, The SCIAMACHY pixels are smaller (30×60=1800 km^2) than the GOME SSM pixels (40×80=3200 km^2). However, from the typical plume extent derived from the GOME SSM-NSM comparison in 9.3.1, we can deduce that the expected increase of the SCIAMACHY observations due to the reduced pixel size is <10%.

The measured SCIAMACHY TVCDs (4th column of Table 9.2) are generally of the order of the GOME NSM observations (3rd column). In most cities, the SCIAMACHY/NSM ratio (column 6) does not exceed 1.2, and is even lower than 1 in some cases (for reasons (a), (b) and/or (d)). The high ratios of ~1.4 (Beijing, Shijiazhuang) up to 2 (Zhengzhou) can not be explained by the reduced pixel size.

(d) Emission trends:

The GOME NSM composite (1997-2001) was measured before the ENVISAT launch, in contrast to the recent SCIAMACHY measurements (2003-2004). Thus differences in both datasets may indicate a change in emissions.

The most impressive difference of SCIAMACHY and GOME NSM composites shows up in China where it is more than 2×10^{15} molec/cm^2 for a large area. This large difference clearly indicates a trend in Chinese NO_x emissions and will be discussed in detail below (9.4.4).

9.4. Benefit of the improved spatial resolution: Results

The GOME NSM and SCIAMACHY spatial resolution is a great improvement as compared to GOME SSM. In this section we illustrate the new insight in the tropospheric NO_2 distribution that we gained from the highly resolved satellite data. As SCIAMACHY pixel size is even smaller than that of GOME NSM, and at the same time the amount of data is larger, we mainly show SCIAMACHY results in this section. However, we want to point out the use of the GOME NSM data that serves as a first reference of a high resolved data set of global TVCDs, and we will use the NSM data to discuss the large discrepancies for China.

In the following we consider four regions in detail that show enhanced TVCDs: Europe, North America, the Middle East ad Far East. We furthermore compare the spatial distribution of TVCDs with the location of large cities, that are directly plotted in the TVCD composites. In section 9.5, we also compare our results to the spatial distribution of NO_x sources as given by the EDGAR emission inventory and with satellite images of light pollution during night.

9.4.1. Europe

For Europe, we illustrate the benefit of the higher spatial resolution by directly comparing mean composites of GOME SSM SCIAMACHY (Fig. 9.11). Whereas for the SSM, mainly two centers of enhanced NO_2 TVCDs can be identified (1. from London towards the Ruhr region and 2. the Po valley in northern Italy), SCIAMACHY reveals numerous details. Several large cities (e.g. Moscow, Madrid, Istanbul or London) coincide with strongly enhanced NO_2 TVCDs. However, there are also some megacities (e.g. Berlin, 3 Mio. inhabitants, Germany; Warszawa, 1.6 Mio., Poland; Kyyiv (2.6 Mio., Ukraina) that show comparably low levels of NO_2, while the highest levels of NO_2 are found in the industrial regions of northern Italy (Po Valley) and the Ruhr region.

Compared to other European countries, NO_2 TVCDs over France are (besides Paris) rather low. This is probably due to the use of nuclear energy instead of coal and gas burning power plants.

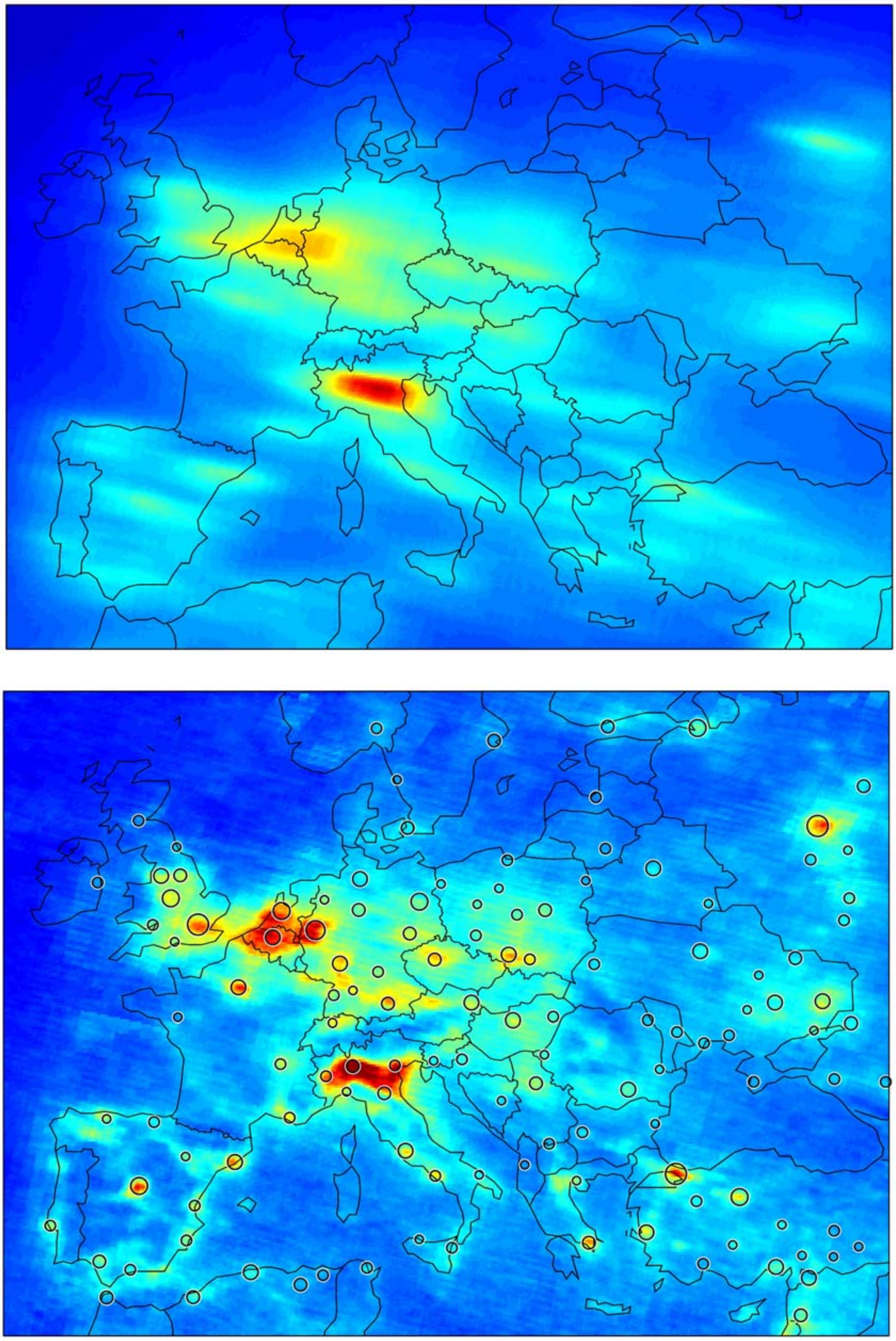

Fig. 9.11. Mean NO_2 TVCD for Europe as derived from GOME SSM data (1996-2001) (above) and SCIAMACHY data (January 2003-June 2004) (below). Colorbar as in Fig. 9.3. For the SCIAMACHY composite also cities with more than 500,000 inhabitants are marked (cities within a 100 km distance are cumulated).

9.4.2. North America

Also in the USA, nearly all major cities can be associated directly to a NO_2-“hot spot” in Fig. 9.12, and vice versa. Between Chicago and New York, a larger (densely populated) region shows enhanced NO_2 levels. However, highest TVCDs of the world are found over Los Angeles (see table 9.2). This region is prone to urban air pollution as ventilation is hindered by mountains. Please note, however, that the “rank” of pollution does also depend on the grid chosen for mapping.

Beside the many spots of urban NO_x plumes, there also is a spot of significantly elevated NO_2 in a remote region (marked white in Fig. 9.12). This enhancement is due to a field of large coal power plants (e.g. “Four Corners” with a capacity of 2 GW, see http://www.srpnet.com/power/stations/fourcorners.asp and http://www.pnm.com/systems/4c.htm). In North Mexico (marked grey) is a NO_2 source associated with coal power plants as well (“Carbon 1/2”, Piedras Negras).

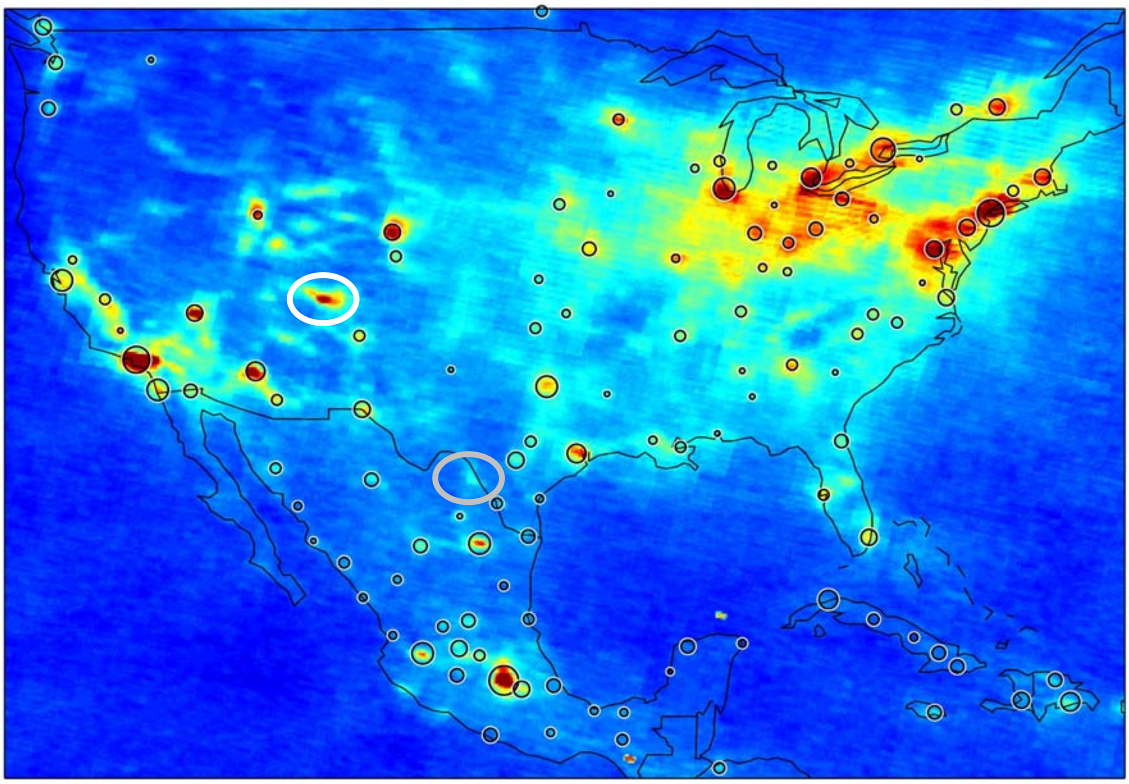

Fig. 9.12: Mean NO_2 TVCD for USA and Mexico as derived from SCIAMACHY (January 2003 - June 2004). Colorscale as in Fig. 9.3. Cities with more than 200,000 inhabitants are indicated by cycles. The marked spot is associated to a large power plant (“Four corners”) with >2 GW power.

9.4.3. Middle East

Main sources of NO_x in the Middle East are the large cities Cairo, Jiddah, Riad, Teheran, Isfahan, Damasque, cities at the Persian Gulf (especially Kuwait, Ad-Dammam, Dubai) and Israel. Besides SCIAMACHY NO_2 TVCDs also clearly reflect the high population density close to the Nile river, in contrast to the rather sparsely populated rest of Egypt. Please note also the line of enhanced NO_2 TVCDs in the Red Sea that is due to emissions by ships (Andreas Richter, personal communication; see also Chapter 11).

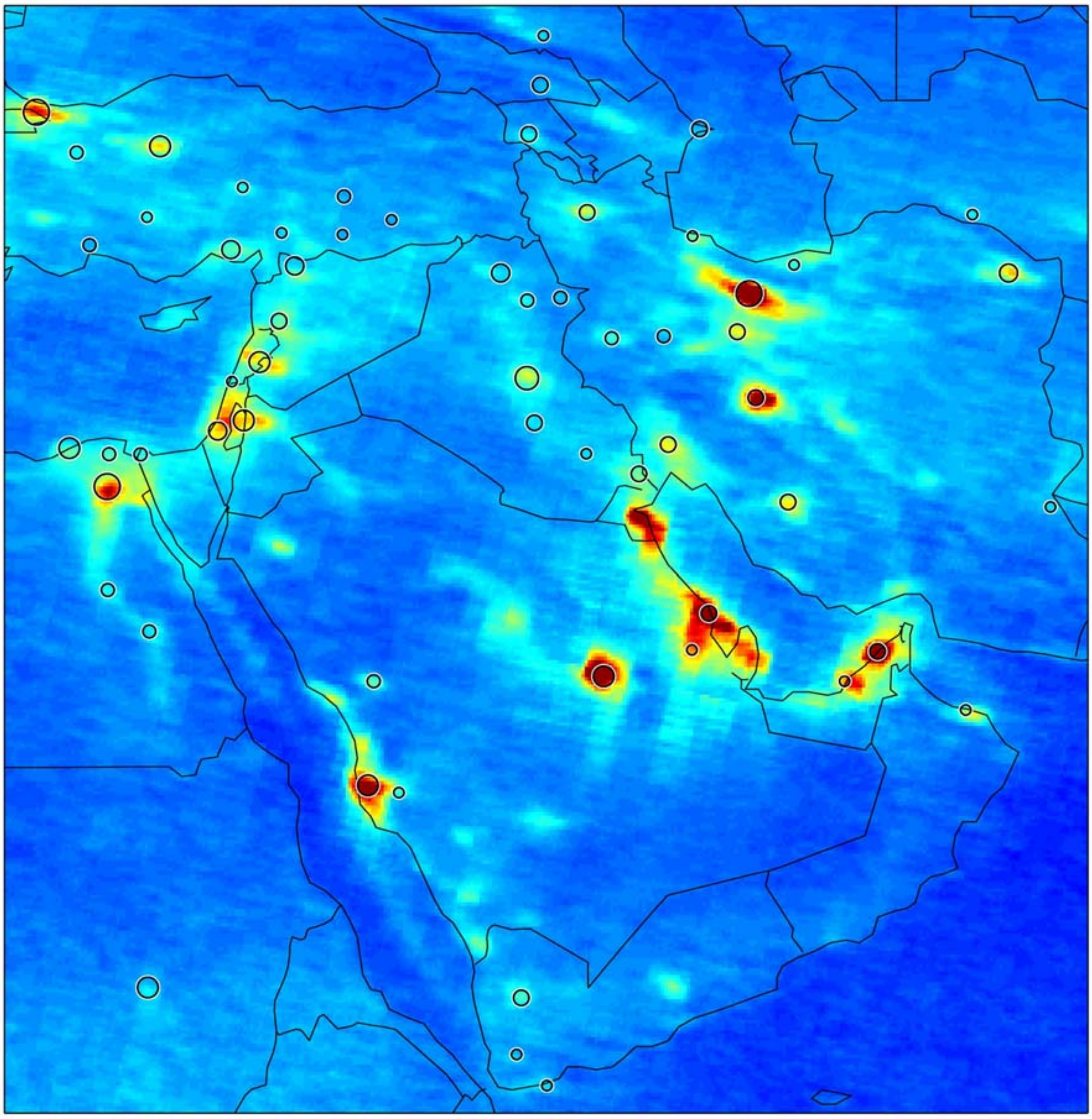

Fig. 9.13: Mean NO_2 TVCD for the Middle East as derived from SCIAMACHY (January 2003 - June 2004). Colorscale as in Fig. 9.3. Cities with more than 500,000 inhabitants are indicated by cycles.

9.4.4. Far East

For China (Fig. 9.14), NSM and SCIAMACHY TVCDs show the highest differences, as discussed earlier in section 9.3.3 (see Fig. 9.10). Therefore we directly compare NSM and SCIA data with a modified colorscale in Fig. 9.15. SCIAMACHY NO_2 TVCDs reaches 7×10^{15} molec/cm^2 for 113.4°E, 35.0°N, i.e. the Chinese Megacity Zhengzhou, where GOME NSM VCDs were lower by a factor of two (see Table 9.2). This large and significant increase of TVCDs over China is not explainable by spatial resolution changes and indicates drastically increased emissions over the last years (see also [A. Richter, 2004c]), going ahead with the current boom of Chinese economy. Furthermore, the direct comparison of the spatial patterns indicate, that there is not only an overall scaling up of emissions, but also a fast growth of former rather moderate industry centers, like for Zhengzhou. Thus, also the patterns of the spatial distribution of NO_x sources is modified, which is an important information for modelling emissions and their impact.

Going along with the Chinese boom, also large amounts of SO_2 are released from coal burning, which can also be seen from GOME/SCIAMACHY data [Khokhar et al., 2004] (Fig. 9.16). Also aerosol burden is highly enhanced in Eastern Chinese (see Fig. 9.17), and SCIAMACHY IR data reveals enhanced levels of CO over the Chinese east coast throughout the year [Frankenberg et al., 2004] (compare Fig. 7.4). Thus the Chinese development causes the same environmental effects seen in Europe and in North America in the fifties through the seventies. It is obvious that the Chinese environment will suffer from the same consequences, i.e. acid rain and smog. As the large sources are located in the East of China, eastward transport following dominant weather in the region will probably also affect the neighbouring countries in the east, i.e. Korea and Japan.

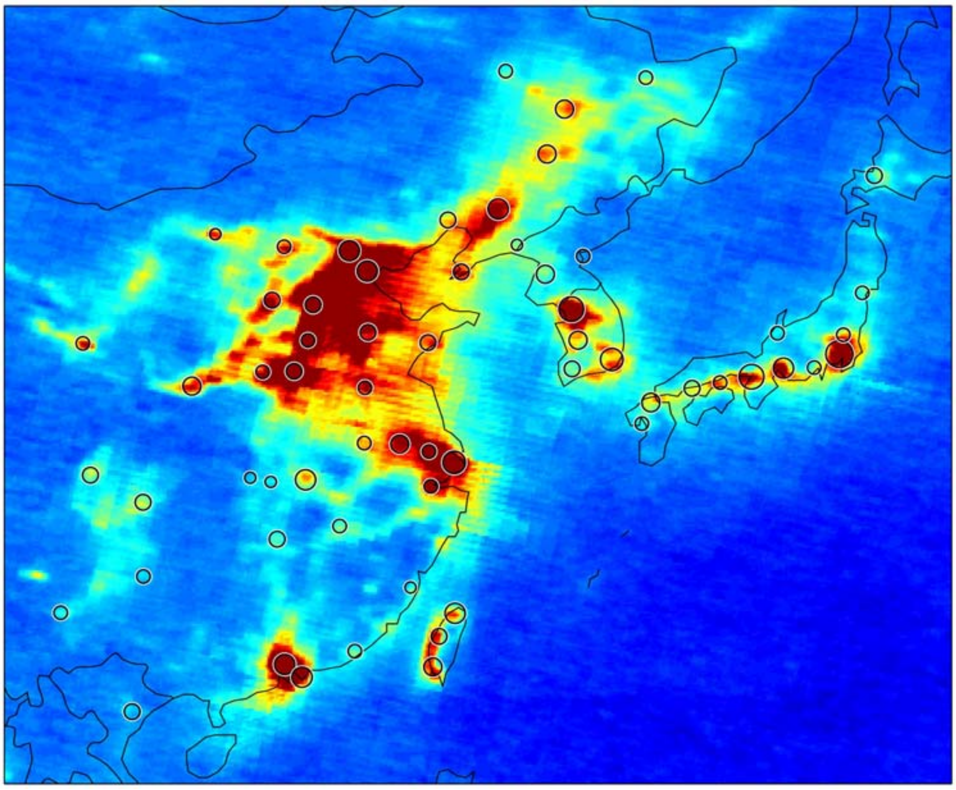

Fig. 9.14: Mean NO_2 TVCD for Far East as derived from SCIAMACHY (January 2003 - June 2004). Colorscale as in Fig. 9.3. Cities with more than 1,000,000 inhabitants are indicated by cycles.

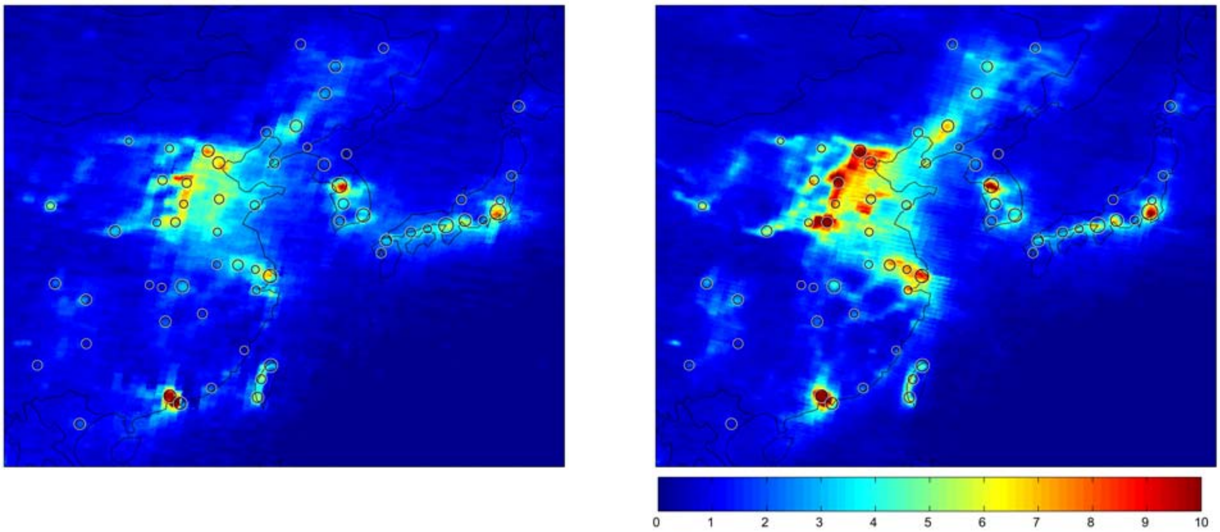

Fig. 9.15: Mean NO_2 TVCD (10^{15} molecules/cm^2) for Far East, as derived from GOME NSM (left) compared to SCIAMACHY (January 2003 - June 2004) (right). Please note that the colorscale is different from the previous plots, because the Chinese NO_2 TVCDs seen from SCIAMACHY are higher than 6×10^{15} molecules/cm^2 for large areas (Fig. 9.14).

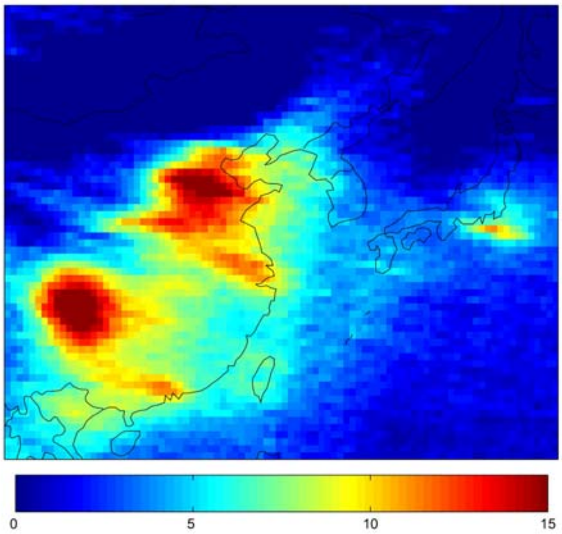

Fig. 9.16: Mean SO_2 SCD (10^{15} molecules/cm^2, background corrected) over China as observed from GOME (1997-2001) [Khokhar et al., 2004].

9.4.5. Extent of NO_2 pollution "hot spots"

Besides large congested areas (like the US eastcoast, the Po valley in Italy, or the Chinese Eastcoast), the "hot spots" of enhanced NO_2 TVCD detected round the globe sharply contrast with the background and have well defined edges. The NO_2 peaks corresponding to large cities have a spatial extent of typically 100 km (see Fig. 9.3 (d)). This low extent indicates that the lifetime of tropospheric NO_x is rather short. In Chapter 10, we will use the extent of the Riad hotspot from the SCIAMACHY composite to estimate the mean lifetime of NO_x for this location to be below 6 hours. The wind conditions may be different for other locations, but the missing signal of significant downwind transport gives an upper limit for the tropospheric lifetime of NO_x of about 12 hours for polluted cities, even for e.g. Moscow at 56°N.

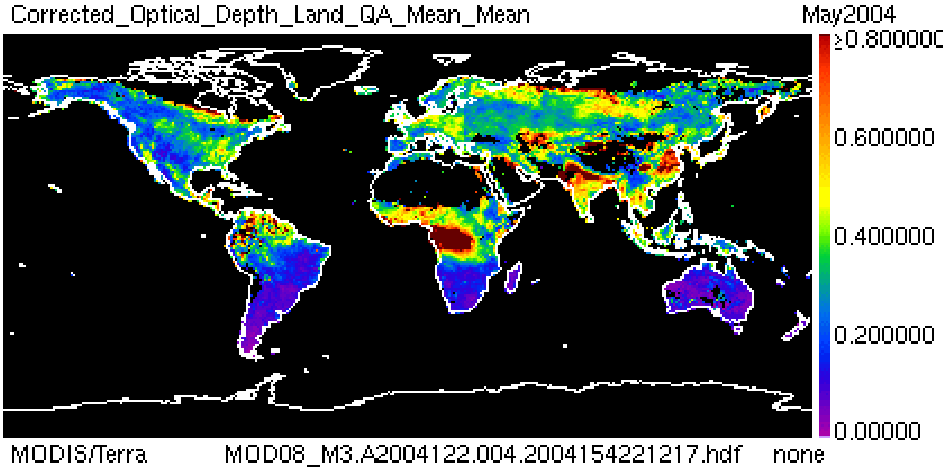

Fig. 9.17: Mean aerosol optical depth for May 2004 as derived from MODIS (figure taken from http://modis-atmos.gsfc.nasa.gov/IMAGES/mod08m_menu.html)

9.5. Comparison of the spatial distribution of SCIAMACHY NO_2 TVCDs with EDGAR and Light pollution

The GOME NSM and SCIAMACHY data provides for the first time a unique global dataset of the tropospheric NO_2 distribution based on measurements. In this section we compare our results on NO_2 distribution to independent, spatially resolved datasets:

- The EDGAR 3 emission inventory [Olivier and Berdowski, 2001] gives global NO_x emissions on a 1°x1° grid. Emissions are estimated for 1995 in a bottom-up approach.
- The Operational Linescan System (OLS), that is part of the Defense Meteorological Satellite Program of the US airforce, provides satellite images of the earth at night [Cinzano et al., 2001] These data hold information on anthropogenic activity; bright spots are a result of lighting of streets and buildings. Thus the light pollution by night is a proxy for population density combined with industrial development. Doll et al. [2000] found a correlation of lighted area and CO_2 emissions of R=0.89. We therefore check how well this independent dataset can be used as proxy for NO_x emissions.

An extensive correlation study of EDGAR and light pollution with NO_2 datasets from GOME (from IUP Heidelberg and IUP Bremen) was performed on global scale by Nicola Toenges-Schuller and Franz Rohrer from the FZ Jülich [Toenges-Schuller et al., 2004]. Here we concentrate on comparisons of the spatial patterns for the different regions of interest, using the high resolved SCIAMACHY dataset.

It is important to note that the EDGAR data and light pollution give the spatial distribution of ***emissions***, whereas the satellite observes the resulting TVCDs *after* dilution and transport processes. Because the lifetime of NO_x in the boundary layer is rather short (see Chapter 10), we expect to find still a good correlation of emission sources and NO_2 TVCDs. However, especially for sources close to the ocean we observe also enhanced TVCDs over sea, where EDGAR NO_x and light pollution are both absent. Cases of high TVCD for low EDGAR NO_x / light pollution are thus generally expected, whereas the other case (a high proxy, but low signal in the TVCD data) is probably of interest.

For the correlation studies, we adjust the datasets of NO_2 TVCDs (0.1°) and light pollution (0.025°) to EDGAR resolution (1°).

Figs. 9.18-9.21 show the comparison of the three datasets. Subplots (a)-(c) show the spatial distribution, the scatter-plots (d) and (e) indicate the correlation of the datasets. We also label some specific points that show large deviations.

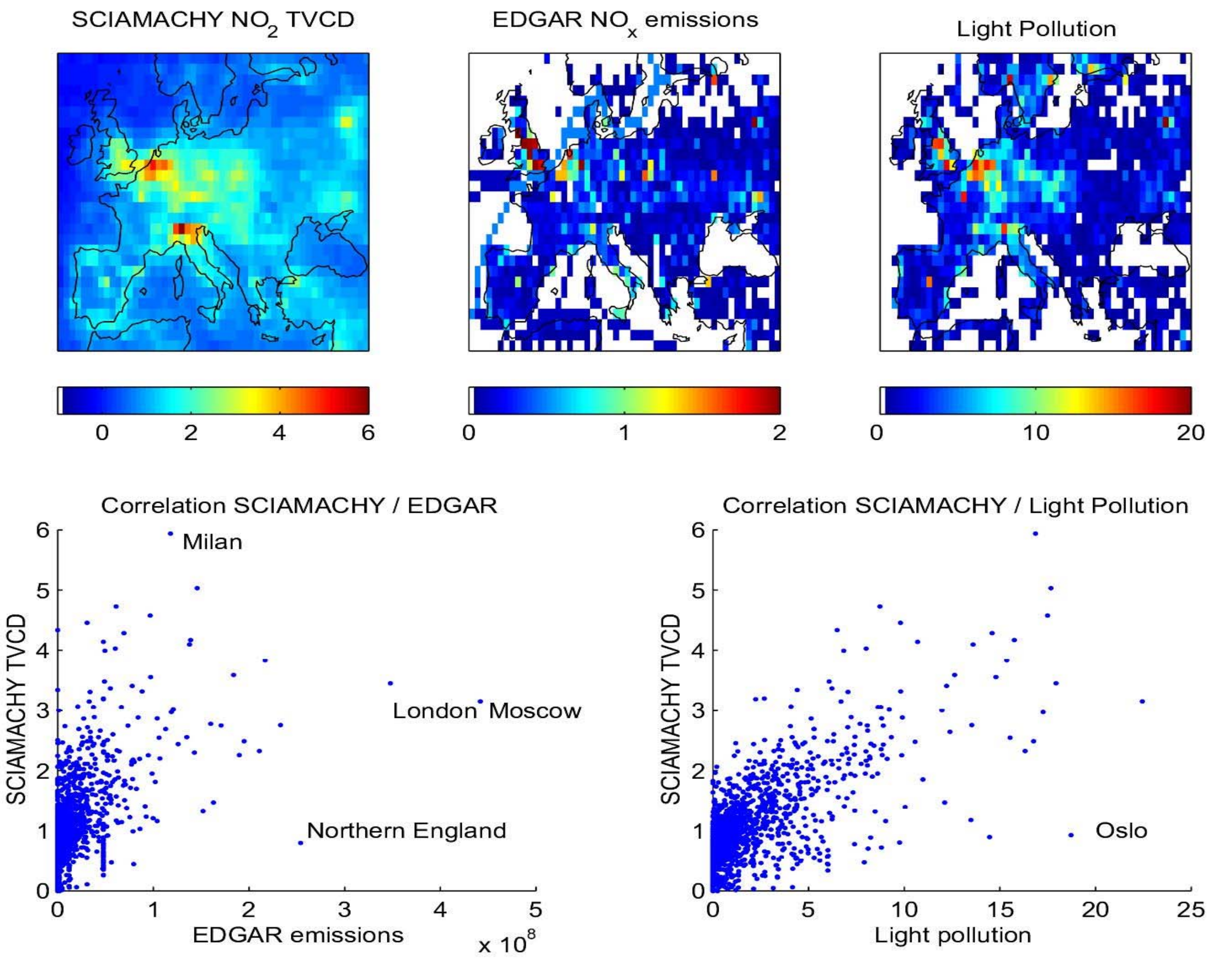

Fig. 9.18: Comparison of (a) the SCIAMACHY TVCD distributions [10^{15} molec/cm^2], (b) the EDGAR NO_x emission inventory [10^8 kg NO_x per year and pixel (1°×1°)] and (c) light pollution by night [artificial units] as observed from satellite, for Europe. Subplots (d) and (e) show correlation scatter plots of NO_2 TVCDs with EDGAR and light pollution, respectively.

9.5.1. EDGAR

EDGAR seems to considerably overestimate NO_x emissions for some spots. For the US (Fig. 9.19), New York has strongest EDGAR sources and highest NO_2 TVCDs, but the SCIAMACHY composite shows other pixels in the west (Detroit, Chicago) of similar high TVCD, but a factor 4 less NO_x emissions. On the other hand, the second strongest EDGAR source (Houston) shows only moderate enhanced NO_2 VCDs. A very striking deviation was found for the EDGAR source at 35°N, 102°W, that is the fourth largest EDGAR value for North America (categorized as F10, industrial sector). Here no large city is found, and measured NO_2 TVCDs (as well as light pollution) are rather low. A similar deviation can be found for Europe (Fig. 9.18), where the 3rd strongest EDGAR source is in Northwest England, but NO_2 TVCDs are quite low. On the other hand, the highest NO_2 TVCDs are found for Milan, where EDGAR emissions are rather low.

Another interesting region is the industrial region at Chengdu and Chongqing in central china (~30°N, 105°E), where EDGAR NO_x emissions are rather high (Fig. 9.20). Here also SO_2 SCDs show strong enhancements (compare Fig. 9.16). But NO_2 TVCDs are only slightly enhanced for these regions (as CO VCDs (compare Fig. 7.4). Overall, we find correlations of EDGAR NO_x and SCIAMACHY NO_2 TVCDs of about R=0.5-0.6.

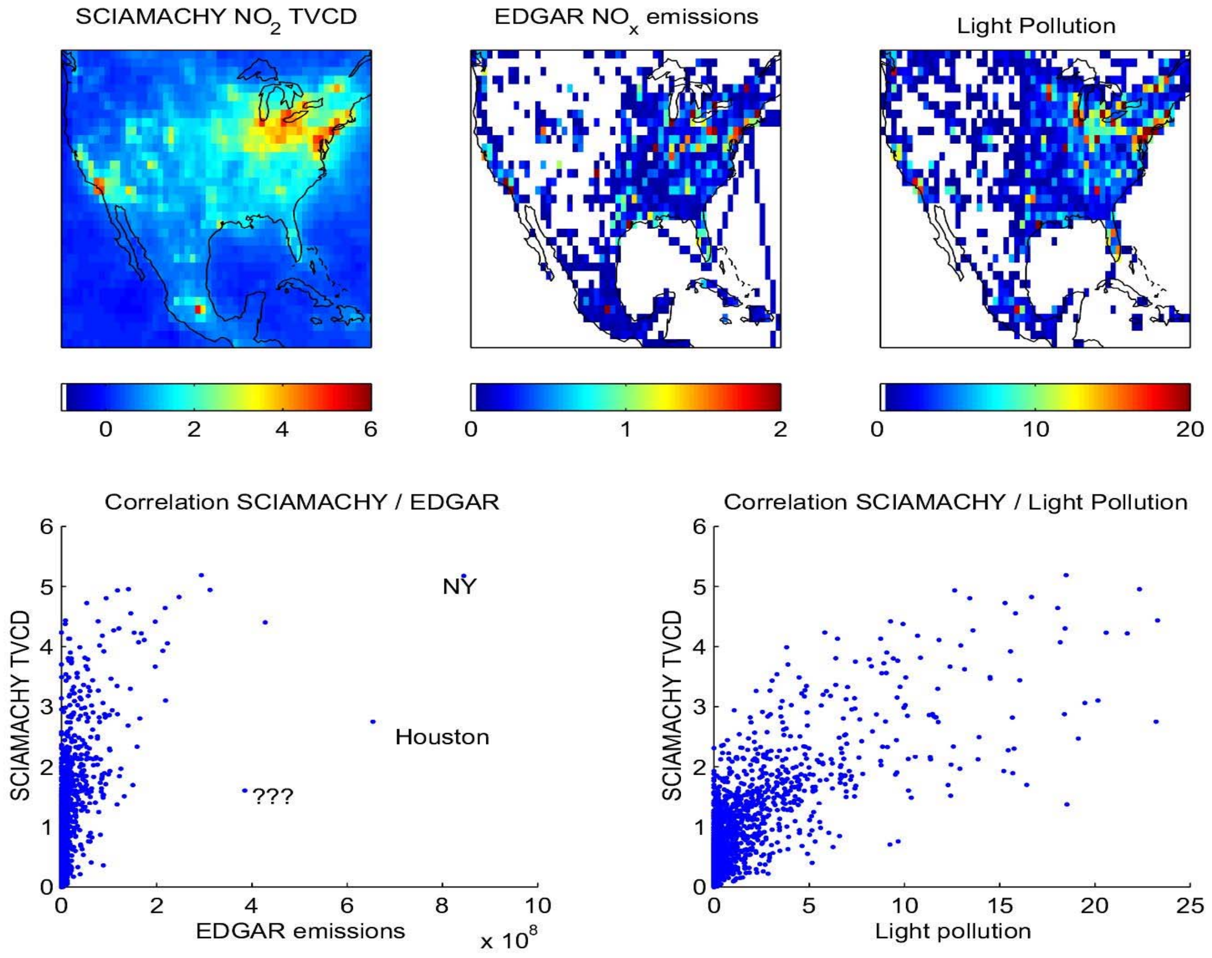

Fig. 9.19: As Fig. 9.18, but for USA/Mexico.

9.5.2. Light pollution

The light pollution dataset shows generally a much better correlation (R~0.7) with SCIAMACHY TVCDs than the EDGAR data. In particular, only few cases of high NO_2 TVCD (>3x10^{15} molec/cm^2) at missing light pollution occur - in opposite to EDGAR, that gives zero emissions for several cases with such high NO_2 TVCDs. Also the opposite case, i.e. high light pollution at low NO_2, is not as frequent as for EDGAR, but occurs e.g. for Oslo (Fig. 9.19) that is bright at night without showing high NO_2 TVCDs. This is probably due to the high ground albedo for snow cover in winter.

The zoom on western Europe (Fig. 9.21) clearly illustrates that the light pollution gives a more realistic proxy for the actual spatial distribution of sources than EDGAR: Whereas EDGAR is dominated by the pixels containing London, Rotterdam and the Ruhr Area, and shows a distinct minimum in between, the distribution of light pollution shows a smoother pattern from the Ruhr Area towards the North Sea. The light pollution and SCIAMACHY NO_2 TVCDs over Western Europe show approximately a linear correlation with R=0.82.

For far east (Fig. 9.20), the correlation of lights and TVCDs is worst on first view (R=0.47). However, this is due to the fact that China is rather dark at night (or at least was in 1996/1997 when the light pollution was measured), whereas the large cities in South Korea and Japan are rather bright. By looking at China (red dots) and Korea/Japan separately, we find two separate regimes that both show a good correlation (R=0.73).

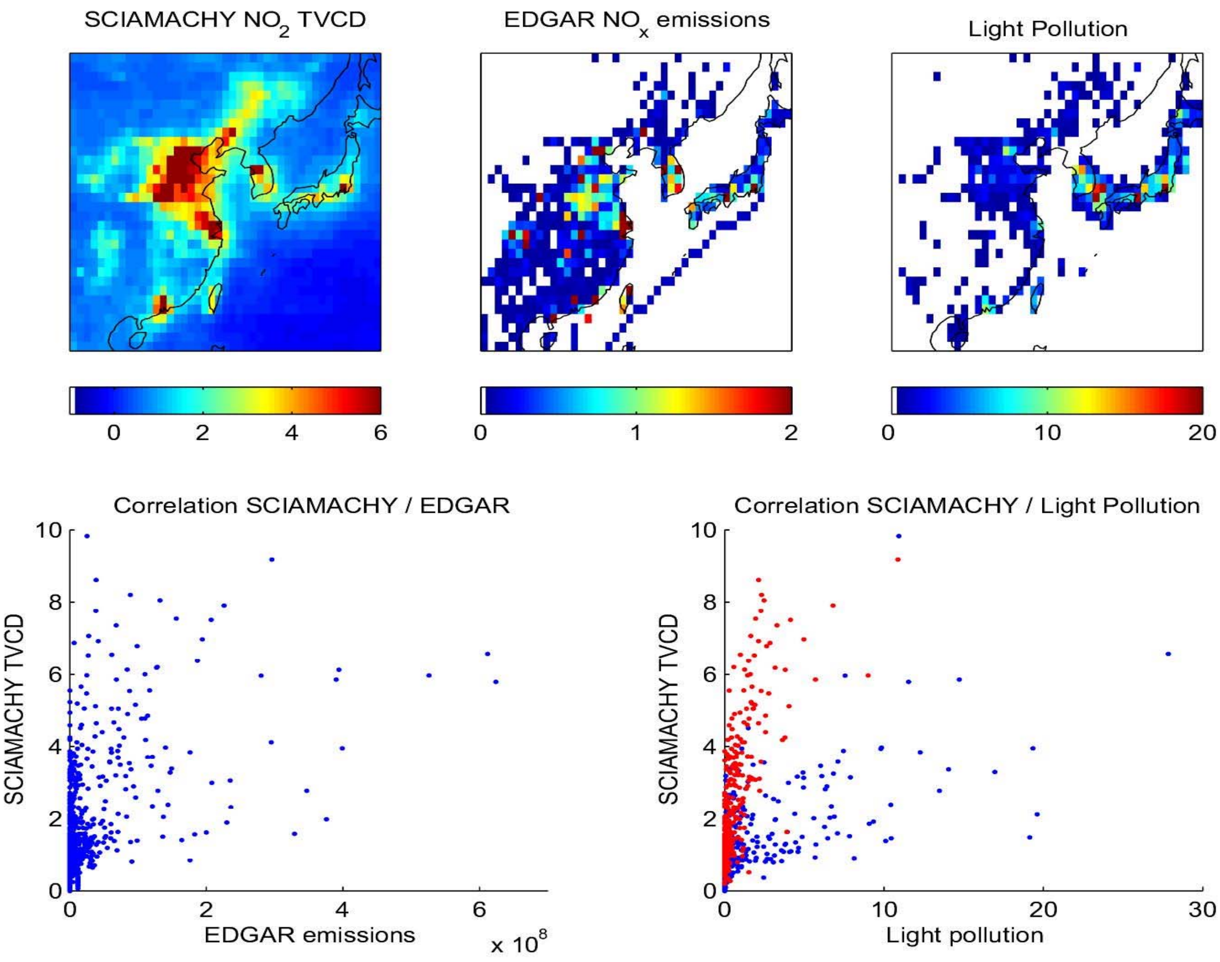

Fig. 9.20: As Fig. 9.18, but for Far east.

Of course, for a detailed comparison of these datasets also other factors have to be kept in mind: the dilution of emissions depend on wind distribution and the NO_x lifetime, and the visibility of tropospheric NO_2 is influenced by ground albedo, trace gas profile, aerosols and clouds. All these parameters differ from place to place and thus could possibly cause differences of the observed distributions. Nevertheless, the high resolved satellite data of NO_2 TVCDs obviously holds valuable spatial information. For the first time, emission inventories can be checked by measurement data on a global scale. The new insight into the spatial distribution of NO_2 as derived from GOME NSM and SCIAMACHY opens new questions on the location and type of different sources. The results from satellite retrieved NO_2 has the potential to find inconsistencies in current knowledge and will hopefully help to improve emission inventories.

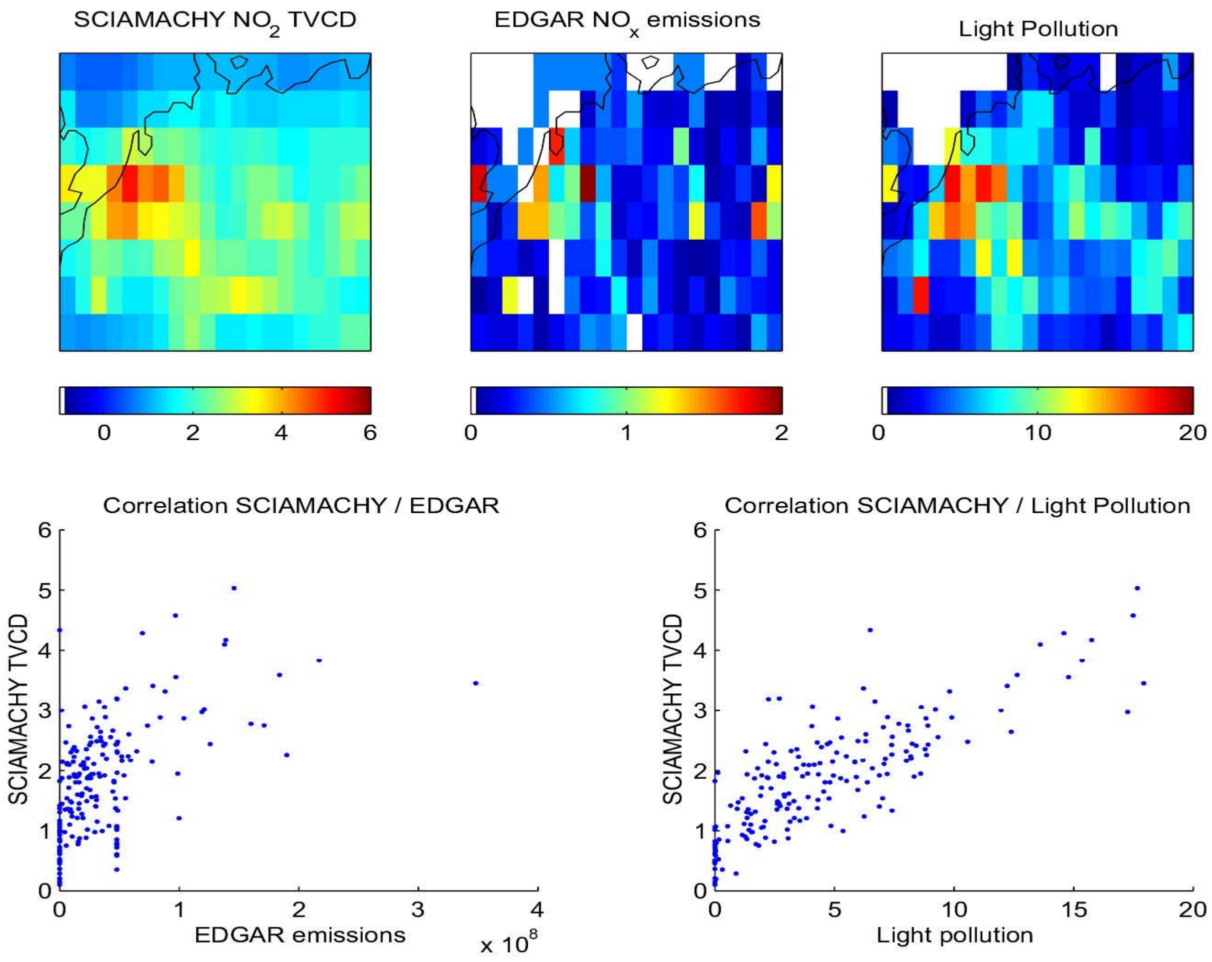

Fig. 9.21: As Fig. 9.18, but for Germany.

Chapter 10
Estimating the NO_x lifetime from satellite data

10.1. Current knowledge of the NO_x lifetime

The lifetime τ of NO_x is a very important parameter for tropospheric chemistry in general, and for the interpretation of satellite based TVCDs of NO_2 in particular. Firstly, τ directly determines OPE, which is inversely proportional to the loss of NO_x (see eq. 1.3). Secondly, it controls the area affected by NO_x emissions via transport. Thirdly, a lifetime information is essential for the conversion of TVCDs to actual emissions, as more NO_x accumulates for longer lifetimes.

Due to high variability of the factors controlling the lifetime of NO_x, i.e. meteorology, chemical composition and actinic flux, τ is itself highly variable. Mean values are of the order of hours for the lower troposphere up to days for the upper troposphere.

A common way to "measure" the lifetime of NO_x is to follow the plume of a strong source (as a coal power plant), e.g. by aircraft transsects, and to measure the NO_x depletion with distance to derive τ. Table 1 shows the results of some measurements of this kind. The conditions were quite similar for all of these measurements: polluted air was analyzed during daytime in the US in summertime, and most of them were taken in the course of the Southern Oxidants Study in Nashville/Tennessee. The measurements all correspond in a rather short lifetime of NO_x of several hours. These kind of measurements are restricted to few days for only some sites around the globe.

Apart from direct measurements of NO_x, the deposition rates of HNO_3 (that are measured at several ground stations around the globe) also allow the estimation of the order of the NO_x lifetime on a more global scale [Levy et al., 1999]. However, in this case the derived depletion rates are the combined NO_x and HNO_3 removal rates and not just the NO_x removal rate alone.

Table 10.1: Estimates of $\tau(NO_x)$ (in hours) from measurements

Study	Estimated lifetime NO_x	NO_y (mostly HNO3)	Site
Spicer [1982]	**5.5 (4.2-7.1)**		Boston (urban plume)
John et al. [1998]		**8**	Nashville (Power plant plume)
Ryerson et al. [1998]	**2.5 - 3.7**		Nashville (Power plant plume)
Gillani et al. [1998]		**8.3**	Nashville (Power plant plume)
Nunnermacker et al. [2000]	**2.0 - 4.2**	**7.0 - 8.7**	Nashville (Power plant plume)

Information on the NO_x lifetime can also be retrieved from output of chemistry transport models (CTMs). Table 10.2 lists some published results of different models for different conditions.

The general limitations of models arise from uncertainties in emissions as well as boundary- and initial conditions. Furthermore, there are still unanswered questions concerning the detailed modelling of tropospheric chemistry (i.e. for the night-time removal of NO_x or modelling other OH sources than ozone photolysis). Another important factor is the temporal and spatial resolution, as the NO_x chemistry is highly nonlinear. Davis et al. [2001] pointed out the importance of in-plume processes (for ship plumes) on the NO_x lifetime. Due to the released mixture of NO_x and VOCs, ozone production commences, resulting in higher [OH] levels; due to the emissions higher $[NO_3]$ and $[N_2O_5]$ also occur. The implications on τ are significantly underestimated if the emissions are instantaneously spread out homogeneously over one grid cell of several hundred square kilometers. In the studies of von Glasow et al. [2003] and Song et al. [2003], these effects are accounted for, and the resulting daytime lifetimes are significantly reduced.

The model used by Levy II et al. [1999] gives higher numbers for the mean lifetime of NO_x of about 1 hour throughout the lower troposphere. Both Martin et al. [2003] and Levy et al. [1999] state τ to be longer than two days for polar regions.

Table 10.2: Estimates of $\tau(NO_x)$ (in hours) from models

Study	Model	Estimated lifetime NO_x	Site / Conditions
Levy et al. [1999]	global CTM	**18-24**	tropics, summer midlatitudes
		>48	for latitudes>70°
Martin et al. [2003]	GEOS-CHEM	**3-10**	
		30	winter, 60°N
Song et al. [2003]		**2-5**	daytime, ship plume, tropics
		10-20	nighttime
von Glasow [2003]		**5-10**	daytime, ship plume, tropics
		15	nighttime

Please note that the values of τ measured at daytime (Table 10.1) as well as the very short lifetimes from Song et al. [2003] and von Glasow et al. [2003] are instantaneous lifetimes (or daytime means), whereas daily mean lifetimes, i.e. 24 hours means, are lower (see also the discussion below and Appendix B).

It has been demonstrated by Leue et al. [2001], that GOME data can be used to estimate τ. This is a valuable, independent information to the few in-situ measurements as well as to model results. In this chapter, we discuss two different methods of lifetime estimations using GOME/SCIAMACHY data (sections 10.3 and 10.4).

However, the daily cycle of the lifetime of NO_x and NO_x emissions are highly relevant for these estimations; hence, we first discuss this in 10.2.

10.2 Temporal variations of emissions and lifetime

10.2.1 Connection of lifetime, emissions and TVCDs

The TVCDs of NO_x, here called V, are determined by the balance of production, i.e. emissions E, and loss reactions as discussed in Chapter 1. We assume the loss of NO_x to be of first order, i.e. it can be described by the rate constant k:

(10.1) $dV/dt=-kV+E$

In the simple case of a constant source E and constant loss, this differential equation has the simple steady state solution

(10.2) $V(t)=V=E/k=ET$.

Here T=1/k is the mean lifetime of NO_x (see Appendix B).

Eq. 2 is used to derive the emissions E out of measured TVCDs [Leue et al., 2001]. However, reality does usually not provide such constant conditions. Emissions are usually time dependent, and variations of k (and thus τ) also occur on different time scales: for different seasons, general meteorological conditions and actinic flux are different, and day to day values also change due to natural fluctuations. However, the most distinct variation is the daily cycle of τ. We begin our analysis of effects of temporal variations with considering the impact of this daily cycle on TVCDs that are always measured for the same time of day for sun-synchronous satellites like GOME.

In the following, we distinguish the *instantaneous* lifetime $\tau(t):=1/k(t)$ and the *mean* lifetime T, that is the harmonic mean of τ(t) (see Appendix B).

10.2.2 Daily cycle of τ

The instantaneous lifetime of NO_x has a strong daily cycle. As an example we show a typical daily cycle of k(t) in Fig. 10.1a and $\tau(t)=1/k(t)$ in Fig. 10.1b [von Glasow, personal communication]. These values result from model calculations for polluted tropical marine conditions, i.e. a ship plume. For this daily cycle, the mean lifetime T is 9.6 hours. For other sites and conditions, numbers differ, but the general characteristics are similar.

The nighttime loss of NO_x is rather constant. In contrast, daily values for τ (t) show a strong cycle with a minimum at noon, where OH concentrations are highest due to the maximum in actinic flux. At dawn, lifetimes are very large; the reason for this is photolysis being too weak to produce OH, but too strong to allow formation of NO_3 and N_2O_5.

10.2.3 Daily cycle of TVCDs

In this section we will discuss the effect of the daily cycle of τ on the daily cycle of NO_x. For the realistic case of a time dependent rate constant k(t) and emissions E(t), eq. (10.1) has to be modified:

(10.3) $dV(t)/dt=-k(t)xV(t)+E(t)$

The particular solution for this differential equation is more complex [Bronstein, 1971]:

(10.4) $$V(t)=e^{-\int k(t')dt'}\cdot\int E(t'')\cdot e^{\int k(t')dt'}dt''$$

Please note that this is generally not the same as E/K given in eq. 10.2! Thus it is remarkable that the mean lifetime (as defined in (B.8), see Appendix B), is not automatically applicable to convert the measured VCD into emissions. The time of day when the measurement takes place plays a crucial role as a consequence of the strong daily cycle of τ illustrated in Fig 10.1b. Concerning estimations of τ from GOME/SCIAMACHY data, the relevant time of day is the ERS-2/ENVISAT overpass time, i.e.

(10.5) t_{GOME}:=10:30 (local time).

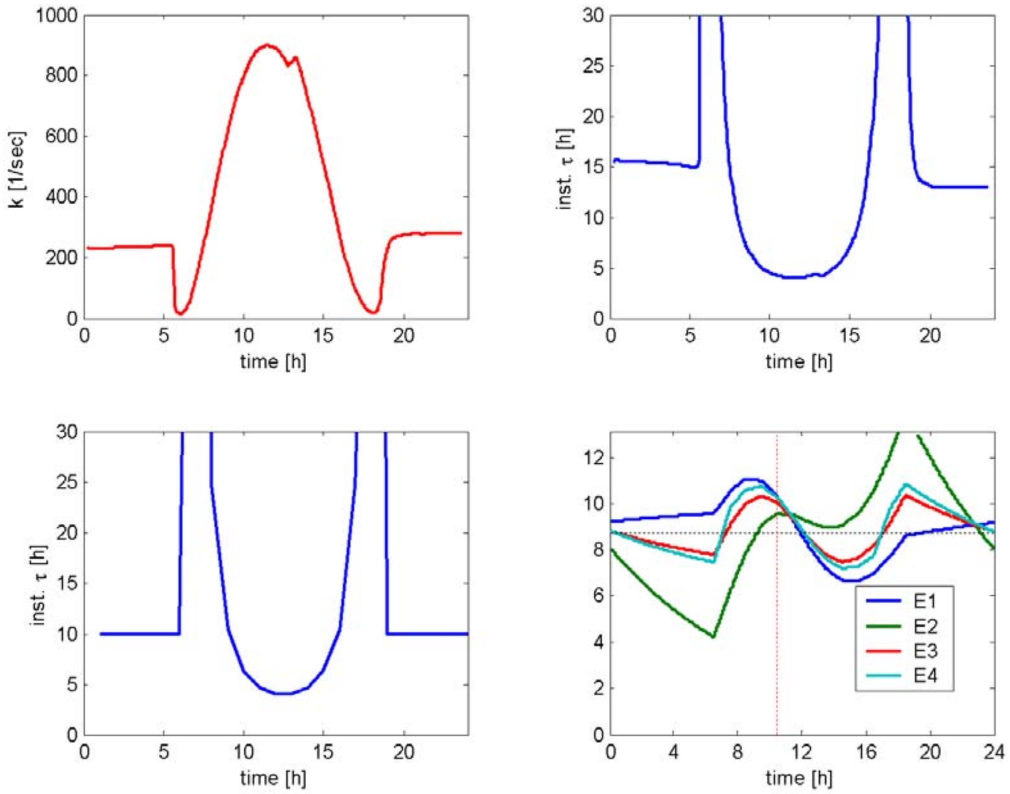

Fig. 10.1: a) Daily cycle of rate constant k for a ship plume [von Glasow, personal communication]

b) Daily cycle of instantaneous lifetime $\tau(t)=1/k(t)$

c) Daily cycle of $\tau(t)$ *parameterized by* $\tau_{night}=10h$, $\tau_{min}=4h$, *and 12 hours length of day.*

d) Daily cycle of TVCDs (artificial units) modelled for τ *(t) from (c) for different emission scenarios (see Table 10.3)*

To estimate the impact of varying emissions and instantaneous lifetime on V(t), we solve (eq. 10.4) numerically. As input we consider

a) a set of 4 simplified scenarios for the daily cycle E(t) of emissions. These are listed in Table 10.3.

b) a daily cycle of $\tau(t)$ parameterized by three parameters: τ_{night}, τ_{noon} and duration of night. During night, $\tau(t)$ is set to τ_{night}. For daytime, $\tau(t)$ is determined by assuming a cosine function for k(t) centered at noon, with $k_{max}=1/\tau_{noon}$. Fig. 1c shows the modelled daily cycle $\tau(t)$ exemplarily for τ_{night}=10 hours, τ_{noon}=4 hours and duration of night being 12 hours.

Table 10.3: Set of emission scenarios used. All emissions have the same daily mean of 1 (artificial unit)

Emission scenario	Characteristics	
E1	$E(t)=1$	
E2	$E(t_{night})=0$	$E(t_{day})=2$
E3	$E(t_{night})=2/3$	$E(t_{day})=4/3$
E4	As E3, but with additional peaks at 7am and 4pm (lasting one hour each with doubled daytime emissions), simulating rush hour	

We illustrate the resulting function V(t) exemplarily in Fig. 10.1d, choosing $\tau(t)$ from Fig. 10.1c. As all emission scenarios are unity on average, eq. 10.2 suggests V to fit the mean lifetime T that is 8.8 (black dotted line). The red line indicates the ERS-2 overpass time t_{GOME}. V(t) in general depends strongly on the daily cycles $\tau(t)$ and E(t), whereas $V(t=t_{GOME})$ does surprisingly not: for $t=t_{GOME}$, the deviation between V(t) and $E(t)\times\tau(t)$ is less than 20%. However, as far as the general patterns of our assumed cycles of τ and E are correct, $V(t_{GOME})$ is systematically higher than ET (the results for other daily cycles $\tau(t)$ are quite similar):

(10.6) $\qquad V \sim= 1.1\ ET$

This is a result of the longer lifetime during night and at dawn. A contrary effect could occur for deviations of $\tau(t)$, e.g. for high OH concentrations (thus short instantaneous lifetimes) in morning time due to photolysis of HONO, that takes place in urban polluted air [Platt et al., 1980; Alicke, 2000].

Deviations may be higher for some extreme scenarios, especially for emissions that are very inhomogeneous in time, i.e. occuring shortly before or after the GOME overpass.

Furthermore, the daily cycle of V(t) plays an essential part for comparing results from GOME/SCIAMACHY with OMI, as the AURA overpass time is at about 1:30 pm. Thus combining results from GOME/SCIAMACHY and OMI measurements holds information on the daily cycle of emissions and/or lifetime.

In the following sections we use different approaches to estimate the mean lifetime using GOME data:

In section 10.3, we analyze the decay of NO_2 VCDs downwind from strong sources, that directly reflects τ. In section 10.4, we consider the weekly cycle of NO_2 in industrialized regions that holds also a lifetime information: The Monday levels of NO_2 are lower than those of the other working days, because if the lifetime is long enough they are influenced by the low Sunday emissions.

In both cases, we discuss the influence of temporal variations on our method.

10.3 Lifetime estimation 1: Fitting the exponential downwind decay

10.3.1 The exponential fit method

A common method to determine the lifetime of NO_x (or other trace gases) is to trace the plume evolution, and to fit the nearly exponential decay (for a pseudo first-order loss as in (eq. 10.1)). In detail, the measurement gives the amount of NO_2, e.g. in form of a TVCD V for satellite measurements, as function of distance from the source:

(10.7) $\qquad V(x)=V_0 \exp(x/x_0)$

This can be transformed to a function of time if wind speed is known:

(10.8) $\qquad V(t)=V_0 \exp(t/\tau)$

The e-folding distance x_0 (i.e. the distance where V is reduced to the e^{th} part) is linked to the e-folding time τ (i.e. the lifetime of NO_x) via

(10.9) $\qquad \tau = x_0 / v,$

with the wind speed v.

In the following, we call this the “exponential fit method” and abbreviate it as EFM.

Leue et al. [2001] has demonstrated the potential of the EFM to derive a lifetime information from GOME NO_2 data. In this section we discuss the applicability of the EFM for GOME data. In section 10.3.5 some case studies are presented. Firstly, we will analyze the underlying assumptions of the EFM more in detail; in particular, we will study the effect of temporal variations of both v and τ in some sensitivity studies. From this we learn under which conditions the EFM can be correctly applied.

10.3.2 Performance of the EFM for time dependent winds, emissions and lifetime

The EFM makes use of the depletion of V(x) in downwind direction. Thus of course one basic requirement is the presence of wind (for v=0 eq. (10.9) is singular!) In the following we discuss further constraints of the EFM. Eq. is a simplification as it is based on constant lifetime and wind speed. In this section we perform some sensitivity studies on time dependencies of wind, lifetime and emissions.

The basic idea is to model a spatial distribution V(x) for given wind and lifetime functions. Afterwards, an exponential fit is applied, and the resulting value of τ_{est} is compared to the assumptions. For these sensitivity studies, we use a simple 1d-model with 10km resolution. A constant source (Gaussian with 30km FWHM) is assumed, and transport is realised by shifting the NO_2 distribution to the east/west, depending on v. In every time step the NO_2 content of every box is reduced by exp(-dt/τ). Thus the model determines a NO_2 distribution V(x) for the input parameters $\tau_{input}(t)$ and v(t). Optionally, V(x) is convolved with a box function simulating the GOME/SCIAMACHY measurement. Afterwards, we apply the EFM, i.e. we fit an exponential decay (resulting in a best matching 1/e length) to the modelled distribution V(x), giving us τ_{est}, that is compared to the assumed lifetime τ_{input}. The results using either GOME or SCIAMACHY resolution do not differ much. However, a large error would be introduced if the convolution would be omitted in the exponential fitting routine; therefore the exponential function has to be convolved prior to fitting with the same resolution as the model data.

10.3.2.1. Impact of varying wind

Even for regions with a predominant wind direction, conditions change due to natural fluctuations as well as daily and seasonal cycles of meteorology. In this section we analyze fluctuations of wind speeds on three different time scales:

- Seasonal variations: meteorological conditions are totally different between e.g. summer and winter. Thus wind speeds and directions might change.
- Daily variations: especially for regions close to sea, day and night wind directions are often opposite.
- Day to day variations: due to natural variability, variations also occur from day to day.

Although these three cases are idealized assumptions, we can learn the general effects of changing winds on the exponential lifetime fit method. Fluctuations on a time scale shorter than one hour lead to mixing of air masses, resulting in a smoothing of the NO_2 distribution rather than effective transport, and thus have a negligible effect on the EFM.

10.3.2.1.1. Seasonal variations

As the general existence of wind with a predominant direction is a prerequisite for applying the EFM, we assume the mean wind speed v_{mean} to be 5 m/s. The actual wind speed shall be different for two seasons, "v_{summer}" and "v_{winter}", where v_{winter}=10 m/s - v_{summer}. I.e. v(t) is constant during one half of the year and switches to another constant value (resulting in 5 m/s as mean v) for the second half. Please note that this is a rather extreme modeling; a more realistic seasonal cycle (with a sine shape rather than a step function) results in weaker effects on the EFM.

We have modelled the yearly mean NO_2 distribution V(x) for this wind field for a set of constant lifetimes τ_{input} and performed an exponential fit afterwards. Fig. 10.2 shows the resulting (estimated) lifetime τ_{est} in dependency of v_{summer}. The modelled distribution V(x) is displayed in Fig. 10.3 together with the EFM result for some examples discussed below.

For $v_{summer}=v_{winter}=5$m/s, the fit works well (Fig. 10.3a) and reconstructs the input lifetimes satisfactorily. However, τ_{est} does not exactly match τ_{input}; this is mainly due to the fact that for the modelling of V(x) we assume an extended source (Gaussian with s=30 km), whereas the fit searches for one specific exponential decay curve, implicitly assuming a point source. The discrepancy is minimized by convolving the fitted curve with the Gaussian source distribution. Further factors are the time discretisation of our simple model and the fact that the fit is only applied downwind, i.e. not west from the source maximum.

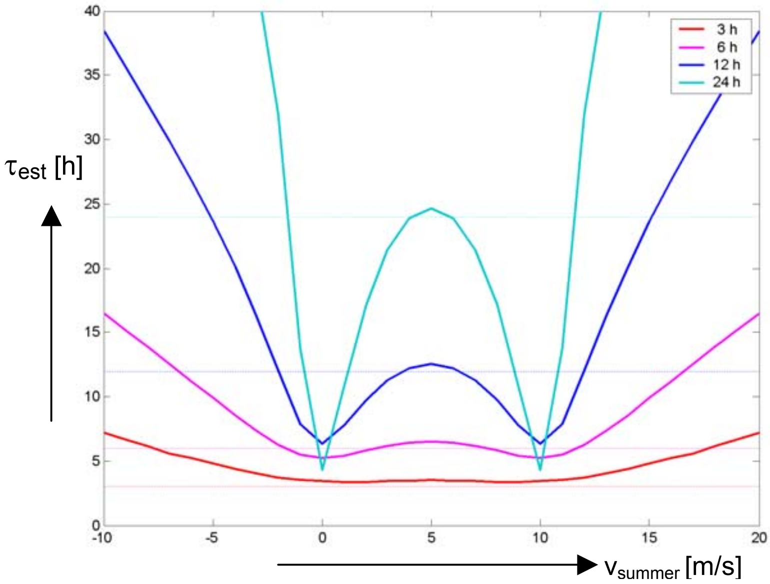

Fig. 10.2: Effect of seasonal variations of v: Resulting mean lifetime τ_{est} from EFM for a set of input lifetimes, depending on v_{summer}. Winter wind speed is 10 m/s - v_{summer} so that mean windspeed is fixed to 5 m/s.

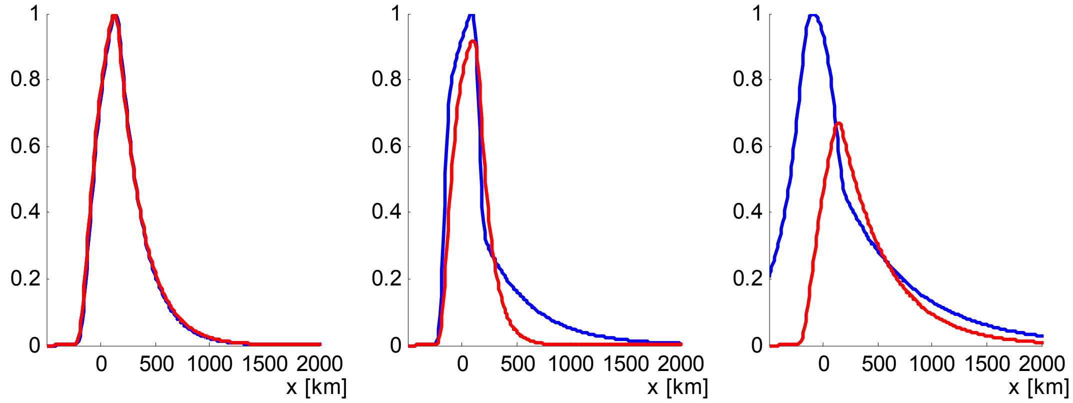

Fig. 10.3: Examples of modelled (blue) and EFM fitted (red) spatial distribution V(x) (normalized to max(V)=1) for τ_{input}=12 h and
a) $v_{summer}=v_{winter}=5$ m/s, b) $v_{summer}=10$ m/s, c) $v_{summer}=15$ m/s

For higher summer wind speeds, i.e. increasing differences between v_{summer} and v_{winter}, the fit more and more underestimates the input lifetime. This can be understood by looking at the extreme case of v_{summer}=10m/s, i.e. v_{winter}=0 (Fig. 10.3b). In this scenario, the down wind decay is determined only by the transport in summer. In winter, pollution accumulates at the position of the source. Thus the maximum of the resulting NO_2 distribution is enhanced, and the fit finds an e-folding distance x_0 which is too short, thus a τ_{est} which is too short (see eq. 10.9).

For summer wind speeds above 10 m/s, v_{winter} becomes negative. Consequently, emissions are not cumulated any more at the source, but are transported westwards and are thus not considered for the fit. Hence the resulting NO_2 distribution is close to that from summer, resulting in a high fitted x0, i.e. a lifetime which is too high (Fig. 10.3c).

Especially for lifetimes longer than 12 hours, τ_{est} is too low even for rather moderate wind variations (e.g. for τ_{input}=24 h, v_{summer}=2 m/s, v_{winter}=8 m/s, τ_{est} is underestimated by 30%). However, such problems can be avoided by using seasonal means instead of yearly averages for the EFM.

Please note that the curves in Fig. 10.2 are symmetric to v_{summer}=5m/s, as there is no principal difference between the artificially defined seasons “summer” and “winter” in the model.

10.3.2.1.2 Daily variations

To analyze daily variations we have applied the same procedure as for seasonal variations, but wind is switched between the two values v_{day} and v_{night} every 12 hours now. The results are displayed in Fig. 10.4.

Please note that there is a principal difference for the daily time scale compared to seasonal variations, as GOME (and SCIAMACHY) measurements are always taken at 10:30 local time. I.e. every measurement is taken for daytime wind conditions. This was accounted for in our simulations. As a consequence, Fig. 10.4 is not symmetric any more.

For short lifetimes (t_{input}<=6h) and v_{day}<0, the fit finds lifetimes close to zero. This can be understood as follow: For negative daytime winds, nighttime wind speeds are high (v_{night}>10 m/s), resulting in transport of the NO_2 plume towards east. However, during the four hours of daytime wind no further NO_2 is transported eastwards, and the NO_2 east from the source is quickly removed due to the short lifetime. Thus there is almost no NO_x east from the source, and the fit finds zero lifetimes (Fig. 10.5a). On the other hand, τ_{est} is overestimated for longer lifetimes (Fig. 10.5b), since the lifetime is sufficient to leave over enough NO_x from the transport at night. For high positive daytime winds, τ_{est} is generally overestimated, as the fit mainly “sees” the transport at day. Generally, moderate daily variations of v are of minor importance if τ >12 hours.

10.3.2.1.3. Day to day variations

To model day to day fluctuations of wind speed, we have calculated the mean NO_2 distribution for a year for v_{day} varying from day to day, but being constant within the day. The mean of the wind field is again fixed to 5 m/s, and the fluctuations are modelled by normally distributed random numbers. Fig. 10.6 displays the estimated lifetimes τ in dependency of the chosen standard deviation of the Gaussian distribution. Compared to the effects (a) and (b), day to day variations obviously have a rather small impact on the EFM.

Figs. 10.2 and 10.4 vividly illustrate that even for the simple assumption of only two alternating wind directions the impact on the EFM is highly complex and especially non monotonous. Thus a daily cycle in v can cause both, an underestimation as well as an overestimation of τ by the EFM. Thus caution has to be maintained by interpreting the EFM results for locations with high fluctuations in wind.

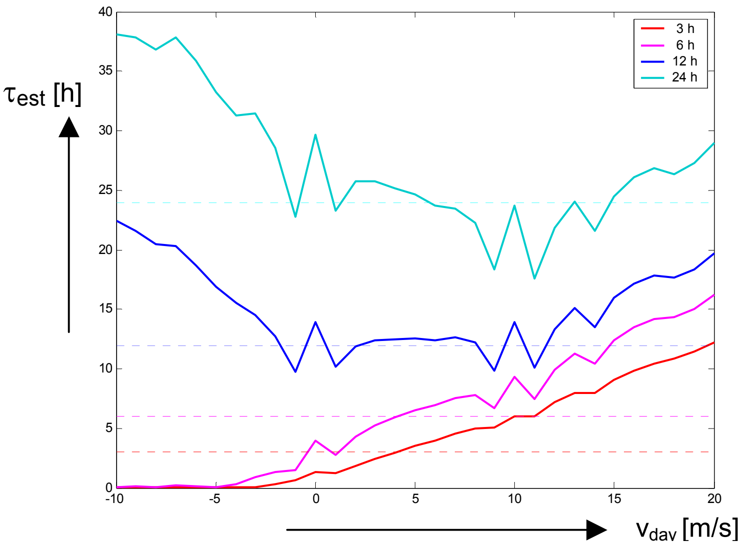

Fig. 10.4: Effect of daily variations of v: : Resulting mean lifetime τ_{est} *from EFM for a set of input lifetimes, depending on* v_{day}*. Nighttime wind speed is 10 m/s -* v_{day} *so that mean windspeed is fixed to 5 m/s.*

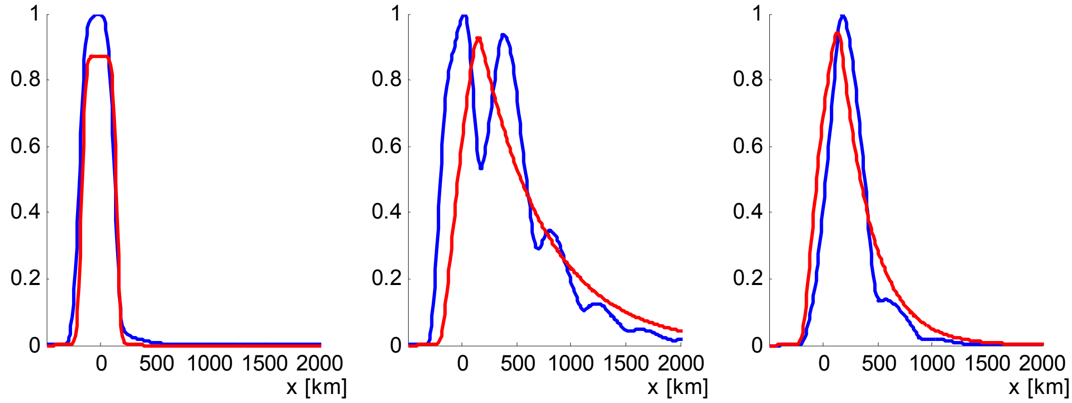

Fig. 10.5: Examples of modelled (blue) and EFM fitted (red) spatial distribution V(x) (normalized to max(V)=1) for
a) τ_{input}*=3 h and* v_{day}*=-10 m/s, b)* τ_{input}*=24 h and* v_{day}*=-10 m/s, c)* τ_{input}*=12 h and* v_{day}*=15 m/s*

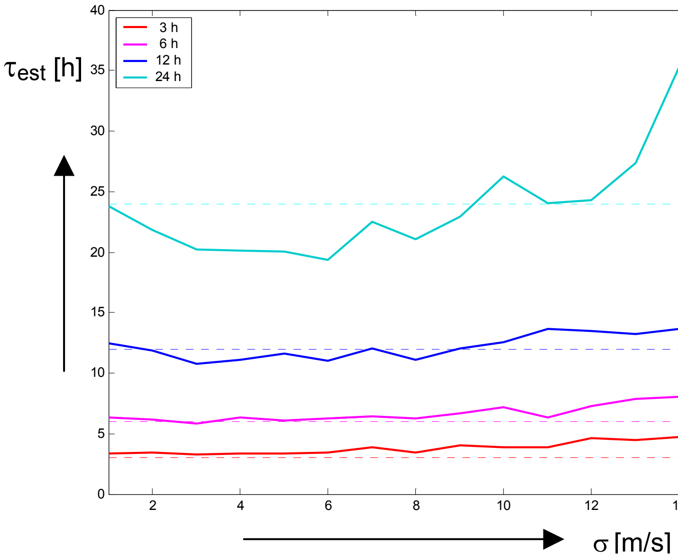

Fig. 10.6: Effect of day to day variations: Resulting mean lifetime τ_{est} from EFM for a set of input lifetimes, depending on the σ parameter [m/s] of the normally distributed random wind speed with v_{mean} fixed to 5 m/s.

10.3.2.2. Variation of τ

Apart from v, τ also is a function of time, as already discussed in section 10.2.2. This affects the EFM as well. As the e-folding length x_0 is

(10.10) $x_0 = v \times \tau$,

variations of τ affect the e-folding distance, thus the NO_x distribution, in a similar way as variations of v. On longer timescales (day to day and seasonal), the range of possible variations of τ is not as large as for v (especially as τ cannot be negative), thus the impact of variations on this timescales on the EFM is comparably low. However, daily variations are of importance due to the distinct daily cycle of τ(t). We compared the fitted lifetimes τ_{est} to input parameters for a set of daily lifetime cycles. In all cases of $\tau_{night} > \tau_{day}$, the fit overestimates the actual lifetime. This effect is most prominent for the scenario of short lifetime. This can be explained by the fact that NO_x has accumulated over night (~11 hours), and almost no depletion takes place during dawn (~1 hour); the faster daytime depletion is only active for about 3 hours before GOME overpass. The fit therefore overestimates the e-folding distance x_0 and thus τ. The effect can be as strong as 80% for very short daytime lifetimes (τ_{min} =2h), but is generally rather 20-30% for τ_{min} =4h and below 10% for longer daytime lifetimes.

Please note that this overestimation is a general systematic effect of the daily cycle of τ. However, this result depends on the validity of the assumptions leading to τ(t). Situations might be different if τ(t) is affected by factors that we neglect, e.g. an OH peak in morning time by HONO photolysis in urban polluted regions [Platt et al., 1980].

A further aspect is that the lifetime τ is likely to change with distance from the source, since OH concentration as well as NO_3 and N_2O_5 depend on NO_x themselves. Generally the lifetime is expected to increase for lower NO_2 levels, i.e. downwind of the plume. However, the EFM is mainly sensitive to the decrease in NO_2 over the first hundred kilometers. For higher distances the importance of noise and especially the bias from stratospheric estimation increases and makes quantitative estimates rather difficult. In this study we neglect a possible change of τ within the plume evolution.

10.3.2.3. Variation of emissions

NO_x emissions also show variations on different time scales, i.e. seasonal (e.g. biomass burning in during summer in the tropics or heating during winter in Europe), day to day (e.g. lightning, fires) and daily (enhanced anthropogenic emissions in daytime, rushhour). For most cases, these variations have less influence than variations of v and τ, but generally also affect the EFM. In particular, a pronounced daily cycle will lead to over- or underestimation of τ, depending on the daily cycles of v(t) and τ(t) and whether emission are predominant before or after GOME overpass.

10.3.2.4. Summary

Overall, the EFM is a powerful method to estimate mean lifetimes of NO_x for regions with existing winds (v_{mean}~>3 m/s) and a predominant mean wind direction. The retrieved lifetimes of the EFM are reasonable, if variations of wind, lifetime and emissions are not too large. The method can probably not be applied in regions with a strong daily cycle of wind field with alternating wind directions. The expected cycle of τ, i.e. higher nighttime lifetime and reaching infinity during dawn, generally leads to an overestimation of τ_{est}, most pronounced for short lifetimes, and the results from EFM thus have to be scaled down by a factor of about 1.1-2. Due to the impact of variations of v(t), τ(t) and E(t) and uncertainties on the "real" daily cycles, errors of τ_{est} are in general of the order of about a factor of 2. A short review of the results is given in Table 10.4.

Despite the impact of temporal variations, with respect to existing uncertainties on τ, the EFM is a powerful tool to derive mean lifetime estimates. Combined with the power of satellite data, especially the global coverage, the EFM is applicable for several locations around the globe.

Table 10.4. Impact of temporal variations of v, τ and E on the EFM

	v	τ	E
daily cycle:			
moderate variations	Not critical	**τ overest. by 10-100%**	Minor importance
strong variations	Critical		
day to day fluctuations	Not critical	Minor importance	Minor importance
seasonal cycle:			
moderate variations	Not critical	Minor importance	Minor importance
strong variations	Critical (τ overest.)		

10.3.3. Two dimensions

Our restriction to one dimension for the discussion above is of course a simplification. In practice, however, usually sections of constant latitude (longitude) and mean zonal (meridional) winds are considered, respectively. Transport within the non-considered coordinate can be accounted for by taking the mean distribution in a latitudinal (longitudinal) band instead of a 1-d line.

10.3.4 FLEXPART

As discussed in 10.3.2.1, variations of wind on seasonal as well as daily timescales can affect the ECM significantly and may lead to over- as well as underestimated lifetimes τ_{est}. To account for wind variations in a more realistic way than assuming one constant mean wind speed, we have studied the effects of transport with the FLEXPART [Stohl et al., 1998] model. This study is performed within the AFO-2000 project "NOXTRAM" in cooperation with the University of Munich. FLEXPART runs were performed by Nicole Spichtinger.

The idea of this study is to model 2-dim distributions of NO_x: emissions (e.g. taken from the EDGAR database) are transported by wind fields and depleted with a constant lifetime. Therefore the effects discussed in 10.3.2.3. have to be kept in mind for cases of short lifetimes. Future FLEXPART runs will be also capable to allow for temporal variations of the lifetime parameter (and emissions) [Andreas Stohl, personal communication]. Afterwards, the retrieved distribution, averaged over a month or year, is compared to the respective GOME/SCIAMACHY measurements, and from this comparison a most probable lifetime is derived that gives the best agreement. Please note that we do not compare absolute TVCD numbers, but only spatial patterns instead. The long term aim is to compare TVCDs and emission inventories (with correct transport) quantitatively. However, here we estimate the necessary mean lifetime τ in a first step; for the further use of this quantity, it has to be independent from total emission estimates.

10.3.5. Applications of the EFM and FLEXPART simulations: Case studies

In this section we present some case studies that illustrate the general potential of the EFM and FLEXPART approach to estimate the lifetime of NO_x. We also discuss some remaining shortcomings that can be hopefully resolved in future studies.

10.3.5.1. US eastcoast

Fig. 10.7 shows the modelled distributions of NO_2 TVCDs for the US eastcoast for January 1997. In (a)-(d), the FLEXPART results for different lifetimes (6h, 12h, 24h, 48h) are plotted. For comparison, the mean of GOME NO_2 TVCD distribution for January 1997 is shown in (e). For comparison, we have also added the 18 month mean of SCIAMACHY results in (f). In addition, Fig. 10.8 displays sections of constant latitude (at 41°N, i.e. crossing New York) for all these datasets.

The figures illustrate the general potential of the FLEXPART method, but also points out the major shortcomings:

(a) The general pattern of NO_x sources does not agree between EDGAR and the GOME/SCIAMACHY observations (see also Chapter 9). In particular, the New York emissions dominate EDGAR by far. GOME and SCIAMACHY reveal that emissions of the Chicago/Detroit region are of comparable magnitude. Of course this discrepancy affects the comparison of spatial distributions of FLEXPART and GOME TVCDs, that cannot fit if the spatial pattern of emissions is inappropriate.

(b) The GOME composite of a single month is based on only ~10 observations per location. As conditions (especially cloudiness) differ for these observations, one month of GOME data is probably not sufficient to reflect spatial patterns as precisely as would be sufficient for a quantitative comparison to EDGAR data.

(c) The GOME ground pixel has an extent of 320km east-west. This leads to a smearing out of the downwind plume (see also Chapter 9). This is a very important factor for comparing the sections in Fig. 10.8, as the smoothing makes the curves less steep and leads to an overestimation of τ if not accounted for.

(d) The simple section choice is made for constant latitude (for 1° resolution), i.e. only transport eastwards is considered. However, main transport direction is rather east north east as can be seen in Fig. 10.7. For sections following the mean direction we expect a higher sensitivity for differences of τ .

We have worked on solutions for these shortcomings that have been already partly realized, partly will be adopted in future:

(a) To be independent on the spatial patterns given by EDGAR, we try other assumptions on the spatial distribution of sources. In a first step, we concentrate on strongly localized emissions that can be regarded as point source (for the 1° grid). This will be illustrated exemplarily in section 10.3.5.2. In a second step we plan also to use the light pollution as proxy for NO_x emissions, as the correlation studies in Chapter 9 give hope that this distribution matches better than EDGAR.

(b) To avoid the problem of sparse data amount, we concentrate on monthly means for several years as well as seasonal and even yearly means.

(c) The improved SCIAMACHY resolution avoids the problems of GOME observations. We will thus concentrate on SCIAMACHY comparison studies in future. GOME data however might be useful for some special cases, where sections in north-south direction are considered, or where wind speeds are so high that the FLEXPART results can be smoothed with GOME resolution without losing sensitivity for different lifetimes.

(d) In the future, we also plan to consider more flexible sections beyond north-south and east-west.

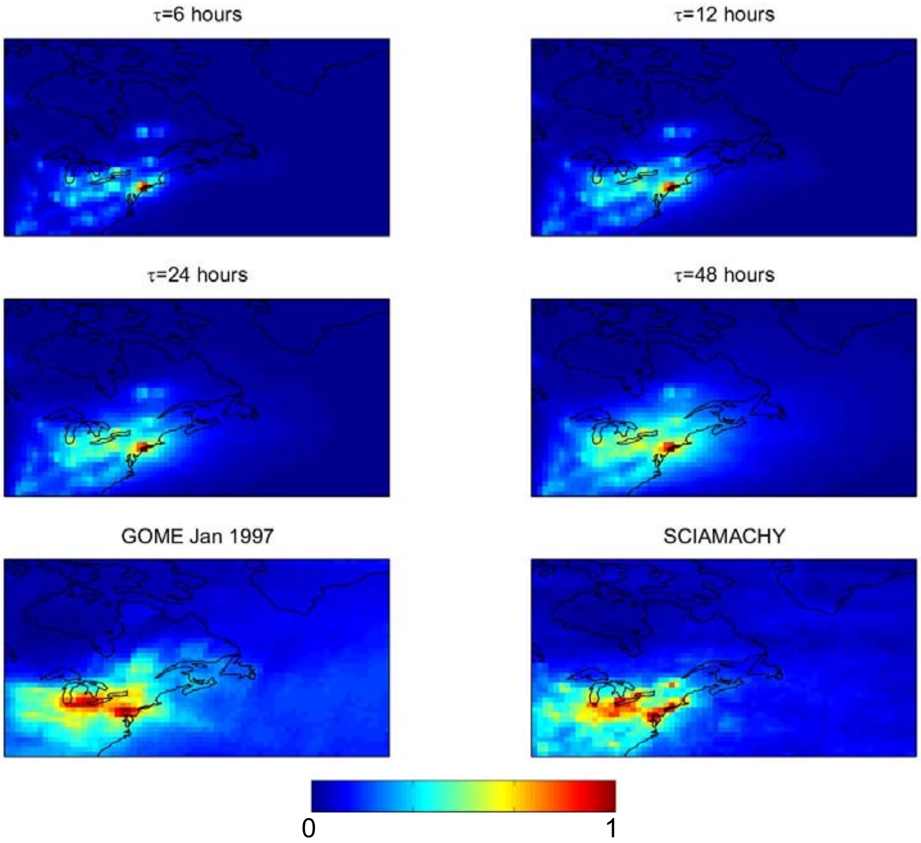

Fig. 10.7: Spatial distribution of NO_2 TVCDs as modelled from FLEXPART assuming EDGAR emissions and τ = 6h (a), 12h (b), 24h (c) 48h (d). (e) shows the composite of GOME measurements in January 1997, (f) the SCIAMACHY 18 months composite. All plots are normalized to fill the colorbar range from 0 to 1.

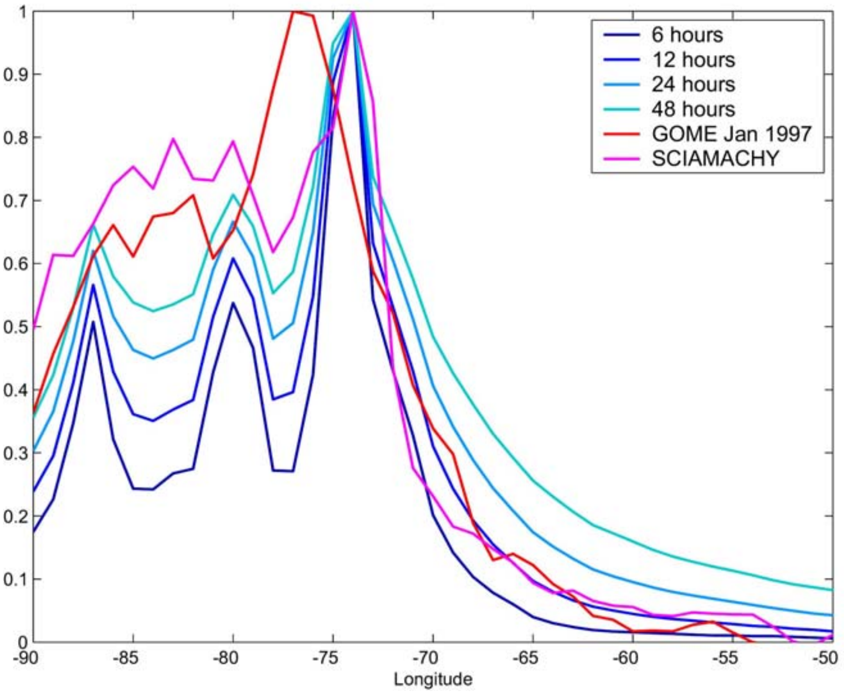

Fig. 10.8: Normalized sections of constant latitude (41°N) crossing New York for the datasets of Fig. 10.7. The modelled FLEXPART distributions are shown in blue, where the lowest curve corresponds to τ = 6h. The GOME data for January 1997 is shown in red, the SCIAMACHY section in magenta.

The lifetime estimation for the US eastcoast is mainly affected by the spread out of sources over a large area, and we cannot give a tight number for τ within the FLEXPART comparison study. However, the steep decrease of TVCD for the SCIAMACHY section indicates a rather short lifetime, significantly lower than one day (the study by Leue et al. [2001] probably overestimated τ as the GOME resolution was not accounted for). The situation is even more complex as the US eastcoast is struck also by lightning (see Fig. 6.1), with lightning frequency also decreasing eastwards. Thus this region is not best suited for lifetime estimates, though outflow of NO_x can be seen at first glance in mean composites.

10.3.5.2. Riad

For a second case study, we tried to identify a well isolated “point source” which is hardly affected by surrounding emissions. We found that Riad, Saudi Arabia, very well matches these requirements. The FLEXPART runs were performed assuming emissions only in the grid cell (1° resolution) including Riad. Fig. 10.9 (a-f) shows the resulting FLEXPART distributions for different lifetimes (3-18 hours). Please note that these are FLEXPART composites for a complete year model run (1997). Fig. 10.9 (g) displays the GOME composite for 1997, Fig. (h) for all GOME years 1996-2001. Finally, the SCIAMACHY composite is shown in plate (i).

The FLEXPART run reveals that transport occurs predominantly northwards. Thus Fig. 10.10 shows sections of constant longitude crossing Riad. For the latitudinal coordinate, resolution of both GOME and SCIAMCHY is rather good (40/30 km), avoiding the problems discussed in (c) (section 10.3.5.1).

At first view, it can be seen that the assumption of a point source (of below 1°x1° size) is justified. Maxima of FLEXPART and GOME/SCIAMACHY coincide in place in contrast to the US eastcoast study. The GOME sections, however, do not approximate zero in downwind direction, but rather reveal high background values. The reasons are further NO_x sources at the Persian Gulf (see also Chapter 9), which due to the large GOME ground pixels interfere with the Riad plume. For SCIAMACHY, however, the sources can be separated and the Riad section is almost not affected by other sources. The comparison of the spatial patterns, i.e. the very steep decrease of TVCD north from Riad, reveals that τ is about 4 hours, and probably not longer than 6 hours.

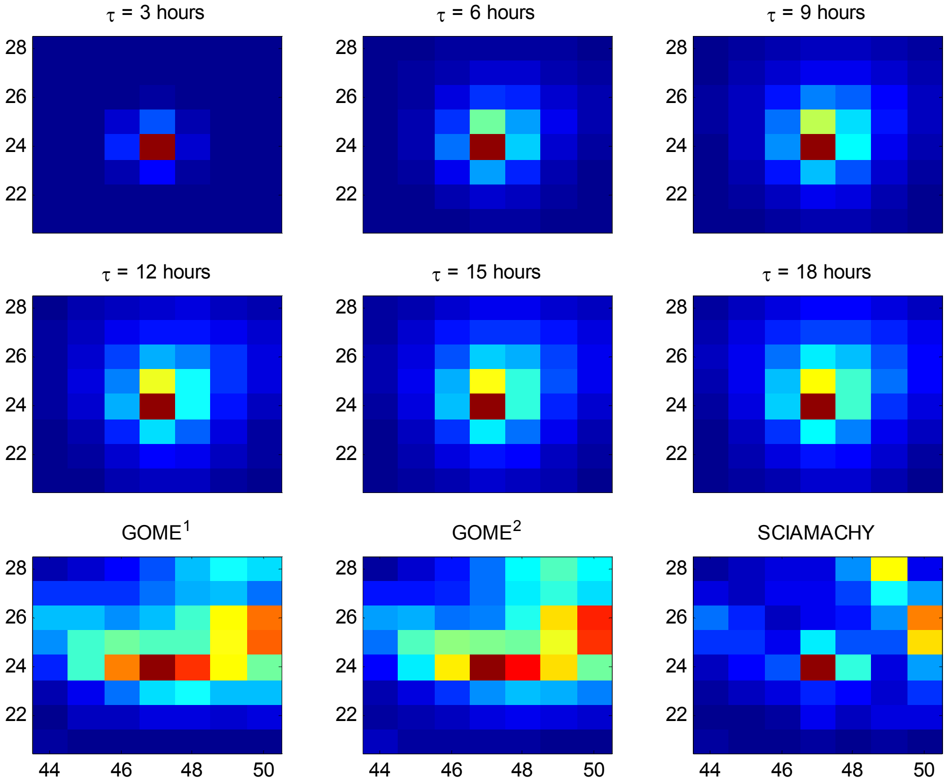

Fig. 10.9: Spatial distribution of NO_2 as modelled from FLEXPART assuming a point source (Riad) and τ as indicated in the subplots (a)-(f), compared to mean composites of GOME 1997 (g), GOME 1996-2001 (h) and SCIAMACHY (18 months) (i). All plots are normalized to fill the colorbar range from 0 to 1 (Compare Fig. 10.7).

This study demonstrates the potential of the SCIAMACHY/FLEXPART comparison for the determination of τ, especially the advantage over similar studies using GOME datasets with coarse spatial resolution. The method will be applied for several other sources of small spatial extent around the globe in the near future. For these studies we also plan to improve the FLEXPART resolution to 0.5°.

As Fig. 9.3 (d) revealed, the spatial extent of several hot spots around the world is comparable to that of Riad. If mean wind velocities are about 3 m/s, we thus expect similar results for the evaluation of τ for other sites, i.e. mean lifetimes below about 12 hours.

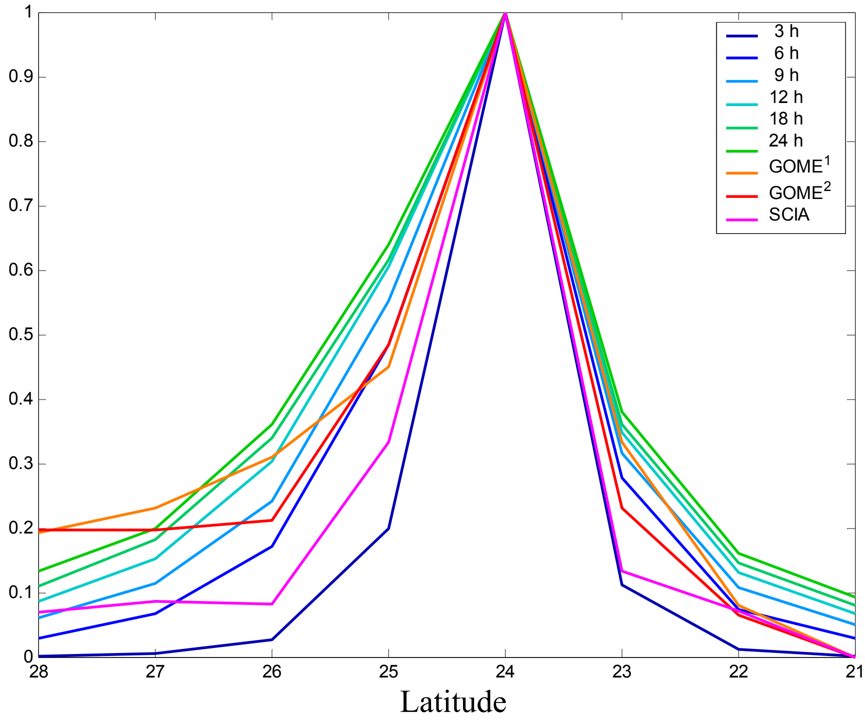

Fig. 10.10: Sections of constant longitude (46° E) crossing Riad for the datasets of Fig. 10.9.

10.3.5.3. Prudhoe Bay

Prudhoe Bay is a city in North Alaska, where the largest oil fields of Alaska are located. Fig. 10.11 shows the mean SCIAMACHY TVCD for Alaska. Please note the adjusted colorbar; because for the colorbar chosen e.g. in Fig. 9.3, no structures would be visible. The mean composite comprises data from the available 18 month dataset, but winter months (November-February) are excluded as the SZA exceeds 70°.

Prudhoe Bay shows a clearly enhanced level of NO_2 TVCDs. Also the transport westwards can be seen at first glance. This allows us, for the first time as far as we know, to derive a mean NO_x lifetime from measurement data for such a high latitude (70°N). As FLEXPART runs were not available yet, we have used a simple EFM approach. The result of the EFM is shown in Fig. 10.12.

Wind direction and speed are taken from observational data at Barrows. Winds are predominantly easterly throughout the year, and the mean wind speed is about 5 m/s. With this wind speed, an EFM results in a surprisingly short mean lifetime of about 4 hours. Despite the general problems of the EFM discussed above and the error being of the order of 2, we can definitely exclude τ being longer than 12 hours from our data. This stands in contradiction to the modelled lifetimes of some days for the arctic (see Table 10.2). A possible reason might be that the models underestimate the OH release from snow [Domine and Shepson, 2002]. It is also possible that the models have underestimated [OH] or heterogeneous NO_x removal during night.

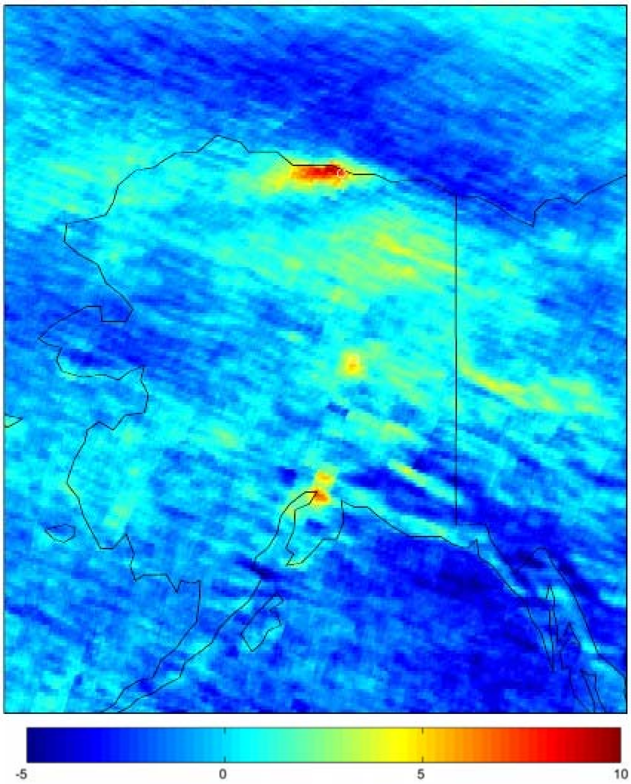

Fig. 10.11: Mean NO_2 TVCD (10^{14} molec/cm^2) from SCIAMACHY (March-Oct 2003 and March-May 2004) for Alaska. The relative strong source in northern Alaska is Prudhoe bay where the largest oil fields of Alaska are located.

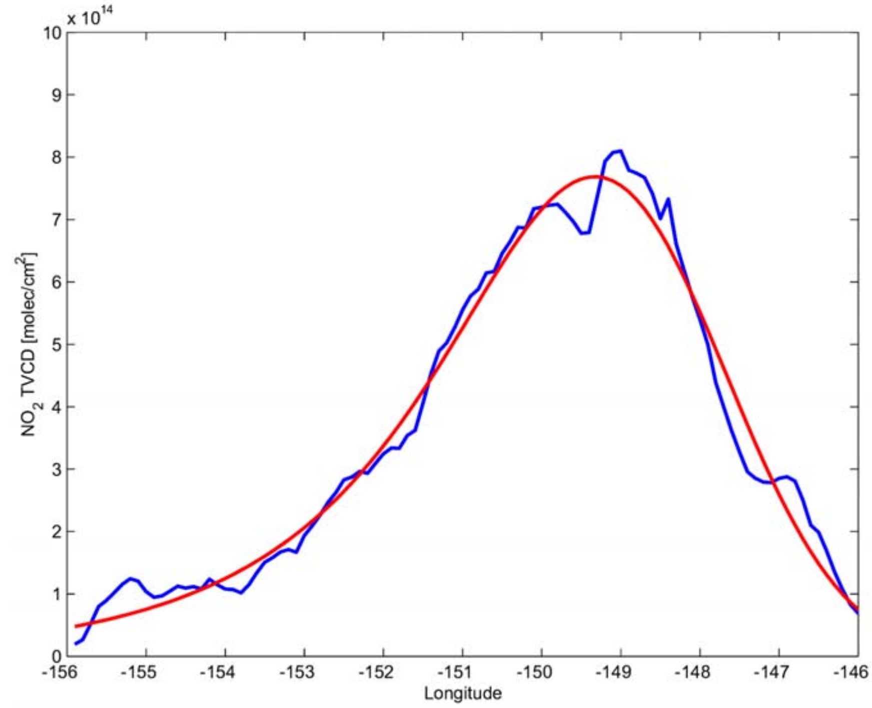

Fig. 10.12: Section of constant latitude (70°N) crossing Prudhoe Bay. The blue curve shows the mean NO_2 TVCD (10^{14} molec/cm^2) from SCIAMACHY (March-Oct 2003 and March-May 2004) (compare Fig. 10.11). The red curve is the result of the EFM that finds an e-folding distance x_0=76 km, corresponding to τ =4.2 h for v=5 m/s.

10.4 Lifetime estimation 2: Weekly Cycle

An alternative method for estimating mean NO_x lifetimes with GOME data makes use of the weekly cycle of NO_2 observed for several industrialized regions (see Chapter 4). The basic idea of the "Weekly Cycle Method" (WCM) is that the TVCD measured for a specific day of the week does not only depend on the emissions of the same day, but also on those from the day before (the effect of NO_x of 2 days age is rather small, if we accept the general range of lifetimes of tropospheric NO_x derived in 10.2). This means, Monday "inherits" the comparable clean Sunday air masses, and thus Monday TVCDs are lower than those for the rest of the week. Prerequisite for this reasoning is that there is no removal of air masses. We therefore have to consider the weekly cycle for a larger area, in contrast to the study in Chapter 4, to include the air masses blown away.

The big advantage of this method is that it is not sensitive to wind variations (as far as the considered region is large enough), and thus to possible effects discussed in section 10.3.2.1. Also the daily cycle of τ has only minor influence.

The big drawback of the WCM is that it of course can only be applied for regions with a strong weekly cycle: the features of the weekly cycle, especially the Monday levels compared to Sunday, must be detected clearly above noise level. However, the necessary enlargement of the considered area at the same time reduces the overall amplitude of the weekly cycle. Thus the WCM can only be applied to a handful of regions fulfilling these conditions. However, these are some of the regions of particular interest for studies on anthropogenic NO_x emissions. Thus, we have applied the WCM to four regions: (a) Germany, (b) the Po Valley, (c) the US eastcoast, (d) Los Angeles and (e) Japan.

Before analyzing the regions (b)-(d), we want to illustrate the general idea for the case of Germany (a), i.e. the area 7°-14° East and 48°-54° North (Fig. 10.13). Since the main sources are located in the western part of Germany and the mean wind direction is eastwards, the emitted pollutants should remain within the area for at least one day. (A mean wind velocity of approx. 5 m/sec corresponds to a daily transport of 432 km, whereas the east-west extension of Germany is about 700 km.)

Our analysis is based on some simple assumptions:

1. The ratio NO_2/NO_x does not depend on the day of week. That means, the normalized weekly cycles of NO_x and NO_2 are the same.
2. There is a constant NO_x emission during daytime (12 hours), while there are no emissions at night. As shown in Fig. 10.1 (d), the TVCDs measured by GOME do not strongly depend on the actual daily cycle of emissions.

Saturday emissions are 66%, Sunday emissions 60% of working day level (adopted from Wickert, 2001), see Fig. 10.14a.

3. The chemical loss of NO_x is first order in NO_x characterised by a constant lifetime τ. We neglect possible changes of τ due to different VOC/Ozone concentrations on Sundays.
4. For the considered area, there is neither in- nor outflow of NO_x due to wind transport. With this approach we particularly neglect the pollution in the Netherlands/Belgium, that itself is subject to a weekly cycle. The error of this simplification was estimated by extending the box size (dotted rectangle in Fig. 10.13).

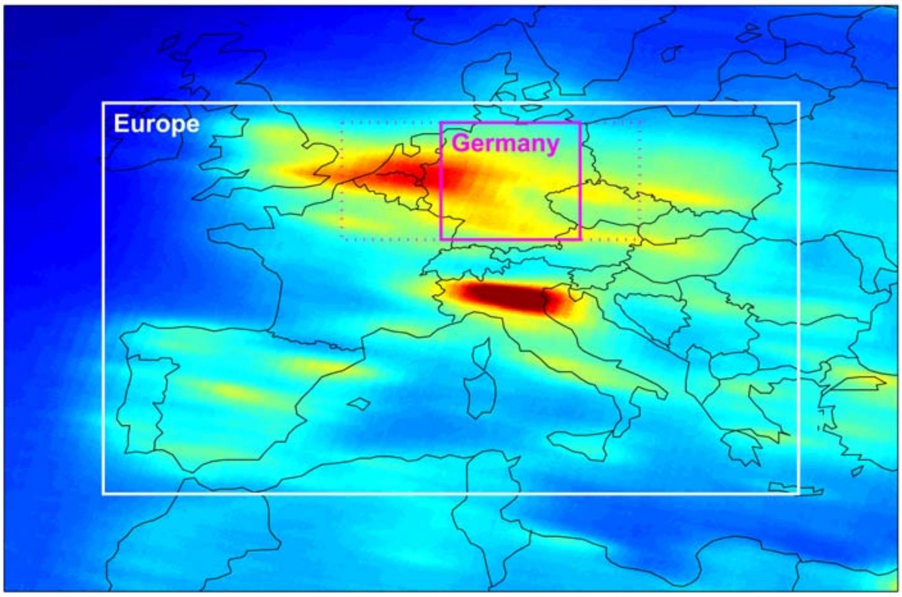

Fig. 10.13: Areas considered for the WC lifetime estimation. The straight box (magenta) indicates Germany; the dotted box was used to estimate the influence of the actual choice of the region borders.

Therefore, the change of the NO_x TVCD, V(t), can be described as dV/dt = E(t) - V/τ.

This differential equation was solved numerically. Fig. 10.14b shows the retrieved average weekly cycle of German NO_2 VCD at the ERS-2 overpass time for different lifetimes τ. This is compared to the actual measurements of GOME in Fig. 10.14c. This comparison was performed for winter and summer data separately. The dotted lines in Fig. 10.14c are related to the extended area (dotted rectangle in Fig. 10.13). As can be seen, the actual weekly cycle is nearly unaffected by the extent of the considered area.

The Sunday reduction is underestimated in the modelled weekly cycle. This might indicate that the reduction of weekend emissions is actually more extensive than assumed. Moreover, in assumption 2 (Fig. 10.14a) we neglected that Sunday emissions start later in the morning. Another important reason, especially for winter, is the overestimation of the stratosphere for the North Atlantic region. If we add a constant offset of, for instance, 10^{15} molec cm^{-2} (that would compensate the negative values over Ireland), the Sunday minimum would be 61% instead of 53% only.

In any case, in spite of the deviations of the absolute magnitude, the detailed temporal pattern of the weekly cycle of the modelled VCD crucially depends on the assumed lifetime (Fig. 10.14b). The weekly cycle of the summer data (Fig. 10.14c) shows Monday values on the normal workday level. Therefore, the summer weekly cycle is smaller than 12 hours and in good agreement with a lifetime of 6 hours (a shorter lifetime would result in Saturday values lower than observed, whereas a longer lifetime would show reduced Monday values). In winter, the observed Monday values are lower than the Saturday ones, indicating a lifetime of about 18-24 hours (any lifetime longer than 36 hours would lead to Monday values lower than Sunday values, which is not observed).

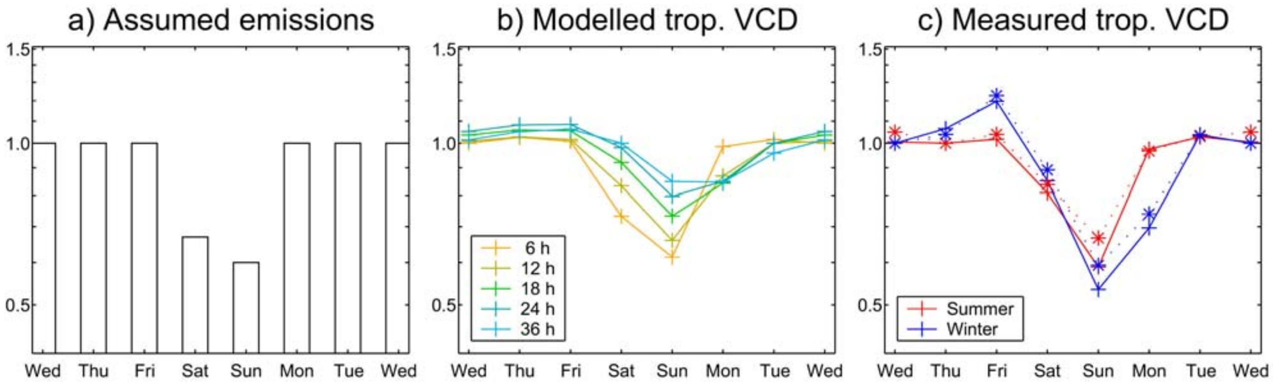

Fig. 10.14: Weekly cycle of NO_x (modelled and measured) for Germany (as shown in Fig. 10.13). All plots are normalized to the median weekly value (relative units). a) Assumed weekly cycle of NO_x emissions (adopted from Wickert, 2001). b) Modelled TVCD at ERS-2 overflight time for different lifetimes of NO_x. c) Mean TVCD of NO_2 measured with GOME. Dotted lines refer to the dotted rectangle in Fig. 10.13.

The next step uses the weekly cycle to determine τ quantitatively for the considered regions and different seasons separately. Therefore we let drop assumption 2 on the specific weekly cycle of emissions, because this data is valid only for Germany. Instead, we use a simple parameterization of the weekly cycle by four parameters: the emissions on weekdays (E_w), on Saturday (E_{Sat}) and on Sunday (E_{Sun}), and the lifetime τ. These four parameters are forced to fit the GOME observations by applying a least squares fit. Thus the actual weekly cycle of emissions is itself a result from the fit. In detail, the fit forces V(t) to match the parameterized weekly cycle on Saturday, Sunday, Monday and for the mean of Tuesday-Friday, i.e. we have four equations for four unknowns. This approach weights weekend variations stronger than in-week fluctuations. The more straightforward approach of fitting all seven days of the week generally gives quite similar results, but sometimes fails if weekday levels scatter too much.

Fig. 10.15 shows the weekly cycles for the considered regions for winter (a), spring (b), summer (c) and autumn (d). The coloured data displays the actually measured weekly cycle, the black lines correspond to the fit result. Most pronounced differences are Monday values for summer and winter: they are rather low, sometimes even lower than Sunday levels, for winter, whereas they reach working day levels (as for Germany) in summer.

Table 10.5 lists the resulting lifetimes from the least squares fit. In some cases the fit finds unrealistic values for Saturday or Sunday emissions. Whenever Sunday emissions are stated to be higher than Saturday or weekday values, the fit result is questionable and given in grey.

Table 10.5: Resulting lifetimes τ_{est} [hours] from the WCM for the regions considered in Fig. 10.15 for different seasons. Grey numbers indicate fit results with $E_{Sat}<E_{Sun}$ (see text).

	Spring	Summer	Autumn	Winter
Germany	16.1	5.5	15.5	24.2
Po valley	11.2	8.8	12.6	11.3
US Eastcoast	11.6	11.2	23.8	33.2
Southern California (LA)	10.8	6.4	18.2	25.9
Japan	16.0	11.9	24.0	22.1

The retrieved summer lifetimes are in the range of 5-12 hours, the winter lifetimes are significantly higher (22-33 hours). Values for spring and autumn are in between (10-16 hours). The retrieved Saturday- and Sunday emission levels are generally reasonable for summer. In winter, however, the resulting Saturday emissions are lower than the Sunday emissions for Germany. This is a result of the measured maximum of GOME VCDs on Friday: if the Friday TVCD would be forced to the Thursday TVCD, this inconsistency would be resolved. The fit results for spring are reasonable, but for autumn in 3 of 5 cases the resulting Saturday levels are too high.

For summer, the measured weekly cycles can very well be reproduced by the fit. In other seasons, however, in some cases there are large deviations (e.g. for Tuesday in winter in the Po Valley). The summer measurements yield similar results for all working days, whereas in winter there is a higher scatter of the data and some large jumps occur, e.g. the Thursday minimum in Southern California.

The weekly cycle (where it exists) obviously holds valuable information on the mean lifetime of NO_x for different regions and seasons. Winter lifetimes are significantly longer than summer lifetimes for all considered regions (located in the northern hemisphere). The winter results can help to estimate the removal via NO_3 / N_2O_5 for regions like Germany, where the latter are the dominating NO_x loss processes (as wintertime OH concentration is several times lower than in summer).

10.5 Conclusions

The estimation of the lifetime of NO_x is influenced by several factors, like variations of τ, wind speed and emissions. We could quantify the impact of these variations on τ estimates. Further constraints however arise from the other assumptions we made:

- the Leighton ratio may differ during the stage of the plume or from weekdays to Sundays, with possible impact on both estimations.
- the lifetime τ is not only a function of time, but probably also of place, as for larger distances from the source the plume gets more and more diluted, possibly increasing τ.
- the NO_x profile is different for source regions compared to downwind transported airmasses. The latter are mixed within the boundary layer and thus better visible for GOME than direct emissions at ground level. This effect would lead to a further overestimation of τ.

Nevertheless, GOME data provides valuabale information on the mean lifetime of τ that can be analyzed for different regions and different seasons.

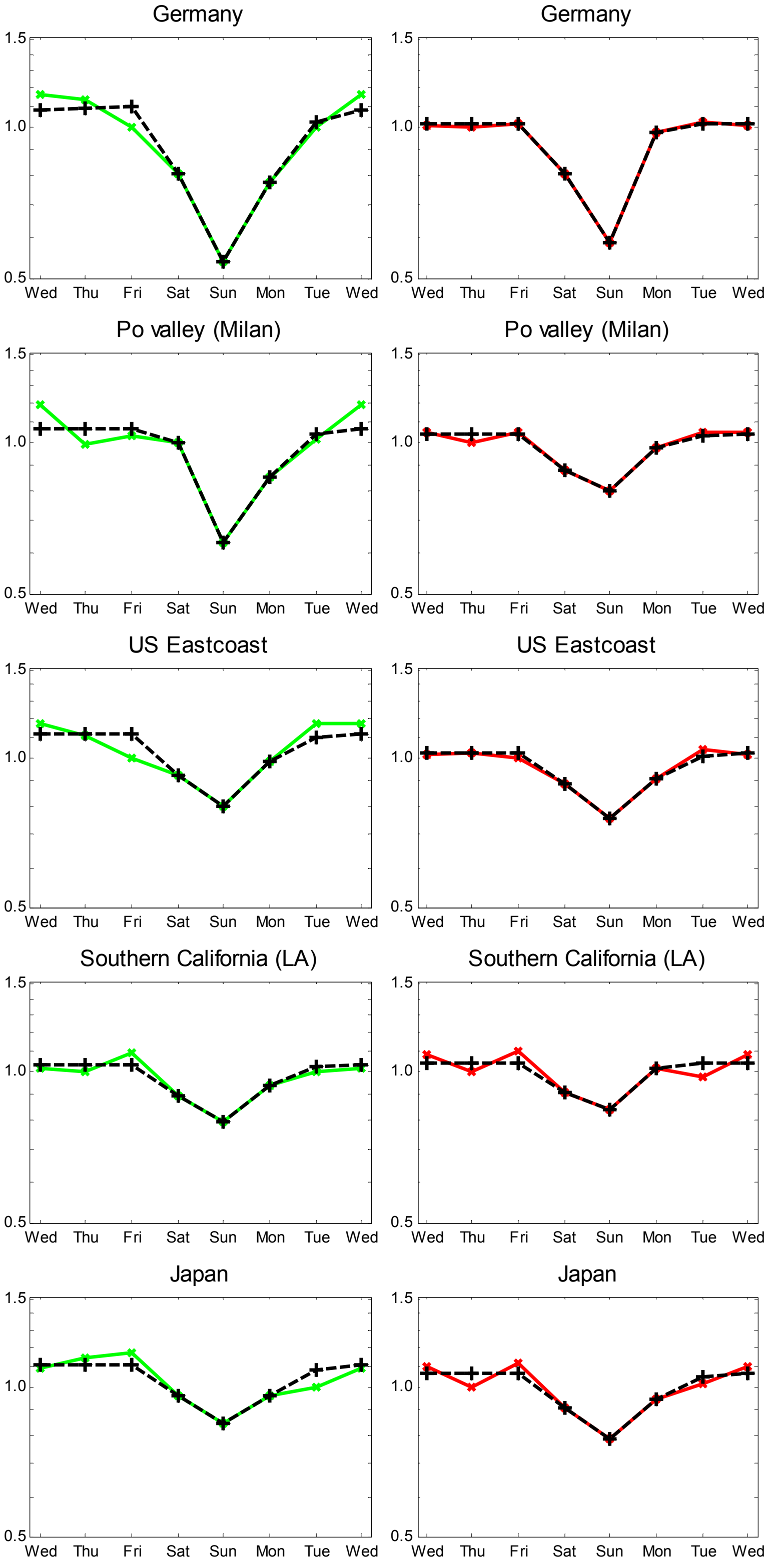

Fig. 10.15: Weekly cycles of NO_2 TVCDs (normalized) for the considered regions for Spring and Summer. Colored plots are measured cycles from GOME data, black curves show the fit result.

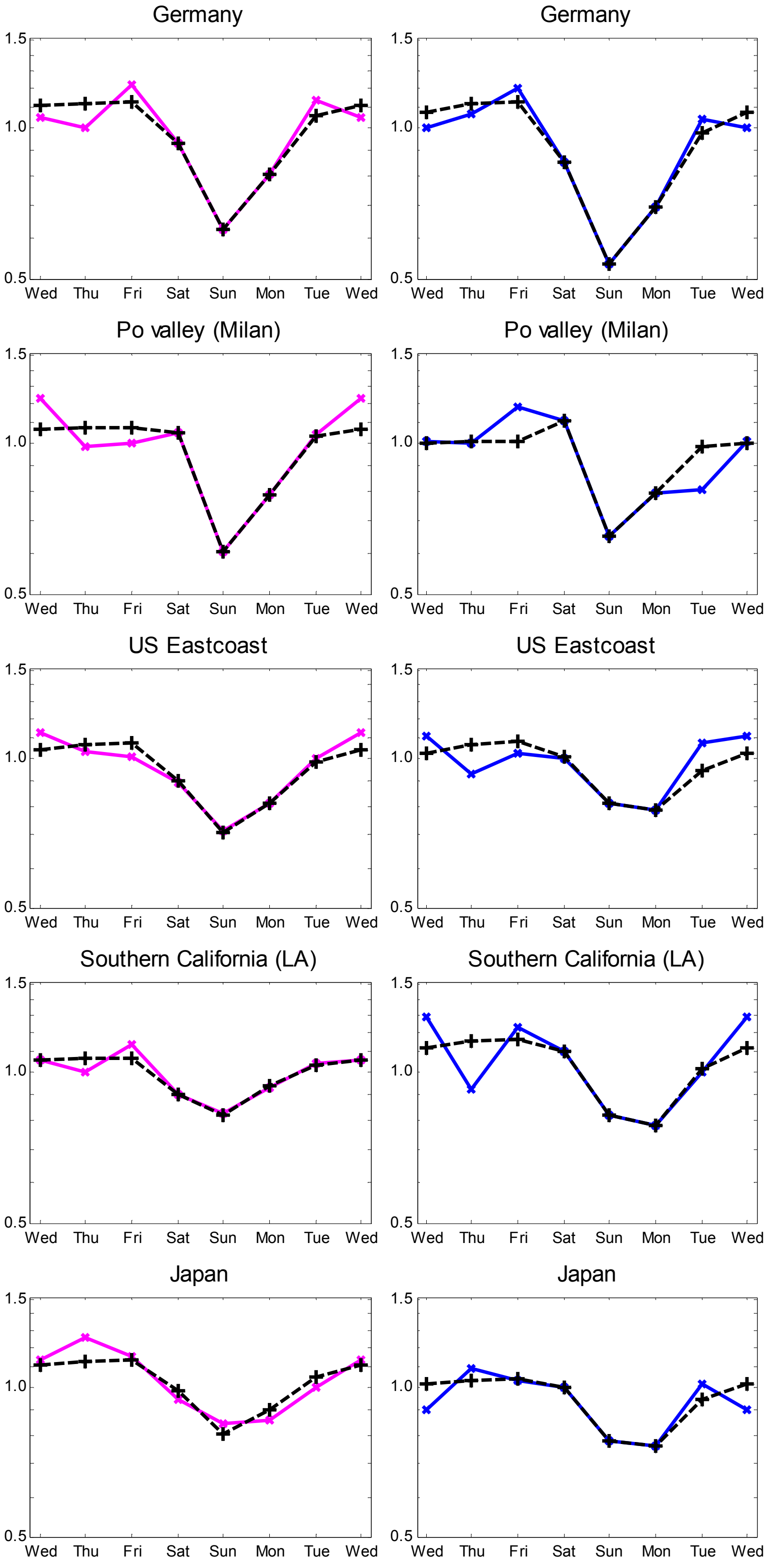

Fig. 10.15 (cont): Weekly cycles for the considered regions for Autumn and Winter.

Chapter 11
Ship emissions

We finally present a study on ship emissions of NO_x, as it comprises several aspects discussed before: For the first time, ship emissions of NO_x could be observed from space; the clear identification was possible by the long time series of spatially resolved GOME data (see chapter 3), allowing the detection of a characteristic pattern of enhanced NO_2 TVCDs corresponding with a ship track, despite the weak signal. We furthermore could use the GOME data itself to derive a mean lifetime of NO_x (chapter 10). For this particular event, we could apply an appropriate AMF correction and used the derived NO_2 TVCDs and lifetime to estimate the emissions from ships for the considered track that compare well with literature. This study has been published in Beirle et al. [2004c].

11.1. Impact of ship emissions

In recent years, the role of ship emissions has attracted increasing attention. Latest inventories estimate ships to contribute 3.6 to 6.9 Tg [N]/yr [Endresen et al., 2003; Corbett and Köhler, 2003], i.e. about 16-31% of total anthropogenic emissions (corresponding to the estimate by Lee et al. [1997]). These numbers reflect the importance of ship emissions as well as the still high uncertainty. Model calculations postulate a remarkable change in tropospheric composition due to ship emissions (e.g. [Lawrence and Crutzen, 1999; Davis et al., 2001; Endresen et al., 2003; von Glasow et al., 2003]), since they are the only anthropogenic source of NO_x in the marine boundary layer, and the effect of additional NO_x sources on ozone production is larger for low NO_x background levels. Recent studies analysed the dispersion and chemical evolution of ship plumes [Davis et al. 2001; Song et al., 2003; von Glasow et al., 2003] and point out the importance of in-plume-chemistry: as a result of ship emissions, daytime levels of OH as well as nighttime levels of NO_3/N_2O_5 are increased drastically, thus reducing the lifetime of NO_x. Model calculations estimate in-plume lifetimes to be about 2-6 hours [daytime] and 10-20 hours [nighttime], respectively [Song et al., 2003; von Glasow et al., 2003]. As a consequence, global models tend to overestimate NO_x concentrations in and close to ship tracks [Kasibhatla et al., 2000] as they do not resolve in-plume processes. However, the number of observational studies for evaluating ship inventories as well as their impact on chemical composition and processes is still rather small.

11.2. Detection of NO_x emissions from ships: A case study

According to recent studies on ocean going ship traffic [Corbett et al., 1999; Endresen et al., 2003], the Atlantic ocean is the most travelled ocean of the world, but ship tracks are distributed quite homogenously (Fig. 11.1). In contrast, in the Indian ocean between Sri Lanka and Sumatra, all ships cruise a single uniquely narrow track.

Fig. 11.2a shows estimated NO_x emissions for this particular ship track [Endresen et al., 2003]. This particular track is clearly detectable in the NO_2 TVCDs from GOME as illustrated in Fig. 11.2b (showing cloud free measurements for springtime observations 1996-2001).

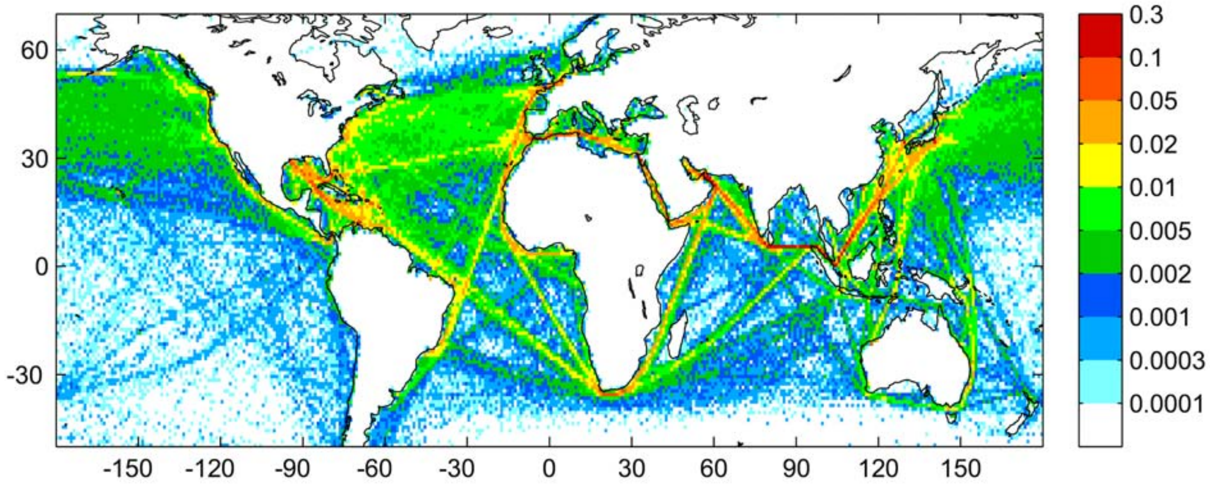

Figure 11.1: Global ship traffic density as reported by the Automated Mutual-assistance Vessel Rescue system (AMVER) (O. Endresen, personal communication). Numbers give the percentage of total observations per 1° x 1° grid point.

Please note that the absolute TVCDs are rather small and the colorscale was adjusted. Continental TVCDs exceed the colorscale and are masked out in Fig. 11.2b. Besides the ship track, we find nonvanishing NO_2 TVCDs northwards (probably due to transport of continental NO_2 pollution) and negative TVCDs southwards (due to an inappropriate stratospheric estimation). To remove this background signal, we additionally show the high-pass filtered signal in Fig. 11.2c, where we applied a recursive filter with a cut off frequency of 1/(1000 km) only to the latitude coordinate. Fig. 11.2c additionally indicates the ship routes connecting India and the Gulf of Aden and the Gulf of Oman, respectively. The nearly perfect agreement between the trace gas patterns and the ship routes allows the doubtless identification of ship emissions as source of the observed NO_2.

We use the GOME measurement to estimate the NO_x emissions from ships for the heavily cruised shiptrack in the Indian ocean. Therefore a tropospheric AMF of 0.65±0.15 is applied for the retrieved TVCDs of NO_2. This AMF was calculated with TRACY (see chapter 2.3) for a sea surface albedo of 5% (at 440 nm) [Koelemeijer et al., 2003], a characteristic sea salt aerosol profile, and NO_2 well mixed in the maritime boundary layer (MBL) with a typical height of 700 m (500 m - 1000 m) [Heikes et al., 1996]. To minimize a bias of our estimate due to clouds, only cloud free pixels (i.e. the HICRU cloud fraction being less than 5%) are considered. The remaining cloud effect (mostly shielding) on the TVCD is less than 12%. For the considered 6 years of GOME data (1996-2001), on average about 180 observations (out of 700) remain for each grid pixel.

Fig. 11.3 shows zonal means of the high pass filtered NO_2 TVCD for the box indicated in Fig. 11.2c. For all seasons, the sections show a clear maximum at 6°N. However, the shape of the peak differs significantly for the seasons and shows a strong asymmetry for summer (i.e. June-August) and winter (December-February). This is due to the fact that the ship track is traversed by the Intertropical Convergence Zone (ITCZ) twice a year [Lutgens and Tarbuck, 1997]. As a result, the mean wind directions of summer and winter are nearly opposite. The mean meridional wind component is 6.5 m/s in summer and -4 m/s in winter (NCEP/NCAR reanalysis, [Kanamitsu et al., 2002]). The respective curves are broadened to the North (summer) and the South (winter) respectively, while they are quite symmetric in spring and autumn when meridional wind speeds are lower (1-2 m/s).

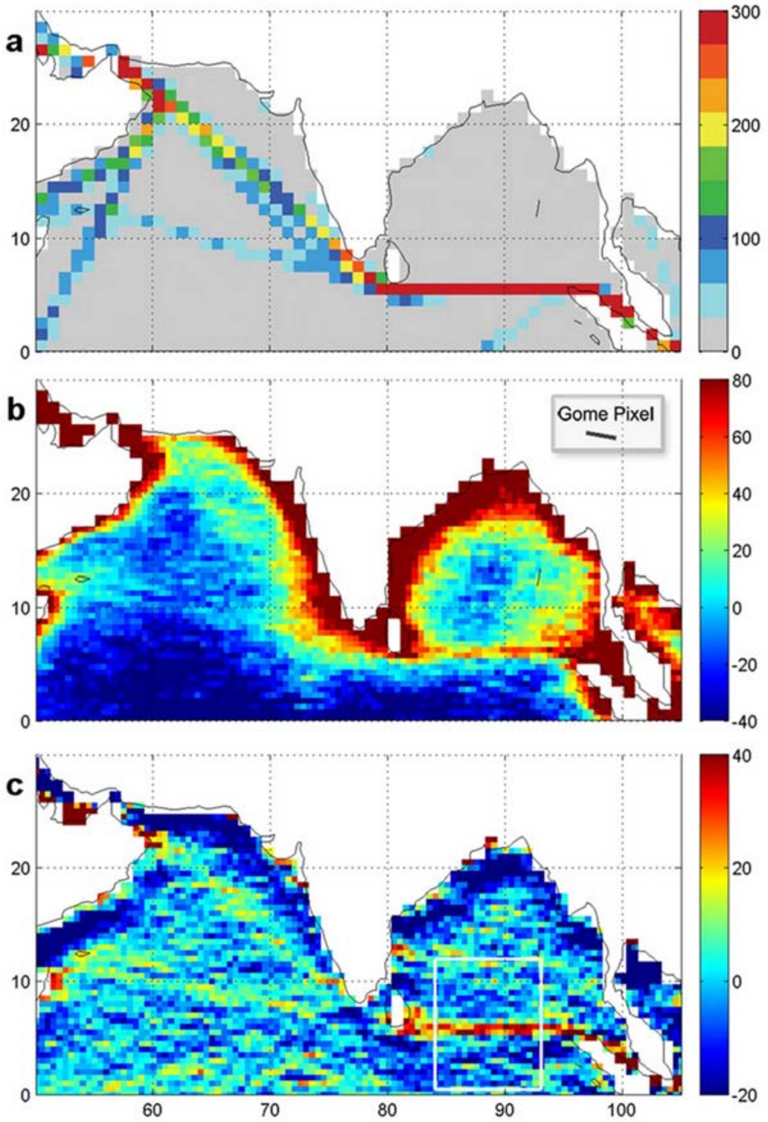

Figure 11.2: Nitrogen oxide emissions from ships in the Indian ocean (from [Beirle et al., 2004c]). Land masses are masked out.

a) Inventory data (mg [N] per m^2 and year) by Endresen et al. [2003], using the AMVER distribution of ship reporting frequencies, weighted by the ship size.

b) Tropospheric vertical column densities (TVCDs) of NO_2 (10^{13} molec/cm^2). GOME measurements of spring 1996-2001 with cloud fractions below 5% are averaged. The narrow ship track between Sri Lanka and Indonesia is clearly visible. For illustration, size and orientation of a single GOME pixel is displayed.

c) High-pass filtered (along latitudinal component) NO_2 TVCD. Additionally, the two major tracks west of India emerge. The box (84°-93° E, 0°-12° N) indicates the data used for the quantitative estimate of NO_x emissions from ships (see text).

The decay of the downwind NO_2 VCD allows us to deduce the mean lifetime of boundary layer NO_x with the exponential fit method (EFM) described in chapter 10. The resulting 1/e-lengths are 90 km for summer and 122 km for winter with an uncertainty of 20%. The corresponding lifetimes τ (obtained by dividing the 1/e-lenghts by the respective wind speeds) are 3.8 hours in summer and 8.5 hours in winter. However, as discussed in 10.3.2.3, the strong daily cycle of τ leads to a systematical overestimation of the mean lifetime by the EFM. We quantified this effect for the daily cycle of τ given by Song et al. [2003]. It turned out that we have to downscale the EFM results by 0.6, resulting in $\tau = 2.3$ hours in summer and 5.1 hours in winter.

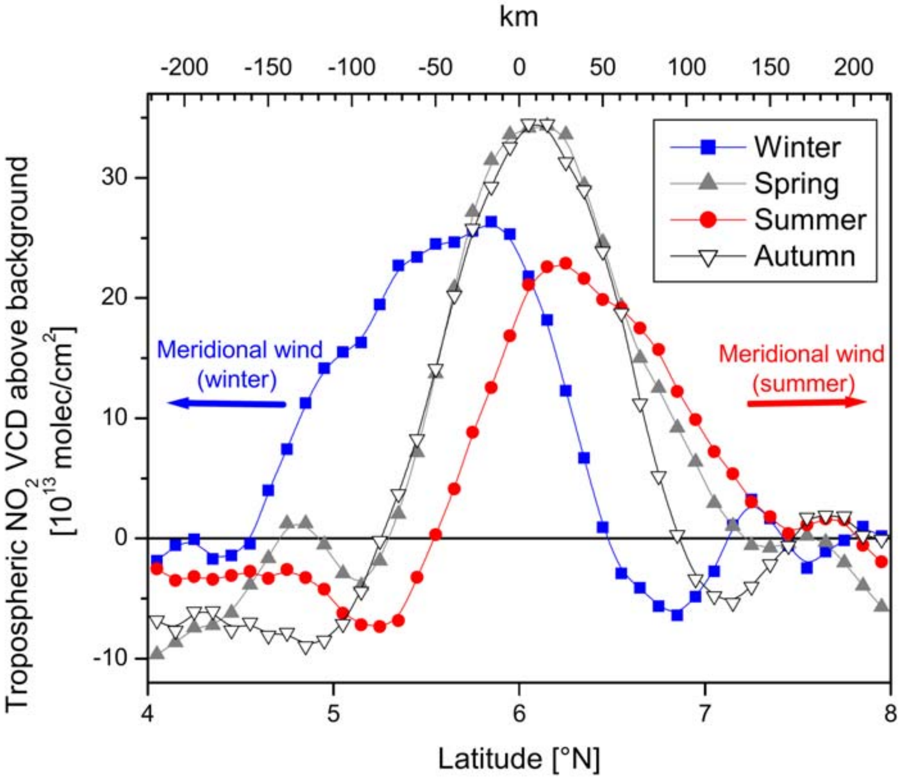

Figure 11.3: High-pass filtered NO_2 TVCD, zonally averaged over the box in Fig. 11.1c, as function of latitude (below) with an additional km-scale (above) (from [Beirle et al., 2004c]). For all seasons, a clear maximum at the ship track position (≈6°N) can be seen. The graphs for winter and summer are asymmetric due to strong meridional winds, indicated by the arrows.

This large difference between summer and winter lifetime cannot be explained merely by variations of temperature, ozone concentrations or photolysis rates. The shorter summer lifetime is probably a result of the different meteorological conditions, i.e. higher water vapour concentrations (as can be seen e.g. from GOME) as well as higher precipitation rates (NCEP/NCAR reanalysis) in summer. Therefore we expect higher OH concentrations as well as maybe increased scavenging of N_2O_5, thus implying a shorter lifetime. However, assuming the ship emissions to be constant throughout the year, the ratio of the lifetimes for winter and summer should be directly reflected in the ratio of the respective integrals over the sections in Fig. 11.3. The latter is 1.33 (whereas spring and autumn give the same integral as winter), indicating that the lifetime is indeed larger in winter, but rather by 33% than by 100%. We therefore expect the summer and winter lifetimes to be comparable, and take the retrieved lifetimes for summer and winter as representative for a lower and upper bound of the overall mean lifetime, and their average (3.7 hours) as best guess.

We use this mean lifetime to quantify absolute NO_x emissions from ships. Integrating the annual mean signal from 4.5°N to 7.5°N and multiplying with the box width of 9°, i.e. 995 km (at 6°N), we find the daily enhancement to be 3.0×10^{29} molecules [NO_2]. To deduce daily emissions from the observed VCD, we have to scale this number with 24 h / τ [hours], resulting in a factor of 6.5. Furthermore, the ratio of NO_2 to total NO_x at 10:30 local time is about 0.72 (0.67-0.77) (modeled by von Glasow et al. [2003]), giving a further factor of 1.54. The resulting ship emissions in the respective box are 2.7×10^{30} molec [NO_x]/day or 63 t [N]/day, i.e. 23 Gg [N]/year.

Due to the high pass filtering, errors arising from the estimate of stratospheric NO_2, superimposed NO_x (lightning and/or transport of continental pollution) and the degradation of the GOME instrument [Richter and Wagner, 2001] are nullified. Thus, the remaining uncertainties arise from the RTM (~25%), the precise recognition of the ship induced enhancement in the raw data (~25%), the NO_2/NO_x ratio (~8%), and the lifetime estimate (~50%). Thus we derive the emissions to be 10-73 Gg [N]/year by taking the minimum/maximum values for all factors. The largest contribution to the overall uncertainty arises from the lifetime estimate. However, additional information on this quantity would significantly reduce our uncertainty to about 16-37 Gg [N]/year (assuming τ = 3.7 hours as correct value).

In principle, the GOME observations underestimate the actual VCD in the first stage of plume evolution (when the NO_x is close to the ground) due to an inappropriate RTM correction factor. However, the expansion of the plume is quite fast: after 6 minutes the plume height is already ~200m (see eq. 2 in von Glasow et al. [2003]). The fraction of NO_2 that we miss is below 5%, thus negligible.

Table 11.1 compares our estimate to recent emission inventory datasets. Since the inventory of Corbett and Köhler [2003] is not spatially resolved, we derive a simple estimate by scaling the prior (spatially resolved) numbers of Corbett et al. [1999] with the ratio of 5.00 Tg N (global cargo fleet emissions as estimated in Corbett and Köhler, [2003]) and 3.08 Tg N (total global emissions, [Corbett et al., 1999]), yielding a factor of 1.62.

Table 11.1: Total NO_x emissions for the Indian-Indonesian ship track (84°-93°E, 0°-12°N) (from [Beirle et al., 2004c]).

Source	NO_x emissions (Gg [N]/year)
EDGAR 3.2 [Olivier and Berdowski, 2001]	34
Corbett et al. [1999][a]	22
Corbett and Köhler [2003]	36[b]
Endresen et al. [2003][c]	41[d] 54[e]
This study	23 (10-73)[f] 23 (16-37)[g]

[a] Data kindly provided by J. Corbett, see http://www.ocean.udel.edu/cms/jcorbett/sea/nitrogen.html

[b] Estimated by simply scaling up the overall ship emissions of NO_x in Corbett et al. [1999] by a factor of 1.62 (see text).

[c] Data kindly provided by O. Endresen, personal communication

[d] using the ship distribution from the Automated Mutual-assistance Vessel Rescue system (AMVER)

[e] AMVER distribution weighted by ship size

[f] including lifetime uncertainties

[g] assuming 3.7 hours as correct mean lifetime

Overall, we find a good agreement of our results with the literature values. Please note that these numbers are affected by the underlying total global emission estimate as well as the assumed ship traffic distribution that may be biased for specific routes (see the discussions of Corbett and Köhler [2003] and Endresen et al. [2003]).

Apart from the three tracks indicated in Fig. 11.1c, we could not detect any other ship track in the GOME data, mainly for two reasons: a) the Indian ocean tracks are extremely narrow (in contrast to the smeared out Atlantic routes) and b) they have the peculiarity of being oriented in the east-west direction, almost parallel to the GOME pixel. Thus, the large east-west extent of the GOME pixel has no unfavourable effect.

11.3. Ship emissions of NO_x as observed by SCIAMACHY

The higher spatial resolution of SCIAMACHY allows the detection of ship tracks that are not oriented in east-west direction [Richter et al., 2004]. Fig. 11.4 shows the mean NO_2 TVCD as derived from SCIAMACHY measurements from January 2003 - June 2004. Please note that (in contrast to Fig. 11.2) no cloud mask could be applied. However, besides the heavily cruised track between Sri Lanka (1) and Indonesia (2), further tracks can be identified: To the east, ship traffic passes the Malakka streat and proceeds towards Taiwan (3). Further northeastwards, the tracks split up towards China, Korea and Japan (see Fig. 11.1), and cannot be traced in the SCIAMACHY data any more.

The tracks from Sri Lanka towards the Gulf of Aden and the Gulf of Oman are rather faint in the SCIAMACHY data. A longer time series and the skipping of cloudy pixels is expected to lead to a clearer signal.

However, the ship track crossing the Red Sea is clearly visible, especially the northern part close to the Sinai (5). Also the further main route (leaving Suez channel (6) and directing Sicily (7)) can be identified.

Though SCIAMACHY clearly reveals far more information on ship tracks from Far East to Europe, still no signals of ship NO_x emissions can be found in the Atlantic, where ship traffic takes place almost everywhere rather than on one particular route. However, even the pronounced track crossing the Gulf of Mexico (Fig. 11.1) that is as strongly cruised as the Red Sea, cannot be traced in the SCIAMACHY data.

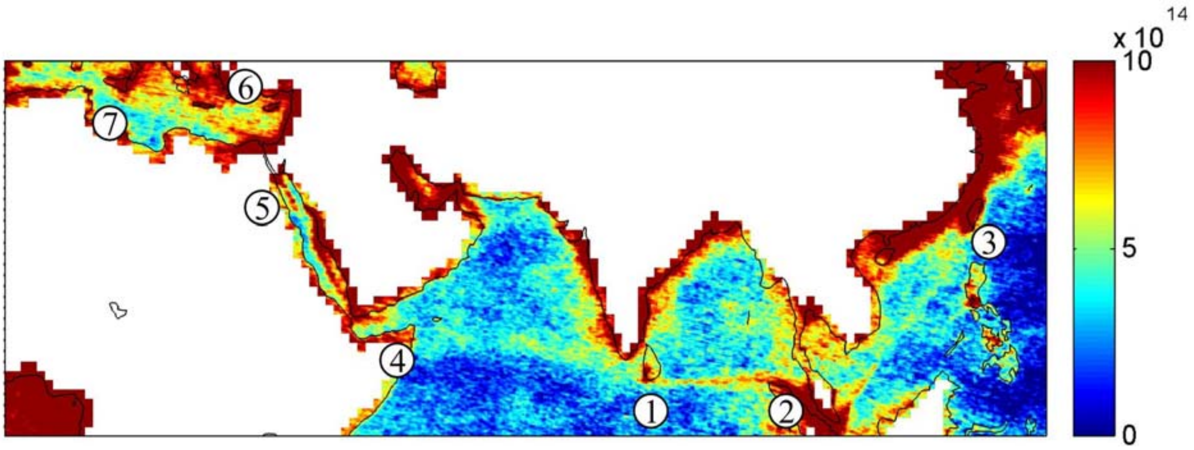

Fig. 11.4: Ship plumes of NO_2 (TVCDs in 10^{13} molec/cm^2) as observed by SCIAMACHY (Jan 2003-June 2004).

11.4. Conclusions

In this study we present the first detection and quantification of ship NO_x emissions from satellite. The line of enhanced NO_2 in the Indian ocean as seen in the 6-year composite of cloud free GOME observations clearly coincides with the distinct ship track from Sri Lanka to Indonesia. We used seasonal differences in the wind direction to derive the mean lifetime of ship exhaust NO_x to be about 3.7 (2.3-5.1) hours. Our result (achieved by using an independent method) confirms recent modeling studies that predict rather low NO_x lifetimes within ship plumes. Using our lifetime estimate, we derived the total emissions within the considered area to be 23 (10-73) Gg [N]/yr in good agreement with recent inventories.
Consequently, our new and independent method helps verify existing inventories as well as model calculations. Prospective refinements of our method are likely to reduce current uncertainties. Measurements from SCIAMACHY, OMI and GOME II with improved spatial resolution allow the detection of further ship tracks.

Conclusion

In this thesis, we have used GOME and SCIAMACHY data to determine tropospheric column densities of NO_2. From these datasets we could analyze temporal and spatial patterns of tropospheric NO_2. As result from our studies, several new, independent information on NO_2 in the troposphere could be gained:

- The analysis of the weekly cycle allows in principle to discriminate different anthropogenic sources like traffic, heating or power generation.
- NO_x from biomass burning has been analyzed for different regions. Boreal fires seem to release by far less NO_x than tropical fires.
- GOME is actually capable to detect NO_x from lightning, allowing even quantitative estimates. This is very important as the NO_x production from lightning is least known and at the same time of high importance for ozone production.
- Also ship emissions of NO_x have been detected for the first time in satellite data and were investigated quantitatively.
- Comparisons of transport events observed by GOME and modelled with FLEXPART result in very good agreement.
- The high spatial resolution from GOME narrow swath mode and SCIAMACHY data allows to locate sources of NO_x precisely. The comparison of the spatial patterns of NO_2 TVCDs and emission inventories generally agrees well, but some inconsistencies have been detected. Hence the results from satellite measurements improve our knowledge on the location and (relative) strength of sources.
- The results from SCIAMACHY impressively demonstrate the benefit of the higher spatial resolution compared to GOME. Nevertheless, the GOME dataset is still valuable as it provides a long time series of the past, and will probably also be of use for further studies, despite the existence of SCIAMACHY and OMI. The evaluation of the GOME narrow swath mode data allows the quantitative comparison to SCIAMACHY results with similar resolution, so that changes in the spatial patterns of NO_x sources can be identified (as for China).
- For the first time, the mean lifetime of NO_2 could be derived from *measurements* with consistent methodology for several regions around the globe (from the tropics towards the Arctic) and for different seasons. This in principle allows to quantify also day and night loss rates separately. Generally we find rather short lifetimes (12 hours and below), and especially the result for Prudhoe Bay (τ=4 hours) at 70°N is in contradiction to current model results.

Outlook

The ongoing measurements from SCIAMACHY, OMI and future satellite instruments (e.g. GOME 2) provide the continuation of time series of NO_2 TVCDs. This is important for future trend studies on NO_x emissions, and will also be used for continuation and improving our estimates on source strengths and NO_x lifetime.

So far our studies stayed rather qualitative for some cases (like for biomass burning) or emphasize on spatial patterns and relative quantities. For more quantitative statements the retrieval has to be further improved. Concerning this aspect, at the IUP Heidelberg effort is set on the improvement of radiative transport modelling, including realistic aerosol properties (TRACY, S. Sanghavi) and the retrieval of cloud fractions and cloud top heights from SCIAMACHY PMD measurements and O_2/O_4 absorptions (M. Grzegorski).

The uncertainties of the stratospheric estimation, especially for the Arctic polar vortex (affecting also Europe) are hopefully resolved by the potential of the SCIAMACHY limb measurements. The implementation of the limb evaluation and the inversion methods for profile retrieval are challenging present and future tasks.

The simultaneous measurements of the different ENVISAT instruments hold valuable information e.g. for the detection of aerosols, cloud cover, snow cover and ground albedo as well as stratospheric trace gas profiles (MIPAS), thus providing a sound basis for the calculation of tropospheric AMFs.

One major shortcoming in current satellite data of NO_2 is the fact that - due to the sun-synchronous orbit - all measurements are taken at a fixed local time. To analyze daily cycles of different trace gas abundances and to avoid the temporal gaps of 3(6) days, an UV-vis spectrometer onboard a geostationary satellite is essential which hopefully will be realized in future.

Appendix A

Abbreviations and acronyms used in this PhD thesis

AATSR	Advanced Along Track Scanning Radiometer
AMAXDOAS	Airborne Multi Axis DOAS
AMF	Air-Mass Factor
AMVER	Automated Mutual-assistance Vessel Rescue system
AOD	Aerosol Optical Depth
ATSR	Along Track Scanning Radiometer
AURA	NASA earth observing satellite
BIRA-IASB	Belgian Institute for Space Aeronomy
BL	Boundary Layer
CF	Cloud fraction
CFC	Chlorofluorocarbons
CG	Cloud to ground (flash)
CTM	Chemistry Transport Modell
DLR	German Aerospace Centre
DOAS	Differential Optical Absorption Spectroscopy
ECMWF	European Center for Medium Range Weather Forecasts
EDGAR	Emission inventory database
EFM	Exponential Fitting Method
ENVISAT	Environmental Satellite
ERS	European Remote Sensing Satellite
ESA	European Space Agency
ESRIN	European Space Research Institute
EUMETSAT	European Organisation for the Exploitation of Meteorological Satellites
Falcon	DLR research aircraft
FATE	Four-dimensional calculation of Aircraft Trajectories and Emissions
FLEXPART	Lagrangian particle dispersion model
FLEXTRA	Model for trajectory calculation
FRESCO	Fast Retrieval Scheme for Cloud Observables

FTS	Fourier Transform Spectrometer
FWHM	Full Width at Half Maximum
GASCOD	Gas Absorption Spectrometer Correlating Optical Differences
GCM	General Circulation Model
GOES	Geostationary weather satellite over America.
GOME	Global Ozone Monitoring Instrument
HICRU	Heidelberg Iterative Cloud Retrieval Utilities
HITRAN	High-resolution transmission molecular absorption database
IC	Intra-Cloud (flash)
ICT	Intercontinental Transport
IR	Infra Red
ITCZ	Intertropical Convergence Zone
IUP	Institut für Umweltphysik (Institute for environmental physics)
KNMI	Royal Netherlands Meteorological Institute
LIS	Lightning Imaging Sensor
LNO_x	Lightning produced NO_x
MFC	User program for the recording and evaluation of DOAS spectra
MODIS	Moderate Resolution Imaging Spectroradiometer
NAO	North Atlantic Oscillation
NCAR	National Center For Atmospheric Research (United States)
NCEP	National Centres for Environmental Prediction (United States)
NH	Northern Hemisphere
NLDN	National Lightning Detection Network
NO_x	Nitrogen oxide (NO) and Nitrogen Dioxide (NO_2)
NO_y	Further nitrogen containing molecules, e.g. HNO_3, NO_3, N_2O_5, HONO, $HONO_2$, HO_2NO_2, PAN
NSM	Narrow Swath Mode (GOME resolution of 80×40 km^2)
OLS	Operational Linescan System
OMI	Ozone Monitoring Instrument
OTD	Optical Transient Detector
PAN	Peroxyacetyl Nitrate
PMD	Polarisation Measuring Device
PSC	Polar Stratospheric Cloud

RTM	Radiative transfer modelling
SAA	Southern Atlantic Anomaly
SCD	Slant cloumn density
SCIAMACHY	SCanning Imaging Absorption spectroMeter for Atmospheric CartograpHY
SLIMCAT	Stratospheric chemistry model
SSM	Standard Swath Mode (GOME resolution of 320×40 km^2)
SZA	Solar Zenith Angle
TEMIS	Tropospheric Emission Monitoring Internet Service
TNO TPD	Institute of the Netherlands Organisation for Applied Scientific Research
TOMS	Total Ozone Mapping Spectrometer
TRACY	Monte Carlo based radiative trasfer model
TRMM	Tropical Rainfall Measuring Mission
TVCD	Tropospheric vertical column density
UT	Upper troposphere
UTC	Universal Time Coordinated
UV-vis	near ultraviolet and visible range of the electromagnetic spectrum (~300-800 nm)
VCD	Vertical column density
VOC	Volatile organic compounds
WCM	Weekly Cycle Method

Appendix B

The mean lifetime τ

Consider an amount V(t) of NO_x (e.g. in units of molec/cm^2, i.e. a VCD) that is exposed to chemical decay. In the following we consider the loss of NO_x to be of pseudo-first order with the loss rate k. In the simple case of constant k, the loss per time unit is proportional to V(t):

(B.1) $$\frac{dV(t)}{dt} = \dot{V}(t) = -k \cdot V(t) .$$

This results in an exponential drop of V:

(B.2) $V(t) = V_0 e^{-kt} = V_0 e^{-t/\tau}$, where τ=1/k is the ***lifetime*** of NO_x.

However, as k depends on many factors (see section 1.4.5), it is thus not constant, but a function of time. (In this study, however, we neglect a direct dependency of k on V).

The inverse rate constant

(B.3) $$\tau(t) = \frac{1}{k(t)}$$

is commonly defined as ***instantaneous*** lifetime (see also [Song et al., 2003], [Silman, 2000]).

For a time dependent rate constant k(t), the differential equation

(B.4) $$\frac{dV(t)}{dt} = \dot{V}(t) = -k(t) \cdot V(t)$$

has the solution

(B.5) $V(t) = V_0 e^{-\int k(t)dt}$.

Compared to eq. (B.2), the constant k in the exponent is replaced by the integrated rate constant k(t). By defining the ***mean*** rate constant

(B.6) $K(t) := \frac{1}{t}\int k(t')dt'$, eq. (B.5) can be transferred to a similar form as eq. (B.2):

(B.7) $$V(t) = V_0 e^{-K(t)t} = V_0 e^{-t/\overline{\tau}}$$

with the ***mean lifetime***

(B.8) $$\mathrm{T} := \overline{\tau}(t) = \frac{1}{\overline{K}(t)} = \frac{t}{\int k(t')dt'} = \frac{t}{\int \frac{dt'}{\tau(t')}}$$

Thus the mean rate constant is the *arithmetic* mean of k(t), while the appropriate mean lifetime is the *harmonic* mean of the instantaneous lifetimes.

Appendix C
Datasets used in this PhD-thesis

This PhD thesis was only possible thanks to the availability of the different data sets that have been used. Here we want to express our gratitude to the different institutions providing these datasets:

- First of all we want to thank **ESA** and the **DLR** for providing spectral GOME and SCIAMACHY data.
- Data on GOME **cloud fractions** are taken from
    - the **HICRU** database (Michael Grzegorski, personal communication, see [Grzegorski, 2003]).
    - the **FRESCO** database [Koelemeijer et al., 2001], available at www.temis.nl
- Thanks C. von Friedeburg for providing the **TRACY** software.
- **SLIMCAT** data has been provided by Martyn Chipperfield (personal communication). See *http://www.env.leeds.ac.uk/~martyn/slimcat.html* and [Chipperfield, 1999] for further information.
- Data on **aircraft emissions** have been received from Holger Pabst, DLR (personal communication). See *http://www.dlr.de/fw/*. For further information see [Brunner et al., 2002].
- Satellite based lightning counts (**LIS** data, [Christian et al., 1999]) are taken from *http://thunder.nsstc.nasa.gov/data/*. We acknowledge the Global Hydrology and Climate Center, 320 Sparkman Drive, Huntsville, AL 35805.
- Ground based lightning counts (**NLDN** data) are provided by Vaisala-GAI Inc. (T. Turner, personal communication). See *http://www.lightningstorm.com/* and also [Cummins et al., 1998].
- Fire counts are taken from **ATSR** data on *http://dup.esrin.esa.int/ionia/wfa/index.asp* We acknowledge the ATSR World Fire Atlas, European Space Agency - ESA/ESRIN, via Galileo Galilei, CP 64, 00044 Frascati, Italy.
- Composites of other trace gases are derived by colleagues of the IUP Heidelberg:
    - **CH_2O**: Thierry Marbach [Marbach et al., 2004].
    - **SO_2**: Fahim Khokhar [Khokhar et al., 2004].
    - **CO**: Christian Frankenberg [Frankenberg et al., 2004b].

  See *http://satellite.iup.uni-heidelberg.de*
- NO_x emissions of the **EDGAR** (V3.2) inventory [Olivier and Berdowski, 2001] are taken from *http://arch.rivm.nl/env/int/coredata/edgar/*. We acknowledge the EDGAR team, RIVM Office for Environmental Assessment, c/o Jeroen Peters, P.O. Box 1, NL-3720 BA Bilthoven, The Netherlands.
- Data on light pollution is provided by the **DMSP**: *http://dmsp.ngdc.noaa.gov/html/download.html*. We used the dataset of Radiance Calibrated Lights, 1996-1997. See also [Cinzano et al., 2001].

- Aerosol data (**MODIS**) are taken from *http://modis-atmos.gsfc.nasa.gov/IMAGES/mod08m_menu.html*
- Ship traffic distribution maps are received from O. Endresen, personal communication. Information on the **AMVER** database can be found on *http://www.amver.com/*
- NO_x emissions from **ships** are provided by O. Endresen, personal communication, and J. Corbett, personal communication
  (see also *http://www.ocean.udel.edu/cms/jcorbett/sea/nitrogen.html*).
  For further information see [Endresen et al., 2003] and [Corbett et al., 2003].
- Wind fields are taken from **NCEP/NCAR** Reanalysis data: *http://www.cdc.noaa.gov/HistData/*. For further reading see [Kanamitsu et al., 2002].

References

Aben, I., M.R. Dobber, D.M. Stam, and P. Stammes, Error analysis of polarisation measurements by GOME, *ESA, WPP-108 (GOME, Geophysical validation campaign, final results workshop proceedings) compiled by P. Fletcher and F. Lodge, Remote sensing applications consultants, Alton, UK,* 1996.

Alicke, B., The Role of Nitrous Acid in the Boundary Layer, *Ph.D. Thesis*, Universität Heidelberg, 2000.

Aliwell, S.R., P.V. Johnston, A. Richter, M. Van Roozendael, T. Wagner, D.W. Arlander, J.P. Burrows, D.J. Fish, R.L. Jones, K. Karlsen Tornkvist, J.-C. Lambert, K. Pfeilsticker and I. Pundt, Analysis for BrO in zenith-sky spectra - an intercomparison exercise for analysis improvement, J. Geophys. Res., 107, 10.1029/2001JD000329, 2002.

Amiro, B. D., Todd, J. B., Wotton, B. M., Logan, K. A., Flannigan, M. D., Stocks, B. J., Mason, J. A., Martell, D. L., and Hirsch, K.G.: Direct carbon emissions from Canadian forest fires, 1959–1999, Can. J. Forest Res., 31, 512–525, 2001.

Andreae, M. O. and Merlet, P.: Emission of trace gases and aerosols from biomass burning, Global Biogeochem. Cyc., 15, 955–966, 2001.

Andreae M. O. et al., Smoking Rain Clouds over the Amazon, *Science* 303, 1337-1342, 2004.

Atkinson, R., Atmospheric chemistry of VOCs and NO_x, *Atmos. Environ.*, *34*, 2063-2101, 2000.

Barrie, L. A.: Arctic air-pollution – an overview of current knowledge, Atmos. Environ., 20, 643–663, 1986.

Bayer, G., N. Wennström, and A. Kisliakova, Umweltpolitiken, -strategien und -programme der Beitrittsländer in Mittel- und Osteuropa, http://www.oekb.at/1/05/01/umwelt_f210.pdf, 2002.

Bednarz, F. (Ed.), Global Ozone Monitoring Experiment (GOME) Users Manual, 1995.

Beirle, S., J. Hollwedel, S. Kraus, T. Wagner, M. Wenig, W. Wilms-Grabe, and U. Platt, Estimation of NO_2 emissions from lightning and biomass burning: A case study using tropospheric NO_2-data deriverd from GOME, in *Air Pollution 2002*, edited by C.A. Brebbia, and J.F. Martin-Duque, pp. 473-479, WIT Press, Segovia, 2002.

Beirle, S., U. Platt, M. Wenig, and T. Wagner, Weekly cycle of NO_2 by GOME measurements: A signature of anthropogenic sources, *Atmos. Chem. Phys.*, *3*, 2225-2232, 2003.

Beirle, S., U. Platt, M. Wenig, and T. Wagner, NO_x production by lightning estimated with GOME, *Adv. Space Res.*, *34* (4), 793-797, 2004a.

Beirle, S., U. Platt, M. Wenig, and T. Wagner, Highly resolved global distribution of tropospheric NO_2 using GOME narrow swath mode data, *Atmos. Chem. Phys.*, *4*, 1913-1924, 2004b.

Beirle, S., U. Platt, R. von Glasow, M. Wenig, and T. Wagner, Estimate of nitrogen oxide emissions from shipping by satellite remote sensing, *Geophys. Res. Lett.*, *31*, L18102, doi:10.1029/2004GL020312, 2004c.

Beirle, S., U. Platt, and T. Wagner, Monitoring Nitrogen Oxides with Satellite Instruments: High resolution maps from GOME narrow swath mode and SCIAMACHY, in *ENVISAT Symposium*, Salzburg, 2004d.

Bodhaine, B. A.: Barrow surface aerosol: 1976–1987, Atmos. Environ., 23, 2357–2369, 1989.

Boersma, K.F., H.J. Eskes, and E.J. Brinksma, Error analysis for tropospheric NO_2 retrieval from space, *J. Geophys. Res.*, *109* (D04311), doi:10.1029/2003JD003962, 2004a.

Boersma, K. F., H. J. Eskes, and E. W. Meijer, Detection of Lightning NO_x with GOME, Proceedings Quadrennial Ozone Symposium, *1-8 June 2004, Kos, Greece, 1046-1047,* 2004b.

Bovensmann, et al., SCIAMACHY: Mission Objectives and Measurement Modes, *J. Atmos. Sci.*, 56(2), 127-150, 1999.

Bradshaw, J., D. Davis, G. Grodzinsky, S. Smyth, R. Newell, S. Sandholm, and S. Liu. Observed distribution of nitrogen oxides in the remote free troposphere from the NASA global tropospheric experiment programs. *Rev. Geoph.*, *38*, 611-116, 2000.

Brasseur, G., and S. Solomon, Aeronomy of the middle atmosphere, *D. Reidel Publishing company, The Netherlands,* 1984.

Brönnimann, S., and U. Neu, Weekend-weekday differences of near-surface ozone concentrations in Switzerland for different meteorological conditions, *Atmos. Environ.*, *31* (8), 1127-1135, 1997.

Bronstein, I.N., and K.A. Semendjajew, Taschenbuch der Mathematik, Verlag Harri Deutsch, Leipzig, 1971.

Brooks, C. E. P., The distribution of thunderstorms over the globe, Geophys Mem London 3 (24), 147-164, 1925.

Brunner, B., Pabst, H., Döpelheuer, A., Plohr, M.: Aircraft emissions inventories of the second generation. Atmospheric Sciences Programme, Session ST7, European Geophysical Society, Nice, France, 21.-26. April 2002, 27. General Assembly, 2002.

Bruns M., et al. Retrieval of Profile Information from Airborne Multi Axis UV/visible Skylight Absorption Measurements, *App.Opt 43* (22), 4415-4426*,* 2004.

Burrows J., Vountas M., Haug H., Chance K., Marquard L., Miurhead K., Platt U., Richter A., Rozanov V., Study of the Ring effect, Final Report for ESA Contract 109996/94/NL/CN, 1995.

Burrows, J.P., A. Dehn, B. Deters, S. Himmelmann, A. Richter, S. Voigt, and J. Orphal: „Atmospheric Remote-Sensing Reference Data from GOME: 1. Temperature-Dependent Absorption Cross Sections of NO_2 in the 231–794 nm Range", *Journal of Quantitative Spectroscopy and Radiative Transfer 60, 1025-1031,* 1998.

Burrows, J.P., A. Dehn, B. Deters, S. Himmelmann, A. Richter, S. Voigt, and J. Orphal: "Atmospheric Remote-Sensing Reference Data from GOME: 2. Temperature-Dependent Absorption Cross Sections of O_3 in the 231–794 nm Range", *Journal of Quantitative Spectroscopy and Radiative Transfer 61, 509-517,* 1999a.

Burrows, J., M. Weber, M. Buchwitz, V. Rozanov, A. Ladstetter-Weißenmayer, A. Richter, R. De Beek, R. Hoogen, K. Bramstedt, K.U. Eichmann, M. Eisinger, and D. Perner, The Global Ozone Monitoring Experiment (GOME): Mission concept and first scientific results, *J. Atmos. Sci.*, *56*, 151-175, 1999.

Burrows, J.P. and U. Platt (Editors), Probing the atmosphere in three dimensions for SCIAMACHY, ACPD - Special Issue, 2004.

Bussemer, M., Der Ring-Effekt: Ursachen und Einfluß auf die spektroskopische Messung stratosphärischer Spurenstoffe, *Diploma thesis, University of Heidelberg,* 1993.

Cerveny, R.S., and R.C. Balling, Weekly cycles of air pollutants, precipitation and tropical cyclones in the coastal NW Atlantic region, *Nature*, *394*, 561-563, 1998.

Chance, K., Palmer, P. I., Spurr, R. J. D., Martin, R. V., Kurosu, T. P., and Jacob, D. J.: Satellite observations of formaldehyde over North America from GOM, Geophys. Res. Lett., 27, 3461–3464, 2000.

Chipperfield, M., Multiannual simulations with a three-dimensional chemical transport model, *J. Geophys. Res.*, *104*, 1781-1805, 1999.

Christian, H.J., R.J. Blakeslee, S.J. Goodman, and etal, The lightning imaging sensor, *Proceedings of the 11th International Conference on Atmospheric Electricity, Guntersville, Alabama*, 746-749, 1999.

Cinzano, P., F. Falchi and C. D. Elvidge, The first World Atlas of the artificial night sky brightness, Mon. Not. R. Astron. Soc. 328, 689–707, 2001.

Cleveland, W.S., T.E. Graedel, B. Kleiner, and J.L. Warner, Sunday and workday variations in photochemical air pollutants in New Jersey and New York, *Science*, *186*, 1037-1038, 1974.

Conard, S. G. and Ivanova, G. A.: Wildfire in Russian boreal forests–potential impacts on fire regime characteristics on emissions and global carbon balance estimates, Env. Pollut., 98, 305–313, 1997.

Corbett, J.J., P.S. Fischbeck, and S.N. Pandis, Global nitrogen and sulfur inventories for oceangoing ships, *J. Geophys. Res.*, *104*, 3457-3470, doi:10.1029/1998JD100040, 1999.

Corbett, J.J., and H.W. Köhler, Updated emissions from ocean shipping, *J. Geophys. Res.*, *108*, 4650, doi:10.1029/2003JD003751, 2003.

Crutzen, P. J. and Merlet, A.: Biomass burning in the Tropics: Impact on atmospheric chemistry and biogeochemical cycles, Science, 250, 1669–1678, 1990.

Cummins, K. L., M. J. Murphy, E. A. Bardo, W. L. Hiscox, R. B. Pyle, A. E. Pifer, A combined TOA/MDF technology upgrade of the U.S. National Lightning Detection Network, J. Geophys. Res., 103(D8), 9035-9044, 10.1029/98JD00153, 1998.

Damoah, R., N. Spichtinger, C. Forster, P. James, I. Mattis, U. Wandinger, S. Beirle, T. Wagner, and A. Stohl, Around the world in 17 days – hemispheric-scale transport of forest fire smoke from Russia in May 2003, *Atmos. Chem. Phys.*, *4*, 1311-1321, 2004.

Davidson, E.A., and W. Kingerlee, A global inventory of nitric oxide emissions from soils, *Nutrient Cycling in Agroecosystems*, *48*, 37-50, 1997.

Davis, D.D., et al., Impact of ship emissions on marine boundary layer NO_x and SO_2 distributions over the Pacific basin, *Geophys. Res. Lett.*, *28*, 235-238, 2001.

DeCaria, A.J., K.E. Pickering, G.L. Stenchikov, J.R. Scala, J.L. Stith, J.E. Dye, B.A. Ridley, and P. Laroche, A cloud-scale model study of lightning generated NO_x in an individual thunderstorm during STERAO-A, *J. Geophys. Res.*, *105*, 11601-11616, 2000.

Doll, C.N.H., Muller, J-P., Elvidge, C.D., Night-time Imagery as a Tool for Global Mapping of Socio-economic Parameters and Greenhouse Gas Emissions. Ambio, 29(3), pp. 157-162, 2000.

Domine, F. and P. B. Shepson, Air-Snow Interactions and Atmospheric Chemistry, Science 297, 1506-1510, 2002

Dye, J.E., et. al, An overview of the Stratospheric-Tropospheric Experiment: Radiation, Aerosols and Ozone (STERAO)-Deep Convection experiment with result from the July 10, 1996 storm, *J. Geophys. Res.*, *105*, 10,023-10,045, 2000.

Eckhardt, S., A. Stohl, S. Beirle, N. Spichtinger, P. James, C. Forster, C. Junker, T. Wagner, U. Platt, and S.G. Jennings, The North Atlantic Oscillation controls air pollution transport to the Arctic, *Atmos. Chem. Phys.*, *3*, 1769-1778, 2003.

Elkus, B., and K.R. Wilson, Photochemical air pollution: weekend-weekday differences, *Atmos. Environ.*, *11*, 509-515, 1977.

Endresen, Ø., E. Sørgård, J.K. Sundet, S.B. Dalsøren, I.S.A. Isaksen, T.F. Berglen, and G. Gravir, Emission from international sea transportation and environmental impact, *J. Geophys. Res.*, *108* (D17), 4560, doi:10.1029/2002JD002898, 2003.

Fehr, T., H. Höller, and H. Huntrieser, Model study on production and transport of lightning-produced NO_x in a EULINOX supercell storm, *J. Geophys. Res.*, *109*, D09102, doi:10.1029/2003JD003935, 2004.

Ferlemann, F., Ballongestützte Messung stratosphärischer Spurengase mit differentieller optischer Absorptionsspektroskopie, *PhD-thesis, University of Heidelberg, Germany,* 1998.

Flannigan, M. D., Bergeron, Y., Engelmark, O., and Wotton, B.M.: Future wildfire in circumboreal forests in relation to global warming, J. Vegetation Sci., 9, 469–476, 1998.

Forster, C., Wandinger, U., Wotawa, G., James, P., Mattis, I., Althausen, D., Simmonds, P., O'Doherty, S., Kleefeld, C., Jennings, S. G., Schneider, J., Trickl, T., Kreipl, S., Jäger, H., and Stohl, A.: Transport of boreal forest fire emissions from Canada to Europe, J. Geophys. Res., 106, 22 887–22 906, 2001.

Frankenberg, C., U. Platt, T. Wagner, Iterative maximum a posteriori (IMAP)-DOAS for retrieval of strongly absorbing trace gases: Model studies for CH_4 and CO_2 retrieval from near infrared spectra of SCIAMACHY onboard ENVISAT, Atmos. Chem. Phys. Discuss., 4, 6067-6106, 2004a.

Frankenberg, C., U. Platt, and T. Wagner, Retrieval of CO from SCIAMACHY onboard ENVISAT, Proceedings of the ENVISAT & ERS Symposium, *6-10 September 2004, Salzburg, Austria, ESA publication SP-572, (CD-ROM),* 2004b.

Frieß, U., Stratospheric measurements of atmospheric trace gases at Neumayer station, Antarctica, *Ph.D. Thesis*, Universität Heidelberg, 2001.

Galanter, M., Levy II, H., and Carmichael, G. R.: Impacts of biomass burning on tropospheric CO,NOx,and O3, J. Geophys. Res., 105, 6633–6653, 2000.

Garrett, T. J., Radke, L. F., and Hobbs, P. V.: Aerosol effects on cloud emissivity and surface longwave heating in the Arctic, J. Atmos. Sci., 59, 769–778, 2002.

Geyer, A., and U. Platt, The temperature dependence of the NO_3 degradation frequency - a new indicator for the contribution of NO_3 to VOC oxidation and NO_x removal in the atmosphere, *J. Geophys. Res.*, *107*, 4431-4442, doi:10.1029/2001JD001215, 2002.

Gillani, N. V., M. Luria, R. J. Valente, R. L. Tanner, R. E. Imhoff, and J. F. Meagher, Loss rate of NO_y from a power plant plume based on aircraft measurements, *J. Geophys. Res., 103,* 22585-22592, 1998.

Goldenbaum, G.C., and R.R. Dickerson, Nitric oxide production by lightning discharges, *J. Geophys. Res.*, *98* (D10), 18333-18338, doi:10.1029/93JD01018, 1993.

Gomer, T., T. Brauers, F. Heintz, J. Stutz, and U. Platt, MFC user manual, version 1.98, *inhouse publication, Institut für Umweltphysik, University of Heidelberg, Germany,* 1993.

Grainger, J.F., and J. Ring, Anomalous Fraunhofer line profiles, *Nature, 193, 762,* 1962.

Greenblatt G. D., J.J. Orlando, J.B. Burkholder, and A.R. Ravishankara, Absorption measurements of oxygen between 330 and 1140 nm, *J. Geophys. Res., 95, 18577-18582,* 1990.

Grzegorski, M., Determination of cloud parameters for the Global Ozone Monitoring Experiment with broad band spectrometers and from absorption bands of oxygen dimer, Diploma thesis, University of Heidelberg, Germany, 2003.

Grzegorski, M. et al., The Heidelberg Iterative Cloud Retrieval Utility, Manuscript in preparation, 2004.

Heikes, B., M. Lee, D. Jacob, R. Talbot, J. Bradshaw, H. Singh, D. Blake, B. Anderson, H. Fuelberg, and A. Thompson, Ozone, hydroperoxides, oxides of nitrogen, and hydrocarbon budgets in the marine boundary layer over the South Atlantic, *J. Geophys. Res.*, *101*, 24,221-24,234, 1996.

Heirtzler, J., The future of the South Atlantic anomaly and implications for radiation damage in space, *Journal of Atmospheric and Solar-Terrestrial Physics*, *64*, 1701-1708, 2002.

Heue, K.-P., S. Beirle, M. Bruns, J.P. Burrows, U. Platt, I. Pundt, A. Richter, T. Wagner, and P. Wang, SCIAMACHY validation using the AMAXDOAS instrument, Proceedings of the ENVISAT & ERS Symposium, *6-10 September 2004, Salzburg, Austria, ESA publication SP-572, (CD-ROM),* 2004a.

Heue, K.-P., A. Richter, T. Wagner, M. Bruns, J. Burrows, C.v. Friedeburg, W.D. Lee, U. Platt, I. Pundt, and P. Wang, Validation of SCIAMACHY tropospheric NO2-columns with AMAXDOAS measurements, *accepted for publication in Atmos. Chem. Phys. Discuss.*, 2004b.

Hild, L., A. Richter, and J.P. Burrows, Measurements of lightning-produced NO_2 by GOME and LIS, *Symposium 2000 in Göteburg - Session: Atmosphere UV Radiation, Trace Gases Other Than Ozone*, *ID Nr. 349*, 2000.

Höller, H., and U. Schumann (Eds.), EULINOX - The European lightning nitrogen oxides project. *DLR-Forschungsbericht 2000-28*, 2000.

Hönninger, G., C.v. Friedeburg, and U. Platt, Multi Axis Differential Optical Absorption Spectroscopy (MAX-DOAS), *Atmos. Chem. Phys.*, *4*, 231-254, 2004.

Huntrieser, H., H. Schlager, C. Feigl, and etal, Transport and production of NO_x in electrified thunderstorms: Survey of previous studies and new observations at midlatitudes, *J. Geophys. Res.*, *103*, 28,247-28,264, 1998.

Hurrell, J. W.: Decadal trends in the North Atlantic Oscillation: Regional temperatures and precipitation, Science, 269, 676–679, 1995.

Jacob, D., Introduction to Atmospheric Chemistry, Princeton University Press, New Jersey, 1999.

Jaeglé, L., D.J. Jacob, Y. Wang, and etal, Sources and chemistry of NO_x in the upper troposphere over the United States, *Geophys. Res. Lett.*, *25*, 1709-1712, 1998.

Jaegle, L., Satellite mapping of rain-induced nitric oxide emissions from soils, *J. Geophys. Res.*, **109**, D21310, doi:10.1029/2004JD004787, 2004.

Jaffe, D., Anderson, T., Covert, D., et al.: Transport of Asian air pollution to North America, Geophys. Res. Lett., 26, 711–714, 1999.

John, J. C. St., W. L. Chameides, and R. Saylor, Role of anthropogenic NO_x and VOC as ozone precursors: A case study from the SOS Nashville/ Middle Tennessee Ozone Study, *J. Geophys. Res.*, *103*, 22415-22423, 1998.

Johnston, P.V., Studies on the I_0-effect, unpublished manuscript, 1996.

Jourdain, L., and D. Hauglustaine, The global distribution of lightning NO_x simulated on-line in a General Circulation Model, *Phys. Chem. Earth (C)*, *26*, 585-591, 2001.

Kanamitsu, M., W. Ebisuzaki, J. Woollen, S.-K. Yang, J.J. Hnilo, M. Fiorino, and G.L. Potter, NCEP-DEO AMIP-II reanalysis (R-2), *Bull. of the Atmos. Met. Soc.*, *83*, 1631-1643, 2002.

Kasibhatla, P., et al., Do emissions from ships have a significant impact on concentration of nitrogen oxides in the marine boundary layer?, *Geophys. Res. Lett.*, *27*, 2229-2232, 2000.

Khokhar, M. F., C. Frankenberg, J. Hollwedel, S. Beirle, S. Kühl, M. Grzegorski, W. Wilms-Grabe, U. Platt and T. Wagner, Satellite remote sensing of atmospheric SO2: Volcanic eruptions and anthropogenic emissions, Proceedings of the ENVISAT & ERS Symposium, *6-10 September 2004, Salzburg, Austria, ESA publication SP-572, (CD-ROM),* 2004.

Klemm, O., W. R. Stockwell, H. Schlager, and H. Ziereis, Measurements of nitrogen oxides from aircraft in the northeast Atlantic flight corridor, *J. Geopghys. Res., 103,* 31217-31229, 1998.

Koelemeijer, R.B.A., J.F.d. Haan, and P. Stammes, A database of spectral surface reflectivity in the range 335-772 nm derived from 5.5 years of GOME observations, *J. Geophys. Res.*, *108* (D2), 4070, doi:10.1029/2002JD002429, 2003.

Koelemeijer, R.B.A., P. Stammes, J.W. Hovenier, and J.F.d. Haan, A fast method for retrieval of cloud parameters using oxygen A-band measurements from the Global Ozone Monitoring Experiment, *J. Geophys. Res.*, *106*, 3475-3490, 2001.

Kraus, S., Entwicklung eines flexiblen Softwaresystems zur Auswertung spektroskopischer Satelliten-Bildsequenzen, PhD thesis, Technische Informatik, Universität Mannheim, 2004.

Kurosu, T., Die Modellierung des Strahlungstransports in Wolken für atmosphärische Fernerkundungim Ultravioletten und sichtbaren Spektralbereich, *PhD-thesis, University of Bremen, Wissenschaftsverlag, Achen, Germany,* 1997.

Kuze, A., and K.V. Chance, Analysis of Cloud-Top Height and Cloud Coverage from Satellites Using the O_2 A and B Bands, *J. Geophys. Res.*, *99*, 14481-14491, 1994.

Labrador L. J., R. von Kuhlmann, M. G. Lawrence, Strong sensitivity of the global mean OH concentration and the tropospheric oxidizing efficiency to the source of NO_x from lightning, Geophys. Res. Lett., 31, L06102, doi:10.1029/2003GL019229, 2004.

Ladstätter-Weißenmayer, A., J. Burrows, and D. Perner, Biomass burning over Indonesia as observed by GOME, *Earth Obs. Quart.*, *58*, 28-29, 1998.

Langmann, B. and H.F. Graf, Indonesian smoke aerosols from peat fires and the contribution from volcanic sulfur emissions, Geophys. Res. Lett. 30 (11), 1547, doi:10.1029/2002GL016646, 2003.

Lavoue, D. C., Liousse, C., Cachier, H., Stocks, B. J., and Goldammer, J. G.: Modelling of carbonaceous particles emitted by boreal and temperate wildfires at northern latitudes, J. Geophys. Res., 105, 26 871–26 890, 2000.

Lawrence, M.G., W.L. Chameides, P.S. Kasibhatla, H.L. II, and W. Moxim, Lightning and atmospheric chemistry: The role of atmospheric NO production, in *Handbook of Atmospheric Electrodynamics*, edited by H. Volland, pp. 189-202, CRC Press Boca Raton, Fla., 1995.

Lawrence, M.G., and P.J. Crutzen, Influence of NO_x emissions from ships on tropospheric photochemistry and climate, *Nature*, *402*, 167-170, 1999.

Lee, D.S., I. Köhler, E. Grobler, F. Rohrer, R. Sausen, L. Gallardo-Klenner, J.G.J. Olivier, F.J. Dentener, and A.F. Bouwman, Estimations of global NO_x emissions and their uncertainties, *Atmos. Environ.*, *31*, 1735-1749, 1997.

Leue, C., Globale Bilanzierung der NO_x-Emissionen aus GOME Satelliten-Bildfolgen, *PhD thesis, University of Heidelberg,* 1999.

Leue, C., M. Wenig, T. Wagner, O. Klimm, U. Platt, and B. Jähne, Quantitative analysis of NO_2 emissions from GOME satellite image sequences, *J. Geophys. Res.*, *106* (5493-5505), 2001.

Levenberg, K., A method for the solution of certain non-linear problems in least squares, *Quart. Appl., Math., 2, 164-168,* 1944.

Levy II, H., W.J. Moxim, and P.S. Kasibhatla, A global three-dimensional time-dependent lightning source of tropospheric NO_x, *J. Geophys. Res.*, *101* (D17), 22911-22922, doi:10.1029/96JD02341, 1996.

Levy, H., II, W. J. Moxim, A. A. Klonecki, and P. S. Kasibhatla, Simulated tropospheric NO_x: Its evaluation, global distribution and individual source contributions, *J. Geopghys. Res., 104,* 26279-26306, 1999

Li, C., Cornett, J., and Ungar, K.: Long-term decrease of cadmiumconcentrations in the Canadian Arctic air, Geophys. Res. Lett., 30, 1256, doi: 10.1029/2002GL016723, 2003.

Lim, E.-P. and Simmonds, I.: Explosive cyclone development in the Southern Hemisphere and a comparison with Northern Hemisphere events, Mon. Wea. Rev., 130, 2188–2209, 2002.

Lutgens, F.K., and E.J. Tarbuck, *The Atmosphere: An Introduction to Meteorology*, Prentice-Hall, Old Tappan, N. J., 1997.

Mackerras, D., M. Darveniza, R.E. Orville, and etal, Global lightning: Total, cloud and ground flash estimates, *J. Geophys. Res.*, *103* (D16), 19791-19809, 1998.

Marbach, T., S. Beirle, J. Hollwedel, U. Platt, T. Wagner, Identification of tropospheric emission sources from satellite observations: Synergistic use of trace gas measurements of formaldehyde (HCHO), and nitrogen dioxide (NO_2), Proceedings of the ENVISAT & ERS Symposium, *6-10 September 2004, Salzburg, Austria, ESA publication SP-572, (CD-ROM),* 2004.

Marquard, L.C., and U. Platt, AMFTRAN: A new Monte Carlo radiative transport model for calculating air mass factors, *Nato ASI series, Subseries I, Atmospheric ozone dynamics - observations in the mediteranean region (C. Varotsos, edit.), 231-241, Springer, Heidelberg,* 1997.

Marquardt, D.W., An algorithm for least-quares estimation of nonlinear parameters, *J. Soc. Indust. Math., 11, 431-441,* 1963.

Marr, C., and R.A. Harley, Spectral analysis of weekday–weekend differences in ambient ozone, nitrogen oxide, and non-methane hydrocarbon time series in California, *Atmos. Environ.*, *36* (14), 2327-2335, 2002.

Martin, R.V., K. Chance, D.J. Jacob, T.P. Kurosu, R.J.D. Spurr, E. Bucsela, J.F. Gleason, P.I. Palmer, I. Bey, A.M. Fiore, Q. Li, R.M. Yantosca, and R.B.A. Koelemeijer, An improved retrieval of tropospheric nitrogen dioxide from GOME, *J. Geophys. Res.*, *107* (D20), 4437, doi:10.1029/2001JD001027, 2002.

Martin, R.V., D.J. Jacob, K. Chance, T.P. Kurosu, P.I. Palmer, and M.J. Evans, Global inventory of nitrogen oxide emissions constrained by space-based observations of NO_2 columns, *J. Geophys. Res.*, *108*, 4537, doi:10.1029/2003JD003453, 2003.

Martin, R.V., A.M. Fiore, and A. Van Donkelaar, Spaced-based diagnosis of surface ozone sensitivity to anthropogenic emissions, *Geophys. Res. Lett.*, *31*, L06120, 2004.

Meijer, S. N., Ockenden, W. A., Sweetman, A., Breivik, K., Grimalt, J. O., and Jones, K. C.: Global distribution and budget of PCBs and HCB in background surface soils: implications for sources and environmental processes, Environ. Sci. Technol., 37, 667–672, 2003.

Mitchell, J. M.: Visual range in the polar regions with particulate reference to the Alaskan Arctic, J. Atmos. Terr. Phys. Special Suppl., 195–211, 1957.

Monteith, D. T., Evans, C. D., and Reynolds, B.: Are temporal variations in the nitrate content of UK upland freshwaters linked to the North Atlantic Oscillation?, Hydrol. Process. 14, 1745–1749, 2000.

Moritz, R. E., Bitz, C. M., and Steig, E. J.: Dynamics of recent climate change in the Arctic, Science, 297, 1497–1502, 2002.

Nesbitt, S.W., R. Zhang, and R.E. Orville, Seasonal and global NO_x production by lightning estimated from the Optical Transient Detector (OTD), *Tellus*, *52B*, 1206-1215, 2000.

Noxon, J. F., Atmospheric Nitrogen Fixation By Lightning, Geophysical Research Letters, 3:463-465, 1976.

Nunnermacker, L. J., L. I. Kleinman, D. Imre, P. H. Daum, Y.-N. Lee, J. H. Lee, S. R. Springston, and L. Newman, NO_y lifetimes and O_3 production efficiencies in urban and power plant plumes: Analysis of field data, *J. Geopghys. Res., 105*, 9165-9176, 2000

Olivier, J.G.J., and J.J.M. Berdowski, Global emissions sources and sinks, in *The Climate System*, edited by J. Berdowski, R. Guicherit, and B.J. Heij, pp. 33-78, A.A. Balkema Publishers/Swets & Zeitlinger Publishers, Lisse, The Netherlands, 2001.

Ottoy, J., and G. Vansteenkiste, A computer algorithm for non-linear curve fitting, Adv. Eng. Software, 3, 55-61, 1981.

Pearl, H. W. and Whitall, D. R.: Anthropogenically-derived atmospheric nitrogen deposition, marine eutrophication and harmful algal bloom expansion: is there a link?, Ambio, 28, 307–311, 1999.

Penkett, S. A. and Brice, K. A.: The spring maximum in photooxidants in the Northern Hemisphere troposphere, Nature, 319, 655–657, 1986.

Penner, J.E., D.J. Bergmann, J.J. Walton, and etal, An evaluation of upper troposphere NO_x with two models, *J. Geophys. Res.*, *103* (D17), 22097-22113, 1998.

Perner, D. and U. Platt, Detection of nitrous acid in the atmosphere by differential optical absorption, *Geophys. Res. Lett., 7, 1053-1056,* 1979.

Platt, U., D. Perner, G.W. Harris, A.M. Winer, and J.N. Pitts, Observations of nitrous acid in an urban atmosphere by differential optical absorption, *Nature*, *285*, 312-314, 1980.

Platt, U., Differential optical absorption spectroscopy (DOAS), in *Air Monitoring by Spectrometric Techniques*, edited by M. Sigrist, pp. 27-84, John Wilsy, New York, 1994.

Platt, U., L. Marquard, T. Wagner, and D. Perner, Corrections for zenith scattered light DOAS, *Geophys. Res. Lett., 24, 1759-1762,* 1997.

Polissar, A., Hopke, P. K., and Harris, J. M.: Source regions for atmospheric aerosol measured at Barrow, Alaska. Environ. Sci. Technol., 35, 4214–4226, 2001.

Potter, C.S., P.A. Matson, P.M. Vitousek, and etal, Process modelling of controls on nitrogen trace gas emissions from soils worldwide, *J. Geophys. Res.*, *101* (D1), 1361-1377, 1996.

Prentice and Mackerras, The ratio of cloud to cloud - ground lightning flashes in thunderstorms, J. Appl. Meteorol. 16, 545-550, 1977.

Price, C., J. Penner, and M. Prather, NO_x from lightning (1). Global distribution based on lightning physics, *J. Geophys. Res.*, *102*, 5929-5941, 1997.

Richter, A., Absorptionsspektroskopische Messungen stratosphaerischer Spurengase über Bremen, 53°N, *PhD Thesis, University of Bremen,* 1997.

Richter, A., and T. Wagner, Diffuser Plate Spectral Structures and their Influence on GOME Slant Columns, http://www-iup.physik.uni-bremen.de/gome/data/diffuser_gome.pdf, 2001.

Richter, A., F. Wittrock, A. Ladstätter-Weißenmayer, and J.P. Burrows, GOME measurements of stratospheric and tropospheric BrO, Adv. Space Res., 29(11), 1667-1672, 2002a.

Richter, A., and J. Burrows, Retrieval of Tropospheric NO_2 from GOME Measurements, *Adv. Space Res.*, *29* (11), 1673-1683, 2002b.

Richter, A., F. Wittrock, M. Weber, S. Beirle, S. Kühl, U. Platt, T. Wagner, W. Wilms-Grabe, and J. P. Burrows, GOME observations of stratospheric trace gas distributions during the splitting vortex event in the Antarctic winter 2002 Part I: Measurements, accepted for publication in J. Atmos. Sci., 2004a

Richter, A., V. Eyring, J. Burrows, H. Bovensmann, A. Lauer, B. Sierk, and P.J. Crutzen, Satellite Measurements of NO_2 from international shipping emissions, *submitted to Geophys. Res. Lett.*, 2004b.

Richter, A., et al., Long term measurements of NO_2 and other tropospheric species from space, Proceedings Quadrennial Ozone Symposium, 1-8 June 2004, Kos, Greece, pp 213-214, 2004c.

Rodgers, C.D.: Inversion methods for atmospheric sounding - theory and practice, Series on Atmospheric, Oceanic and Planetary Physics, World Scientific Publishing, Singapore, 2000.

Roscoe, H.K., D.J. Fish, and R.L. Jones, Interpolation error in UV-visible spectroscopy for stratospheric sensing: implications for sensitivity, spectral resolution, and spectral range, *Applied optics, 35, 427-432,* 1996.

Rothman, L.S., The HITRAN data base, *J. Quant. Spectrosc. Radiat. Transfer, 48,* 5, 6, 1992.

Ryerson, T. B., M. P. Buhr, G. J. Frost, P. D. Goldan, J. S. Holloway, G. Hübler, B. T. Jobson, W. C. Kuster, S. A. McKeen, D. D. Parrish, J. M. Roberts, D. T. Sueper, M. Trainer, J. Williams, and F. C. Fehsenfeld, Emissions lifetimes and ozone formation in power plant plumes, *J. Geopghys. Res., 103,* 22569-22583, 1998.

Sanders, F. and Gyakum, J. R.: Synoptic-dynamic climatology of the “bomb”, Mon. Wea. Rev., 108, 1589–1606, 1980.

Schurath, U., Lecture on Atmospheric Chemistry, Summer school Heidelberg, 2003.

Seinfeld, J.H., and S.N. Pandis, *Atmospheric Chemistry and Physics*, John Wiley, Hoboken, N. J., 1997.

Sillman, S., Ozone production efficiency and loss of NO_x in power plant plumes: Photochemical model and interpretation of measurements in Tennessee, *J. Geophys. Res.*, *105* (D7), 9189-9202, doi:10.1029/1999JD901014, 2000.

Sillman, S., and D. He, Some theoretical results concerning O3-NO_x-VOC chemistry and NO_x-VOC indicators, J. Geophys. Res., 107, 10.1029/2001JD001123, 2002.

Skamarock, W.C., J.E. Dye, E. Defer, M.C. Barth, J.L. Stith, B.A. Ridley, and K. Baumann, Observational- and model-based budget of lightning produced NO_x in a continental thunderstorm, *J. Geophys. Res.*, *108* (D10), 4305, doi:10.1029/2002JD002163, 2003.

Solomon, S., A. L. Schmeltekopf, and R. W. Sanders, On the interpretation of zenith sky absorption measurements, *J. Geophys. Res, 92, 8311-8319,* 1987.

Solomon, S., Stratospheric ozone depletion: A review of concepts and history, *Reviews of Geophysics, 37(3), 275-316*, 1999.

Song, C.H., G. Chen, S.R. Hanna, J. Crawford, and D.D. Davis, Dispersion and chemical evolution of ship plumes in the maritime boundary layer: Investigation of $O_3/NO_y/HO_x$ chemistry, *J. Geophys. Res.*, *108* (D4), 4143, doi:10.1029/2002JD002216, 2003.

Spicer, C.W., Nitrogen Oxide Reactions in the Urban Plume of Boston, *Science*, *215*, 1095-1097, 1982.

Spichtinger, N., M. Wenig, P. James, U. Platt, and A. Stohl, Satellite detection of a continental-scale plume of nitrogen oxides from boreal forest fires, *J. Geophys. Res.*, *28*, 4579-4583, 2001.

Spichtinger, N., R. Damoah, S. Eckhardt, C. Forster, P. James, S. Beirle, T. Wagner, P.C. Novelli, and A. Stohl, Boreal forest fires in 1997 and 1998: a seasonal comparison using transport model simulations and measurement data, *Atmos. Chem. Phys. Disc.*, *4*, 2747-2779, 2004.

Stammes, P., I. Aben, R.B.A. Koelemeijer et al., GOME polarisation validation study, *ESA SP-414, 669-674,* 1997.

Stark, M.S., J.T.H. Harrison, and C. Anastasi, Formation of nitrogen oxides by electrical discharges and implications for atmospheric lightning, *J. Geophys. Res.*, *101* (D3), 6963-6970, doi:10.1029/95JD03008, 1996.

Stocks, B. J., Fosberg, M. A., Lynham, T. J., Mearns, L.,Wotton, B.M., Yang, Q., Jin, J.-Z., Lawrence, K., Hartley, G. R., Mason, J.A., and McKenney, D. W.: Climate change and forest fire potential in Russian and Canadian boreal forests, Clim. Change, 38, 1–13, 1998.

Stohl, A., Hittenberger, M., and Wotawa, G.: Validation of the Lagrangian particle dispersion model FLEXPART against large scale tracer experiment data, Atmos. Environ., 32, 4245–4264, 1998.

Stohl, A. and Trickl, T.: A textbook example of long-range transport: Simultaneous observation of ozone maxima of stratospheric and North American origin in the free troposphere over Europe, J. Geophys. Res., 104, 30 445–30 462, 1999.

Stohl, A., H. Huntrieser, A. Richter, S. Beirle, O.R. Cooper, S. Eckhardt, C. Forster, P. James, N. Spichtinger, M. Wenig, T. Wagner, J.P. Burrows, and U. Platt, Rapid intercontinental air pollution transport associated with a meteorological bomb, *Atmos. Chem. Phys.*, *3*, 969-985, 2003.

Stohl, A., Forster, C., Eckhardt, S., Spichtinger, N., Huntrieser, H., Heland, J., Schlager, H., Wilhelm, S., Arnold, F., and Cooper, O.: A backward modeling study of intercontinental pollution transport using aircraft measurements, J. Geophys. Res., in press, 2003.

Stutz J., and U. Platt, Numerical analysis and error estimation of Differential Optical Absorption Spectroscopy measurements least-squares methods, *Appl. Optics, 35, 6041-6053,* 1996.

Tanzi, C.P., E. Hegels, I. Aben, K. Bramstedt, and A.P.H. Goede, Performance Degradation of GOME Polarization Monitoring, *Adv. Space Res.*, *23*, 1393-1396, 2000.

Thomas, W., E. Hegels, S. Slijkhuis, R. Spurr, and K. Chance, Detection of biomass burning combustion products in Southeast Asia from backscatter data taken by the GOME spectrometer, *Geophys. Res. Lett.*, *25* (9), 1317-1320, 1998.

Thompson, A. M., et al., Ozone over southern Africa during SAFARI-92/TRACE A, J. Geophys. Res. 101 (D19) 23,793–23,808, 1996.

Toeges-Schuller, N., et al., Global distribution pattern of anthropogenic NO_x emissions: Correlation error analysis of satellite measurements and model calculations, paper in preparation, 2004.

Tie, X., R. Zhang, G. Brasseur et al., Global NO_x production by lightning, *J. Atmos. Chem.*, 43, 61-74, 2002.

Valks P. J. M., R. B. A. Koelemeijer, M. van Weele, P. van Velthoven, J. P. F. Fortuin, H. Kelder, Variability in tropical tropospheric ozone: Analysis with Global Ozone Monitoring Experiment observations and a global model, J. Geophys. Res., 108 (D11), 4328, doi:10.1029/2002JD002894, 2003

Velders, G.J.M., C. Granier, R.W. Portmann, K. Pfeilsticker, M. Wenig, T. Wagner, U. Platt, A. Richter, and J. Burrows, Global tropospheric NO_2 column distributions: Comparing 3-D model calculations with GOME measurements, *J. Geophys. Res.*, *106*, 12643-12660, 2001.

Velthoven, P. F. J. van, R. Sausen, C. E. Johnson, H. Kelder, I. Köhler, B. Kraus, R. Ramaroson, F. Rohrer, D. Stevenson, A. Strand, and W. M. F. Wauben, The passive transport of NO_x emissions from aircraft studied with a hierarchy of models, *Atmos. Env., 31*, 1783-1799, 1997.

von Bargen, A., T. Kuroso, K. Chance, D. Loyola, B. Aberle, and R. Spurr, Cloud retrieval algorithm for GOME (CRAG) Final Report, ESA publication ER-TN-DLR-CRAG-007, http://atmos.af.op.dlr.de/documents/projdocs/crag_freport.pdf, 2000.

von Friedeburg, C., Derivation of trace gas information combining differential optical absorption spectroscopy with radiative transfer modelling, Ph.D. thesis, University of Heidelberg, Germany2003.

von Glasow, R., M.G. Lawrence, R. Sander, and P.J. Crutzen, Modeling the chemical effects of ship exhaust in the cloud-free marine boundary layer, *Atmos. Chem. Phys.*, *3*, 233-250, 2003.

Vountas, M., V.V.Rozanov, and J.P. Burrows, Ring Effect: Impact of rotational Raman scattering on radiative transfer in Earth's Atmosphere, Vol. 60, No. 6, 943-961, *Journal of Quantitative Spectroscopy and Radiative Transfer,* 1998.

Wagner, T., Satellite observations of atmospheric halogen oxides, Ph.D. thesis, University of Heidelberg, http://www.ub.uni-heidelberg.de/archiv/539, 1999.

Wagner, T., C. Leue, M. Wenig, K. Pfeilsticker, and U. Platt, Spatial and temporal distribution of enhanced boundary layer BrO concentrations measured by the GOME instrument aboard ERS-2, *J. Geophys. Res.*, *106*, 24225-24236, 2001a.

Wagner T. et al., The AMAXDOAS instrument and its application for SCIAMACHY validation, *Proceedings of the 15th ESA symposium on rocket and balloon program and related research,* Biarritz France, 28-31 May 2001, ESA SP-471, August 2001b.

Wagner, T., K. Chance, U. Frieß, M. Gil, F. Goutail, G. Hönninger, P.V. Johnston, K. Karlsen-Tørnkvist, I. Kostadinov, H. Leser, A. Petritoli, A. Richter, M. Van Roozendael, U. Platt, Correction of the Ring effect and I0-effect for DOAS observations of scattered sunlight, Proc. of the 1st DOAS Workshop, Heidelberg, 13., 14. Sept., Heidelberg, Germany, 2001c.

Wagner, T., C. von Friedeburg, M. Wenig, C. Otten, and U. Platt, UV/vis observations of atmospheric O4 absorptions using direct moon light and zenith scattered sunlight under clear and cloudy sky conditions, J. Geophys. Res., VOL. 107, NO. D20, 4424, doi:10.1029/2001JD001026, 2002a.

Wagner, T., M. Grzegorski, C. v.Friedeburg, S. Beirle, M.F. Khokhar, S. Kühl, M. Wenig, W. Wilms-Grabe, and U. Platt, SCIA Nadir observations of NO2 and BrO, presentation at the First German GOME / SCIAMACHY workshop, Bremen, November 25th and 26th 2002b (http://www.iup.physik.uni-bremen.de/gcvos/scia_gome_ws_nov02/wagner_uvvis.pdf).

Wagner, T., A. Richter, C. v. Friedeburg, U. Platt, An Advanced Cloud Product for the Interpretation of Tropospheric Data from GOME and SCIAMACHY, Proceedings of the EUROTRAC-2 Symposium 2002, Garmisch-Partenkirchen, Germany, March 11 - 15, 2002, Transport and Chemical Transformation in the Troposphere, P. Midgley and M. Reuther (Eds.), Margraf Verlag, Weikersheim, Germany, 2002c.

Wagner, T., A. Richter, C. von Friedeburg, M. Wenig, and U. Platt, Case Studies for the Investigation of Cloud Sensitive Parameters as Measured by GOME, in *TROPOSAT final report, Sounding the Troposphere from Space: a New Era for Atmospheric Chemistry*, pp. 199-210, Springer, Berlin, 2003.

Wania, F.: Assessing the potential of persistent organic chemicals for long-range transport and accumulation in polar regions, Environ. Sci. Technol., 37, 1344–1351, 2003.

Wenig, M., Wolkenklassifizierung mittels Bildsequenzanalyse auf GOME Satellitendaten, *Diploma thesis, University of Heidelberg, Germany,* 1998.

Wenig, M., Satellite Measurements of Long-Term Global Tropospheric Trace Gas Distributions and Source Strengths, Ph.D. thesis, University of Heidelberg, Germany, http://mark-wenig.de/diss_mwenig.pdf, 2001.

Wenig, M., N. Spichtinger, A. Stohl, G. Held, S. Beirle, T. Wagner, B. Jähne, and U. Platt, Intercontinental transport of nitrogen oxide pollution plumes, *Atmos. Chem. Phys.*, *3*, 387-393, 2003.

Wenig, M., S. Kühl, S. Beirle, E. Bucsela, B. Jähne, U. Platt, J. Gleason, and T. Wagner, Retrieval and analysis of stratospheric NO_2 from the Global Ozone Monitoring Experiment, *J. Geophys. Res.*, *109*, D04315, doi:10.1029/2003JD003652., 2004.

Wickert, B., Berechnung anthropogener Emissionen in Deutschland für Ozonsimulationen, Ph.D. thesis, University of Stuttgart, Germany, 2001.

Wooster M. J., Y. H. Zhang, Boreal forest fires burn less intensely in Russia than in North America, Geophys. Res. Lett., 31, L20505, doi:10.1029/2004GL020805, 2004.

Yienger, J.J., and H.Levy II, Empirical model of global soil-biogenic NO_x emissions, *J. Geophys. Res.*, *100* (D6), 11447-11464, 1995.

Zel'dovich, Y.B., and Y.P. Raizer, Rates of relaxation processes in gases (8/9), in Physics of Shock Waves and High-Temperature Hydrodynamic Phenomena, vol. I, *Academic, San Diego, Calif.*, 374-382, 1967.

Zhang, R., N.T. Sanger, R.E. Orville, and etal, Enhanced NO_x by lightning in the upper troposphere and lower stratosphere inferred from the UARS global NO_2 measurements, *Geophys. Res. Lett.*, *27*, 685-688, 2000.

Ziemke, J. R., S. Chandra, P. K. Bhartia, “Cloud slicing”: A new technique to derive upper tropospheric ozone from satellite measurements, J. Geophys. Res., 106(D9), 9853-9868, 10.1029/2000JD900768, 2001.

Ziereis, H., H. Schlager, P. Schulte, and etal, Distributions of NO, NO_x, and NO_y in the upper troposphere and lower stratosphere between 28° N and 61° N during POLINAT 2, *J.Geophys.Res.*, *105*, 3653-3664, 2000.

Danksagung/Acknowledgements

Abschließend möchte ich mich bei allen bedanken, die mich in den letzten Jahren begleitet und zum Gelingen dieser Arbeit beigetragen haben:

Bei Herrn Prof. Dr. Ulrich Platt möchte ich mich für das interessante Thema und seine vielen begeisterten (und begeisternden) Anregungen und Ideen bedanken.

Herrn Prof. Dr. Jähne danke ich für die interessierte Begutachtung dieser Arbeit.

Thomas Wagner danke ich für die vielen Anregungen und Diskussionen. Stets ist er bei Fragen ein geduldiger und kompetenter Ansprechpartner und überhaupt mehr als ein toller „Chef“.

Bei der Auswertung der GOME-Daten konnte ich auf umfangreiche Routinen zurückgreifen, die auf Thomas Wagner, Carsten Leue, Mark Wenig und Stefan Kraus zurückgehen. Die Auswertung der SCIAMACHY-Daten wurde durch die Programmierung von Tim Deutschmann und Christian Frankenberg ermöglicht.

Meinen Kollegen am Institut für Umweltphysik, besonders den Mitgliedern der Satellitengruppe, danke ich für das gute Miteinander, moralische Unterstützung, Schokolade, Korrekturlesen und Diskussionen; nennen möchte ich Christian Frankenberg, Christoph von Friedeburg, Michael Grzegorski, Klaus-Peter Heue, Jens Hollwedel, Fahim Khokhar, Sven Kühl, Thierry Marbach, Janis Pukite, Suniti Sanghavi, Oliver Sebastian, Roman Sinreich, Mark Wenig und Walburga Wilms-Grabe.
Besonders die Diskussionen mit Klaus Pfeilsticker und Roland von Glasow haben mir viele neue Impulse gegeben.

Die Zusammenarbeit mit der TUM im Rahmen von NOXTRAM habe ich als sehr fruchtbar erlebt. Ein besonderer Dank gilt Andreas Stohl für viele interessante Kommentare und Nicole Spichtinger für viele Diskussionen und ihren Einsatz beim Durchführen der FLEXPART Läufe.

John Burrows möchte ich danken, dass er GOME und SCIAMACHY realisiert und so diese Arbeit überhaupt erst ermöglicht hat.

I would also like to thank many colleagues from other institutes for interesting discussions, suggestions and fruitful cooperations: Andreas Richter from IUP Bremen, Henk Eskes and Folkert Boersma from KNMI, Randall Martin from Halifax University, Martin Schultz from MPI Hamburg, Franz Rohrer and Nicola Toenges-Schuller from FZ Jülich and Bill Simpson from University of Alaska Fairbanks, who called my attention to Prudhoe Bay.

Verena Röhrig danke ich für ihre umfangreiche Englischkorrektur.

Meinen Eltern und meiner Frau möchte ich gerne persönlich danken.